Synthesis and characterization of nanostructured electrode materials for rechargeable lithium ion batteries

Min Sik Park
University of Wollongong

Synthesis and Characterization of Nanostructured Electrode Materials for Rechargeable Lithium Ion Batteries

A thesis submitted in fulfillment of the requirements

for the award of

DOCTOR OF PHILOSOPHY

By

MIN SIK PARK

Institute for Superconducting and Electronic Materials

Faculty of Engineering

2008

Declaration

I, Min-Sik Park declare that this thesis, submitted in fulfillment of the requirements for the award of Doctor of Philosophy, in the Institute for Superconducting and Electronic Materials, in the Faculty of Engineering, University of Wollongong, is wholly original work unless otherwise referenced or acknowledged. This thesis has not been submitted for qualifications at any other academic institution.

Wollongong, Australia

March 2008

“Anybody who has been seriously engaged in scientific work of any kind realizes that over the entrance to the temple of science are written the words: ‘You must have faith.’ It is a quality which the scientist cannot dispense with.”

-Max Planck (The Nobel Prize in Physics, 1918)-

Acknowledgements

This thesis is the result of my research work during the past three and half years, which was conducted in the Institute for Superconducting and Electronic Materials (ISEM) at the University of Wollongong in Australia and in the Tokyo Institute of Technology in Japan. I would like to express my deep and sincere gratitude to all those who gave me the possibility to complete this thesis. In the first place, I want to thank Prof. Shi-Xue Dou, the Director of ISEM, and Prof. Hua-Kun Liu, my academic supervisor, for their financial support and excellent supervision for my PhD degree. I wish to acknowledge the support of Prof. Guo-Xiu Wang for his helpful supervision and encouragement throughout my PhD candidature. I am also grateful to my external supervisors, Prof. Yong-Mook Kang at Kongju National University in the Republic of Korea, and Prof. Atsuo Yamada at the Tokyo Institute of Technology in Japan, for their valuable guidance and fruitful discussions of my research work. Many thanks should be addressed to all the technical and academic members of ISEM at the University of Wollongong in Australia. I also wish to extend my warmest thanks to all those who have helped me with my work at the Tokyo Institute of Technology in Japan. In particular, I wish to thank Dr. Tania Silver, for revising the English of my manuscripts and Dr. David Wexler and Dr. Jung-Ho Kim for their professional advice and experience sharing on analysis work.

I feel a deep sense of gratitude to my mother and brother. Without their encouragement and understanding it would have been impossible for me to finish this work. My special gratitude is due to my father, who passed away during my research abroad, for his loving support of my intellectual growth. I dedicate this thesis to my family.

Abstract

State-of-the-art rechargeable lithium-ion battery technology has now paved the way for advanced energy storage systems to take their place in a variety of portable electronics. High cell voltage, good cycle life, and an attractive combination of energy and power generation are on the verge of being guaranteed for high-power and large-scale applications, such as plug-in hybrid vehicles. This investigation examines the circumstances attending the development of the rechargeable lithium-ion battery, to seek a better understanding of the factors affecting its electrochemical performance. The major objective of this work is to determine the advantages and drawbacks of tin dioxide (SnO_2) nanostructured materials as alternative anode materials and to suggest promising structural modifications in order to improve their electrochemical properties. Another important objective is to identify the correlation between electrochemical performance and particle size minimization in the lithium iron phosphate ($LiFePO_4$) system, a promising cathode material, and to give further evidence supporting the incomplete room-temperature reaction mechanism.

The selection and assembly of nanostructured materials have been considered as central issues in the development of alternative anode materials that possess higher capacity and better cyclic retention compared to commercial graphite. SnO_2 has shown high capacity and a relatively low reaction potential with Li^+, and is thus under consideration as a possible candidate for high-power and high-energy applications. We have synthesized various types of SnO_2 nanostructured materials, such as nanopowders, nanowires, and nanotubes in this work, and their electrochemical properties have been carefully compared in order to demonstrate the effects of their morphological differences on the electrochemical performance, based on

thermodynamic and kinetic considerations. By incorporating structural modifications into the SnO_2 nanostructured materials, we have formed Carbon encapsulated SnO_2 nanopowders and nanowires by simple decomposition of malic acid ($C_4H_6O_5$) at low temperature, which effectively improved specific capacity and cyclic performance. Combining surfactant mediated synthesis and the sol–gel vacuum suction method, SnO_2–mesoporous organo-silica nano-array (MOSN) nanocomposites were prepared for controlling the large volume variation of SnO_2 during cycling, where the MOSN could act as a mechanical buffer, resulting in a strong enhancement of cyclic retention.

On the other hand, the reaction mechanism and phase transition of $LiFePO_4$ at room temperature have not been fully understood yet. In pursuit of extending our understanding, we have prepared $LiFePO_4$/C nanocomposites with different particle sizes and characterized their fundamental crystal structure, which is directly related to the electrochemical behavior. Considering the fact that the room temperature phase diagram is essential to understand the facile electrode reaction of Li_xFePO_4 ($0 < x < 1$), here, we have suggested experimental evidence for isolation of an intermediate solid solution phase at around $x = 0.93$ at room temperature, which strongly supports the incomplete miscibility gap model. More interestingly, the impacts of air exposure on the $LiFePO_4$/C nanocomposites have been systematically investigated as a function of temperature. We found that Li^+ could be spontaneously extracted from the host structure, even at room temperature under air atmosphere. This finding also can explain the room temperature phase transition of $LiFePO_4$ and provide the reason for the undesirable Li^+ loss that is induced by external factors at room temperature.

Table of Contents

1. Introduction

Energy storage technology, including batteries, fuel cells, and supercapacitors, is currently being addressed as a critical issue for a wide range of advanced electronic devices, such as portable power systems and plug-in hybrid vehicles. The rechargeable lithium-ion battery is the most suitable energy storage system for these purposes, because it has several advantages over other competing rechargeable battery systems. In practice, it is much smaller and lighter than nickel cadmium (Ni-Cd) and nickel metal hydride (Ni-MH) rechargeable batteries, and it also offers excellent energy density, which can be traded for high power.

One of the primary objectives behind the research on the rechargeable lithium-ion battery is the development of advanced electrode materials that possess a higher lithium storage capacity, lower cost, better rate capability, and greater safty than the commercial anode and cathode materials, graphite and lithium cobalt oxide ($LiCoO_2$), respectively. Many applied battery research programs are being conducted by governments, research groups, and industry partners to overcome these key barriers inherent to the commercial electrode materials, so that this technology may be rendered practical for use in the high-power and large-scale applications. Considering the fact that these barriers can be addressed by the choice of materials used in the cell chemistry, the development of new electrode materials is essential for the next generation of batteries. New electrode materials will improve the performance of rechargeable lithium-ion batteries, while simultaneously enhancing their inherent stability, leading to longer cycle life and better safety. However, there is a strong need to identify and understand the fundamental crystal structure and charge transfer mechanism of candidate materials, because their

electrochemical performance is thought to be directly related to the intrinsic properties of materials, governing the kinetics of Li^+ diffusion and charge transfer. Nanostructured electrode materials are currently of interest for advanced rechargeable lithium-ion batteries because of their attractive properties, such as higher surface area and shorter Li^+ diffusion length compared to the bulk forms. These features are able to facilitate charge transfer and improve stability and specific charge, even at high current rate during electrochemical reactions. The recent pervasive trends in research into the electrode materials basically fall into three categories: (1) the fabrication of nanostructured materials, (2) structural modifications of the materials on the nanoscale, and (3) acquiring a comprehensive understanding of the crystal chemistry of the materials in order to overcome their practical limitations in commercial use.

The aim of this work is to extend our understanding of the electrochemical properties of nanostrucured electrode materials for the rechargeable lithium-ion battery and highlight their advantages and drawbacks in order to establish new guidelines for further investigations. Part I of the experimental results section describes the synthesis and evaluation of the various types of tin dioxide (SnO_2) based nanostructured materials as potential anode materials for use in high-power and high-energy applications. The general advantages of SnO_2 nanostructured materials are systematically demonstrated, based on the thermodynamics and kinetics during electrochemical reactions. Next in part II, I discuss the crystal chemistry and fundamental properties of lithium iron phosphate ($LiFePO_4$), which is currently considered the most likely candidate for large-scale applications, in order to support the incomplete electrochemical reaction model at room temperature and identify the phase transition mechanism in its nanoscale form.

Chapter 2 contains recent research trends and a comprehensive background on rechargeable lithium-ion battery science, together with a careful literature review, in order to provide new insight to further investigations of nanostructured electrode materials.

In Chapter 3, the overall experimental methodology used for this work is described in detail. All the experimental parameters are carefully defined and have been optimized in advance. New approaches to the preparation of nanostructured materials are introduced.

Part I (Chapter 4−8) introduces the synthesis and electrochemical properties of the various SnO_2 nanostructured materials prepared by various techniques. The SnO_2 nanostructured materials, due to their structural advantages, offer strong enhancement to the capacity and cyclic retention of lithium-ion batteries, so that they have real promise as advanced anode materials. The effects of morphological modification on the electrochemical performance are systematically demonstrated from the thermodynamic and kinetic point of view.

In Chapter 4, we present the electrochemical performance of self-catalyst grown SnO_2 nanowires with the tetragonal rutile structure that were synthesized by a thermal evaporation method without any conventional metal catalysts. Mechanical ball milling was employed to prepare a mixture of Sn and SnO powder as an evaporation source. The anodic performance of SnO_2 nanowires showed higher Li^+ storage and an improved initial coulombic efficiency (47%) compared to SnO_2 powder (31%). The enhanced electrochemical performance of SnO_2 nanowires is believed to result from the combination of unique nanostructures with high length to diameter ratio and the absence of traditional metal catalysts.

In Chapter 5, the electrochemical performances of one-dimensional (1D) SnO_2 nanomaterials, which include nanotubes, nanowires, and nanopowders, are compared to define the most favorable morphology when SnO_2 nanostructured materials are adopted as the electrode material for lithium-ion batteries. Changes in the morphology of SnO_2 are closely related to its electrochemical performance. Some SnO_2 nanomaterials feature not only an increased energy density, but also enhanced Li^+ transfer. The correlation between the morphological characteristics and the electrochemical properties of SnO_2 nanostructured materials is discussed. The interesting electrochemical results obtained here on SnO_2 nanomaterials indicate the possibility of designing and fabricating attractive nanostructured materials for lithium-ion batteries.

In Chapter 6, we introduce carbon encapsulated SnO_2 composites, which were prepared by thermal evaporation and decomposition of malic acid ($C_4H_6O_5$) at low temperature, to demonstrate their potential use for application in lithium-ion batteries. The solution based chemical approach was effective for coating amorphous C layers onto the surface of SnO_2 nanopowders without significant oxygen reduction. The desirable crystalline structure and oxygen stoichiometry of SnO_2 were maintained, while amorphous C homogeneously encapsulated the SnO_2 nanopowders. The strong enhancement that was observed for the anodic reversible capacity and the cyclic performance of the C-encapsulated SnO_2 nanocomposites is discussed in detail. It is expected that low-temperature processing can be a new general route for preparing nanocomposites with C from an economic point of view.

In Chapter 7, I report on the synthesis, characterization, and electrochemical properties of C encapsulated SnO_2 nanowires, which were carefully investigated in an effort to synergistically

enhance the anodic properties. The simple evaporation of malic acid ($C_4H_6O_5$) was sufficient to form an amorphous C phase on the surface of the SnO_2 nanowires at low temperature, leading to a further enhancement of the electrochemical performance. The additional C phase could introduce a higher reversible capacity and an improved initial coulombic efficiency compared to SnO_2 nanowires. It is believed that the conductive C phase could provide more electron migration routes between active materials, as well as effectively reducing the capacity loss due to large volume variation in the metal phase.

In Chapter 8, we suggest a SnO_2–mesoporous organo-silica nanoarray (MOSN) nanocomposite as a promising anode material. The SnO_2–MOSN nanocomposite was prepared by surfactant mediated synthesis combined with a sol–gel vacuum suction method in which SnO_2 is successfully incorporated inside the periodic nanoholes in the MOSN or coated on its surface. The MOSN, with a high aspect ratio of length to width, could not only maintain its structure but also effectively accommodate the volume expansion of the SnO_2 during electrochemical reactions with Li^+. The SnO_2–MOSN composite showed a high reversible capacity of 420 mA $h \cdot g^{-1}$, with greatly improved capacity retention and lower initial irreversible capacity compared to SnO_2 nanopowders. This interesting anodic performance of SnO_2–MOSN nanocomposite supports the potential use of MOSN for lithium-ion batteries.

Part II (chapter 9−10) discusses a significant contribution to the incomplete room-temperature phase diagram of $LiFePO_4$, in an attempt to identify its phase transition mechanism and dependence on particle size modification. Moreover, side reactions are considered, which could be attributed to the undesirable Li^+ loss and could change the surface and bulk properties of the material.

Chapter 9 shows that the room-temperature phase diagram is essential to understand the facile electrode reaction of Li_xFePO_4 ($0 < x < 1$), but it has not been fully understood. Here, we have succeeded in isolating an intermediate solid solution phase at around $x = 0.93$ at room temperature, which strongly supports the incomplete miscibility gap model. Using high-resolution synchrotron X-ray diffraction (XRD) analysis, particle size-dependent modification of the phase diagram is systematically demonstrated.

In Chapter 10, the impact of air exposure on the $LiFePO_4$/C nanocomposite is systematically investigated as a function of temperature. The electrochemical results prove that a significant amount of Li^+ is extracted from the olivine structure during air exposure even at room temperature. A treatment at high temperature under air atmosphere leads to the extraction of an increased quantity of Li^+. This phenomenon changes the initial surface and bulk properties of the material. An important technical precaution has been addressed and should be taken into account when reducing the particle size of $LiFePO_4$.

In Chapter 11, a general overview is provided, and the conclusions of this study are summarized. Suggestions for further investigations are also included.

2. Literature Review

Lithium-ion Battery

Rechargeable Lithium-ion Battery

The rechargeable lithium-ion battery has become a very popular energy storage system, and lithium-ion batteries are commonly used in advanced electronic applications as portable power sources, because of their light-weight and high-energy density. According to a recent analysis by Frost & Sullivan,[1] a market research organization, the increasing market demands for advanced functional energy storage systems and investment in technological developments and innovations are combining to create significant growth in the rechargeable lithium-ion battery market. The market involves revenues of $5.89 billion on shipments of nearly 1.76 billion secondary units, on their latest figures, and the firm estimates that this will grow to nearly 3.99 billion units in 2013.

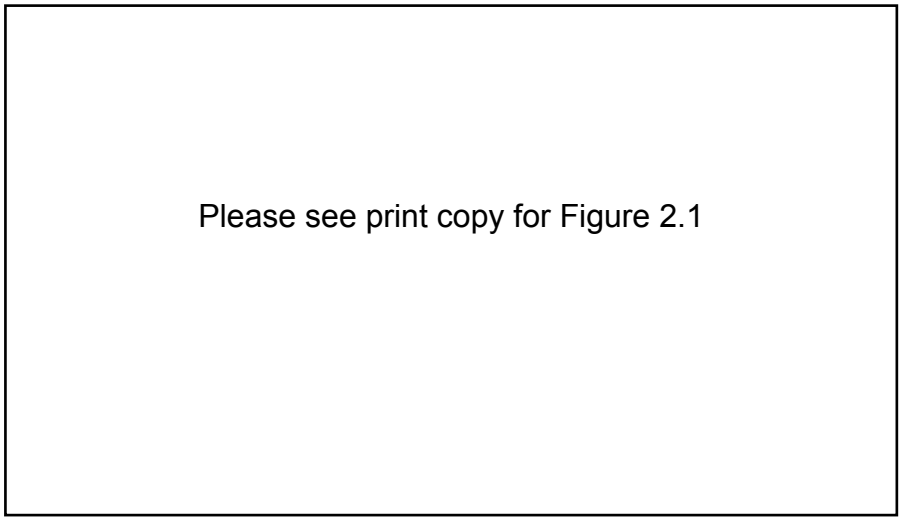

Figure 2.1: *A comparison of energy density for Ni-Cd, Ni-MH, and lithium-ion rechargeable batteries.*[2]

The rechargeable lithium-ion battery provides fundamental advantages over existing, traditional rechargeable battery system, such as nickel cadmium (Ni-Cd) and nickel metal hydride (Ni-MH) systems. The specific energy density for rechargeable lithium-ion cells can approach 200 $Wh \cdot kg^{-1}$, with a typical voltage of 3.6 V, which is much higher than those of Ni-Cd and Ni-MH batteries, as shown in Figure 2.1 and Table 2.1.[2] In addition, the rechargeable lithium-ion batteries have no memory effect, long cycle life, and excellent discharge performance. For these reasons, the demand for rechargeable lithium-ion batteries can continue to grow, largely due to the rapid increase in high-power and high-energy applications in areas such as defense, and the automotive, and aerospace industries.[3-7]

Table 2.1: *Characteristics of some battery systems used commercially.*[7]

Please see print copy for Table 2.1

Although the rechargeable lithium-ion batteries offer high energy density, they have not yet matured enough for use in those applications. Research and development are needed on electrode materials as well as electrolytes. In addition, their key problems due to the repeatability and safety issues related to these highly energetic materials must be overcome.

Reaction Mechanism of Rechargeable Lithium-ion Battery

A rechargeable lithium-ion battery, in principle, is a type of electrochemical cell that converts stored chemical energy into useful electrical energy. It consists of the three primary functional components of a positive electrode (cathode), negative electrode (anode), and electrolyte. The operation of rechargeable lithium-ion batteries is simply based on the theory of Li^+ ions migrating between the cathode and the anode through the electrolyte. Unlike primary batterries, rechargeable batterries, once discharged, can be returned to their fully charged state and repeatedly discharged for up to hundreds of cycles. They are, therefore, fundamentally different from non-rechargeable primary lithium batteries, in that the basic form of the cathode and anode materials does not change.[8-9]

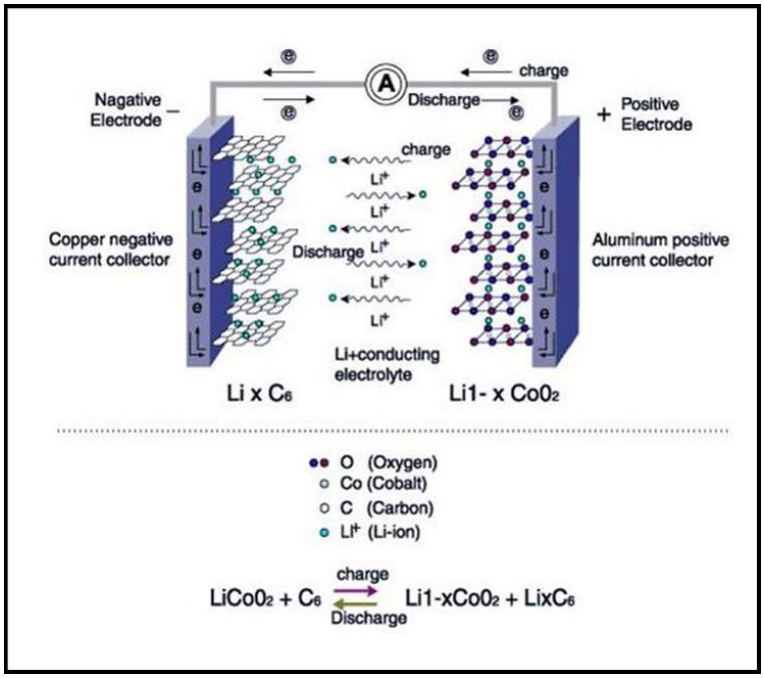

Figure 2.2: *Schematic of the charge and discharge mechanisms in a rechargeable lithium-ion battery.*

The cathode and anode materials of the most common commercial rechargeable lithium-ion battery are lithium cobalt oxide ($LiCoO_2$) and graphite, respectively. The electrolyte is a lithium salt ($LiPF_6$) dissolved in an organic solvent. In this system, the overall chemical reaction is divided into two physically and electrically separated processes: one is an oxidation process at the negative electrode wherein the valence of at least one species becomes more positive, and the other is a reduction process at the positive electrode wherein the valence of at least one species becomes more negative. Li^+ ions transfer from the cathode ($LiCoO_2$) to the anode (graphite) via the electrolyte when the battery is being charged. On discharge, these Li^+ ions are reversibly extracted from the anode (graphite) and spontaneously inserted into the cathode ($LiCoO_2$), releasing energy in the process, as described in Figure 2.2. The reaction mechanisms in the commercial cell are described below:[10]

$$LiCoO_2 \leftrightarrow Li_{1-x}CoO_2 + xLi^+ + xe^- \quad \text{(cathodic reaction)} \qquad (2.1)$$

$$C + xLi^+ + xe^- \leftrightarrow Li_xC \quad \text{(anodic reaction)} \qquad (2.2)$$

A Brief History

In the 1970s, the first concept of rechargeable lithium-ion batteries were proposed by M.S. Whittingham,in batteries in which titanium sulfide (Li_xTiS_2) was employed as the cathode and metallic lithium as the anode.[11-14] However, the safety issue due to the inherent instability of metallic lithium during charging led to the development of safer battery systems.[15-16] In the following several years, rechargeable lithium-ion batteries were designed to overcome the safety problems associated with the highly reactive metallic lithium anode. Various cathode materials,

such as sulfides (MoS_2, $NiPS_2$, and TiS_2),[12,14] oxides (V_2O_5, MoO_3, and V_6O_{13}),[17-19] and layered oxides (MO_2; M = Ti, V, Mn, Mo, W, Nb, Ru, Ir, Os),[20-21] were employed, with a practical implementation of the concept of reversible operation with metallic lithium anode and a choice of electrolytes. Despite many efforts towards stabilization, the critical drawbacks of the metallic lithium have remained as an open problem to be solved.

In the early 1980s, the substitution of reversible Li^+ intercalation host compounds for metallic lithium gave rise to a new generation of rechargeable lithium-ion batteries.[21-23] Certain forms of carbon were developed that are capable of reversible Li^+ intercalation and can be used as materials for negative electrodes.[24-26] In 1991, Sony commercialized the rechargeable lithium-ion battery and is presently the largest supplier of this type of battery. The cell utilized graphite as an alternative to the metallic lithium anode and $LiCoO_2$ as the cathode, where the reaction mechanism between Li^+ and graphite is an intercalation-type reaction. In the intercalation process, the Li^+ are reversibly stored between the layers in a graphite framework. These batteries revolutionized consumer electronics.[27-31] On the other hand, in a pursuit of the development of alternative anode materials, in 1997, Fujifilm claimed that a high capacity Li^+ storage material in metal oxide form had been synthesized that could replace the carbonaceous anode materials currently in extensive use as anodes of rechargeable lithium-ion batteries.[32] However, large irreversible capacity and poor cyclic retention of the metal oxides have remained as major limitations for commercial use.

As regards to the cathode material, M. Thackeray identified manganese spinel ($LiMn_2O_4$) as a cathode material in 1983.[33] Spinel showed great promise because of its low cost, good electronic conductivity, and good structural stability. Although pure manganese spinel shows

fade with cycling, this can be overcome with additional chemical modification of the material. Manganese spinel is also currently used in commercial cells. In 1989, A. Manthiram and J.B. Goodenough at the University of Texas at Austin suggested that cathodes containing polyanions, such as sulfates, show higher voltage than oxides, due to the inductive effects of the polyanion. Following this, in 1996, Goodenough and coworkers discovered the electrochemical utility of an olivine material, lithium iron phosphate ($LiFePO_4$).[34] This is now an important and emerging cathode material for rechargeable lithium-ion batteries, due in part to its enhanced safety compared to other lithium-ion chemistries. Cells containing $LiFePO_4$ cathodes have been commercialized by multiple companies, including Phostech, Valence Technology, A123 Systems, and Aleees.

Electrochemical Considerations

Electrochemical Thermodynamics

In an electrochemical cell, the overall reaction can be described by two half-cell reactions: one for the anode and one for the cathode. The cathodic reaction can be represented as Equation 2.3 and the anodic reaction can be represented as Equation 2.4.[35-36]

$$aA + ne^- \leftrightarrow cC \tag{2.3}$$

$$bB - ne^- \leftrightarrow dD \tag{2.4}$$

where a is the number of moles of A, the standard reaction potential is E_C^0, b is the number of

moles of B, and the standard reaction potential is E_A^0. The anode and the cathode are connected internally through an electrolyte, which is an ionic conductor, thereby providing the medium for charge transfer of ions between the two electrodes. It is typically a solvent containing dissolved salts, acids, or bases. The electronic conduction in the electrolyte should be negligible to avoid self-discharge by internal short-circuiting.[35] The overall reaction is given by Equation 2.5.

$$aA + bB \leftrightarrow cC + dD \tag{2.5}$$

An electrochemical cell in which the overall cell reaction has not reached chemical equilibrium can do electrical work ($-W$) done by the cell is defined as nE, where n is the number of moles of electrons that are transferred and E is the potential difference between its two half-cells (Equation 2.6).[35-36] In this relationship, the Faraday constant F is required to obtain coulombs from moles of electrons.

$$W = \Delta G = -nFE \tag{2.6}$$

$$\Delta G^0 = -nFE^0 \tag{2.7}$$

In the standard state, the change in standard free energy, ΔG^0, is given by Equation 2.7, where the standard cell potential is $E^0 = E_C^0 - E_A^0$. Under conditions other than the standard state, E can be given by Equation 2.8.

$$E = E^0 - \frac{RT}{ZF} \ln \frac{(aC)^c (aD)^d}{(aA)^a (aB)^b} \tag{2.8}$$

$$\Delta G^0 = -nFE - \frac{nRT}{F}\ln\frac{(aC)^c(aD)^d}{(aA)^a(aB)^b} \quad (2.9)$$

where Z is the number of electrons transferred in the cell, *(aC)* is the activity of *C*, etc. The change in ΔG^0 of a reaction is the driving force for a battery (Equation 2.9), which enables it to deliver electrical energy.

The Cell Voltage

The theoretical standard cell voltage can be determined from the electrochemical series using E^o values (Equation 2.10):

$$E_{cell} = E_A - E_C \quad (2.10)$$

This is the standard theoretical voltage. The theoretical cell voltage is modified by the Nernst equation, which takes into account the non-standard state of the reacting components. The Nernstian potential will change with time, either because of use or of self-discharge, by which the activity (or concentration) of an electro-active component in the cell is modified. Thus the nominal voltage is determined by the cell chemistry at any given point of time. The actual voltage produced will always be lower than the theoretical voltage, due to polarization and the resistance losses (I-R drop) of the battery, and is dependent upon the load current and the internal impedance of the cell.[35] These factors are dependent upon electrode kinetics and thus vary with temperature, state of charge (SOC), and the age of the cell. The actual voltage appearing at the terminals needs to be sufficient for the intended application.

On the other hand, when an electrode is not at equilibrium, an overpotential exists, E is the actual potential, and E^o is the equilibrium potential, given by Equation 2.11, where η is the overpotential.

$$\eta = E - E^0 \tag{2.11}$$

Other thermodynamic quantities can be derived from electrochemical measurements. The cell voltage is determined by the change in the Gibbs free energy that is associated with the virtual chemical reaction between the species in the electrode.[35-36] Therefore, the voltage across the cell will vary with temperature if the value of ΔG is temperature-dependent. The entropy change (ΔS) in a cell reaction is given by the temperature dependence of ΔG:

$$\Delta S = -\left(\frac{\partial \Delta G}{\partial T}\right)_P \tag{2.12}$$

$$\Delta S = nF\left(\frac{\partial E}{\partial T}\right)_P \tag{2.13}$$

$$\Delta H = \Delta G + T\Delta S = nF\left[T\left(\frac{\partial E}{\partial T}\right)_P - E\right] \tag{2.14}$$

where ΔH is the enthalpy change and T is the absolute temperature (K). The equilibrium constant (K_{eq}) for the same reaction can be obtained from Equation 2.15. Thus the variation of the cell voltage with temperature depends upon the entropy change that would occur as the result of the virtual reaction of the cell.

$$RT \ln K_{eq} = -\Delta G^0 = nFE^0 \quad (2.15)$$

Electrochemical Kinetics

Thermodynamics can tell us the feasibility of a cell reaction occurring and the theoretical cell voltage, however, it is necessary to consider kinetics to gain a better idea of what the actual cell voltage may be, since rates of charge transfer are usually the limiting factor.[35,37] The rates of the chemical reactions are governed by the Arrhenius relationship, and the rate of reaction can be described by Equation 2.16, where ΔG is the activation energy for the reaction, T is the temperature, and R is the universal gas constant. In this case, the rate of the reaction can be measured from the current produced, since current is the amount of charge produced per unit time and therefore proportional to the number of electrons produced per unit time, i.e. proportional to the rate.

$$k = \alpha \exp\left(\frac{-\Delta G}{RT}\right) \quad (2.16)$$

Considering a general reaction for the oxidation of a metal at an anode, the rate of this reaction, k_a is governed by the Arrhenius relationship, as depicted in Equation 2.18, where K is the rate constant. From Faraday's law, Equation 2.19 can be derived.

$$M \rightarrow M^{z+} + ze^- \quad (2.17)$$

$$k_a = K \exp\left(\frac{-\Delta G}{RT}\right) \tag{2.18}$$

$$i_0 = zFk_a = zFK \exp\left(\frac{-\Delta G}{RT}\right) \tag{2.19}$$

If an overpotential is now applied in the anodic direction, the activation energy of the reaction is reduced to $(\Delta G - \alpha zF\eta)$, where α is the symmetry factor of the electrical double layer, usually 0.5. Therefore, the Tafel equation applies, as described in Equation 2.21.

$$i_a = zFK \exp\left(\frac{-(\Delta G - \alpha zF\eta)}{RT}\right) = zFK \exp\left(\frac{-\Delta G}{RT}\right) \exp\left(\frac{\alpha zF\eta}{RT}\right) \tag{2.20}$$

$$\therefore i_a = i_0 \exp\left(\frac{\alpha zF\eta}{RT}\right) \tag{2.21}$$

By taking natural logs and rearranging, this can be written as Equation 2.22, where b_a is the anodic Tafel slope. Or, in terms of electrode potential (Equation 2.24):

$$\eta = \left(\frac{RT}{\alpha zF}\right) \ln\left(\frac{i_a}{i_0}\right) = b_a \log\left(\frac{i_a}{i_0}\right) \tag{2.22}$$

$$\ln(i_a) = \ln(i_0) + (E - E^0)\left(\frac{\alpha zF}{RT}\right) \tag{2.23}$$

$$E = b_a \log\left(\frac{i_a}{i_0}\right) + \alpha_a \tag{2.24}$$

Similarly, we can consider the reduction of metal ions at the cathode, and the activation energy will be decreased by $(1-\alpha)zF\eta$, giving as shown in Equation 2.28, where b_c is the cathodic Tafel slope.[35,40]

$$M^{z+} + ze^- \rightarrow M \tag{2.25}$$

$$i_c = i_0 + \exp\left(\frac{(1-\alpha)zF\eta}{RT}\right) \tag{2.26}$$

$$\eta = \frac{RT}{(1-\alpha)zF}\ln\left(\frac{i_c}{i_0}\right) \tag{2.27}$$

$$E = b_c \log\left(\frac{i_c}{i_0}\right) + a_c \tag{2.28}$$

In a battery there are two sets of Tafel curves present, one for each material. During discharge, one material will act as the anode and the other as the cathode. During charging the roles will be reversed. The actual potential difference between the two materials for a given current density can be found from the Tafel curve:[35,40] The anodic potential, E_A, and cathodic potential, E_C, can be found from the curve. The total cell potential is the difference between the two. On discharge, the potential is always less than thermodynamics alone predicts. It can be calculated from

Equation 2.29. Upon discharge the cell potential may be further decreased by the Ohmic drop due to the internal resistance of the cell, *r*. Thus the actual cell potential is given by Equation 2.30, where *A* = geometric area relevant to the internal resistance.

$$V'_{cell} = E_C - |\eta_C| + E_A - |\eta_A| \tag{2.29}$$

$$V_{cell} = V'_{cell} - Ar \tag{2.30}$$

Similarly, on charging, the potential is greater than thermodynamics alone predicts and can be calculated by Equation 2.31. The cell potential may now be increased by the Ohmic drop, and the actual cell potential is given by Equation 2.32.

$$V'_{charge} = E_C + |\eta_C| + E_A + |\eta_A| \tag{2.31}$$

$$V_{charge} = V'_{charge} + iAr \tag{2.32}$$

Gibbs Phase Rule

A phase diagram presents the different possible phases of a system at equilibrium as a function of intensive properties, such as temperature, pressure, or composition. In general, when a system undergoes a thermodynamic process, there is some sort of energetic change within the system, associated with changes in pressure, volume, internal energy, or any sort of heat transfer. These changes bring the system into thermodynamic equilibrium, which can be defined by a

fundamental relation, the Gibbs phase rule below.[41]

$$F = C - P + 2 \tag{2.33}$$

where F is the number of degrees of freedom, C is the number of components, P is the possible number of stable phases. The phase rule amounts to setting the number of constraints equal to the number of variables so that an equilibrium state is determined.

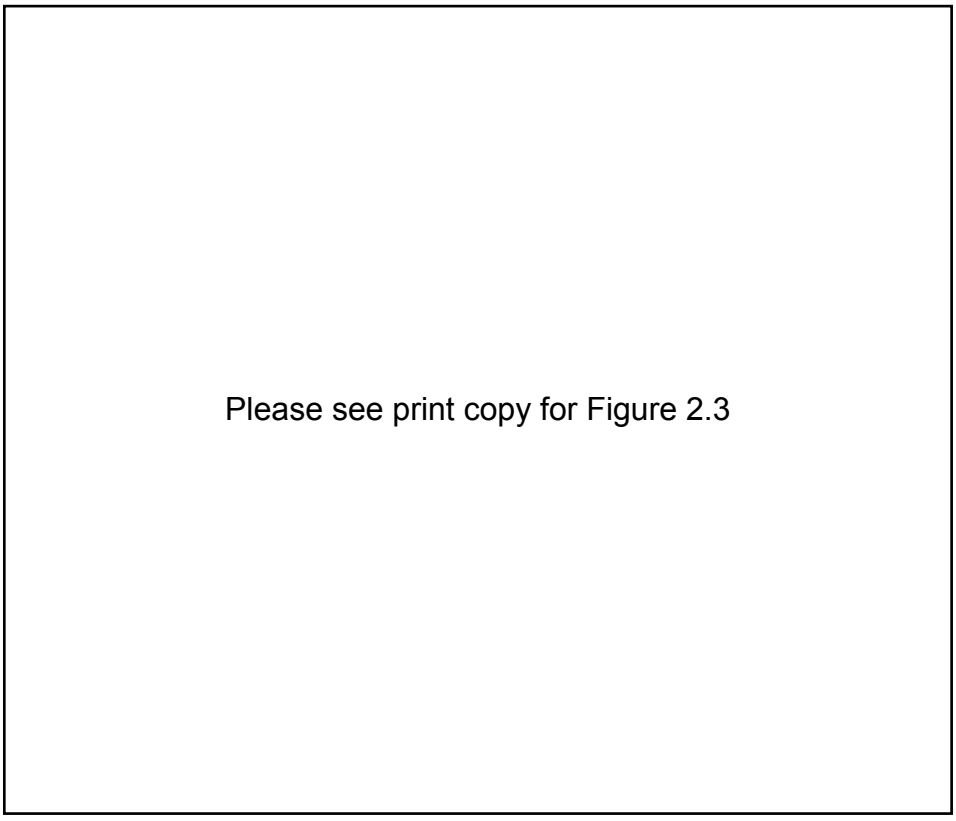

Figure 2.3: *Temperature and voltage binary phase diagram of lithium alloy (Li_xM). A voltage plateau corresponds to a phase coexistence region.*[41]

The charge and discharge process of an electrochemical cell is always accompanied by the transport of Li^+ and electrons. When the amount of the transported Li^+ or electrons exceeds a

certain threshold, a phase transition may occur either in the cathode or in the anode materials. Then, the phase transition can be observed by monitoring the cell potential because variables in this thermodynamic system are governed by the Gibbs phase rule as presented in Figure 2.3. In the lithium-ion cell, the electrode can be considered as a binary system ($C = 2$), consisting of a lithiated phase and its corresponding delithiated phase ($P = 2$). Under constant temperature and pressure, the degree of freedom is zero ($F = 0$), which means that all of the intensive variables then have fixed values in zero-degree-of freedom (ZDF) electrodes. The values of the chemical potentials of all species, as well as the electrical potential are constant ($F = 0$), regardless of the state of charge, and thus the amounts of phases present in such an electrode are also constant. This means that a charge or discharge experiment on a two-phase binary battery electrode will show a constant value of electrical potential, even though the overall composition and the amounts of the two phases present will vary. This has been demonstrated experimentally and is illustrated schematically in Figure 2.4.

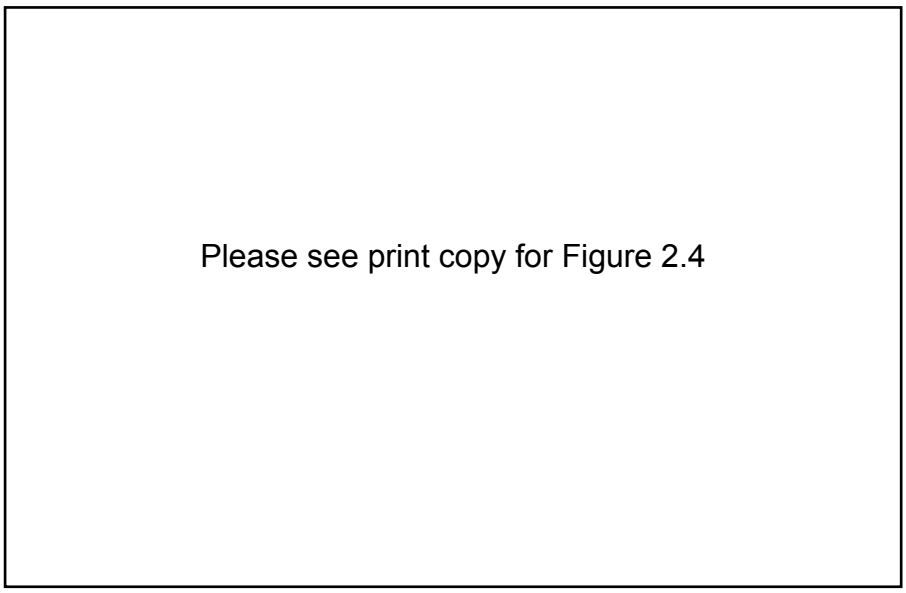

Figure 2.4: *A simplified isothermal phase stability diagram for the Li-Sn-O system assuming that the degree of freedom is zero (F = 0).*[41]

On the other hand, if there is only one phase present in a binary system, $C = 2$, $P = 1$, and thus $F = 1$, which means that the properties are dependent upon the composition within that phase. An example of this is the variation of the potential of an insertion reaction electrode as its composition changes during charge or discharge in a battery. An example of such a discharge curve is shown schematically in Figure 2.5. Its shape is due to a combination of factors, including the compositional dependence of the Fermi level of the electrons and the configurational entropy of guest ions within the host crystal structure.

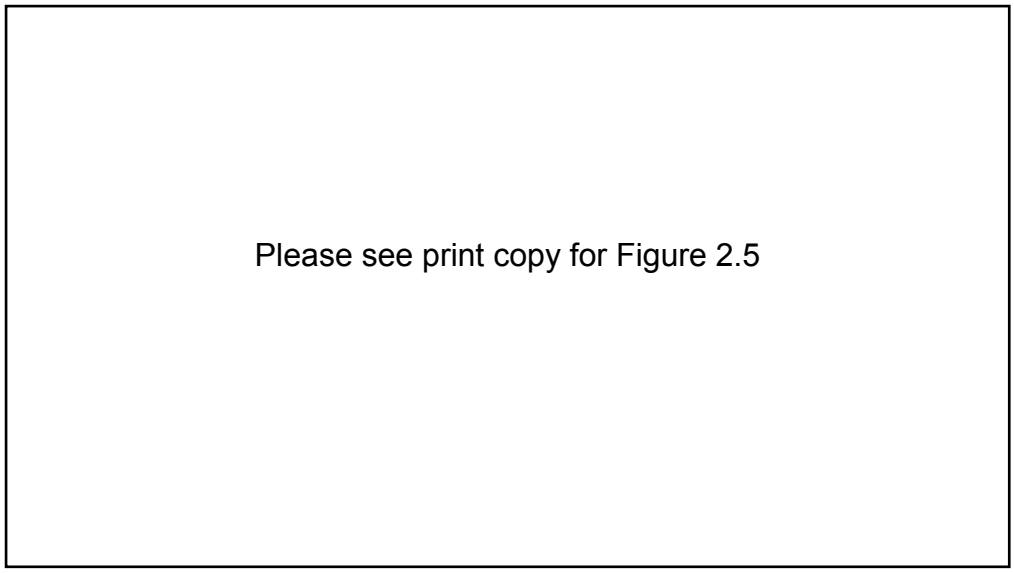

Figure 2.5: *A simplified isothermal phase stability diagram for the Li-Sn-O system assuming that that the degree of freedom is one (F = 1).*[41]

In the electrochemical system, variations in the slope of the galvanostatic discharge profile depend upon variations in the chemical potential of Li^+ at the surface of the bulk cathode. The chemical potential is determined by the intercept of μ_{Li}, with the line drawn tangent to the free energy curve. μ_{Li} is invariant in the two phase regime, as illustrated in Figure 2.6.[35,42]

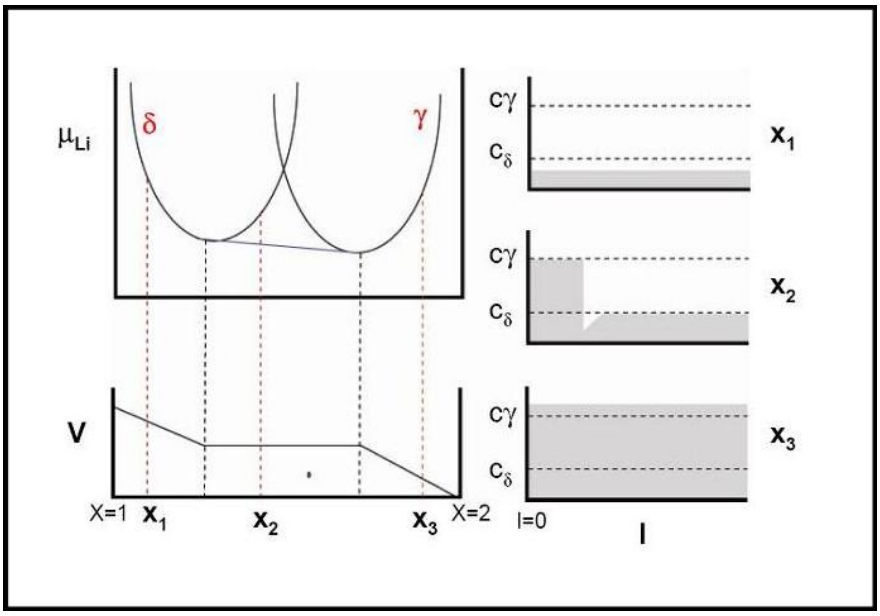

Figure 2.6: *Schematic of the relationship between the galvanostatic potential and the chemical potential in a rechargeable lithium-ion battery.*

In a multiphase system, the chemical potential of the i^{th} component (μ_i) is defined as the partial derivative of the Gibbs free energy with respect to n_i, the moles of component i, while other variables are held constant.

$$\left(\frac{\partial G}{\partial n_i}\right)_{T,P,n_{j\neq i}} = \mu_i \tag{2.34}$$

$$dG = \sum_i \mu_i dn_i \quad \text{with} \quad dn_i = v_i d\xi \tag{2.35}$$

where T is the temperature, P is the pressure, n_j is the quantity of component j at constant

temperature and pressure, ξ is the extent of the reaction in one mole, a quantity that is equal for the reactants at a certain stage of a reaction. For simplicity, v_i can be used as the universal symbol for the coefficient of the i^{th} reactants in the reaction equation, which is positive for the formation of substances and negative for the consumption of substances. When a reaction proceeds with v_i moles of reactant *i* involved, as in Equation 2.36, therefore, the theoretical potential can be calculated in Equation 2.37.

$$\Delta G = \sum_i \mu_i v_i \tag{2.36}$$

$$V = -\frac{1}{nF}\sum_i \mu_i v_i \tag{2.37}$$

Electrode Materials

In order to develop advanced electrode materials, two fundamental requirements must be satisfied for rechargeable lithium-ion batteries: (1) a high specific charge (in $Ah \cdot kg^{-1}$) and energy density (in $Ah \cdot L^{-1}$), and (2) a high (cathode) and low (anode) standard redox potential of the respective electrode reactions, leading to a high cell voltage.[3-5] Moreover, both cathode and anode materials have to be highly reversible to maintain the specific charge for hundreds of charge-discharge cycles. Thus, alternative electrode materials for high-power and high-energy density should combine a high specific charge with good rechargeability.

Anode Materials

Various materials have been proposed as anode materials for rechargeable lithium-ion batteries,

such as metallic lithium, transition metal oxides and chalcogenides, carbonaceous materials, and lithium alloys.[43-46] However, the practical use of these new materials has not been assessed yet. At present, graphite is employed as the commercial anode material, because it is the most capable anode material, considering its cycling efficiency and electrochemical reaction potential. The aim of recent research is the development of alternative materials that possess higher capacity and better stability than graphite.

Carbonaceous Materials

A variety of carbonaceous materials have been extensively investigated as intercalation anode materials. The morphological differences in the different carbonaceous materials have a great impact on their Li^+ intercalation behavior. The carbonaceous anode materials with sp^2 bonding between C atoms can be roughly classified as graphite, soft carbon, hard carbon, and carbon nanotubes (CNTs), from a crystallographic point of view.[47-49] Graphite has a layered structure with a perfect stacking order of graphene layers. Soft carbon refers to highly ordered carbon with a number of structural defects, whereas hard carbon refers to highly disordered carbon. The CNTs consist of multiple layers of graphite rolled in on themselves to form a tube shape. Among them, graphite is extensively used as the anode material of commercial rechargeable lithium batteries because it exhibits a more negative redox potential (~ 0.1 V) and its structural stability allows better cycling performance than other candidates, such as most metal oxides, chalcogenides, and lithium alloys.[50-54] The insertion of Li^+ into the graphite proceeds according to:

$$Li_xC \leftrightarrow xLi^+ + xe^- + C \qquad (2.38)$$

Li^+ from the cathode reversibly intercalates between graphene layers of the graphite, then forms LiC_6 (Figure 2.7(a)). A general feature of intercalation into graphite is the stepwise formation of a periodic array of unoccupied layer gaps at low concentrations of Li^+. Despite the great advantages of graphite, only one Li^+ can intercalate per six carbon atoms, as shown in Figure 2.7(b), which limits the specific charge of the electrode ($372 mAh \cdot g^{-1}$).[55-58] Besides the low capacity, the excess charge consumption in the first cycle is generally ascribed to solid electrolyte interphase (SEI) formation and corrosion-like reactions of Li_xC_6.[59-64] The lithium intercalation compounds are thermodynamically unstable in all known electrolytes, and the surface can be kinetically protected by the SEI films. This formation of passive films causes the irreversible consumption of charge, corresponding to a loss of capacity and deterioration of the graphite. Therefore, alternative anode materials should have higher Li^+ storage capacity and electrochemical stability.

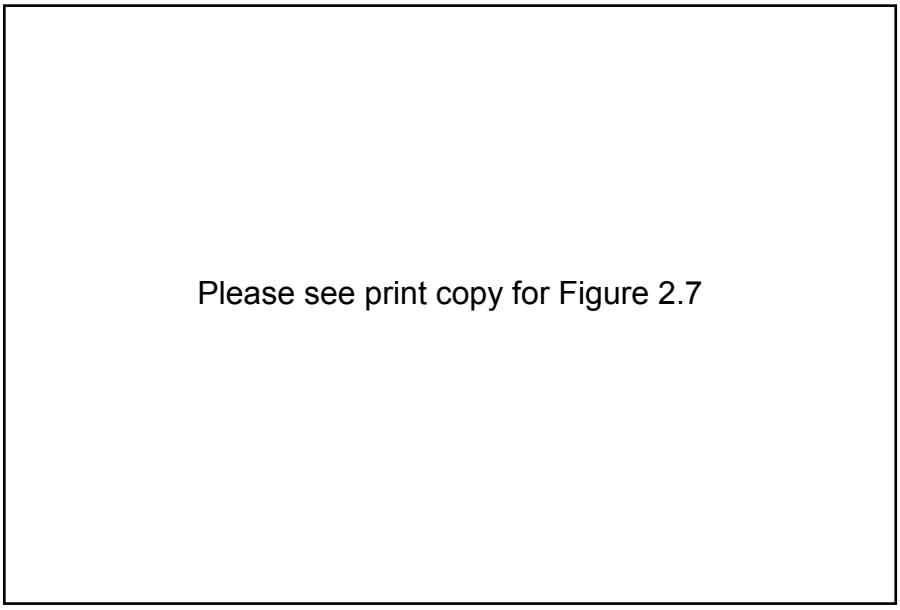

Figure 2.7: *Structure of LiC_6. a) Left: schematic drawing showing the AA layer stacking sequence and the aa interlayer ordering of the intercalated lithium. Right: simplified representation. b) View perpendicular to the basal plane of LiC_6.*[9]

On the other hand, much attention recently has been paid to the use of carbon nanotubes (CNTs) as an anode material because of their extraordinary thermal and mechanical stability, as well as their high electronic conductivity.[65] Compared to the other carbonaceous materials, the CNTs can react at a relatively low potential and provide a variety of Li^+ accommodation sites, namely, the spacing between the graphene layers, local turbostratic disorder arising from their highly defective structures, and the central core. In practice, the specific charge of CNTs is estimated to be higher than that of graphite.[65-67] Despite these desirable features, the practical use of CNTs is limited by their large irreversible capacity, which is caused by Li^+ trapping on structural defects such as dangling bonds and nanopores.[67-68]

Lithium Alloys

The replacement of commercial graphite anode by lithium alloys has been under investigation because of the feasibility of the electrochemical formation of lithium alloys in liquid organic electrolytes, as well as their higher theoretical capacity (Figure 2.8).[69-70] Various types of lithium alloys have been proposed as alternative anode materials for use in high power applications. The reaction usually proceeds reversibly according to the general scheme below:

$$Li_xM \leftrightarrow xLi^+ + xe^- + M \qquad (2.39)$$

Sequences of stoichiometric intermetallic compounds and Li_xM phases (M = Al, Si, Sn, Pb, In, Bi, Sb, Ag, and some multinary alloys) with considerable phase range are usually formed during lithiation of the metal M. The formation of Li_xM phases is in many cases reversible. Lithium alloys, Li_xM, are of highly ionic character (Zintl phases, $Li_x^{x+}\ M^{x-}$) which are usually fairly

brittle. Thus, mechanical stresses, related to the volume changes, induce a rapid decay in mechanical properties and, finally, pulverization of the electrode.[71-82]

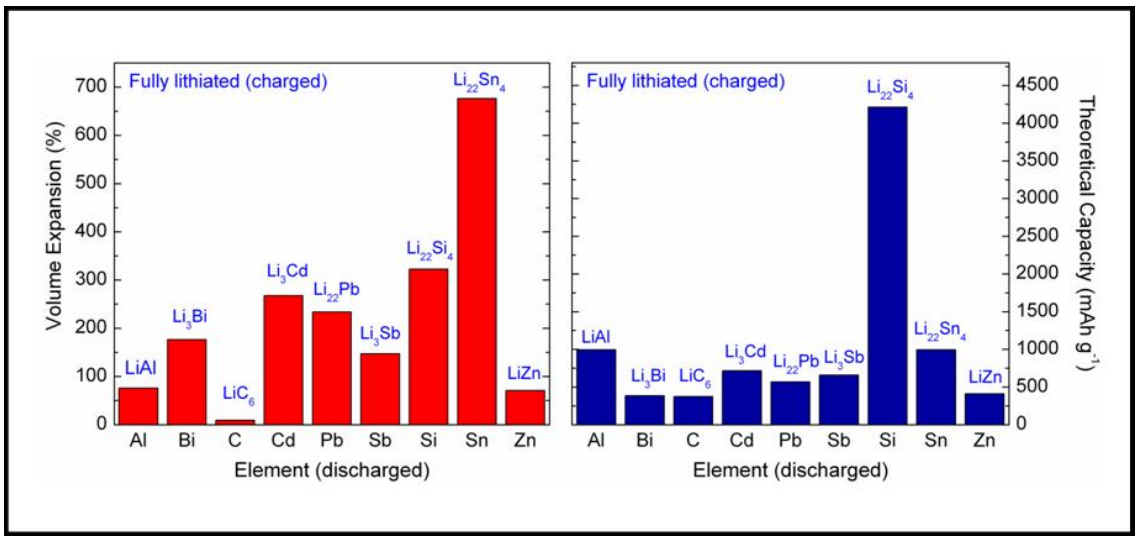

Figure 2.8: *The theoretical capacity and volume expansion of various lithium alloys.*

The main driving forces for research on lithium alloys are their high gravimetric and volumetric Li^+ storage capacities and their safe thermodynamic potentials of 1.0 to 0.3 V versus Li/Li^+. Unfortunately, the accommodation of such large amounts of Li^+ is accompanied by enormous volume changes, which poses severe problems to the mechanical stability of the host material, such as cracking or crumbling of the electrodes. Consequently, a short cycle life is induced, preventing any practical application.

The cycling performance strongly depends on the morphology, in particular on the particle size of the metallic host matrix.[82-87] One possibility for counteracting the mechanical degradation is the use of small particle size materials. In principle, mechanical destruction of the electrode due

to insertion and extraction of Li^+ can be largely avoided if the particle size of the host is chosen small enough to keep the absolute dimensional changes of the particles very small. Thus, electrode pulverization could be effectively suppressed on the nanoscale.[88-90] On the other hand, the volume expansion related to the lithium alloying process can be greatly alleviated by using an inactive matrix, which can be a conductive polymer, a porous membrane, an inert metal, such as copper, or another mixed conductor.[69,81-82,91-93] If the matrix is another ionic conductor, the ductile inactive matrix can buffer the volume increase of the alloy. If the matrix is a nanocrystalline or amorphous phase, there are many pores and cavities in the matrix. The expanded volume of the alloy can occupy this free space in the electrode. Thus the overall volume of the electrode will not display any increase with Li^+ insertion and the formation of lithium alloys. Therefore, nanocrystalline or amorphous intermetallic alloys offer a brilliant prospect for alloy materials to be used as anodes in rechargeable lithium-ion batteries. Also, carbons containing dispersed lithium alloys such as silicon or silver alloys, show good cycling behavior, because independent Li^+ insertion into the metal and the carbon occurs, and ductile carbon could accommodate volume expansion of the metal in this case.

Oxides, Nitrides and Others

The capacity of metal oxides and nitrides originates from a reaction with Li^+ to form another material, which is the electrochemically active phase. Transition metal oxides, such as α-Fe_3O_4, Co_3O_4, NiO, TiO_2, and SnO_2 have been proposed as alternative anode materials with high energy density and moderate reaction voltages.[32,93-100] In these systems, the transition metal cations migrate from the tetrahedral to the empty octahedral sites during Li^+ insertion. They can take up Li^+ at a relatively low voltage, but the reaction mechanism involves the decomposition

of the material with the formation of Li_2O and reduction of cations, all surrounded by a solid electrolyte interface. The reaction of these materials with Li^+ has been shown to entail a general displacement redox reaction, as described in Equation 2.40. In the SnO_2 materials, the initial Li^+ uptake corresponds to the formation of metallic Sn and Li_2O, and subsequently, a reversible alloying and de-alloying reaction occurs between metallic Sn and Li^+, forming intermediate compounds, Li_xSn ($0 \leq x \leq 4.4$), in a Li_2O matrix. [32,101-103] Even though the Li_2O phase is electrically inactive, based on thermodynamic considerations, the binding energy of Li_2O could be reduced by the small particle size and the catalytic activity of the transition metal formed during the discharge.

$$M_xO_y + 2yLi^+ + 2ye^- \leftrightarrow xM + yLi_2O \qquad (2.40)$$

The mechanisms associated with Li^+ insertion and extraction in transition metal nitrides have been investigated to some extent. Transition metal nitrides show a lower intercalation potential compared to the respective oxides, due to the lower formal oxidation state of the metal and the strongly covalent character of the metallic bond, which leads to a high mixed anion metal band and a high degree of electron delocalization. Low Li content nitrides usually form a solid solution with a Li_3N type layered structure and the formation of amorphous LiM_xN (M = Co, Fe, Ni, or Cu) could be induced by Li^+ extraction.[104-108] The theoretical capacity of these materials is thus inversely proportional to the content of transition metal atoms. Besides the transition metal oxides and nitrides, various stoichiometric antimonides, silicides, and phosphides have been proposed as promising alternative anode materials. However, there is a strong need to overcome their fundamental drawbacks before they can be deployed on a commercial scale.

Advanced Anode Materials

Lithium titanium oxide (LTO) can become a "zero strain" material, which means that the material essentially does not change shape upon the insertion and extraction of Li^+ into and from the material.[109-111] This property results in a significant improvement of cyclic retention, because of the absence of the particle fatigue that plagues materials such as graphite. Moreover, the formation of an SEI layer is eliminated, and Li^+ ions are able to be removed more quickly, resulting in more power being generated. The electrochemical properties of LTO allow the Li^+ to intercalate at high rates, thereby reducing the time to charge and allowing operation over a wide range of operating temperatures. Rapid chargeability and thermal stability are important for high power applications. However, its high discharge voltage of 1.5 V, which is much higher than that of graphite, strongly needs to be coupled with a high voltage cathode material for high cell voltage.

Cathode Materials

The identification of novel cathodes is critical because of the high cost and environmental problems of the lithium cobalt oxide ($LiCoO_2$) used in the commercial lithium-ion batteries. An important goal of rechargeable lithium-ion battery technology is to develop new cathode materials that exhibit high capacity and acceptable stability. The specific charge of cathode materials depends upon how much Li^+ can be taken in and provided, while the reaction potential is defined by the materials and their crystal structures.[6-10] For these reasons, recent studies have been focused on crystal chemistry and the fundamental properties of the Li-containing transition metal oxides, such as $LiCoO_2$, $LiNiO_2$ with a layered rock-salt structure, $LiMn_2O_4$ with a spinel structure, and olivine $LiFePO_4$.

Layered Structures

The general crystal structure of layered cathode materials can be expressed as $LiMO_2$, in which M is a *3d* transition metal element or a mixture of several *3d* transition metal elements, which belongs to the space group $R\bar{3}m$. Oxygen atoms form the unit-cell framework by stacking along the *c*-axis. Li and M atoms occupy the octahedral interstitial sites between oxygen atoms as illustrated in Figure 2.9. This layered structure is favorable for reversible Li^+ intercalation, because the Li layers facilitate fast two-dimensional Li^+ diffusion, while the edge sharing MO_6 octahedral arrangement with a direct M-M interaction is believed to provide good electronic conduction.[6-7,112-116]

Lithium cobalt oxide ($LiCoO_2$) been widely investigated due to its favorable electrochemical properties, such as structural stability under cycling, and its high discharge potential of 3.9 V. In addition, the lithium diffusion coefficient of $LiCoO_2$ is in a range approximately from 10^{-11} $m^2 \cdot s^{-1}$ to 10^{-11} $m^2 \cdot s^{-1}$ at room temperature, which is evidence for good Li^+ mobility. However, Co sources are limited, which means that it is subject to increase in price, and its theoretical capacity is relatively low (~130 $mAh \cdot g^{-1}$).[117-120] Besides the low discharge capacity, $LiCoO_2$ can decompose above 150 °C, due to the reactive tetravalent Co in the delithiated state. The collapse of the structure is exothermic, and the energy stored in the battery is released as heat. During collapse, oxygen is released, which can cause combustion of the organic electrolyte and evolve more heat. In order to overcome this drawback, the modification of $LiCoO_2$ by coating a metal oxide on the surface of the $LiCoO_2$ particles has been proposed as a suitable option.[120-123]

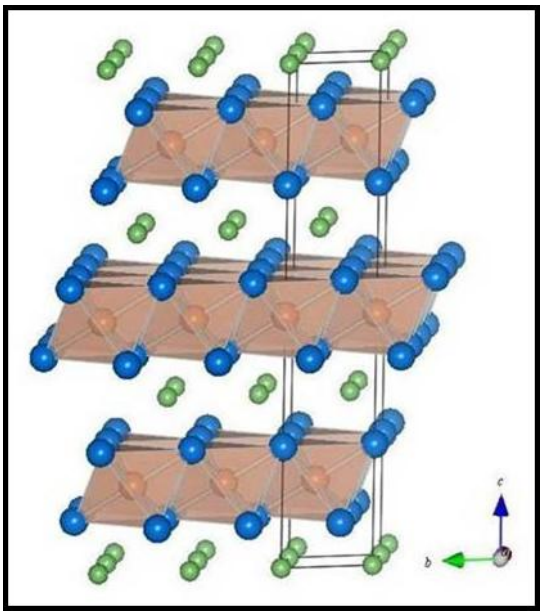

Figure 2.9: *Schematic of the crystal structure of layered $LiCoO_2$.*

Lithium nickel oxide ($LiNiO_2$) is isostructural with $LiCoO_2$, but has not been pursued in the pure state as a battery cathode for a variety of reasons, even though Ni is more readily available than Co. First, it is not clear that stoichiometric $LiNiO_2$ exists. Most reports suggest excess nickel, as in $Li_{1-y}Ni_{1+y}O_2$; thus, Ni is always found in the Li layer, which pins the NiO_2 layers together, thereby reducing the Li^+ diffusion coefficient and the power capability of the electrode. Second, compounds with low Li contents appear to be unstable, due to the high effective equilibrium oxygen partial pressure, so that such cells are inherently unstable and therefore dangerous in contact with organic solvents.[124-127]

The structure of lithium manganese oxide ($LiMnO_2$) can be described as a modified rock-salt type with a distorted cubic close-packed oxygen anion array, which belongs to the orthorhombic space group $Pmmn$. The Li and Mn occupy the octahedral interstitial sites in such a way that

alternating zigzag layers of edge-sharing LiO_6 and MnO_6 octahedra are generated. Although the structure can be described as layered, it differs from the layered structures of $LiNiO_2$ and $LiCoO_2$. It delivers a specific charge of 190 $mAh \cdot g^{-1}$ in the potential interval between 2.0 V and 4.25 V vs. Li/Li^+. However, all the $LiMnO_2$ materials suffer from limited cycling stability. In the final stages of the delithiation process, $LiMnO_2$ transforms irreversibly into a spinel structure, which is responsible for the poor cyclability of the electrode.[128-131]

Spinel Structures

In the framework class of compounds, research has focused on lithium transition metal oxides, LiM_2O_4 (M = Mn, V, Co, Ti, Ni), with a spinel structure because they can be used for both Li^+ insertion and extraction purposes.[132-137] The oxidation potential depends on the metal cation on the octahedral M site and the cell voltage can be tailored accordingly. Among the spinel type materials under consideration, the use of lithium manganese oxides ($LiMn_2O_4$) in rechargeable lithium cells has been promoted due to their low cost, high thermal stability, and small environmental impact. The spinel structure is based on the face centered cubic unit cell (fcc), which belongs to the space group of either $Fd\bar{3}m$ or $P4_332$ in which Li atoms occupy the 8*a* tetrahedral sites in the cubic close-packed (ccp) oxygen array, as illustrated in Figure 2.10. In the $Fd\bar{3}m$ symmetry, Mn atoms occupy the 16*d* octahedral sites, whereas these sites split into 4*a* and 12*c* sites in the $P4_332$ symmetry. This structure provides a three dimensional network of face-sharing tetrahedra and octahedra for Li^+ diffusion.[132-135]

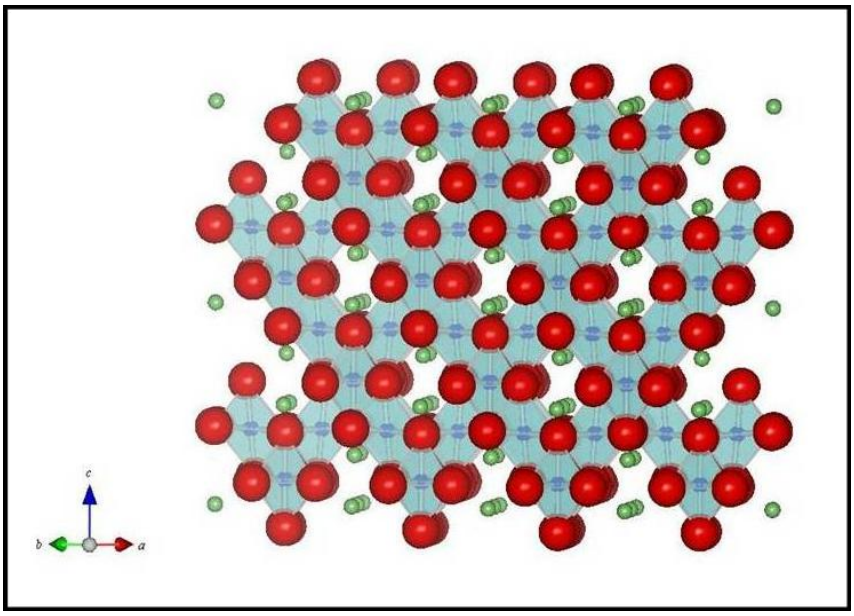

Figure 2.10: *Schematic of the $LiMn_2O_4$ spinel structure.*

However, the discharge process for this spinel is normally limited to the upper plateau around 4 V. The principal reason for the degradation at potentials below 3.5 V is presumably that a cubic to tetragonal transition readily occurs during Li^+ insertion and extraction, due to the difference between the energies of the 8*a* and 16*d* sites. Another possible reason for the poor cycle life of $Li_xMn_2O_4$ in the 3 V plateau is the asymmetry of the expansion and compression processes observed in the $Li_xMn_2O_4$ lattice during cycling, due to the Jahn-Teller effect distortion associated with the Mn^{3+}.[138]

The retention of cycling capacity at elevated temperatures can be helped by simultaneous doping with aluminum and fluoride ions. Moreover, if the potential on the surface of the spinel is kept above that for the formation of the $Li_2Mn_2O_4$ phase, then the formation of Mn^{2+} by the disproportionation of surface Mn^{3+} ions is minimized: $2Mn^{3+} = Mn^{2+} + Mn^{4+}$. It is the divalent

manganese ions that are soluble in the acidic electrolyte, and so every attempt must be made to minimize their formation. Once dissolved into the electrolyte, the Mn ions can diffuse across to the anode and be reduced there to manganese metal, thereby using up the Li and reducing the electrochemical capacity of the cell. Replacing some Mn in $LiMn_2O_4$ with mono- or multivalent cations (e.g., Li^+, Mg^{2+}, or Zn^{2+}) or, alternatively, doping the oxide with additional oxygen increases the average oxidation state of Mn slightly above 3.5 V, suppresses the Jahn-Teller effect on deep discharge, and leads to an improved rechargeability of the oxide.[138] Other approaches have involved the substitution of the Jahn-Teller ion Mn^{3+} by other trivalent cations (Al^{3+}, Fe^{3+}, Ni^{3+}, Co^{3+}, or Cr^{3+}). However, all the reported doping methods have led to a decreased specific charge compared to the un-doped $LiMn_2O_4$ materials so far.[139-141]

Olivine Structures

Lithium iron phosphate ($LiFePO_4$) is one of the most recent materials reported as cathode for the rechargeable lithium-ion battery. $LiFePO_4$ has an olivine structure with space group *Pnma*, which is significantly different from the structure of layered and spinel lithium metal oxides. The framework of the unit cell is constructed from FeO_6 octahedra and PO_4 tetrahedra. Li atoms form chains in the channels along the *b*-axis, as described in Figure 2.11.[142-144] Fe-based cathode materials are environmentally compatible, cheap, simple to process, and thermally stable compared to $LiCoO_2$, $LiNiO_2$, and $LiMn_2O_4$. The $LiFePO_4$ can act as a cathode material due to its high discharge potential around 3.4 V versus Li/Li^+ and moderate theoretical capacity (170 $mAh \cdot g^{-1}$). In spite of these advantages, olivine $LiFePO_4$ presents low conductivity (~10^{-9} Scm^{-1}) and its electrochemical performance is limited thereby, resulting in poor rate capability.[145-147]

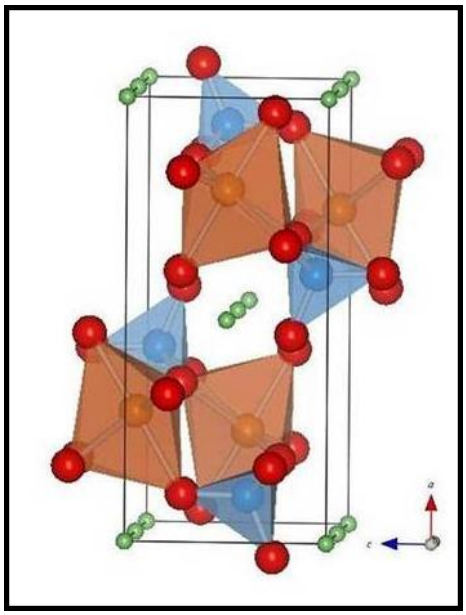

Figure 2.11: *Schematic of the $LiFePO_4$ olivine unit cell structure.*

In order to enhance and optimize the electronic conductivity of $LiFePO_4$, several practical approaches have been proposed for these materials. Up to now, there is no way to change intrinsically the electrical conductivity of $LiFePO_4$. Thus, two alternative methods have been reported. One is the reduction of the grain size and consequently the diminution of the diffusion length, both for electrons and ions, and the other is the manufacture of nanocomposites of $LiFePO_4$ with a conductive phase, such as carbon.[148-152]

Advanced Cathode Materials

A new class of electrode structures has been suggested to replace $LiCoO_2$, in which a layered component such as Li_2MnO_3 is intergrown with either another layered component, such as $LiMn_{0.5}Ni_{0.5}O_2$ or $LiMn_{0.33}Ni_{0.33}Co_{0.33}O_2$, or with a spinel component, such as $Li_4Mn_5O_{12}$.[153-155]

These Mn-rich composite electrode structures are electrochemically activated by charging to a high potential (> 4.6 V) in a lithium-ion cell. They can deliver almost twice the practical capacity of $LiCoO_2$, and they are more stable in non-aqueous electrolytes at elevated temperatures. The data makes them very promising for the development of the next generation of high-energy and high-power lithium-ion batteries.

Electrolytes

A liquid electrolyte in which lithium salts are dissolved in organic solvents conducts Li^+ and acts as a carrier between the cathode and the anode when a battery passes an electric current through an external circuit. However, solid lithium salts and organic solvents are easily decomposed on anodes during charging, thus preventing battery activation.[156-157] For high-power applications, alternative electrolytes should have high Li^+ conductivity and broad electrochemical stability. Figure 2.12 shows electrode energy relative to the electrolyte stability window (E_g).

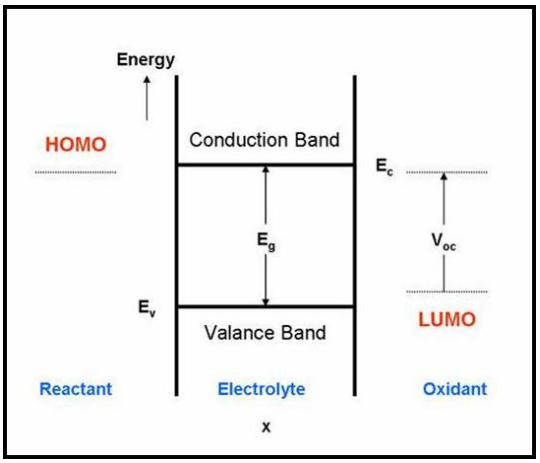

Figure 2.12: *Schematic representation of electrode energy relative to electrolyte stability window (E_g).*

Organic Solvents

Carbonates are the most common choice of organic solvent, because of their superior cyclic performance under ambient conditions. Ethylene carbonate (EC) and propylene carbonate (PC) provide sufficiently high conductivity and a broad stability window. EC is one of the preferred solvents with a high dielectric constant, but it is a solid at room temperature.[62] Therefore, EC could be used in a mixture with other solvents, such as diethyl carbonate (DEC) and dimethyl carbonate (DMC), so that a wider operating temperature interval can be obtained. Unfortunately, PC can cause some exfoliation of intercalation materials, especially graphite, due to extensive co-intercalation during cycling.[158-164] Addition of surface film formation agents, such as carbon sulfide (CS_2) and sulfur dioxide (SO_2) could effectively reduce the degree of solvent co-intercalation.[165-166] The physical properties of some important organic solvents used in the rechargeable lithium-ion battery are summarized in Table 2.2.

Table 2.2: *Structure and properties of some solvents used for lithium-ion battery electrolytes.*[161]

Please see print copy for Table 2.2

Lithium Salts

Soluble lithium salts are very important, because they act as charge carriers in the electrolytes during the electrochemical process.[157] Many lithium salts are currently used or are being considered for use in practical cells, such as $LiClO_4$, $LiAsF_6$, $LiPF_6$, $LiBF_4$, $LiCF_3SO_3$, and $LiN(SO_2CF_3)_2$. Among them, $LiPF_6$ exhibits a high ionic conductivity in carbonate based solvents and excellent cyclic performance at room temperature. However, it shows poor thermal stability at elevated temperature and it can be easily hydrolyzed by traces of water.

Prospects for Nanostructured Materials

Nanostructured materials have opened up new avenues in the development of the next generation rechargeable lithium-ion battery with high energy density and high power, because of their potential advantages: (1) better accommodation of the strain during Li^+ insertion and extraction, improving cyclic performance; (2) new reaction mechanisms on the nanoscale, resulting in higher capacity and power density; and (3) higher surface area and a relatively shorter path length for Li^+ diffusion and charge transfer, leading to higher rate capability during electrochemical reactions. In practice, the favorable structural features of nanostructured materials could offer strong enhancement of their electrochemical performance.[167-173] The mechanical strain, which is usually caused by the large volume variation due to Li^+ insertion or extraction, leading to capacity fading upon cycling and degradation of electrodes, could be effectively reduced with decreasing particle size. In addition, the formation of intermediate phases and interfacial charge storage reactions could occur on the nanoscale, due to the thermodynamically metastable nature of the nanostructured materials.[174-178] These new reactions are beneficial to increase Li^+ capacity. Another important aspect of the nanostructured

materials is that a larger surface area and a shorter transport length for Li^+ diffusion and charge transfer could significantly facilitate electrochemical reactions, resulting in stable cyclic performance at a high current rate. Considering the fact that nanostructured materials have better performance than the existing bulk materials, a comprehensive understanding of the physical and electrochemical properties of nanostructured materials is necessary to develop advanced electrode materials.

3. Experimental

3.1. Overview

The research on alternative electrode materials can be systematically divided into the following three areas as described in the flow chart (Figure 3.1) below: (1) the preparation of active materials, (2) morphological and structural characterizations, and (3) the evaluation of electrochemical performance. The specific experimental details performed by author in this work are presented below.

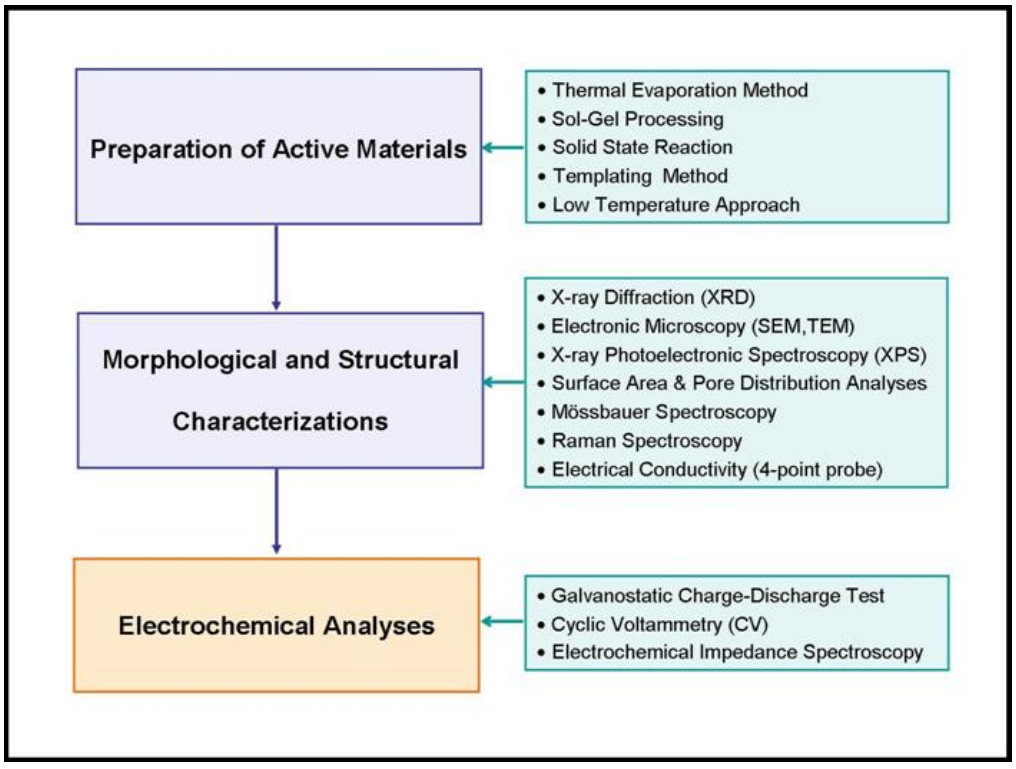

Figure 3.1: *A flow chart detailing the experimental techniques and procedures.*

3.2. Preparation of Materials

3.2.1. Thermal Evaporation Method

Thermal evaporation is one of the simplest and most popular synthetic methods, and it has been very successful and versatile in fabricating one-dimensional (1D) nanostructured materials with various characteristics. The basic process of this method is sublimating the source materials in powder form at high temperature, followed by a subsequent deposition of the vapor in a particular temperature zone to form the desired nanostructures.[179-181]

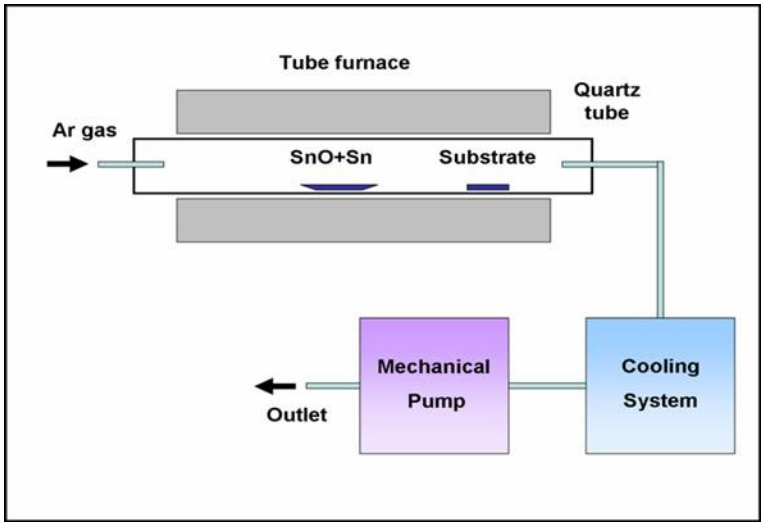

Figure 3.2: *A schematic diagram of a thermal evaporation deposition system for synthesis of one dimensional (1D) nanostructures.*

A typical experimental system used in this work is shown in Figure 3.2. The SnO_2 nanowires were synthesized in a quartz tube, which is set into a horizontal tube furnace. A high purity mixture of SnO and Sn powders contained in an alumina boat is loaded into the middle of the furnace, the highest temperature zone. The Si wafer substrates for collecting the SnO_2 nanowires

are usually placed downstream following the carrier gas (Ar). Both ends of the tube are covered by stainless steel caps and sealed with O-rings. Cooling water flows inside the cover caps to achieve a reasonable temperature gradient in the tube. During the experiments, the system is first pumped down to around 10^{-3} Torr. Then the furnace is turned on to heat the tube to the optimized reaction temperature of 900 °C at a specific heating rate. Inert Ar gas is then introduced into the system at a constant flow rate of 50 sccm to bring the pressure in the tube back to 100 Torr. The reaction temperature and pressure are held constant for an hour to vaporize the source material and achieve a reasonable amount of deposition. The source material, which has been previously ball milled for 40 hours under Ar atmosphere, can be vaporized under the optimized conditions. The vapor is then carried by the inert carrying gas down to the lower temperature region, where the vapor gradually becomes supersaturated. Once it reaches the substrate, nucleation and growth of nanostructures will occur by the VLS (vapor-liquid-solid) growth mechanism.[180]

3.2.2. Sol–Gel Processing

Sol–gel processing is a wet chemical route that involves synthesis of a colloidal suspension of solid particles or clusters in a liquid (sol) and subsequently the formation of a dual phase material consisting of a solid skeleton filled with a solvent (wet gel) through the sol–gel transition (gelation). When the solvent is removed, the wet gel can be converted to various types of nanostructured materials through an appropriate drying or sintering process.[182-186]

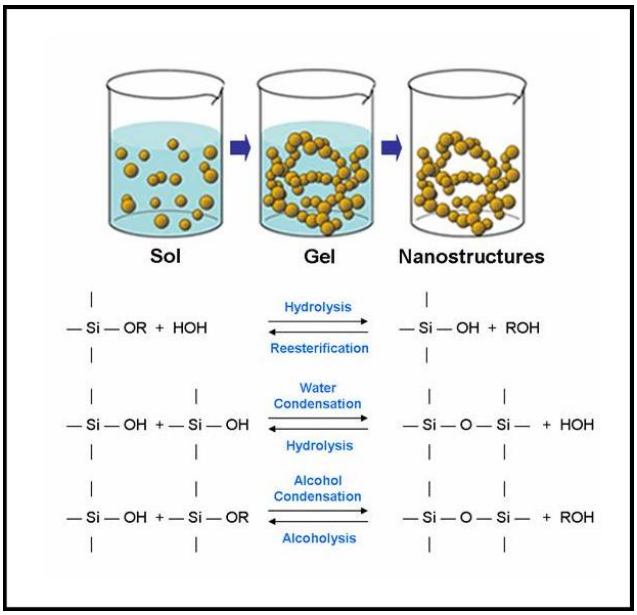

Figure 3.3: *A schematic of a sol-gel processing for synthesis of one dimensional (1D) nanostructures and a general description of the chemical reactions.*

Nanocrystalline SnO_2 nanopowders were prepared by the sol–gel process in this work. In the Sn based sol preparation, 0.338 g of $SnCl_2 \bullet 2H_2O$ is dissolved in ethanol (0.47 ml), and the precursors undergo two chemical reactions: hydrolysis and condensation or polymerization, typically with 36% HCl acid (0.03 ml) as the catalyst, to form the sol. Subsequently, the sol is aged for 24 hours, and then water (0.03 ml) is added under continuous stirring for 12 hours to form a gel. The solid particles or clusters are so small that gravitational forces are negligible, and interactions are dominated by van der Waals, coulombic, and steric forces. Sols are stabilized by an electric double layer, or steric repulsion, or their combination. After the gelation process, the product is dried at 120 °C for 2 hours and sintered at 600 °C for 3 hours in a vacuum furnace under an Ar (95%) and O_2 (5%) atmosphere. To remove Cl^-, the final product is was washed with distilled water via a centrifugal process and dried at 120 °C for 2 hours in a

vacuum oven. The advantages of the sol–gel process in general are high purity, homogeneity, and low temperature processing. In addition, some materials that cannot be made by conventional means because of thermal and thermodynamical instability can be made by this process. The sol–gel process has many applications in the synthesis of novel materials.[183-184]

3.2.3. Templating Method

Template synthesis technology is an ideal tool to fabricate oxide nanotubes and offers benefits in terms of either designing new nanostructured materials or modifying their morphologies. SnO_2 nanotubes with diverse structures and morphologies were synthesized by using anodic aluminum oxide (AAO) templates in this work. The applications employ the inherent characteristics of oxide nanotubes, which involve hollow core structures, large specific surface areas, very narrow inner pores, and catalytic surface properties. Templates can be employed in various synthetic techniques, such as sol–gel synthesis, chemical vapor deposition, thermal decomposition, electrodeposition, solvothermal preparation, and so on.[184-185]

The overall process generally involves the following procedures: (1) Sn based solution as a precursor is incorporated into the AAO by a reduced vacuum suction method; (2) solid species form through reaction, nucleation, and growth during the sintering process; and (3) the final SnO_2 nanotubes are obtained after template removal by NaOH solution, as described in Figure 3.4.[184-185]

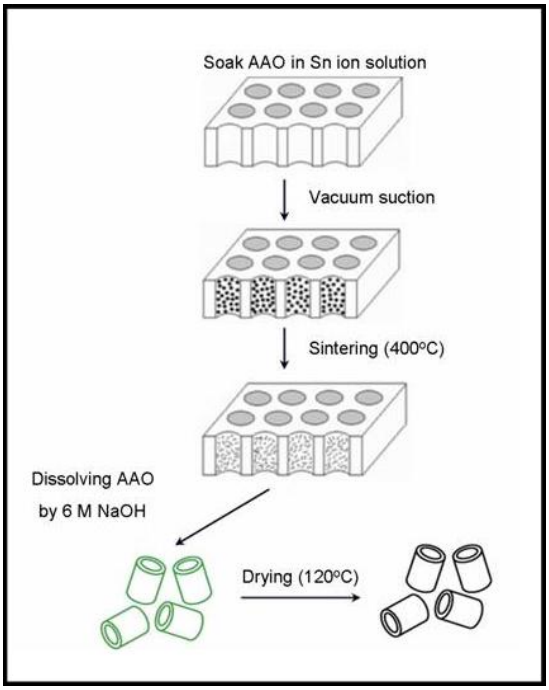

Figure 3.4: *A schematic diagram of the preparation of SnO_2 nanotubes by the templating method.*

3.2.4. Solid State Reaction

Conventional solid state synthesis techniques involve heating mixtures of two or more solids to form a solid phase product. Unlike gas phase and solution reactions, the limiting factor in solid–solid reactions is usually diffusion, which follows Fick's law (Equation 3.1).[187]

$$J = -D\left(\frac{dc}{dx}\right) \tag{3.1}$$

where J is the flux of diffusing species, D is the diffusion coefficient, and dc/dx the concentration gradient. The average distance traveled by diffusing species is given below (Equation 3.2), where t is the time:

$$< x >= (2Dt)^{1/2} \quad (3.2)$$

The diffusion coefficient increases with temperature and rapidly increases as the temperature approaches the melting point, based on Tamman's Rule that extensive reaction will not occur until the temperature reaches at least 2/3 of the melting point of one or more of the reactants. In this work, olivine $LiFePO_4$ powders with different particle sizes were synthesized by solid state reaction of lithium carbonate (Li_2CO_3, Wako, 99.9 %), iron(II) oxalate dehydrate ($FeC_2O_4 \cdot 2H_2O$, JUNSEI, 99 %) and diammonium hydrogen phosphate ($(NH_4)_2HPO_4$, Wako, 99%). To maximize the contact between reactants we employed a mechanical milling process for preparation of precursors with large surface area. The $LiFePO_4$ phase was formed by sintering at 700 ºC for 6 hours under a purified Ar gas flow. Pelletization encourages intimate contact between crystallites during the sintering process. Two ways to increase the rate of diffusion are to increase the temperature and to introduce defects by starting with reagents that decompose prior to or during reaction, such as carbonates or nitrates.[188]

3.2.5. Low Temperature Approaches

3.2.5.1. Synthesis of the Mesoporous Nanomaterials

In order to produce mesoporous organo-silica nano-arrays (MOSN), a surfactant mediated method was employed, as described below. Octadecyltrimethylammonium (ODTMA) chloride surfactant (6.66 g) was dissolved in an aqueous solution of 6 M NaOH (50 ml) and distilled water (200 ml) at 50 °C, and then 8 ml of 1,4-bis(triethoxysilyl) benzene (BTEB) was added

drop by drop under stirring at room temperature. The as-prepared solution was ultrasonicated for 20 min and stirred for 20 hours. The solution was dried at 95 °C for 20 hours and sieved through a filter paper (Whatman 5). The collected white product was dried in a vacuum oven. To remove the surfactant, the dried product was washed in a solution of ethanol (450 ml) and 36% HCl (18 ml) under stirring at 70 °C for 8 hours. The final product was dried at 95 °C for 20 hours again.[186]

3.2.5.2. Carbon Encapsulation Process

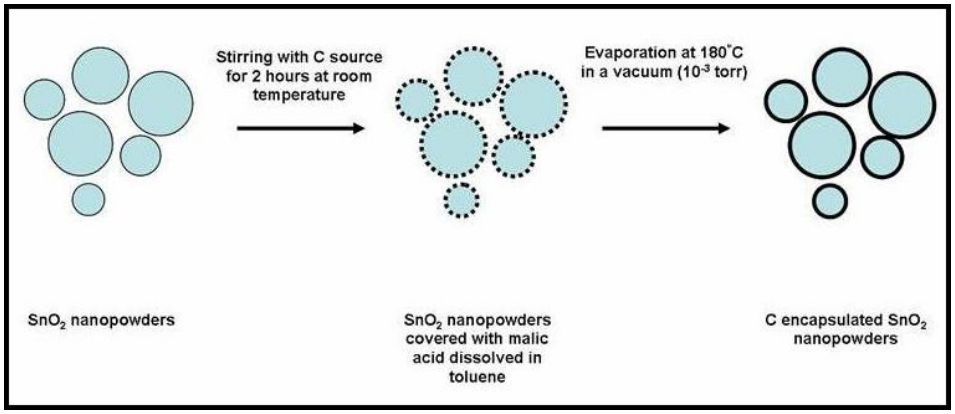

Figure 3.5: *A schematic diagram of the C encapsulation process via a chemical solution route using malic acid ($C_4H_6O_5$) as the C source.*

The C encapsulated SnO_2 nanopowders and nanowires were prepared by a low temperature process in this work. The SnO_2 nanopowders and nanowires were prepared by sol–gel processing and the thermal evaporation method, respectively. On the other hand, the C sources were prepared by dissolving malic acid ($C_4H_6O_5$, 99%) with the same amount of SnO_2 nanopowder or nanowires by weight in toluene (C_7H_8, 99.5%). Considering our experimental

strategy, malic acid was selected as the C source because it can be decomposed at low temperature and dissolved in a solvent. The solutions were mixed with SnO_2 nanopowders or nanowires under stirring at room temperature for 2 hours. These slurries were dried at 180 °C for 6 hours in a vacuum (10^{-3} Torr) oven.[183]

3.3. Methods of Characterization

3.3.1. X-ray Diffraction

3.3.1.1. Powder X-ray Diffraction

Powder X-ray diffraction (XRD) is the most powerful tool for the identification of crystalline materials and the determination of their structure in solid state chemistry. Because the wavelength of X-rays is comparable to the size of atoms, they are ideally suited for probing the structural arrangement of atoms and molecules in a wide range of materials. Each crystal has its unique characteristic X-ray powder pattern based on Bragg's law (Equation 3.3), which can be used for the identification of materials, as shown in Figure 3.6. In addition, crystallite size, D, can be estimated using the Scherrer equation (Equation 3.4).[189-190]

$$\lambda = 2d \sin\theta \tag{3.3}$$

$$D = \frac{0.9\lambda}{\beta \cos\theta} \tag{3.4}$$

where λ is the wave length of the incident beam, β is the full width at half maximum (FWHM) of the diffraction peak, θ is the Bragg angle and d is the d-spacing.

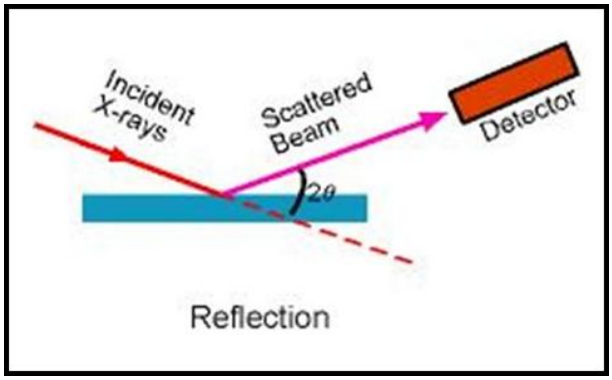

Figure 3.6: *A schematic diagram of the powder X-ray diffraction (XRD) technique.*

All materials prepared in this work have been characterized by powder X-ray diffraction using a Philips PW-1730 diffractometer (40 kV, 25 mA) with monochromatized Cu K_α radiation. The wavelength of the incident X-ray was 1.5418 Å, and the scan rate was fixed at 1° min^{-1}. The lattice parameters, full width at half maximum (FWHM) of peaks, and strain values were carefully refined by using a TOPAS ver. 3.0 software to process the collected data.

3.3.1.2. Pole Figure X-ray Diffraction

Texture measurements are used to determine the distribution of crystalline grain orientations in prepared samples. A material is textured if the grains are aligned in a preferred orientation along certain lattice planes. One can view the textured state of a material as an intermediate state in between a completely randomly oriented polycrystalline powder and a completely oriented single crystal. The texture is usually introduced in the fabrication process and affects the material properties by introducing structural anisotropy. A texture measurement is also referred to as a pole figure, as it is often plotted in polar coordinates, consisting of the tilt and rotation angles with respect to a given crytallographic orientation.[190] A pole figure is measured at a

fixed scattering angle (constant *d*-spacing) and consists of a series of ϕ-scans at different tilt or ψ (azimuth) angles, as illustrated in Figure 3.7. The pole figure data are displayed as contour plots or elevation graphs with zero angle in the center. An orientation distribution function (ODF) can be calculated using the pole figure data.

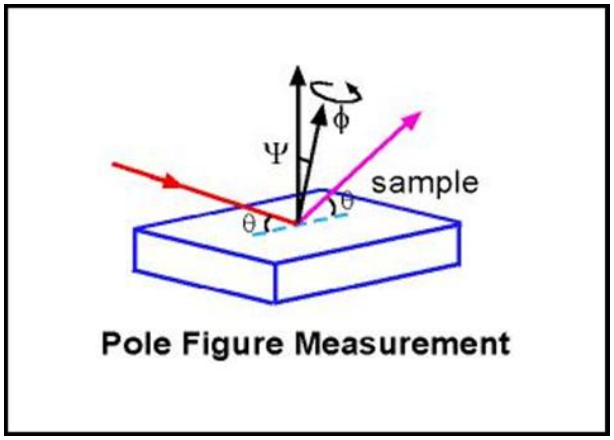

Figure 3.7: *A schematic diagram of a pole figure measurement using the X-ray diffraction (XRD) technique.*

In this work, texture analysis was conducted for SnO_2 nanostructured materials using four incomplete (110), (101), (200) and (211) pole figures with an X-ray goniometer (BRUKER-AXS, D8 discover). Cu-K_α radiation with a wavelength of 1.5406 Å was used for an area of 5 × 10 mm^2. We observed ψ angles in the range of 0° to 60° and ϕ angles in the range of 0° to 355°, with an interval of 5° and dwell time of 1 s.

3.3.2. Electron Microscopy

3.3.2.1. Scanning Electron Microscopy

Scanning electron microscopy (SEM) is used for inspecting topographies of materials at very

high magnifications and can provide significant information on the surface of the materials, including that relating to fracture surfaces, bond failures, and physical defects.[191] The basic principle of SEM is illustrated in Figure 3.8. In addition, backscattered electron imaging is useful in distinguishing one material from another, since the yield of the collected backscattered electrons increases monotonically with the atomic number. Backscatter imaging can distinguish elements from their atomic number differences, with good contrast on the image. Energy dispersive X-ray (EDX) analysis is also useful in identifying materials and contaminants, as well as estimating their relative concentrations on the surface of the specimen.

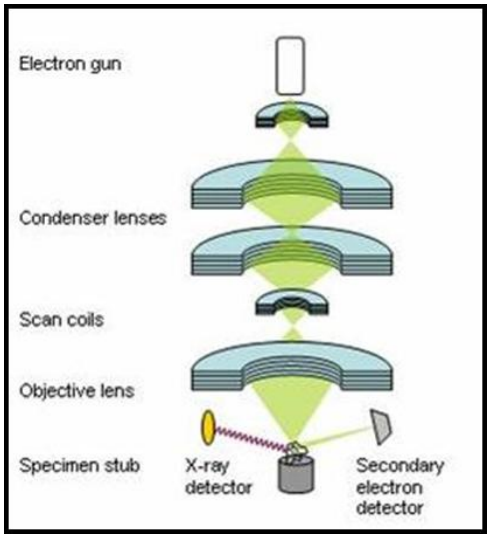

Figure 3.8: *A schematic drawing of a scanning electronic microscope (SEM).*

Field Emission SEM (JEOL JEM-3000) was employed to characterize the morphology and microstructure of prepared materials at different magnifications in this work. For element analysis on the surface of materials, the backscattered electron imaging was used together with EDX analysis. A thin layer of gold (Au) was deposited on the surface of the materials using a Dynavac Mini Coater sputtering system if the material was less conductive.

3.3.2.2. Transmission Electron Microscopy

Transmission Electron Microscopy (TEM) is used to identify imperfections in the atomic level structure of materials by analysis of microscopic surfaces.[191] A very thin slice of the material to be tested is exposed to a beam of electrons. When the electrons interact with a consistent material structure, a constant fraction of electrons is transmitted back from the sample to a detector. Once a structural imperfection is encountered, the fraction of transmitted electrons changes, resulting in change of contrast. Diffraction contrast is useful in identifying large structures and crystallographic features. Phase contrast is used for high magnification imaging of atomic columns. The basic principle of TEM is illustrated in Figure 3.9. Higher magnification visual observations were conducted using a JEOL 2011 transmission electronic microscope (TEM) in this work. All samples were carefully prepared for better inspection of the atomic level structure. TEM sample preparation consisted of placing a small amount of sample powder on a holey-carbon film on a copper grid by ultrasonication.

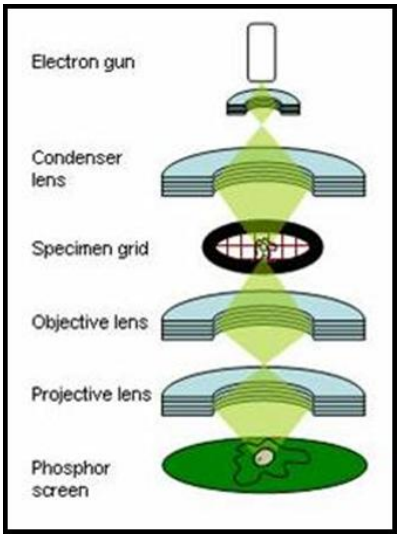

Figure 3.9: *A schematic drawing of a transmission electronic microscope (TEM).*

3.3.3. Raman Spectroscopy

Raman spectroscopy provides information about molecular vibrations and can therefore be used for sample identification, as well as for quantization. The technology is based on the measurement of scattered light from a sample, which is illuminated with a monochromatic light source such as a laser. Raman spectroscopy is based on the Raman effect, which is the inelastic scattering of photons by molecules.[187,191] The majority of the scattered light is of the same frequency as the excitation source, known as the Rayleigh scattering. A very small amount of the light is shifted in energy from the laser frequency. The shift is due to the interaction between the incident electromagnetic waves and a vibration energy level of the sample molecules. These spectra are plotted with respect to the laser frequency, such that the Rayleigh band lies at 0 cm^{-1}. A simplified energy diagram that illustrates these concepts is given in Figure 3.10. The energy of the scattered radiation is less than the incident radiation for the Stokes line and more than the incident radiation for the anti-Stokes line. The energy increase or decrease from the excitation is related to the vibrational energy spacing in the ground electronic state of the molecule and therefore the wavenumber of the Stokes and anti-Stokes lines are a direct measure of the vibrational energies of the molecule. In this work, structural information on the prepared materials was obtained using room temperature Raman spectroscopy (Jobin Yvon HR800) with a He–Ne laser (excitation line 632.8 nm) and a microscope objective (×50, Olympus MPlan, 0.38 mm working distance, numerical aperture 0.75). The Raman spectra were collected sequentially in a multipoint mode for each sample under investigation.

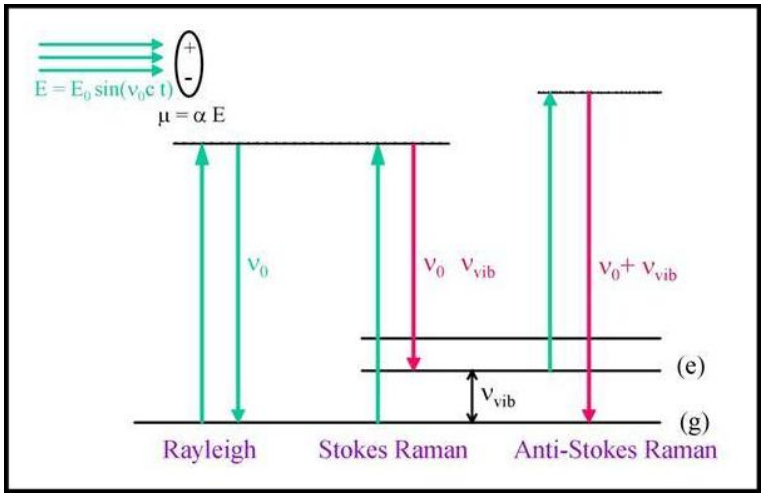

Figure 3.10: *A simplified energy diagram illustrating the concept of Raman spectroscopy.*

3.3.4. X-ray Photoelectron Spectroscopy

X-ray photoelectron Spectroscopy (XPS) is a surface sensitive spectroscopy technique that allows chemical identification of the elements in the top atomic layers of a sample by recording the binding energies of the electrons associated with these atoms. Furthermore, because the binding energies differ, not only from chemical species to species, but also with the bonding conditions in which the element is found, this technique also provides information on the actual compounds present on the surface. In essence, it probes the electronic structure of the surface. The fundamental principle of XPS is described in Figure 3.11.[191] The kinetic energy, E_k, of these photoelectrons is determined by the energy of the X-ray radiation, $h\nu$, and the electron binding energy, E_b, as given by Equation 3.5. The experimentally measured energies of the photoelectrons are given by Equation 3.6.

$$E_k = h\nu - E_b \tag{3.5}$$

$$E_k = h\nu - E_b - E_w \tag{3.6}$$

where, E_w is the work function of the spectrometer. XPS instruments consist of an X-ray source, an energy analyzer for the photoelectrons, and an electron detector. The analysis and detection of photoelectrons requires that the sample be placed in a high-vacuum chamber. Since the photoelectron energy depends on X-ray energy, the excitation source must be monochromatic. The energy of the photoelectrons is analyzed by an electrostatic analyzer, and the photoelectrons are detected by an electron multiplier tube or a multichannel detector such as a microchannel plate.

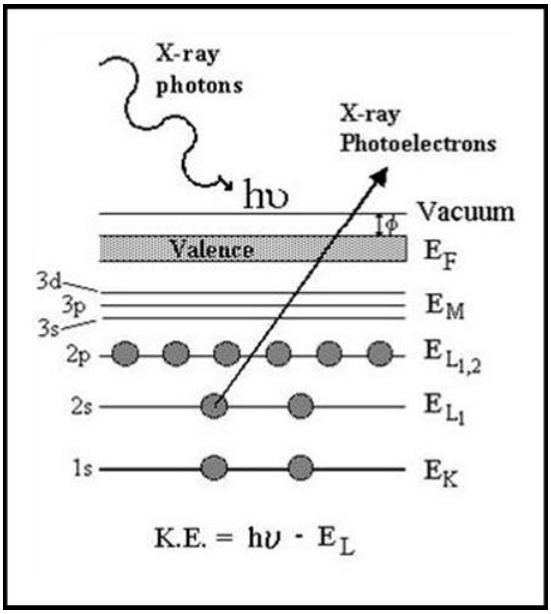

Figure 3.11: *A simplified energy diagram illustrating the concept of X-ray photoelectron spectroscopy (XPS).*

The changes of binding nature on the surface of the prepared materials are characterized by XPS technique. It was useful to identify the effects of various structural modifications on the materials in this work. The XPS analysis and data collection were conducted at Korea Basic Science Institute in South Korea.

3.3.5. Electrical Conductivity

The purpose of the 4-point probe is to measure the resistivity of materials, either bulk or thin film specimens. The probe consists of four equally spaced tungsten metal tips with finite radius. The 4-point probes are arranged in a linear fashion, where the two outer probes are connected to a current supply, and the inner probes to a voltage meter, as illustrated in Figure 3.12. As current flows between the outer probes, the voltage drop across the inner probes is measured. The relationship between the current and voltage values is dependent on the resistivity of the material under test, as given by Equation 3.7.[191]

$$R_s = \rho \times \frac{V}{I} \tag{3.7}$$

where the sheet resistance is R_S (Ω); V (mV) is the voltage drop across the inner two probes; I (mA) is the current flow between the outer two probes; and ρ (rho) is the geometric factor for the thin film measured on the four-point probe, which equals 4.5324.

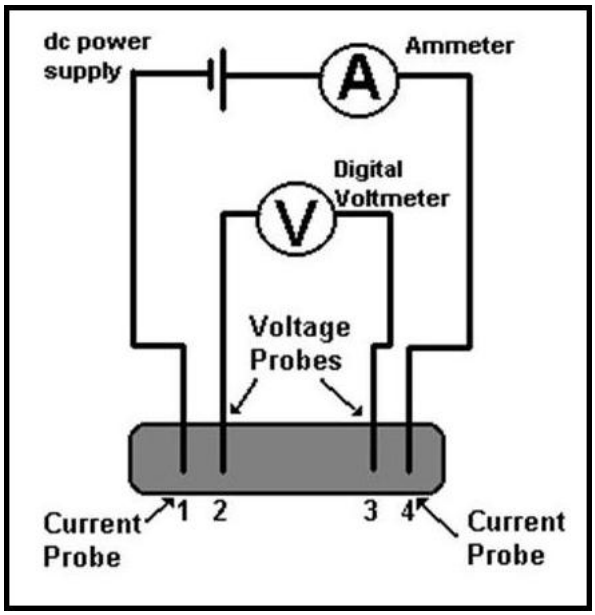

Figure 3.12: *A schematic of the configuration of four-point probe resistivity measurements.*

The samples were prepared for electrical conductivity measurements in this work as follows: a suspension was prepared via addition of 10 mg of prepared materials and 0.1 g of a surfactant, Triton X-100, into 20 ml of Milli-Q water, followed by ultrasonication for 2 hours. A polyvinylidene fluoride (PVDF) membrane with a pore size of 0.22 μm was cut into a 4-cm disk to fit the filtration cell. Passing the prepared suspension through the wetted PVDF filter in a filtration cell under N_2 gas pressure of 400 kPa produced a film. Subsequently, the film was washed with 100 ml of Milli-Q water followed by 50 ml of methanol, where methanol was used to remove any residual surfactant. Resistivity measurements of the composite films were performed on strips (0.3 cm x 2.5 cm), using the Jandel four-point probe technique (model RM2). A constant current of 1 mA was passed through the outer two electrodes and the voltage difference between the two inner electrodes was measured after 10 s. This measurement was repeated 4 times for each sample.

3.3.6. Surface Area and Particle Size Measurements

The surface area and porosity of materials can be calculated from the volume of gas adsorbed onto the surface of the materials, as described in Figure 3.13. The surface area, thus measured, includes the entire surface accessible to the gas, whether external or internal, based on the isothermal adsorption of nitrogen (N_2).[192] The BET (Brunauer−Emmett−Teller) method is widely used in surface science for the calculation of surface areas of solids by physical adsorption of gas molecules. The total surface area S_{total} (Equation 3.8) and the specific surface area S (Equation 3.9) are evaluated by the following equations:

$$S_{BET,total} = \frac{v_m N s}{V} \tag{3.8}$$

$$S_{BET} = \frac{S_{BET,total}}{a} \tag{3.9}$$

where N is Avogadro's number, s is the adsorption cross section, V is the molar volume of adsorbent gas, and a is the molar weight of the adsorbed species.

The specific surface areas of prepared materials were measured using a Quantachrome NOVA 1000 nitrogen absorption apparatus in this work. 10 mg of each material was weighed and placed in the sample holder. The measurement was carried out at 140 °C with an inert gas flow. The specific surface area was estimated by the BET method, and the pore size distribution was calculated using the Barret−Joyner−Halenda (BJH) algorithm on the collected data.

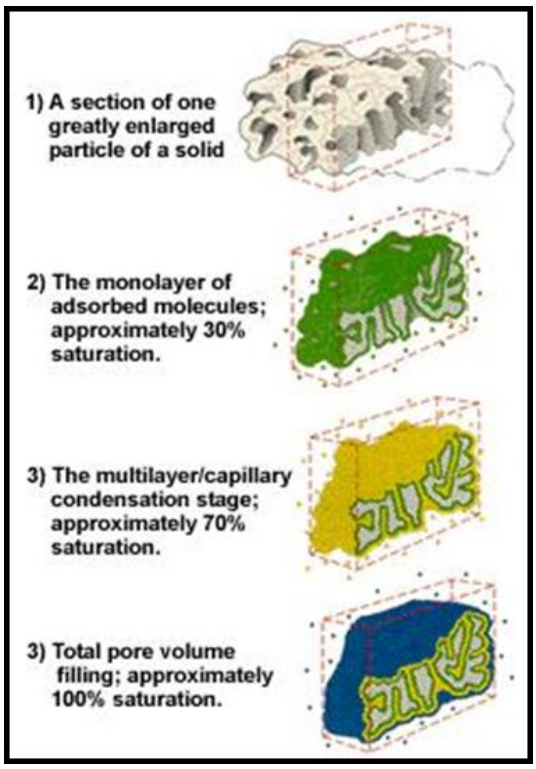

Figure 3.13: *A schematic drawing of the principle of the gas absorption process for surface area and pore distribution measurements.*

3.3.7. Mössbauer Spectroscopy

The technique of Mössbauer spectroscopy is widely used to examine the valence state of iron (Fe), which is found in nature as Fe^0 (metal), Fe^{2+}, and Fe^{3+}, as well as the type of coordination polyhedron occupied by iron atoms. Mössbauer spectroscopy is also used to assist in the identification of Fe oxide phases on the basis of their magnetic properties. The Mössbauer effect is the recoil-free emission of gamma radiation from a solid radioactive material. Since the gamma emission is recoil-free, it can be resonantly absorbed by stationary atoms. The nuclear transitions are very sensitive to the local environment of the atom, and Mössbauer spectroscopy

is a sensitive probe of the different environments an atom occupies in a solid material.[193] Approximately 90% of the ^{57}Fe nuclear excited state decays through an intermediate level to produce 14.4 keV gamma radiation. These gamma photons can then be absorbed by ^{57}Fe in a sample (Figure 3.14). The gamma ray source is a radioactive element that is mechanically vibrated back and forth to Doppler shift the energy of the emitted gamma radiation.

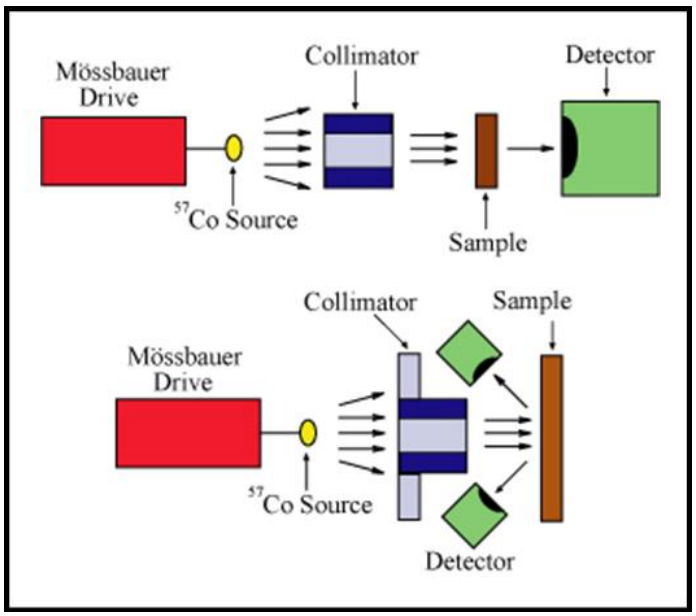

Figure 3.14: *Schematic diagrams of transmission (top) and reflection (bottom) Mössbauer experiments.*

For the Mössbauer measurements, the samples were carefully sealed in an Ar filled glove box and then lodged in the ^{57}Fe transmission Mössbauer spectroscope with a ^{57}Co source. A combination of isomer shift and quadrupole splitting was used to identify the valence state and site occupancy of Fe in a given individual sample in this work.

3.4. Electrochemical Assessment

3.4.1. Electrode Fabrication and Cell Assembly

3.4.1.1. Electrode Fabrication

A mixture of 75-85 wt% of each active material and 8-15 wt% acetylene black (AB) was added to a solution containing 7-10 wt% polyvinylidene fluoride (PVdF) in n-methyl-2-pyrrolidinone (NMP). After homogeneous mixing, the resultant slurry was uniformly pasted onto a copper foil current collector and dried at 120 °C for 2 hours in vacuum (10^{-3} Torr), then pressed under a pressure of about 200 $kg \cdot cm^{-2}$ in a uniaxial hydraulic press. In the case of cathode material, a piece of aluminium foil was used as the current collector, considering that opper foil could be dissolved electrochemically in a non-aqueous lithium salt solution at operating voltage over 3.0 V.[195-196]

3.4.1.2. Test Cell Assembly

CR2032 coin-type half cells were fabricated to evaluate the anodic or cathodic performance of the active materials. The assembly was carried out in an Ar-filled glove box with less than 0.1 ppm each of oxygen and moisture. Cellgard 2400 (Cellgard LLC, USA) was used as the separator membrane in the cell. Li metal foil was used as the counter and reference electrode, and 1 M of lithium hexafluorophosphate ($LiPF_6$) dissolved in a 1:1 (v/v, Merck KGaA) mixture of ethylene carbonate (EC) and dimethyl carbonate (DMC) was employed as the electrolyte. Figure 3.15 shows a schematic of the typical structure of a completed coin test cell.

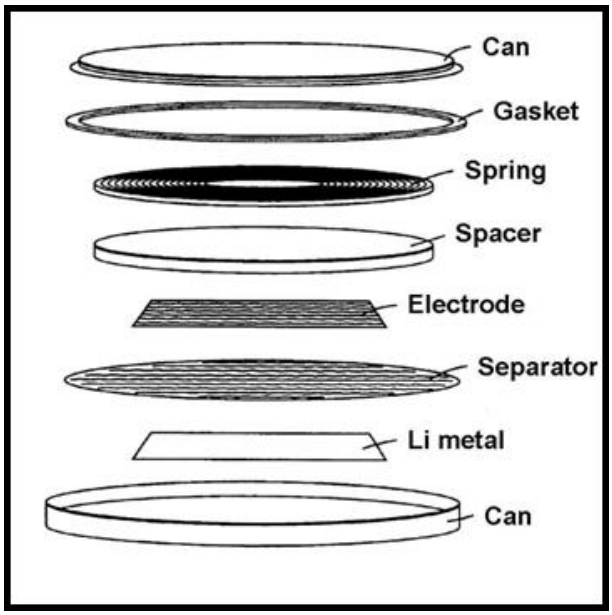

Figure 3.15: *A schematic diagram of the configuration of the coin type test cell.*

3.4.2. Galvanostatic Charge-Discharge Testing

Galvanostatic charge-dischare tests of the coin cells were conducted using various voltage cut-offs on a Neware battery testing system at a constant current of 0.01–0.2 mA. The current rate was determined in this work on the basis of the theoretical capacity of the active materials. The theoretical capacity of a battery is the quantity of electricity involved in the electrohemical reaction. It is denoted Q and is given by Equation 3.10:[35]

$$Q = xnF \tag{3.10}$$

where x is the number of moles of reaction, n is the number of electrons transferred per mole of reaction, and F is Faraday's constant. The capacity is usually given in terms of mass, not the

number of moles (Equation 3.11):

$$Q = \frac{nF}{M_r} \tag{3.11}$$

where M_r is the molecular mass. This gives the capacity in units of Ampere-hours per gram ($Ah \cdot g^{-1}$). From the theoretical capacity of the prepared materials, the discharge current rate could be determined, and the anodic or cathodic performance of the prepared materials was evaluated over the voltage range of 0.05 V to 1.5 V or 2.0 V to 4.5 V, respectively.

3.4.3. Cyclic Voltammetry

Cyclic voltammetry (CV) is a type of potentiodynamic electrochemical measurement, in which a voltage is applied to a working electrode and current flowing at the working electrode is plotted versus the applied voltage to give a cyclic voltammogram. Cyclic voltammetry can be used for characterization and mechanistic studies of redox reactions at electrodes in electrochemical cells. The potential is measured between the reference electrode and the working electrode, and the current is measured between the working electrode and the counterelectrode. This data is then plotted as current (i) vs. potential (E).[35,191] The electrode potential is ramped linearly to a more negative potential, and then ramped in reverse back to the starting voltage. The forward scan produces a current peak for any analytes that can be reduced through the range of the potential scan. The current will increase as the potential reaches the reduction potential of the analyte, but then falls off as the concentration of the analyte is depleted close to the electrode surface (Equation 3.12). As the applied potential is reversed, it will reach a potential that will reoxidize the product formed in the first reduction reaction and

produce a current of reverse polarity from the forward scan. This oxidation peak will usually have a similar shape to the reduction peak. The peak current, i_p, is described by the Randles-Sevcik equation:[35]

$$i_p = (2.69 \times 10^5) n^{3/2} A C D^{1/2} v^{1/2} \quad (3.12)$$

where n is the number of moles of electrons transferred in the reaction, A is the area of the electrode, C is the analyte concentration, D is the diffusion coefficient, and v is the scan rate of the applied potential. In this work, cyclic voltammograms (CV) were obtained by measuring the I-V response at a scan rate of 0.1 $mV \bullet s^{-1}$ in the rage of 0.05 to 2.5 V, using a CH Instruments 660A electrochemical workstation. All parameters were carefully considered to obtain an optimized response of the materials under investigation.

3.4.4. Electrochemical Impedance Spectroscopy

Electrochemical impedance spectroscopy (EIS) is a powerful tool for examining a complex sequence of coupled electrochemical processes, such as electron transfer, mass transport, and chemical reactions. An important advantage of the EIS technique is the possibility of using very small amplitude signals without significantly disturbing the properties being measured.[35,194] To make an EIS measurement, a small amplitude signal, usually a voltage between 5 and 50 mV, is applied to a specimen over a range of frequencies from 0.001 Hz to 100,000 Hz. In EIS studies of battery systems, a dc bias is applied at different potentials in order to investigate the corrosion or kinetic processes taking place during charging or discharging. EIS may be performed in either potentiostatic (constant voltage) or galvanostatic (constant current) mode,

depending on the type of analysis. Electrochemical impedance measurements were performed using a CH Instruments 660A electrochemical workstation. An alternating voltage of 20 mV amplitude was applied to the cell in a frequency range from 0.001 Hz to 100,000 Hz in this work. The collected data were plotted with an equivalent circuit and analyzed using Zview software ver. 2.8. The parameters of the equivalent circuit were dynamically fitted using appropriate methods for each sample.

PART I

I.A. Overview

The development and optimization of advanced anode materials are very necessary for efficient energy storage in the rechargeable lithium-ion battery. Recent investigations have shown that nanostructured materials exhibit improved electrochemical behaviors, in such aspects as superior rate-capability and cyclability. These improvements could be induced by enhanced interfacial kinetics due to the high surface area and short Li^+ diffusion length of the nanostructured materials.[167-178] For further investigations, an accurate diagnosis of the advantages and drawbacks of nanostructured materials is still needed at this moment. Moreover, the diversity in the physical or chemical nature of the materials on the nanoscale should be identified to give the development of advanced nanostructured materials.

The aim of this work is to elucidate understand alternative possibilities that have emerged from the use of SnO_2 based nanostructured materials that reversibly form alloys with Li^+. This systematic study takes into account the need for a comprehensive understanding of the chemical and physical nature of the SnO_2 nanostructured materials directly involved in reversible reactions with Li^+, in order to identify their major advantages and drawbacks as alternative anode materials for high-power and large-scale applications. Herein, we introduce the distinctive electrochemical performances of different types of SnO_2 nanostructured materials, such as nanopowders, nanowires, and nanotubes, to determine the effects of structural features on the electrochemical performance. In addition, promising structural modifications of SnO_2 nanostructured materials, such as carbon encapsulation and the formation of nanocomposites with mesoporous organo-silica, have been employed to determine their potential.

I.B. SnO_2 Anode Materials

Tin dioxide, SnO_2, is an environmentally friendly semiconductor with band gap of 3.6 eV at room temperature, which has attracted much attention as a possible candidate for use as a next generation anode material due to its high specific charge and low reaction potential with Li^+.[197-201] The SnO_2 has the tetragonal rutile structure, which belongs to space group $P4_2/mnm$, where the Sn atoms are sixfold coordinated and the O atoms are three coordinated, as shown in Figure I.1.

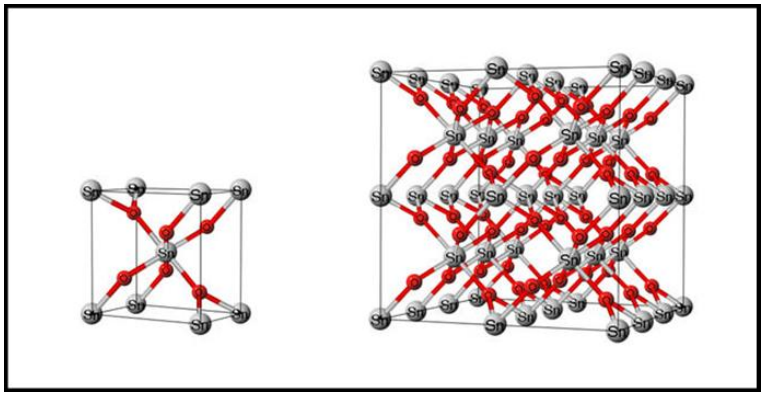

Figure I.1: *The unit cell structure and crystal structure of SnO_2, which has tetragonal symmetry and belongs to the space group $P4_2/mnm$.*

SnO_2 can theoretically store Li^+ at capacities of up to 783 mAh·g^{-1}, a significant improvement over the 372 mAh·g^{-1} provided by graphite. During the first discharge, Li^+ ions are supposed to react with SnO_2 according to the following two-step reaction:[199,201]

$$SnO_2 + 4Li^+ + 4e^- \rightarrow Sn + 2Li_2O \qquad \text{(large irreversible capacity)} \qquad \text{(I.1)}$$

$$Sn + xLi^+ + xe^- \rightarrow Li_xSn \quad (0 \leq x \leq 4.4) \quad \text{(large volume variation)} \qquad \text{(I.2)}$$

The first step in the reduction of SnO_2 results in the formation of metallic Sn phases dispersed within a Li_2O matrix, as described in Equation (I.1). The formation of Li_2O is considered to be a major reason for the large initial irreversible capacity of 711 $mAh \cdot g^{-1}$ resulting in a loss of reversible capacity. The irreversible reduction of Sn^{IV} into Sn^0 decreases the reversible specific charge of the following cycles to 783 $mAh \cdot g^{-1}$ and severely limits interest in this material. However, the reversible capacity is still higher than for graphite (372 $mAh \cdot g^{-1}$). In the second step, Li^+ reacts with metallic Sn phase to form Li_xSn alloys according to Equation (I.2). It is this reaction that mainly provides the reversible Li^+ storage capacity. The formation of the Li_xSn alloys (LiSn, Li_7Sn_3, Li_5Sn_2, $Li_{13}Sn_5$, Li_7Sn_2, $Li_{22}Sn_5$) is reversible and causes large volume changes between the Sn phases, leading to an abrupt capacity fade.[6] In practice, the electrode volume at the end of the first discharge is four times bigger than for the initial state. After the decomposition of Li_xSn alloy, its volume is still two times bigger than the initial volume, showing that the electrode will not recover its original volume. Both a large initial irreversible capacity and the volume changes remain as practical limitations to be solved.

The structural modifications of SnO_2 on the nanoscale are of particular interest, because the electrochemical performance of SnO_2 seems to have a strong correlation with the structural features of the SnO_2 phase. The different morphologies may play an important role in Li^+ diffusion and charge transfer in the SnO_2 nanostructured materials to be used as anode materials in the rechargeable lithium-ion battery. Over the past few years, remarkable progress has been made in the synthesis of nanostructured materials, and various nanostructured SnO_2 materials,

including nanoparticles, one-dimensional (1D) nanostructures, and nanocomposites with other materials, as well as thin films, have been widely investigated. However, there is practically no information so far on the correlation between electrochemical properties and the different crystallographic structures of SnO_2 nanostructured materials. On the other hand, several studies have been reported on the combination of SnO_2 with carbonaceous materials in an attempt to reduce capacity fade. The approach has been to prevent the Sn from becoming electrically disconnected through the use of a conductive carbonaceous matrix, which can also reversibly store Li^+.[6] However, the composites still show significant capacity fade that could be attributed to the Sn phase of the material. Another approach is based on the idea that if the metallic Sn phases are small enough initially and if they are prevented from aggregating, the capacity fade could be effectively reduced. Nanocomposites with B_2O_3 or P_2O_5 could create a dilution effect, so that the formation of Li_2O could be reduced by consumption of O atoms and keep the metallic Sn phases small.[6] These approaches have attracted significant attention when synergistically combined with structural modifications of SnO_2 on the nanoscale, because such modifications might then allow us to reduce the initial irreversible capacity and improve the cyclic retention in the SnO_2 nanostructured materials.

I.C. Thermodynamic Considerations on the Li-Sn-O System

Considering the basic principles involved in the use of SnO_2 as an anode material, SnO_2 is converted to lithium alloys, Li_xSn, during the first discharge cycle under near equilibrium conditions, as mentioned above. The properties of SnO_2, therefore, should be essentially those of the resulting binary Li–Sn alloy system. Because SnO_2 is thermodynamically less stable than lithium oxide (Li_2O), there is a displacement reaction in which Li_2O could be formed at the

expense of SnO_2, as described in Equation I.3. The difference in the values of their Gibbs free energies of formation (ΔG_f) at 298 K (-562.1 kJ·mol^{-1} for Li_2O and -256.8 kJ·mol^{-1} for SnO) provides the driving force, which is quite strong, equivalent to 1.58 V.[202-207]

$$2Li + SnO_2 \leftrightarrow 2Li_2O + Sn \qquad \text{(I.3)}$$

The other product is the metallic Sn phase. As additional Li^+ is brought in this Sn phase tends to react further to form the various Li_xSn alloys that exist in the Li–Sn binary phase diagram. If the formation of Li_2O is irreversible, the electrode would maintain a composite microstructure and behave as a binary Li–Sn alloy after the first cycle. This initial Li_2O formation represents a significant initial capacity loss at the first cycle. Under complete equilibrium, the Gibbs phase rule specifies that the electrochemical potential varies with composition in the single phase regions of the binary phase diagram, whereas the potential is independent of composition in two-phase regions if the temperature and total pressure are kept constant. Thus the variation of the electrode potential during discharge and charge, as well as the phases present and the charge capacity of the electrode, directly reflect the thermodynamic properties of the alloy system.[41-42,202-207]

Assuming that there is no stable ternary phase, a simple ternary isothermal phase stability diagram can be constructed, as shown in Figure I.2. If Li^+ reacts with SnO_2 phase, the overall composition will move toward the Li corner of the ternary diagram, and under conditions close to equilibrium, it will move along the dotted lines shown in Figure I.2. The ΔG_f data allow us to determine the phases that are stable with each other and the reactions that will tend to take

place when Li^+ is introduced into an electrode.[41,208] The overall composition will move through a series of three phase triangles, crossing the two-phase tie lines between them.

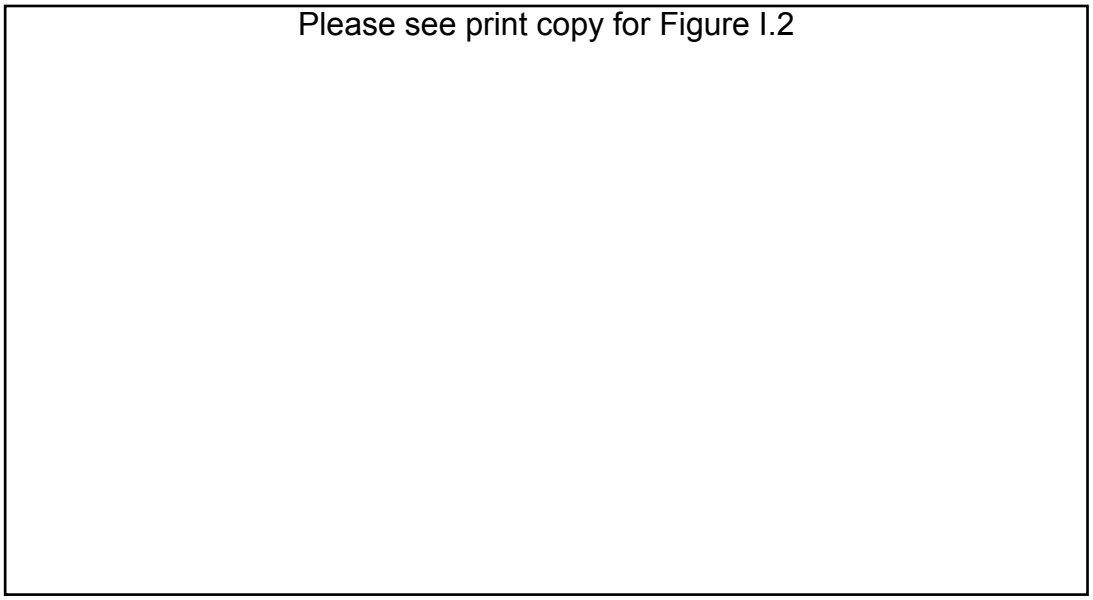

Figure I.2: *A simplified isothermal phase stability diagram for the Li-Sn-O system, assuming that there is no stable ternary phase.*[41]

This result can be expressed in terms of a theoretical electrochemical titration curve, in which the potential is plotted versus the composition as shown in Figure I.3. There are three phases present in a ternary system, and if the temperature and the overall pressure are held constant, the degree of freedom is zero ($F = 0$), according to the Gibbs Phase Rule. This means that the electrical potential must be independent of composition, i.e. there will be a potential plateau. This potential can be calculated from the Gibbs free energy change (ΔG) involved in the virtual reaction that takes place within the three-phase region.[41-42,208] The result is a series of constant-voltage plateaus as the composition moves across the three-phase regions of the diagram.

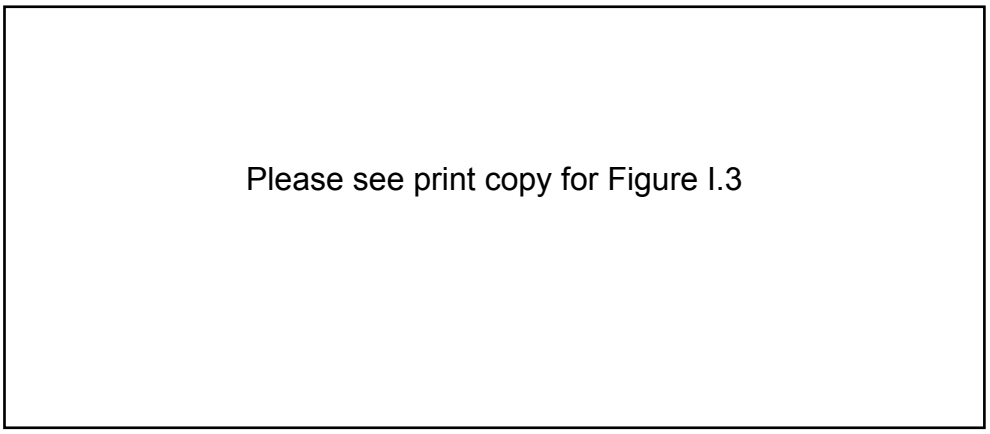

Figure I.3: *A theoretical electrochemical titration curve of SnO_2, in which the potential is plotted versus the composition.*[42]

At the initial stage, two Li^+ will initially react with SnO_2 to form Li_2O and SnO at a potential of 1.88 V. Following this, an additional two Li^+ will react with the SnO to form more Li_2O and Sn at a potential of 1.58 V. If these two reactions are irreversible, four Li^+ are consumed in SnO_2, resulting in a large irreversible capacity of 711.3 $mAh \cdot g^{-1}$. Considering the active reversible capacity, which is obtained by the reaction of additional Li^+ with the Sn, from the theoretical titration diagrams, an additional 4.4 Li^+ can react with pure Sn after the conversion of the oxides, corresponding to a reversible capacity of 783 $mAh \cdot g^{-1}$.

I.D. Thermodynamics of Nanostructured Materials

In the case of SnO_2 having a reconstitution reaction with Li^+, if there are no residual degrees of freedom, the voltage is independent of the extent of the cell reaction. That means that the

voltage could depend on other factors, such as the crystal structure, morphology or energy state of the material. There could be several energy states of a phase with different structures that might be stable in the sense that they have lower values of the Gibbs free energy than would be the case with minor changes. Such a situation, in which a phase is stable against small perturbations, is described by the term metastable equilibrium, as schematically illustrated in Figure I.4.[41-42]

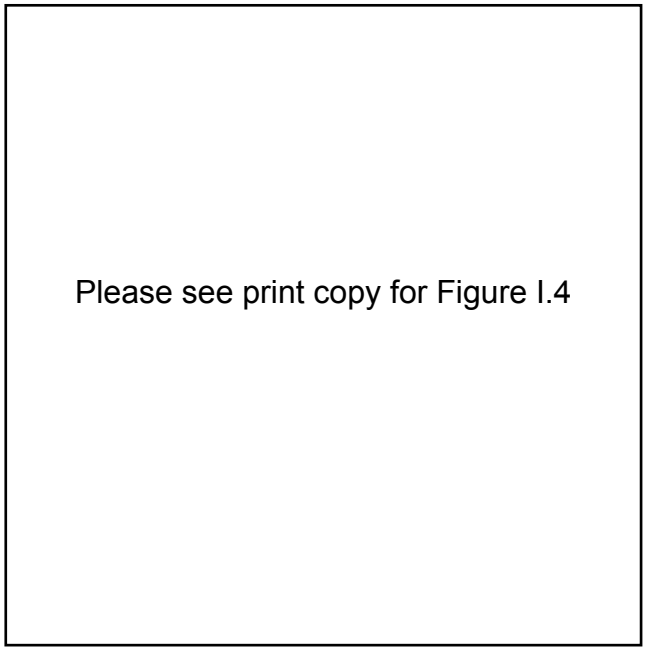

Figure I.4: *Simple mechanical model illustrating complete stability, metastability, and instability.*[42,208]

This situation can also be described in terms of the changes in the energy of the system. If the material is in a metastable state, minor changes will raise its Gibbs free energy, and it will tend to revert back to the metastable condition. It will take a larger perturbation to get it over the energy hump that will enable it to get to the absolutely stable state, even though the absolutely stable state has a lower energy than the metastable state, as described in Figure I.5.

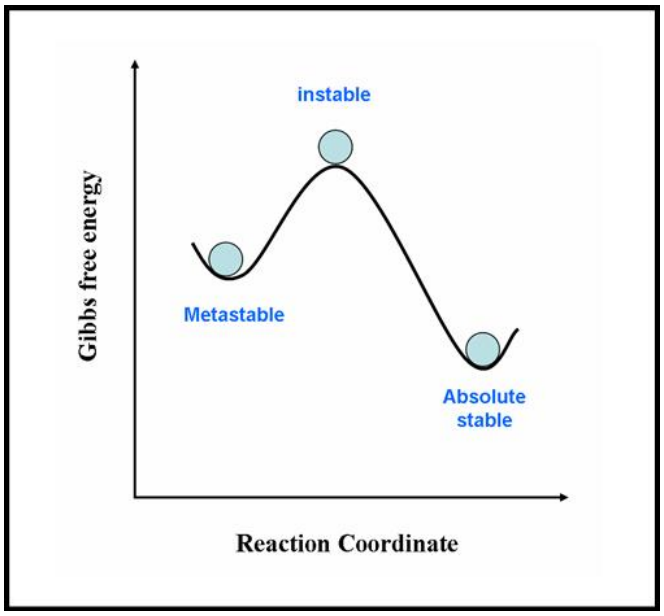

Figure I.5: *A schematic representation of a system with instable, metastable and absolutely stable states.*

Metastable phases and crystal structures often play significant roles at ambient temperature. The amorphous structure is well known as a metastable phase. It is like the nanostructured materials from a thermodynamic point of view, because an amorphous structure can be formed when a complete equilibrium cannot be attained. Amorphous structures are always less stable than the crystalline structure with the same composition. Thus, they have less negative values of the Gibbs free energy of formation, which means that the electrical potential of a reaction involving an amorphous phase will be different from that if the phase were crystalline. Consider a possible case where Li^+ reacts with a material *M* to form *LiM*, and then a further reaction can form Li_2M. These reactions can be written as: [41,202-208]

$$Li + M \leftrightarrow LiM \qquad \text{(I.4)}$$

$$E = -\frac{\Delta G_f(LM)}{kT} \tag{I.5}$$

$$Li + LiM \leftrightarrow Li_2M \tag{I.6}$$

$$E = -\frac{\left[\Delta G_f(Li_2M) - \Delta G_f(LiM)\right]}{kT} \tag{I.7}$$

where *k* is Boltzmann's constant and *T* is the temperature in degrees Kelvin. Thus, if one has the appropriate values of the ΔG_f for these phases, the variation of the voltage with composition in this simple system can be predicted, as schematically depicted in Figure I.6.

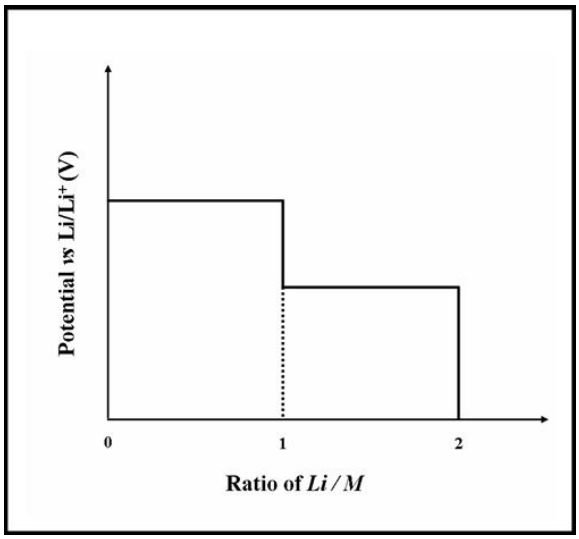

Figure I.6: *The variation of the voltage with composition under complete equilibrium conditions.*

The area under these voltage curves corresponds to the total Gibbs free energy change of the respective reactions. On the other hand, if the phase *LiM* is amorphous, the potential plateau corresponding to the first reaction will appear at a lower voltage, and the potential plateau corresponding to the second reaction will occur at a higher voltage (Figure I.7). However, the total Gibbs free energy of the two reactions does not change. The interesting result is that the step in the voltage plateau is reduced, so that the total two-phase reaction looks and behaves more like a single-phase reaction, but with the capacity of the two-phase reaction.[41,208]

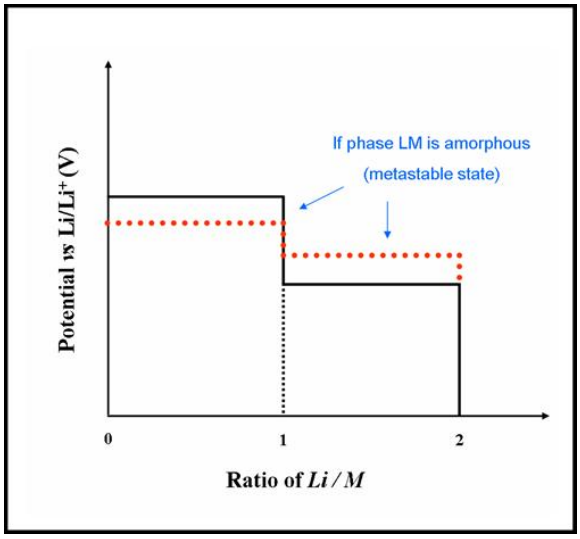

Figure I.7: *The variation of the voltage with composition if the LiM phase is in a metastable state.*

Based on the thermodynamic considerations, the electrochemical performance of SnO_2 materials could be different if the dimensions of materials are minimized down to the nanoscale, in which case the materials would be in a metastable state. For these reasons, the interfacial kinetics could be dramatically facilitated in these nanostructured materials, because the transport tortuosity of the Li^+ ion path could be minimized. In addition, these nanostructured materials

exhibit higher surface areas, which lower the local current density. The Li^+ diffusion distances are correspondingly shorter, resulting in a decrease in the concentration polarization. Furthermore, assembly of the ultra-fine electrode materials into continuous structures can enhance contacts and suppress free particle movement, so as to hinder aggregation of mobile electrode materials. Thus, the major challenge in this work is to fabricate nanostructured SnO_2 materials as negative electrodes for lithium-ion batteries.

4. Preparation and Electrochemical Properties of SnO_2 Nanowires for Application in Lithium-Ion Batteries

4.1. Introduction

One-dimensional (1D) nanostructured materials have received considerable attention for advanced functional systems, as well as for extensive applications owing to their attractive electronic, optical, and thermal properties.[209-210] In lithium-ion-battery science, recent research has focused on nanoscale electrode materials to improve electrochemical performance. The high surface-to-volume ratios and excellent surface activities of 1D nanostructured materials have stimulated great interest in their development for the next generation of power sources.[211-212]

Materials based on tin oxide have been proposed as alternative anode materials with high-energy densities and stable capacity retention in lithium-ion batteries.[32,70,101] Various SnO_2-based materials have displayed extraordinary electrochemical behavior, such that the initial irreversible capacity induced by Li_2O formation and the abrupt capacity fading caused by volume variation could be effectively reduced when the SnO_2 is in nanoscale form.[213-215] From this point of view, SnO_2 nanowires can also be suggested as a promising anode material, because the nanowire structure is of special interest, with predictions of unique electronic and structural properties. Furthermore, the nanowires can be easily synthesized by a thermal evaporation method. However, in its current form, this method of manufacture of SnO_2 nanowires has several limitations: it is inappropriate for mass production, as high synthesis

temperatures are required and there are difficulties in the elimination of metal catalysts that could act as impurities or defects. This results in reversible capacity loss or poor cyclic performance during electrochemical reactions.[216-217] The critical issues relating to SnO_2 nanowires as anode materials for lithium-ion batteries are how to avoid the deteriorative effects of catalysts and how to increase production.

Herein, we report on the preparation and electrochemical performance of self-catalysis-grown SnO_2 nanowires to determine their potential use as an anode material for lithium-ion batteries. SnO_2 nanowires have been synthesized by thermal evaporation combined with a self-catalyzed growth procedure, by using a ball-milled evaporation material to increase production at lower temperature and prevent the undesirable effects of conventional catalysts on electrochemical performance. The self-catalysis-grown SnO_2 nanowires show higher initial coulombic efficiency and improved cyclic retention compared with SnO_2 powder and SnO_2 nanowires produced by Au-assisted growth.[216]

4.2. Experimental

4.2.1. Preparation of SnO_2 Nanowires

The thermal evaporation process was employed to synthesize SnO_2 nanowires. As an evaporation source, high purity SnO (99.99%, Aldrich) and Sn (99.99%, Aldrich) powders were homogeneously mixed in a 1:1 weight ratio by a planetary mechanical milling process for 40 hours under an atmosphere of argon. Ball-milled powder (1 g) was placed in an alumina boat, which was inserted into a tube furnace. Silicon substrates without metal catalysts were placed downstream one by one at a distance of about 15 cm from the powder. The heating temperature

and time were optimized at 900 °C and 1 hour, respectively. The deposition pressure was 100 Torr of high purity Ar gas at a flow rate of 50 sccm (standard cubic centimeters per minute).

4.2.2. Structural and Electrochemical Characterization

The morphology and microstructure of self-catalysis-grown SnO_2 nanowires were characterized by XRD (Philips 1730), SEM (JEOL JEM-3000), TEM (JEOL 2011), and Raman spectroscopy (Jobin Yvon HR800). The SnO_2 nanowires were mixed with acetylene black (AB) and a binder (poly(vinylidene fluoride); PVdF) in a weight ratio of 75:15:10, respectively, in a solvent (N-methyl-2-pyrrolidone). The slurry was uniformly pasted on Cu foil. Such prepared electrode sheets were dried at 120 °C in a vacuum oven and pressed under a pressure of approximately 200 $kg \cdot cm^{-2}$. CR2032-type coin cells were assembled for electrochemical characterization. The electrolyte was 1M $LiPF_6$ in a 1:1 mixture of ethylene carbonate and dimethyl carbonate. Li metal foil was used as the counter and reference electrode. The cells were galvanostatically charged and discharged at a current density of 100 $mA \cdot g^{-1}$ over a range of 0.05 V to 1.50 V.

4.2.3. Self-catalyzed Growth

For the self-catalysed growth of SnO_2 nanowires, the evaporation source, which consists of Sn and SnO powder, was prepared by mechanical milling for 40 hours under Ar atmosphere. The preparation conditions were optimized in advance, in order to reduce the deposition temperature and increase production of nanowires. As can be seen from Figure 4.1, the particle size was visibly reduced as a function of milling time, as shown in Figure 4.1(c) and 4.1(d). The reduced particle size resulted in greatly increased reactivity of the evaporation source and consequently in abundant production of high purity SnO_2 nanowires at a lower temperature than was required before milling.

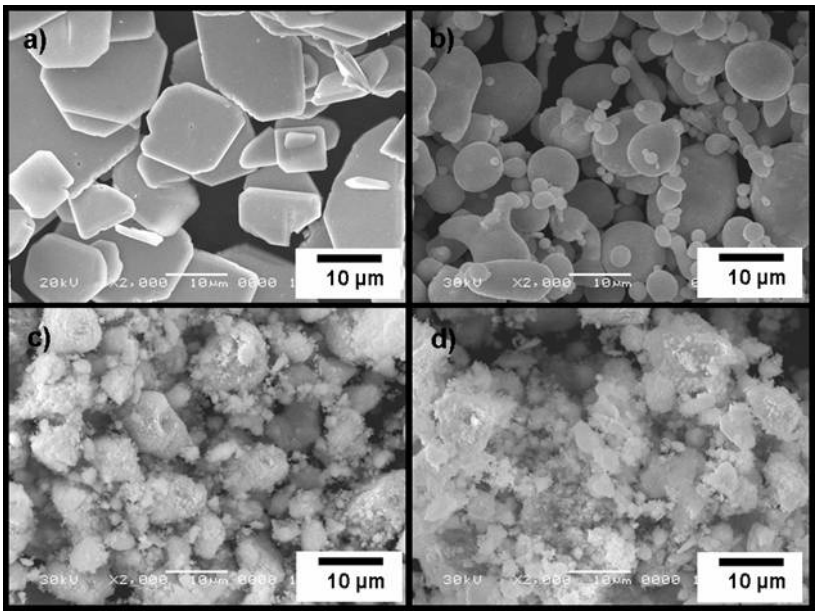

Figure 4.1: *The microstructure of evaporation sources: (a) SEM image of commercial SnO powder; (b) SEM image of commercial Sn powder; (c) SEM image of ball-milled mixture of SnO and Sn (1:1 by weight ratio), after milling for 20 hours and (d) SEM image of ball-milled mixture of SnO and Sn (1:1 by weight ratio) after milling for 40 hours.*

SnO_2 nanowires could be synthesized by a thermal evaporation process, even without any conventional metal catalysts. Therefore Sn powder without any conventional catalyst was chosen for growth of the nanowires. However, Sn can be easily oxidized to SnO or SnO_2 upon milling. These oxides have higher melting points than pure Sn. In order to keep the Sn phase in the evaporation source, the mechanical milling was performed under Ar atmosphere. Figure 4.2 shows different patterns of the evaporation source prepared under different atmospheres. In the case of the sample ball-milled in air, all of the Sn was oxidized to SnO (JCPDS 06-0395) during the milling process. On the other hand, pure Sn (JCPDS 86-2265) was present in the sample ball-milled under Ar atmosphere. Sn in the evaporation source can be vaporized at low temperatures and will act as a catalyst for the formation of SnO_2 nanowires.

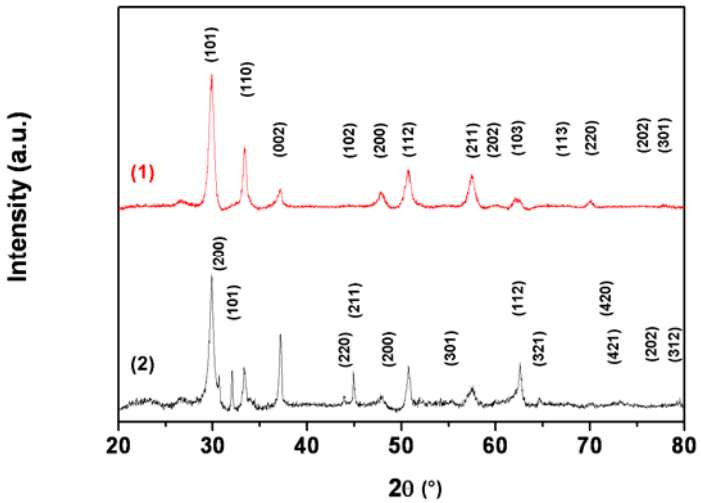

Figure 4.2: *X-ray diffraction patterns of a mixture of Sn and SnO (1:1 by weight ratio) after ball milling for 40 hours: (1) ball-milled under air (indexed by: SnO (JCPDS 06-0395)) and (2) ball-milled under Ar atmosphere (indexed by: Sn (JCPDS 86-2265)).*

In order to define the temperature effects on the morphology of self-catalysis grown SnO_2 nanowires, the deposition temperature was varied from 800 ˚C to 950 ˚C, while the other synthetic parameters were fixed, as mentioned in experimental section 4.2.1. The morphology of nanowires is highly dependent on the deposition temperature, as shown in Figure 4.3. Overall, the diameter and length of nanowires increase with increasing deposition temperature. At 800 ˚C, some agglomerations of nanowires with relatively small diameter and length were observed, owing to an inadequate supply of Sn vapor, while some nanoribbons could be formed by oversupply of Sn vapor at 950 ˚C. SnO_2 nanowire formed at 900˚C, however, is non-defective compared to nanowires formed at other temperatures.

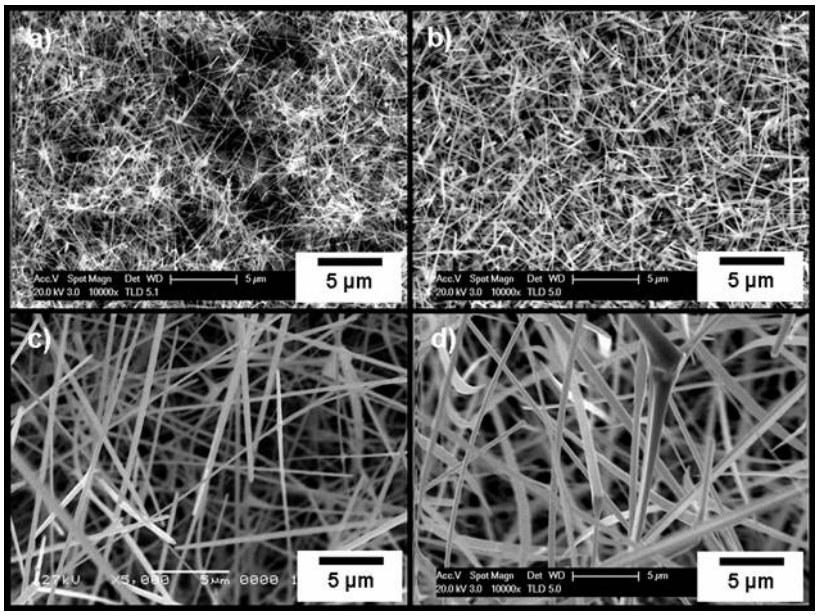

Figure 4.3: *SEM images of SnO_2 nanowires prepared at different temperatures: (a) 800˚C; (b) 850˚C; (c) 900˚C;, and (d) 950˚C.*

4.3. Results and Discussion

4.3.1. Structural and Morphological Characterization

The self-catalysis growth method, which uses a ball-milled mixture of SnO and Sn powder as an evaporation source, is appropriate for obtaining SnO_2 nanowires with high purity. The deposited products on the Si substrates contain almost 100% of the SnO_2 nanowires formed. Observation by scanning electron microscopy (SEM) clearly shows a general view of randomly aligned SnO_2 nanowires with diameters of 200-500 nm and lengths extending to several tens of micrometers (Figure 4.4(a)). Sn droplets at the tips of nanowires were observed and confirmed by energy dispersive X-ray (EDX) spectroscopy (Figure 4.4(b) and 4.4(c)). In regards to the low melting point of Sn (231.9 °C), it is suggested that Sn particles in the starting material form

liquid nuclei on the Si substrate at the initial stage of the evaporation above 300 °C, leading to vapor−liquid−solid (VLS) growth of the SnO_2 nanowires at 900 °C. The Sn droplets were essential for growth of SnO_2 nanowires without conventional catalysts and for determining the diameters of nanowires. More interestingly, close inspection of the stem of an individual nanowire showed a quadrilateral cross-section (Figure 4.4(d)), which is in agreement with a tetragonal structure.

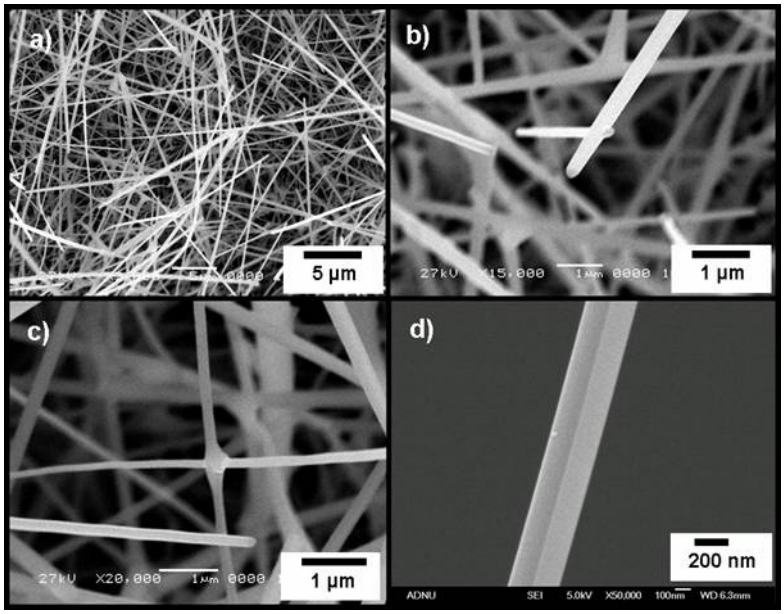

Figure 4.4: *The microstructure of self-catalysis-grown SnO_2 nanowires: a) SEM image of SnO_2 nanowires; b) SEM image of tips, including Sn droplets; c) SEM image of junction; and d) field-emission SEM (FESEM) image of an individual nanowire stem.*

Figure 4.5(a) shows an X-ray diffraction (XRD) pattern of SnO_2 nanowires compared with that of SnO_2 powder. All reflections of SnO_2 nanowires are in excellent accordance with a tetragonal rutile structure (JCPDS 41-1445), which belongs to the space group $P4_2/mnm$ (136). The lattice parameters of the nanowires were $a = b = 4.738$ Å and $c = 3.188$ Å. It is well known that a

nanowire form with a high aspect ratio experiences more tensile stress along the *c*-axis direction on the surface than the powder form, which leads to an increase in the *c* value. In accordance with this, *c*-axis-related peak shifts to lower angles were detected for SnO_2 nanowires when compared with the powder; the shifts of the nanowires were $\Delta(2\theta)$ = 0.063°, 0.067°, and 0.058° for the (101), (002), and (301) peaks, respectively. The full width at half maximum (FWHM) of the (002) peak for SnO_2 nanowires and SnO_2 powder were calculated to be 0.2800° and 0.3400°, respectively. The apparently smaller FWHM for the (002) peak indicates that the nanowires have better crystallinity with fewer lattice distortions along the *c*-axis in the tetragonal system. From the XRD results, the *c*-axis-related peak shifts and FWHM behavior provided evidence of an increase in the *c*-axis parameter in the nanowire lattice structure. Figure 4.5(b) shows Raman spectra of the SnO_2 nanowires compared with SnO_2 powder. The fundamental Raman scattering peaks for SnO_2 powder were observed at 477 cm^{-1}, 636 cm^{-1}, and 777 cm^{-1}, corresponding to the E_g, A_{1g}, and B_{2g} vibration modes, respectively.[214] We also found these peaks in the Raman spectra of SnO_2 nanowires at 477 cm^{-1}, 636 cm^{-1}, and 775 cm^{-1}. The downwards shift of the B_{2g} vibration mode for SnO_2 nanowires could be caused by the size effect of the structure.[217] These results are also consistent with formation of self-catalysis-grown SnO_2 nanowires with a single crystalline structure.

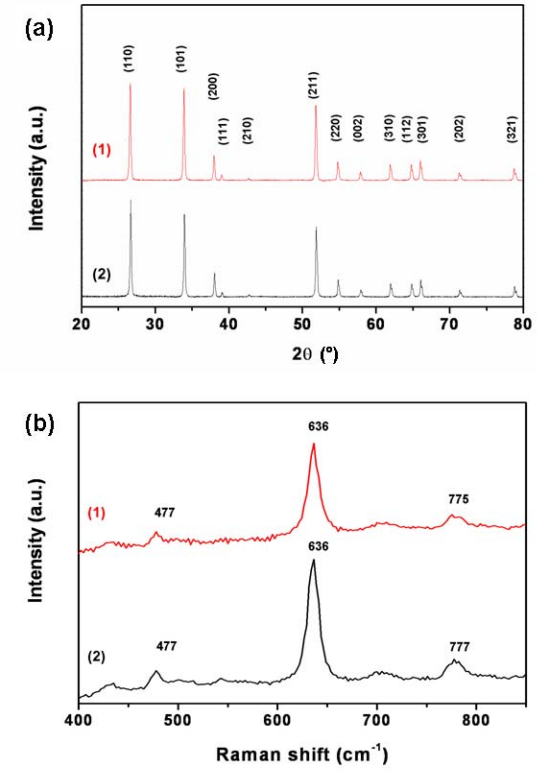

Figure 4.5: *a) X-ray diffraction patterns of SnO_2 nanowires (1) and SnO_2 nanopowders (2). b) Room-temperature Raman spectra of SnO_2 nanowires (1) and SnO_2 nanopowders (2).*

TEM bright-field imaging combined with selected-area electron diffraction (SAED) revealed the fine microstructure of the SnO_2 nanowires, with each wire being a monocrystal with a tetragonal structure (Figure 4.6(a)). Tilting experiments also revealed no evidence of extended defects within the individual crystals. High-resolution (HR) imaging was combined with SAED to investigate the nanowire growth direction. For the wire shown in Figure 4.6(a), the zone axis is [001], and the growth direction of the nanowire is parallel to [100]. The HRTEM image (Figure 4.6(b)) confirms this, with an interplanar spacing of approximately 0.47 nm between neighboring [100] planes of tetragonal SnO_2.

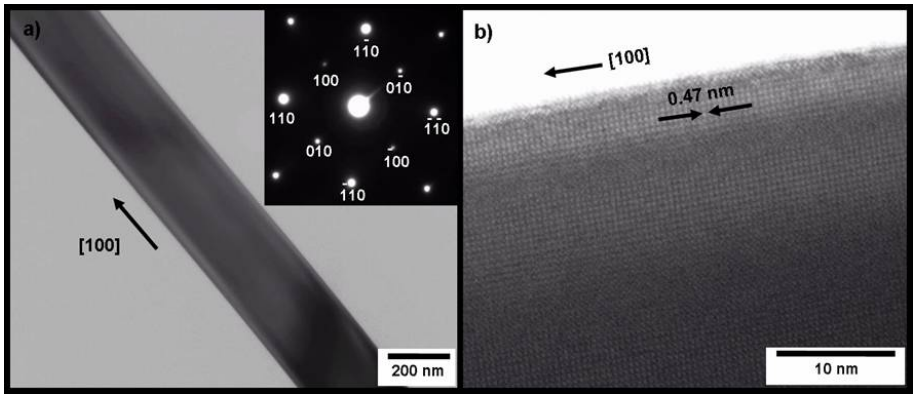

Figure 4.6: *a) TEM image and SAED pattern (inset) of a SnO_2 nanowire. Zone axis is [001]. b) HRTEM image of a section of a SnO_2 nanowire.*

4.3.2. Electrochemical Properties

The anodic performance of SnO_2 nanowires was tested over the potential range of 0.05 to 1.50 V (versus Li/Li^+). For comparative purposes, SnO_2 powder was also examined under the same conditions. The SnO_2 nanowires show much higher Li^+ storage and a relatively smaller initial irreversible capacity of 1134 $mAh \cdot g^{-1}$ in the galvanostatic voltage profiles for the first cycle, as shown in Figure 4.7(a). Note that the SnO_2 nanowires show an initial coulombic efficiency of approximately 46.91%, which is notably higher than that of the SnO_2 powders (31.01%). The improvement in the electrochemical behavior should be attributed to the 1D nanowire structure with a large surface area and high length/diameter ratio. The 1D nanowire structure could provide more reaction sites on the surface, and the smaller diameter of the nanowires provides a short diffusion length for Li^+ insertion, which could enhance the charge transfer and electron conduction along the length direction. More importantly, the Sn droplets on the tips of nanowires could also contribute to the Li^+ storage and reduce the pulverization owing to lattice

mismatches at the interfaces between nanowires and catalysts, which would result in improvements in the initial coulombic efficiency and Li^+ storage. To identify electrochemical reactions during cycling, cyclic voltammograms (CV) of SnO_2 nanowires were obtained and are presented in Figure 4.7(b). The CV profiles show two apparent reduction peaks around 0.95 V and 1.20 V derived from Li_2O formation and electrolyte decomposition when SnO_2 nanowires react with Li^+, as described in Equation 4.1.[213] These peaks should disappear, leaving a large initial irreversible capacity after the first cycle in SnO_2 powder electrodes. However, these irreversible reactions were still taking place until the fifth cycle in the SnO_2 nanowire electrodes. We suggest that the single-crystalline structure of the nanowires may disturb the smooth isertion of Li^+ into the interior of the nanowires, which leads to a slow lithiation. Furthermore, the additional electrolyte decomposition on the new surface induced by volume expansion may result in irreversible capacity, even after the first cycle. Based on these considerations, the Li_2O formation and electrolyte decomposition might continue through subsequent cycles, leading to an increasing irreversible capacity up to the fifth cycle, as shown in Figure 4.7(c).

$$SnO_2 + 4Li^+ + 4e^- \rightarrow Sn + 2Li_2O \quad (4.1)$$

$$Sn + xLi^+ + xe^- \rightarrow Li_xSn \quad (0 \le x \le 4.4) \quad (4.2)$$

The other pairs of reduction and oxidation peaks at 0.25 V and 0.60 V during the discharge and at 0.50 V and 0.70 V during the charge cycles are related to the formation of Li_xSn, as described in Equation 4.2.[213] The self-catalysis-grown SnO_2 nanowires exhibit improved cyclic performance and a higher reversible specific charge of over 300 $mAh \cdot g^{-1}$ up to the 50th cycle, as shown in Figure 4.7(c). This suggests that the 1D nanowire structure with a high aspect ratio of

length to diameter effectively increases the charge-transfer properties along the length direction compared with the powder form. Moreover, the self-catalysis-grown SnO_2 nanowires show a smaller capacity fading of 1.45% per cycle after the fifth cycle, which is much smaller than that of SnO_2 nanowires grown through Au assistance (3.89%).[216] It is likely that the reversible capacity loss or electrical disconnection induced by the traditional metal catalysts could be effectively reduced in the self-catalysis-grown SnO_2 nanowires.

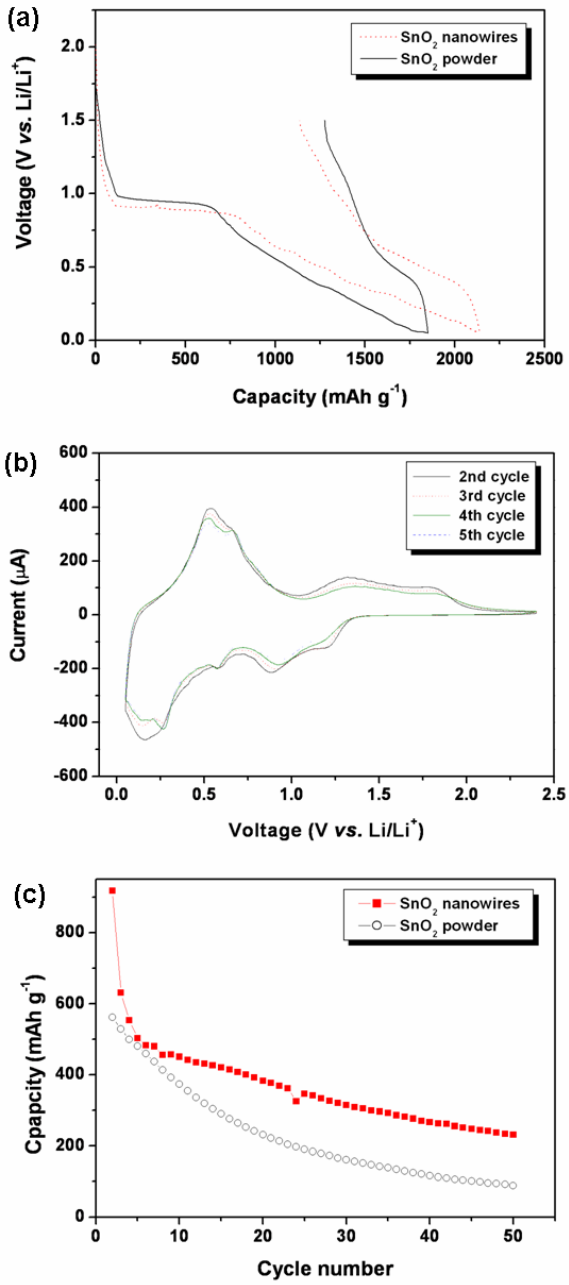

Figure 4.7: *The anodic performance of the SnO_2 nanowires. a) The galvanostatic voltage profile for the first cycle between 0.05 V and 1.50 V compared with pure SnO_2 nanopowder. b) Cyclic voltammograms from the second cycle to the fifth cycle at a scan rate of 0.05 $mV \cdot s^{-1}$ in the voltage range of 0.05–2.50 V. c) The cyclic performance from the second cycle to the 50th cycle of SnO_2 nanowires and pure SnO_2 powder at the same current density, 100 $mA \cdot g^{-1}$.*

4.4. Summary

In summary, we have fabricated self-catalysis-grown SnO_2 nanowires by a thermal evaporation process. The ball-milled evaporation source served to increase production and decrease the synthesis temperature. The Sn particles in the evaporation source played the role of the catalyst, allowing VLS growth of the SnO_2 nanowires. The 1D nanowire structure could provide more reaction sites on the surface and enhance the charge transfer in the electrochemical reactions. Moreover, Sn particles at the tips of nanowires also contributed to the Li^+ storage and prevented the capacity loss that is induced by the existing metal catalysts.

5. The Effect of Morphological Modification on the Electrochemical Properties of SnO_2 Nanostructured materials

5.1. Introduction

One-dimensional (1D) nanostructured materials have attracted a great deal of interest because of their various possibilities in nanoscience and nanotechnology.[218-221] Significant progress has been reported in the use of nanostructured materials as electrode materials for lithium-ion batteries. In practice, their large surface-to-volume ratio and relatively short diffusion length could enhance the electrochemical as well as the kinetic properties.[172,180,222-223] Because of their controlled shape and size on the nanometer scale, these nanostructured materials may help in the development of the next generation of advanced lithium-ion batteries. An interesting aspect of the development of lithium-ion batteries is the drive to design and manufacture new anode materials with stable cyclic retention and higher reversible capacity for Li^+ compared to the commercial anode material, graphite (372 $mAh \cdot g^{-1}$).[2,9,49] Because SnO_2-based materials have already been suggested as the most promising candidates for anode materials in terms of their theoretical reversible capacity (783 $mAh \cdot g^{-1}$), structural modifications of SnO_2 have been attempted to make its electrochemical performance adequate for commercialization.[32,70,101] However, the undesirable Li_2O phase formation and volume expansion of the Sn phase constitute the main barriers that have to be overcome. The oxidation reactions in Equations 5.1 and 5.2 below describe not only Li_2O formation, but also the volume expansion of Sn:[213]

$$SnO_2 + 4Li^+ + 4e^- \rightarrow Sn + 2Li_2O \qquad \text{(large irreversible capacity)} \qquad (5.1)$$

$$Sn + xLi^+ + xe^- \rightarrow Li_xSn \quad (0 \leq x \leq 4.4) \qquad \text{(large volume variation)} \qquad (5.2)$$

It is well documented that the Li_2O phase is electrochemically inactive and non-conductive, which is the main reason for the large initial irreversible capacity and the large volume variation of the Sn phase, leading to an abrupt capacity fading during cycling. However, the Li_2O phase could be decomposed, and the volume expansion of the Sn phase could be effectively reduced, if the material were in the nanoscale form, according to some earlier reports.[96,213,224-225] These reports have attracted significant attention to structural modifications of SnO_2 on the nanoscale, because the electrochemical performance of SnO_2 seems to have a strong correlation with the structural features of the SnO_2 phase. Such modifications might then allow us to reduce the initial irreversible capacity and improve the cyclic retention in the SnO_2 nanostructured materials. So far, there is practically no information on the correlation between electrochemical properties and the different crystallographic structures of SnO_2 nanostructured materials. However, there is reason to expect that structural modification could be a general solution to the problem of large initial irreversible capacity and poor cyclic retention of SnO_2-based anode materials.

Herein, we introduce the distinctive electrochemical performances in different types of SnO_2 nanostructured materials, such as nanotubes, nanowires, and nanopowders. The relationships between the different structural features such as surface area, porosity, and electronic conductivity, from different crystallographic structures and the observed electrochemical

properties are discussed to determine the advantages of 1D nanostructured materials. Furthermore, the promising possibilities of 1D SnO_2 nanostructured materials are emphasized from the electrochemical point of view.

5.2. Experimental

5.2.1. Preparation of SnO_2 Nanopowders

Nanocrystalline SnO_2 nanopowders were synthesized by a conventional sol–gel method as follows: 3 M of Sn^{II} solution was prepared by dissolving 0.338 g of $SnCl_2 \bullet 2H_2O$ (99.99%, Aldrich) in a mixture of ethanol (0.47 ml) and 36% HCl (0.03 ml). The solution was aged for 24 hours, and then water (0.03 ml) was added under continuous stirring for 12 hours. After the formation of the gel, it was dried at 120 °C for 2 hours and sintered at 600 °C for 3 hours in a vacuum furnace under an Ar (95%) and O_2 (5%) atmosphere. To remove Cl^-, the final product was washed with distilled water via a centrifugal process and dried at 120 °C for 2 hours in a vacuum oven.

5.2.2. Preparation of SnO_2 Nanotubes

SnO_2 nanotubes were prepared via a sol–gel vacuum-suction method. 10 ml of a 3 M Sn^{II} solution was prepared as outlined above. The Sn-based solution was inserted into the nanoholes of anodic aluminum oxide (AAO) templates by a reduced vacuum-suction process. The product was dried at 120 °C for 2 hours and sintered at 400 °C for 3 hours in a vacuum furnace under an Ar (95%) and O_2 (5%) atmosphere. The AAO templates were dissolved in a 6 M NaOH solution. The product was washed with distilled water by centrifuging, finally dried in a vacuum oven.

5.2.3. Preparation of SnO_2 Nanowires

A thermal-evaporation process was employed to synthesize the SnO_2 nanowires. For the evaporation source, high-purity SnO (99.99%, Aldrich) and Sn (99.99%, Aldrich) powders were homogeneously mixed in a 1:1 weight ratio by planetary mechanical milling for 40 hours under an Ar atmosphere. An alumina boat containing 1 g of ball-milled powder was placed inside a tube furnace. Silicon substrates without metal catalysts were placed downstream one by one at a distance of about 15 cm from the powder. The processing temperature and time were optimized at 900 °C and 1 hour, respectively. The deposition pressure was around 100 Torr of high-purity Ar gas at a flow rate of 50 sccm (standard cubic centimeters per minute).[180]

5.2.4. Electrochemical Experiments

To make electrodes, a mixture of 75 wt% of each active material and 15 wt% acetylene black (AB) was added to a solution containing 10 wt% polyvinylidene fluoride (PVdF) in n-methyl-2-pyrrolidinone (NMP). This slurry was pasted onto a copper foil current collector and dried at 120 °C for 2 hours in vacuum (10^{-3} Torr). After pressing under a pressure of about 200 $kg \cdot cm^{-2}$, half cells (CR2032 coin-type) were fabricated to evaluate the anodic performance of the SnO_2 nanostructured materials. The assembly was carried out in an Ar-filled glove box with less than 0.1 ppm each of oxygen and moisture. A Li metal foil was used as the counter and reference electrode, and 1 M of $LiPF_6$ dissolved in a 1:1 (v/v, Merck KGaA) mixture of ethylene carbonate (EC) and dimethyl carbonate (DMC) was employed as the electrolyte. Charge–discharge tests and cyclic voltammetry (CV) tests on the SnO_2 nanostructured materials were performed up to the fiftieth cycle in the range of 0.05 to 1.5 V (vs. Li/Li^+).

5.2.5. Structural and Morphological Characterization

The microstructure and morphology of SnO_2 nanostructured materials were characterized by X-ray diffraction (XRD, Philips 1730), Raman spectroscopy (Jobin Yvon HR800), field-emission scanning electron microscopy (FESEM, JEOL JEM-3000), and transmission electron microscopy (TEM, JEOL 2011). In order to measure the conductivity of the SnO_2 nanostructured materials, a Jandel four-point probe technique was adopted. Finally, the pore volume and surface area of our SnO_2 nanostructured materials were estimated by Barret–Joiner–Halenda (BJH) and Brunauer–Emmett–Teller (BET) analyses, respectively.

5.3. Results and Discussion

5.3.1. Material Preparation and Characterization

For the purpose of demonstrating the effect of morphological modification on the electrochemical performance of SnO_2, three different types of SnO_2 nanostructured materials (nanotubes, nanowires, and nanopowders) were synthesized for use as anode materials. Typical field-emission scanning electron microscopy (FESEM) images of SnO_2 nanostructured materials at different magnifications are displayed in Figure 5.1. The SnO_2 nanotubes prepared by the sol–gel templating route combined with a vacuum-suction method are characterized by a tubular structure with open tips. They have a uniform outer diameter of around 200 nm and well-defined inner holes, as shown in Figure 5.1(a) and 5.1(b). It was expected that the tubular structure of SnO_2 nanotubes would be providing more reaction sites, with the additional advantage that their porous wall structure could accommodate a volume variation of the Sn phase during cycling. In the case of SnO_2 nanowires synthesized by thermal evaporation, SEM

observations clearly show randomly aligned SnO_2 nanowires with diameters of 100–300 nm and lengths extending to several tens of micrometers (Figure 5.1(c) and 5.1(d)). It has been well documented that single-crystalline nanowires have some advantages for electronic conduction and Li^+ diffusion, which leads to the improvement of the kinetic properties.[180] In comparison, SnO_2 nanopowders prepared by the conventional sol–gel method have a particle size of less than 100 nm on average and a clean surface without obvious irregular ravines (Figure 5.1(e) and 5.1(f)). The particle agglomeration observed in SnO_2 nanopowders results from local van der Waals forces.

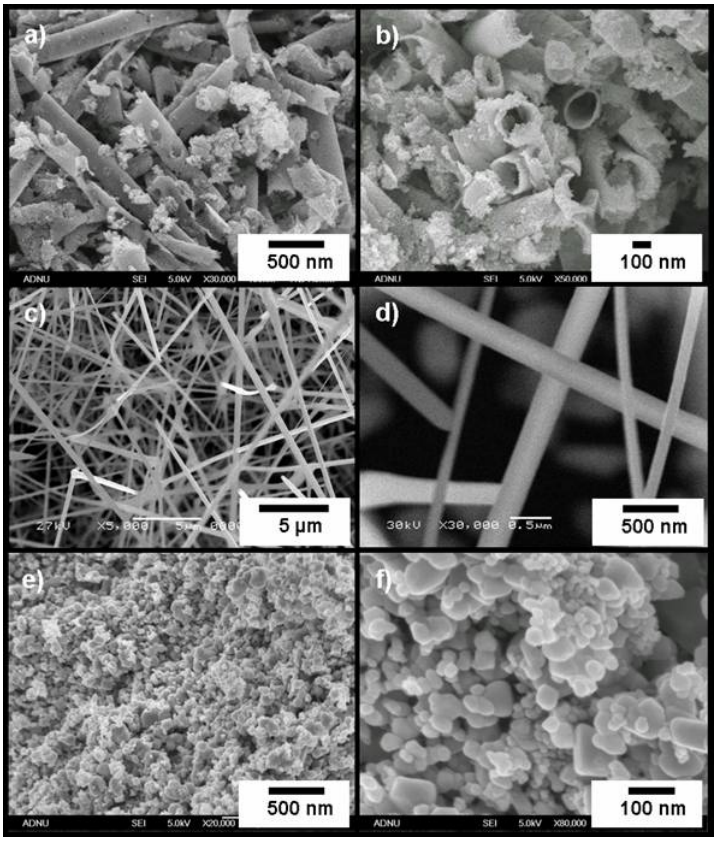

Figure 5.1: *The microstructures of SnO_2 nanostructured materials: a,b) FESEM images of SnO_2 nanotubes; c,d) FESEM images of SnO_2 nanowires; e,f) FESEM images of SnO_2 nanopowders at different magnifications.*

In order to determine the structural features of these nanostructured materials with different morphological characteristics, their phase and crystallinity were confirmed by X-ray diffraction (XRD) and Raman spectroscopy. As shown in Figure 5.2, all reflections of SnO_2 nanostructured materials were in excellent accordance with the tetragonal rutile structure (JCPDS 41-1445), which belongs to the space group $P4_2/mnm$ (136). There was no notable peak shifting or intensity variation induced by secondary phases or impurities. Within the margins of error, the lattice parameters, volume, lattice strain, and density of the nanostructured materials could be estimated by using Rietveld refinement, as summarized in Table 5.1.

Table 5.1: *Rietveld refinement results for SnO_2 nanostructured materials.*

	a (Å)	c (Å)	Volume (Å^3)	Strain (%)	Density (g·cm^{-3})
NT [a]	4.7384(3)	3.1874(7)	71.62	0.497(7)	7.0358
NW [b]	4.7386(2)	3.1882(1)	71.57	0.117(5)	7.1309
NP [c]	4.7372(5)	3.1864(2)	71.53	0.113(2)	6.9985

[a] SnO_2 nanotubes, [b] SnO_2 nanowires, [c] SnO_2 nanopowders.

Because the reference SnO_2 phase has lattice parameters of $a = b = 4.7386$ Å and $c = 3.1872$ Å, it can be said that for our nanostructured materials, there is no significant difference related to substitutional or interstitial occupancy of impurities compared to the reference material. We only found a small extension of the *c*-axis lattice parameter of the nanowires and nanotubes, which might be caused by more tensile stress along the *c*-axis, and a small reduction of the *c*-axis for the nanopowders because of their small dimensions.[180] With regard to the behavior of the full width at half maximum (FWHM) values, the SnO_2 nanotubes show an apparently

larger peak broadening compared to the other nanostructured materials. So far as strain is concerned, the lattice strain is directly caused by variations in the *d*-spacing, if there is no uniform stress over a long distance induced by dislocations or lattice distortions. The nanotubes show much larger strain values compared to that of the nanopowders in Table 5.1. The larger strain induced by the internal stress from maintaining its unique nanostructure and from the nanopores in the walls could lead to peak broadening. In addition, a small value of the coherence area, which results in broadening of the reflections in the XRD patterns, is found for the polycrystalline nanotubes, which is unlike the pattern for single-crystalline nanowires. This is thought to be characteristic of the fine tubular structure.[172,224] In the case of nanowires, there were small reductions in the FWHM values compared to the nanopowders, corresponding to grain growth or enlargement of the crystal size.

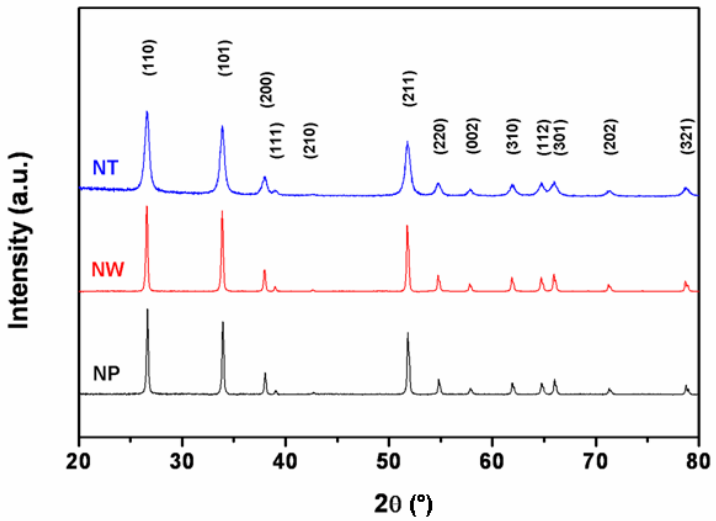

Figure 5.2: *X-ray diffraction patterns of SnO_2 nanostructured materials: nanotubes (NT), nanowires (NW), and nanopowders (NP).*

Figure 5.3 shows room-temperature Raman spectra of the SnO_2 nanostructured materials. The fundamental Raman scattering peaks for the SnO_2 nanopowders were observed at 477 cm^{-1}, 636

cm^{-1}, and 777 cm^{-1}, corresponding to the E_g, A_{1g}, and B_{2g} vibration modes, respectively.[214] We also found these peaks in the Raman spectra of the nanotubes and nanowires. As shown in Figure 5.3, the downwards shift of the B_{2g} vibration mode in SnO_2 nanotubes (776 cm^{-1}) and nanowires (775 cm^{-1}) could be caused by the size effect of the structures.[217] It is well known that the spectra are highly dependent on excitations from the resonance behavior. They could also be influenced by structural factors or the wavelength of the laser. Inspection of these spectra indicates that the resonance might be influenced by the different nanostructures in our samples.[217] The typical specific surface areas and pore volumes of the SnO_2 nanostructured materials were estimated by Brunauer–Emmett–Teller (BET) and Barrett–Joyner–Halenda (BJH) analyses, respectively (Table 5.2).

Table 5.2: *Surface areas and electrical conductivities of SnO_2 nanostructured materials.*

	Conductivity σ ($S \cdot cm^{-1}$)	Surface area ($m^2 \cdot g^{-1}$)	Pore volume ($cm^3 \cdot g^{-1}$)
NT [a]	$6.023*10^{-8}$	231.28	0.84
NW [b]	$2.531*10^{-7}$	146.56	0.25
NP [c]	$1.242*10^{-8}$	97.32	0.38

[a] SnO_2 nanotubes, [b] SnO_2 nanowires, [c] SnO_2 nanopowders.

The variations in the surface area and pore volume were highly dependent on the morphological features, as shown in the FESEM images. The porous polycrystalline nanotubes and the single-crystalline nanowires have larger surface areas than the nanopowders. This means that the nanotubes and nanowires with their high aspect ratios (length/diameter) could provide more reaction sites for Li^+ than the nanopowders. In addition, a comparison of the electrical

conductivity for the SnO_2 nanostructured materials convinced us that there is a correlation between the morphological characteristics and Li^+ transfer. Even though the mechanism of Li^+ transfer in the solid state is not clear, it is believed that nanowires show a better Li^+ transfer efficiency compared to the other nanostructured materials. Note that the nanowires show a relatively higher conductivity (Table 5.2).

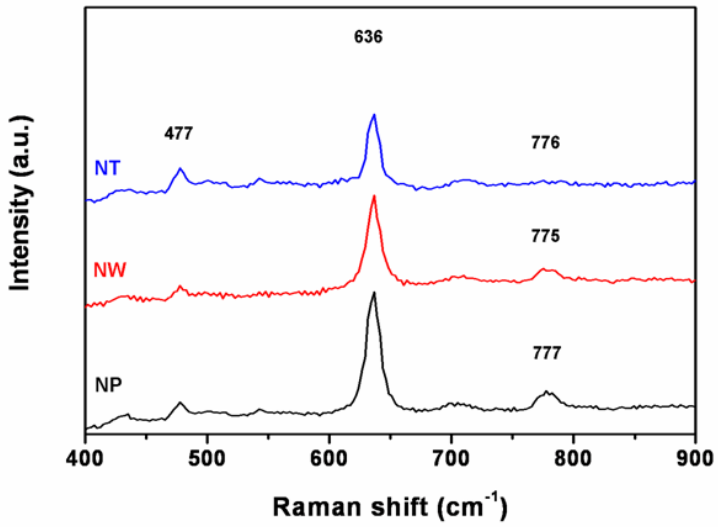

Figure 5.3: *Room-temperature Raman spectra of SnO_2 nanostructured materials: nanotubes (NT), nanowires (NW), and nanopowders (NP).*

Transmission electron microscopy (TEM) observations confirmed the microstructures of our SnO_2 nanostructured materials. The nanotubes have a porous wall structure composed of ultra-fine nanopowders with sizes of less than 100 nm, as shown in Figure 5.4(a). There seems to be an agglomeration of nanopowders with a high aspect ratio along the length direction and hollow inner holes, including fine nanopores on the wall. The corresponding ring-like selected-area electron diffraction (SAED) pattern indicates that the nanotubes have a polycrystalline structure, and the diffraction rings from inside to outside can be indexed to the (110), (101), (200), (211), (301), and (002) planes of rutile SnO_2, respectively. These indexed

patterns are in good accordance with the XRD reflections above. Comparing the SAED patterns of the nanotubes with those of the nanopowders, only blurred patterns and small spots could be derived from the porous structure of the nanotubes. On the other hand, TEM images of the SnO_2 nanowires reveal a fine microstructure, with each wire a single crystal with a tetragonal structure (Figure 5.4(b)). Tilting experiments also revealed no evidence of extended defects within the individual crystals. From the TEM image and SAED patterns, we found that the zone axis is [001], and the growth direction of the nanowire is parallel to [100]. In accordance with our previous observations, we also confirmed that the nanopowders exist in the form of agglomerated nanoparticles with a size of less than 60 nm, as shown in Figure 5.4(c).

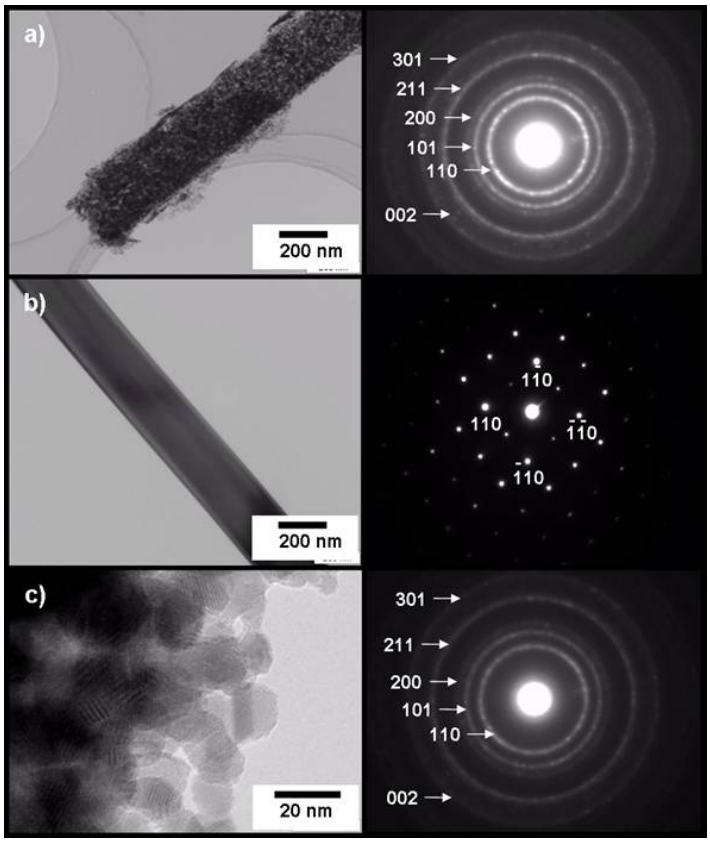

Figure 5.4: *TEM images and selected-area electron diffraction (SAED) patterns of a) SnO_2 nanotubes, b) SnO_2 nanowires*[180]*, and c) SnO_2 nanopowders.*

5.3.2. Electrochemical Properties

The electrochemical reactivity of the SnO_2 nanostructured materials over the potential range of 0.05 V to 1.50 V was tested for up to fifty cycles. There are apparent differences in the electrochemical behavior of the different morphological structures. From the galvanostatic voltage profiles for the first cycle, we found that the nanowires and nanotubes show improved initial coulombic efficiencies compared to the nanopowders, as illustrated in Figure 5.5(a). The first discharge capacities of the nanowires (2137 $mAh \cdot g^{-1}$), the nanotubes (2304 $mAh \cdot g^{-1}$), and the nanopowders (1850 $mAh \cdot g^{-1}$) are in proportion to the surface area, whereas the initial irreversible capacities of the nanowires (1134 $mAh \cdot g^{-1}$), the nanotubes (1384 $mAh \cdot g^{-1}$), and the nanopowders (1277 $mAh \cdot g^{-1}$) are in proportion to the pore volume. It should be noted that the SnO_2 nanowires and nanotubes show initial coulombic efficiencies of approximately 46.91% and 39.31%, respectively, which are notably higher than that of the SnO_2 nanopowders, 31.01%. The electrochemical dependence of the SnO_2 nanostructured materials on their morphological characteristics could be explained by the enhanced electronic conduction and charge transfer of SnO_2 nanowires and nanotubes along the length direction. This is because the SnO_2 nanowires and nanotubes feature a high aspect ratio, which may provide better Li^+ transfer and more reaction sites.

From Table 5.2 it can be seen that the resistance of the nanowires and nanotubes is much lower than that of the nanopowders. This phenomenon implies that the reversible movement of Li^+ into SnO_2 nanowires or nanotubes is much less restrained than that into SnO_2 nanopowders. Actually, the initial Li^+ insertion into nanopowders induced a more drastic potential drop compared to the insertion into nanowires and nanotubes, as shown in Figure 5.5(a). Because the

initial ion insertion is accompanied by activation polarization linked to the electronic conductivity of the electrode materials, this result may prove that the electrochemical performance of SnO_2 greatly depends on its electronic conductivity.[227] This kinetic advantages of nanowires and nanotubes also induced more stable cyclic retention compared to the nanopowders.

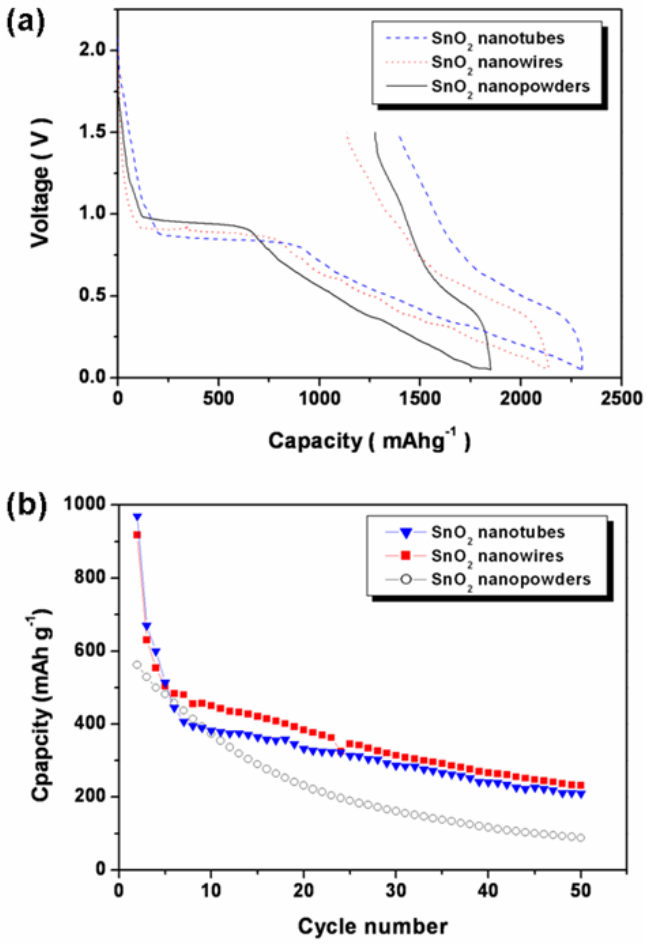

Figure 5.5: *The anodic performances of the SnO_2 nanostructured materials: a) the galvanostatic voltage profiles between 0.05 V and 1.50 V for the first cycle, b) the cyclic performance of SnO_2 nanostructured materials up to the fiftieth cycle at the same current density, 100 $mA \cdot g^{-1}$.*

In Figure 5.5(b), the SnO_2 nanowire and nanotube electrodes exhibited a higher reversible specific charge of over 300 $mAh \cdot g^{-1}$ up to the fiftieth cycle with relatively stable cyclic performance, whereas the nanopowder electrode showed an abrupt capacity fading. The average capacity fading of the nanowires and nanotubes was estimated to be 1.45% and 1.87% per cycle after the second cycle, which was much smaller than that of the SnO_2 nanopowders, 3.46%. Based on these results and this discussion, it could be concluded that suitable morphological modification can lead to strong enhancement of the electrochemical performance of electrode materials. When the cyclic retentions of nanostructured materials are compared, it seems likely that undesirable Li^+ trapping or loss of electronic connection between active materials caused by volume variation could be most effectively prevented in the single crystalline nanowire form. The very small disparity between the cyclic retention of nanowires and nanotubes implies that the electrochemical improvement in nanowires and nanotubes should be mainly attributed to their 1D microstructure. To identify the electrochemical reactions during cycling, cyclic voltammetry (CV) measurements were performed on the SnO_2 nanowires and nanotubes, and the results are presented in Figure 5.6. The CV profiles for the nanowires show two apparent reduction peaks around 0.95 V and 1.20 V, which can be derived from Li_2O formation and electrolyte decomposition when the SnO_2 nanowires react with Li^+, as described in Equation 5.1. These peaks are leaving a large initial irreversible capacity in the first cycle of SnO_2 nanowire electrodes. The other pairs of reduction and oxidation peaks at 0.25 V and 0.60 V during discharging and at 0.50 V and 0.70 V during charging are related to the formation of Li_xSn, as described in Equation 5.2. Even though there is peak broadening in the CV of the nanowires, we found the same peaks in the CV profiles for the SnO_2 nanotubes over the same potential range. Thus, it was confirmed that the morphological modification of materials does not have an effect on the kind of redox reactions.

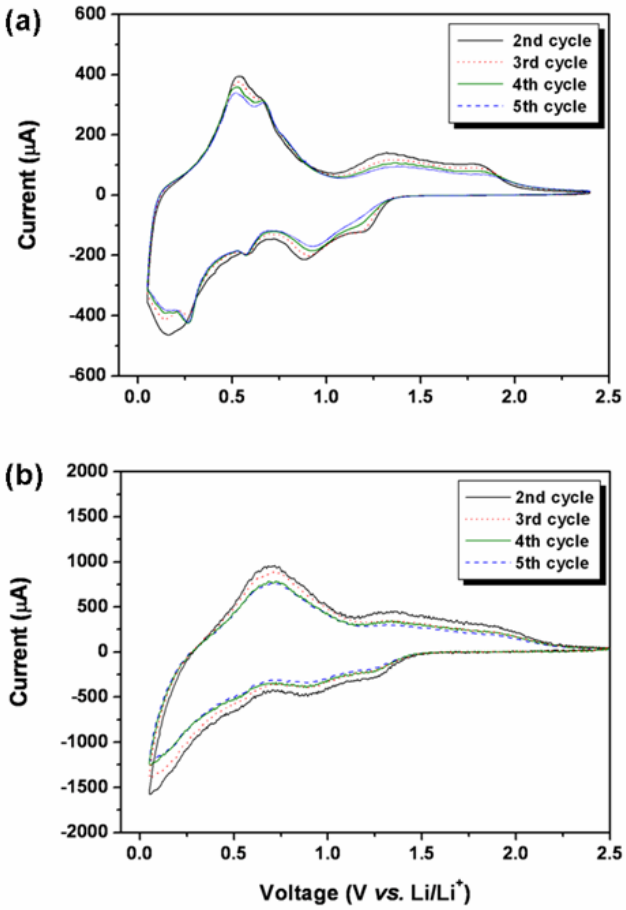

Figure 5.6: *Cyclic voltammetry (CV) profiles of SnO_2 nanostructured materials: a) CV curves of SnO_2 nanotubes and b) CV curves of SnO_2 nanowires from the second cycle to the fifth cycle.*

Electrochemical impedance spectroscopy (EIS) was conducted to determine the Li^+ transfer behavior in SnO_2 nanotubes and nanowires. It is well known that the high frequency semicircle can be attributed to the contact resistance occurring because of the solid-electrolyte-interphase (SEI) film, the medium-frequency semicircle is related to the charge-transfer resistance at the interface between the electrolyte and the electrode material, and the inclined lines correspond to the Li^+ diffusion process inside the electrode material.[228]

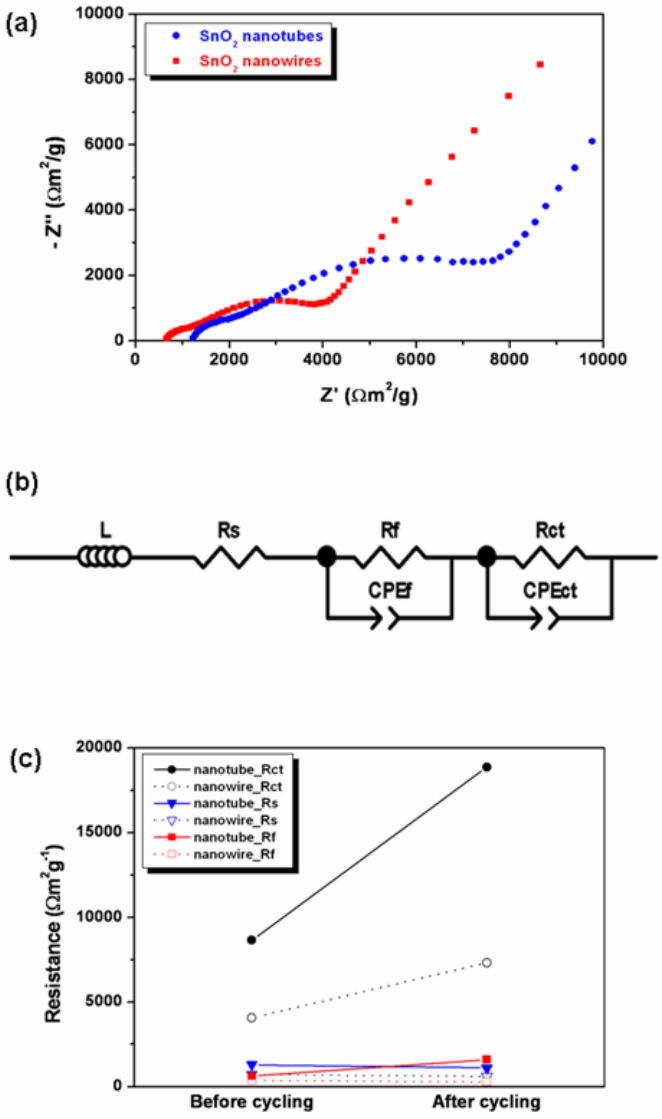

Figure 5.7: *Impedance spectra of SnO_2 nanotubes and SnO_2 nanowires measured at the open circuit potential of 2.0 V: a) Nyquist plots with normalized impedance before cycling, b) the equivalent circuit that was used to fit the impedance data, c) the variation of intrinsic resistances (R_s, R_f, R_{ct}).*

From a purely electrical point of view, the experimental data could be satisfactorily fitted using an equivalent circuit, with only slight differences in the goodness of the fit. As observed in carbonaceous material, Li^+ insertion tends to diminish the impedance. Because the alloying between Li^+ and Sn involves the augmentation of surface area, which is in inverse proportion to the impedance, Li^+ insertion into SnO_2 could make the reduction in impedance more prominent.[216,229-230] Figure 5.7(c) shows the variation of the intrinsic resistances (R_s, R_f, and R_{ct}). From Figure 5.7(a), it can be observed that the nanotubes have a larger contact resistance (R_f) in the high-frequency region, while the charge-transfer resistance (R_{ct}) in the medium-frequency range is also larger for nanotubes than for nanowires. This may be related to the disparity between the nanotubes and nanowires in their surface area and electronic conductivity. Considering that the faradaic reaction is determined by ion transfer and electron conduction, the better electronic conductivity of the nanowires may play the crucial role in the reduction of the resistance. After cycling (5 cycles), the nanowire electrode still shows a smaller resistance compared to the nanotube electrode, as indicated in Figure 5.7(c). Therefore, it should be noted that charge transfer is highly dependent on the morphological features of the electrode material.

5.4. Summary

The experiments described here clearly demonstrate that the electrochemical performance of SnO_2 nanostructured materials is likely to be related to their morphological features. The specific surface areas are mainly attributable to Li^+ storage, and single-crystalline structures are better for maintaining electronic conductivity and allowing enhancement of Li^+ diffusion into the SnO_2 structure. Despite the fact that porous structures are generally more suitable for accommodating volume variations of the Sn phase during cycling, they may also trap more Li^+

during electrochemical cycling, resulting in large irreversible capacities. The use of SnO_2 nanostructured materials gives an important indication of the direction to take for the further improvement of the electrochemical properties of SnO_2 systems.

6. Effects of Low-Temperature Carbon Encapsulation on the Electrochemical Performance of SnO_2 Nanopowders

6.1. Introduction

Intensive research on practical alternatives to commercial graphite anode in lithium-ion batteries is currently proceeding to overcome the capacity limitation of graphite (372 $mAh \cdot g^{-1}$). The search for new anode materials with high capacity and stable cyclic performance has been considered as the priority in the development of high energy density batteries.[8-9,49] In terms of Li^+ storage capacity, SnO_2 has been suggested as one of the most promising anode materials, because it can store more than twice as much Li^+ as graphite.[32,70,101] However, a large initial irreversible capacity caused by Li_2O formation and poor capacity retention due to volume variations of Sn (~200%) during electrochemical reactions with Li^+ have been the main barriers to limit the practical utilization of SnO_2, as described in Equations 6.1 and 6.2.[213] The critical issues for SnO_2 based materials are how to reduce Li_2O formation and accommodate volume expansion of Sn during cycling.

$$SnO_2 + 4Li^+ + 4e^- \rightarrow Sn + 2Li_2O \quad (6.1)$$

$$Sn + xLi^+ + xe^- \rightarrow Li_xSn \quad (0 \leq x \leq 4.4) \quad (6.2)$$

Much attention has been paid to morphological and structural modification of SnO_2 in order to

alleviate its electrochemical disadvantages. In the previous chapter, various type of SnO_2 nanostructured materials, such as nanowires, nanotubes, and nanopowders, have been proposed with several structural advantages.[186,216,222] They provide more reaction sites with Li^+ due to their high surface area, as well as better charge transfer properties induced by their short Li^+ diffusion length. Even though SnO_2 based anode materials show considerable kinetic advantages in the nanoscale form, they still exhibit poor initial coulombic efficiency and capacity retention caused by the electrical disconnection between active materials due to the non-conductive Li_2O phases which are unavoidably formed. On the other hand, it is well documented that conductive additives such as carbon, carbon nanotubes, and transition metal elements can help to enhance the electronic conduction between active materials during electrochemical reactions.[96,231-232] An apparent improvement in electrochemical properties has been reported in C nanocomposite anode materials prepared by mechanical milling, thermal vapor deposition, and spray pyrolysis.[233-235] However, the enlargement of electrical pathways in state-of-the-art methods has been limited by the inhomogeneous distribution or agglomeration of C phases, and the low production efficiency and high-temperature processing required by the existing methods have still remained another open problem from an economic point of view.

Herein, we employed a solution-based C-encapsulation technique using carbohydrates as C sources to form homogeneous amorphous C layers on SnO_2 nanonanocomposites. Considering the low melting point (132 °C) and solubility in an organic solvent, malic acid ($C_4H_6O_5$) was selected as a suitable C source for our synthesis strategy. The microstructure and electrochemical properties of C-encapsulated SnO_2 nanopowders prepared by simple evaporation and decomposition at low temperature are discussed in order to yield a new general route for preparing nanocomposites with C.

6.2. Experimental

6.2.1. Preparation of C-encapsulated SnO_2 Nanonanocomposite

Nanocrystalline SnO_2 nanopowder was synthesized by a conventional sol–gel method. 3 M of Sn^{II} solution was prepared by dissolving 0.338 g of $SnCl_2 \bullet 2H_2O$ in a mixture of ethanol (0.47 ml) and 36% HCl (0.03 ml). The solution was aged for 24 hours, and then water (0.03 ml) was added under continuous stirring, which was continued for 12 hours. After the formation of the gel, it was dried at 120 °C for 2 hours and sintered at 600 °C for 3 hours in a vacuum furnace under an Ar (95%) and O_2 (5%) atmosphere. To remove Cl^-, the final product was washed with distilled water via a centrifugal process and dried at 120 °C for 2 hours in a vacuum oven. On the other hand, the C sources were prepared by dissolving malic acid ($C_4H_6O_5$, 99%) with the same amount of SnO_2 nanopowder by weight in toluene (C_7H_8, 99.5%). The solutions were mixed with SnO_2 nanopowders while stirring at room temperature for 2 hours. These slurries were dried at 180 °C for 6 hours in a vacuum (10^{-3} Torr) oven.

6.2.2. Structure Characterization

The morphology and microstructure of C-encapsulated SnO_2 nanocomposite were characterized by X-ray diffraction (XRD, Philips 1730), field emission scanning electron microscopy (FESEM, JEOL JEM-3000), transmission electron microscopy (TEM, JEOL 2011), and X-ray photoelectron spectroscopy (XPS, Axis Nova).

6.2.3. Electrochemical Experiments

The C-encapsulated SnO_2 nanocomposites were mixed with acetylene black (AB) and a binder (poly(vinylidene fluoride); PVdF) at a weight ratio of 85:8:7, respectively, in a solvent (N-methyl-2-pyrrolidone). The slurry was uniformly pasted onto Cu foil. Such prepared electrode sheets were dried at 120 °C in a vacuum oven and pressed under a pressure of approximately 200 $kg \cdot cm^{-2}$. CR2032-type coin cells were assembled for electrochemical characterization. The electrolyte was 1M $LiPF_6$ in a 1:1 mixture of ethylene carbonate (EC) and dimethyl carbonate (DMC). Li metal foil was used as the counter and reference electrode. The cells were galvanostatically charged and discharged at a current density of 100 $mA \cdot g^{-1}$ over a range of 0.05–1.50 V.

6.3. Results and Discussion

6.3.1 Structural and Morphological Characterization

Figure 6.1 shows the X-ray diffraction (XRD) patterns of SnO_2 nanopowder and C-encapsulated SnO_2 nanocomposite. It can be clearly seen that all reflections for both samples are in excellent accordance with the tetragonal rutile structure (JCPDS 41-1445), which belongs to the space group $P4_2/mnm$ (136). There was no peak shifting or significant intensity change before or after the decomposition of $C_4H_6O_5$. After the decomposition, only a broad diffraction peak was additionally observed at low angles, indicating the signature of a nanosized or amorphous C phase. This is expected to be the amorphous C phase on the surface of the SnO_2 nanoparticles. For further analysis, we calculated the lattice parameters of the *a*-axis and *c*-axis using Rietveld refinement. According to the literature, the reference SnO_2 nanopowder has lattice parameters of

$a = b = 4.7386$ Å and $c = 3.1872$ Å. Within the accuracy of errors, a-axis lattice parameters for SnO_2 nanopowder and C-encapsulated SnO_2 nanocomposite were estimated to be 4.7372(5) Å and 4.7362(5) Å, respectively, corresponding to 3.1864(2) Å and 3.1847(8) Å for the c-axis parameter. It should be noted that there was no significant lattice parameter difference due to interstitial C or C substitution into the lattice of SnO_2, or O release from the SnO_2 structure during the decomposition process. These observations can be further supported by lattice strain calculation and X-ray photoelectron spectroscopy (XPS) analysis, as discussed below. So far as strain is concerned, the lattice strain is directly caused by the d-spacing changes due to the defects and the substitutional or interstitiallocation of impurities inside grains or crystal structures. In our samples, the lattice strain values were estimated to be 0.113% and 0.114% before and after the decomposition, respectively. These results reveal that C-encapsulation at low temperature did not affect the structure and stoichiometry of the SnO_2 nanopowder, when compared with the pure SnO_2 nanopowder without any C interstitials or substitution, or any O loss.

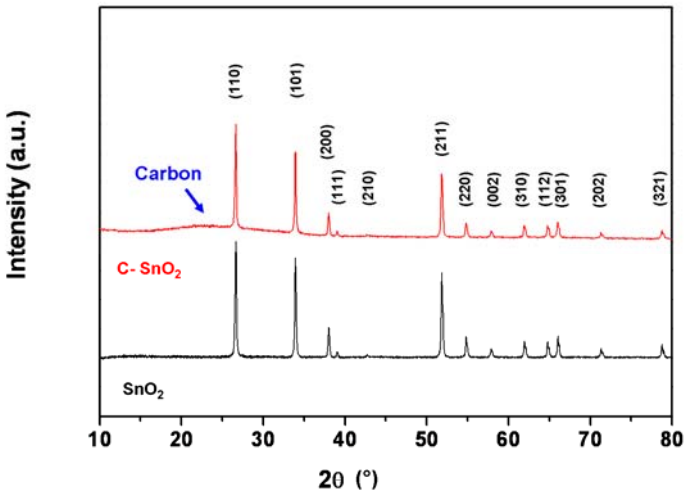

Figure 6.1: *X-ray diffraction pattern of C-encapsulated SnO_2 nanocomposite compared to SnO_2 nanopowders.*

Field emission scanning electron microscopy (FESEM) images of SnO_2 nanopowder and C-encapsulated SnO_2 nanocomposite at different magnifications are displayed in Figure 6.2. The nanopowders have a relatively homogeneous crystalline size of less than 100 nm on average and a clean surface without obvious irregular ravines (Figure 6.2(c)). In contrast, crystal enlargement appears in the local area after the decomposition, with the new microstructure consisting of crystallites from several tens of nanometers in size to 300 nm, as shown in Figure 6.2(d).

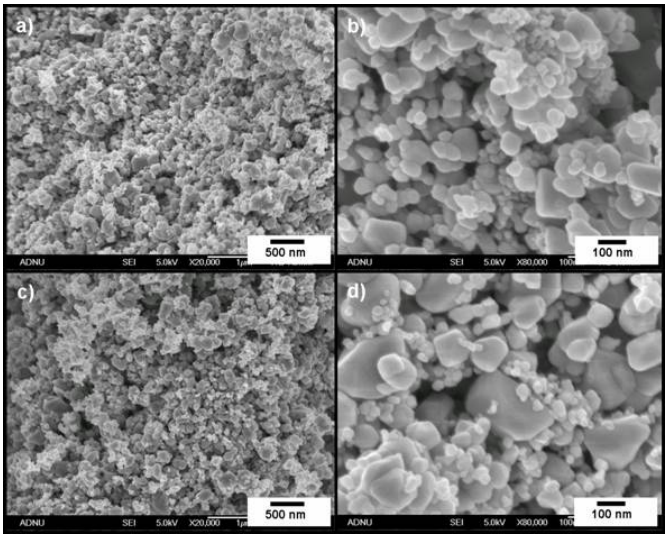

Figure 6.2: *The microstructure of SnO_2 nanopowders and C-encapsulated SnO_2 nanocomposites at different magnifications: (a, b) FESEM images of SnO_2 nanopowders prepared by the sol–gel method; (c, d) FESEM images of C-encapsulated SnO_2 nanocomposites after simple decomposition of malic acid ($C_4H_6O_5$).*

The inhomogeneous crystal enlargement can be attributed to the additional amorphous C phase formed by the decomposition of $C_4H_6O_5$. In order to confirm the crystal size effect, the surface areas and full width at half maximum (FWHM) values of both samples were also estimated by the Brunauer–Emmett–Teller (BET) method and Rietveld refinement, respectively. The surface

areas decreased from 97.32 $m^2 \cdot g^{-1}$ to 82.66 $m^2 \cdot g^{-1}$, and the FWHM values for all reflections were also reduced after the decomposition. The reduction in the surface area and FWHM values are consistent with the irregular enlargement of the crystalline particles in the FESEM images.

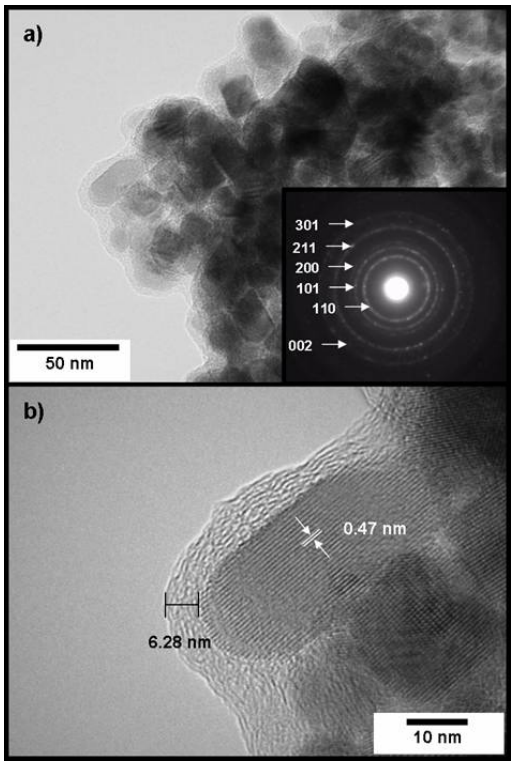

Figure 6.3: *(a) TEM image and selected area electron diffraction (SAED) pattern (inset) of C-encapsulated SnO_2 nanocomposites and (b) HRTEM image of amorphous carbon layers on the surface of SnO_2 nanoparticles.*

Transmission electron microscopy (TEM) observations clarified the existence and thickness of the amorphous C layer on the surface of the SnO_2 nanopowder particles. In Figure 6.3(a), the SnO_2 nanopowders are uniformly encapsulated by amorphous C layers. The indexed ring patterns are consistent with the XRD diffraction patterns, and the blurred ring patterns could be derived from the amorphous C phase. Specifically, the thickness of the carbon layer on the surface of SnO_2 nanopowder is about 6.28 nm, and the d-spacing was estimated to be 0.47 nm,

as shown in Figure 6.3(b). We found that the amorphous C phase was formed without any crumbling of the SnO_2 nanopowder. What is interesting is that the inhomogeneous crystal size distribution in C-encapsulated SnO_2 nanocomposite might be caused by the agglomeration of nanoparticles due to the van der Waals force during the decomposition process. Thus, these agglomerated powders seemed to be subject to crystal enlargement after the decomposition process.

The bonding between the C layers and the SnO_2 was characterized by X-ray photoelectron spectroscopy (XPS). Figure 6.4(a) shows C 1s spectra for SnO_2 nanopowders and C-encapsulated SnO_2 nanocomposites. The C 1s narrow scan spectra of the nanopowders were categorized into two regions of binding energy. The main peak located at about 285.0 eV corresponds to C–C or C–H bonding, whereas the minor peak at 289.3 eV indicates the existence of double bonds between C and O, such as C=O. In the nanocomposites, the relative intensity of C=O bonding was augmented, and the peak located at lower binding energy was significantly broadened. The peak de-convolution considering the single bond between C and O clearly showed that this peak broadening is caused by the emergence of C–O bonding (286.3 eV), as well as the waning of C–C bonding. The abrupt augmentation of single or double bonding between C and O was also observed in the O 1s narrow scan spectra. In Figure 6.4(b), the O 1s binding energy of SnO_2 was 530.5 eV, which corresponds to the typical binding energy of Sn–O bonding. On the other hand, the O 1s spectrum of the nanocomposite was convoluted from not only Sn–O bonding, but also a positively-shifted bonding, aliphatic C–O bonding. The nature of the bonding between C and SnO_2 was finally demonstrated by the bonding states of Sn atoms as determined from the Sn $3d_{5/2}$ spectrum. As shown in Figure 6.4(c), the Sn $3d_{5/2}$ spectrum of SnO_2 is composed of single peak related to Sn–O bonding (486.4 eV). However,

two peaks were evolved at the binding energy of Sn–Sn (485.1 eV) and a positively-shifted binding energy after the decomposition. It could be surmised that the positively shifted binding energy is attributable to a highly oxidized state of Sn–O bonding, because the Sn $3d_{5/2}$ binding energy for Sn–C bonding has been reported to be about 486.3 eV.

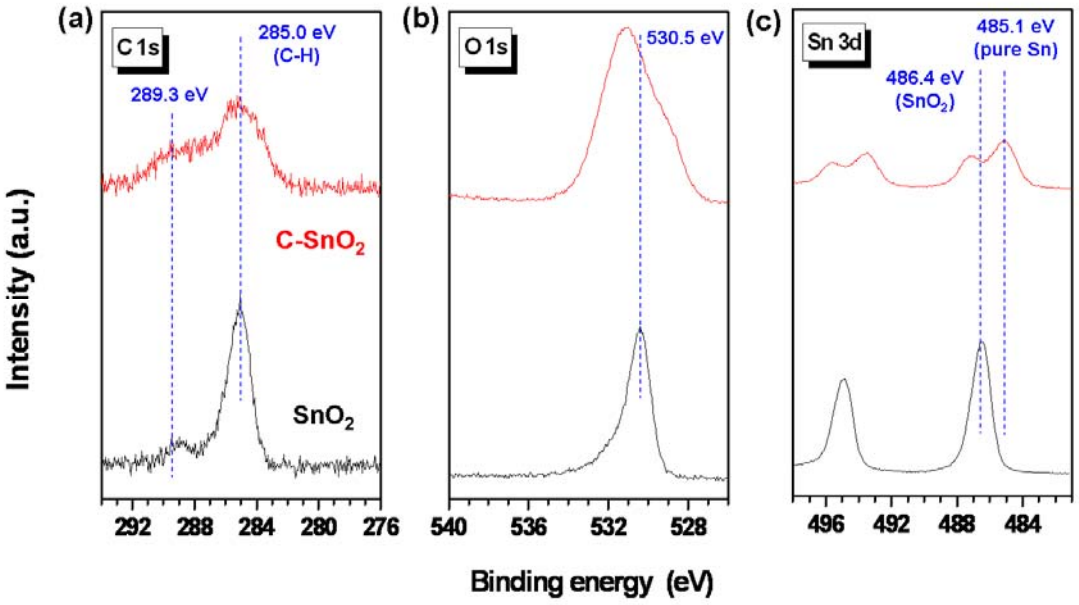

Figure 6.4: *(a) XPS C 1s narrow scan spectra for SnO_2 and C-encapsulated SnO_2 nanocomposites: (b) for comparative purposes, the XPS O 1s spectra are displayed; and (c) XPS Sn 3d narrow scan spectra for SnO_2 and C-encapsulated SnO_2 nanocomposite.*

More importantly, we suggest that there was no O loss from the SnO_2 nanopowder during the decomposition process. Even though C and H could be acting as O getters during the process, most C and H in $C_4H_6O_5$ reacted only with the O coming from $C_4H_6O_5$ rather than from the SnO_2 host structure at the decomposition temperature of 180 °C. The advantages of the low-temperature processing used in this experiment can be demonstrated by a thermodynamic argument. Supposing that reduction of the SnO_2 occurred with a chemical reducing agent such

as C, it is possible to consider the reaction (Equation 6.3) as described below:

$$SnO_2 + 2C \rightarrow Sn + 2CO \quad (6.3)$$

This reaction is composed of the reduction of SnO_2 and the oxidation of C. The formation Gibbs free energy ΔG_f, could be easily calculated from a well-established thermodynamic database. When our experimental conditions (180 °C, 10^{-3} Torr) were considered, ΔG_f of this reaction was 155.384 kJ·mol^{-1}, i.e., the reaction is not spontaneous. In accordance with our previous discussion, SnO_2 phase is favorable under our experimental conditions, which means that the surface of the SnO_2 definitely has a complete structure without non-bonding terminations of Sn atoms or O atoms. According to Bergenmayer et al.[236], the reaction equilibrium temperature (T_s) between oxidation and reduction of SnO_2 significantly depends on the partial pressure and its surface orientation. The lowest critical temperature for the reduction of SnO_2 should be over 447 °C, when the partial pressure is maintained at around 10^{-3} Torr. By correlating our thermodynamic calculation with this description, we could confirm that the O released from the SnO_2 in our experiment is thermodynamically limited during the decomposition process. Therefore, the evolution of nonbonding terminations could be excluded, because of the preferential formation of C–O or C=O bonding between C and O. Considering that non-bonding terminations on the surface of materials result in the irreversible reaction of Li^+, we may suggest that the exclusion of non-bonding terminations is the most important advantage of C-encapsulation from the decomposition of $C_4H_6O_5$ at low temperature.

6.3.2. Electrochemical Properties

The anodic performance of C-encapsulated SnO_2 nanocomposite was tested in the potential range from 0.05 to 1.50 V (vs. Li/Li^+). There is a strong enhancement in the electrochemical behavior associated with the amorphous C layers on the surface of the encapsulated SnO_2 nanopowder. First of all, the initial irreversible capacity of the nanocomposite (732 $mAh \cdot g^{-1}$) is much smaller than that of the nanopowder (1277 $mAh \cdot g^{-1}$), as shown in Figure 6.5(a). It should be noted that the nanocomposite shows an initial coulombic efficiency of approximately 44.87%, which is notably higher than that of the nanopowder, 31.01%. The improvement of the initial coulombic efficiency after C-encapsulation should be attributed to fewer non-bonding terminations of Sn atoms or O atoms on the surface of the SnO_2 nanopowder in the nanocomposite, as well as to the enhancement of the charge transport induced by the C-encapsulation. The amorphous C layer could not only improve electronic conduction, but also increase Li^+ transport between the active phases. Indeed, amorphous C can also reduce electronic disconnection by the formation of Li_2O phase, which would increase the reversible capacity during the first Li^+ insertion and extraction. In order to identify all of the electrochemical reactions, the differential charge–discharge capacity vs. voltage profiles of C-encapsulated SnO_2 nanocomposite are presented in Figure 6.5(b). The first differential discharge profile shows a major reduction peak at around 0.90 V derived from Li_2O formation when SnO_2 reacts with Li^+, while the small reduction peaks around 0.85 V and 1.20 V correspond to solid electrolyte interphase (SEI) film formation and electrolyte decomposition.[180] These peaks disappeared, leaving a large initial irreversible capacity of 732 $mAh \cdot g^{-1}$ at the first cycle, which is relevant to the galvanostatic voltage profile presented in Figure 6.5(a). With regards to the various reduction and oxidation peaks below 0.25 V, they

seem to be attributable to the electrochemical reactions between amorphous C and Li^+ in the nanocomposite.

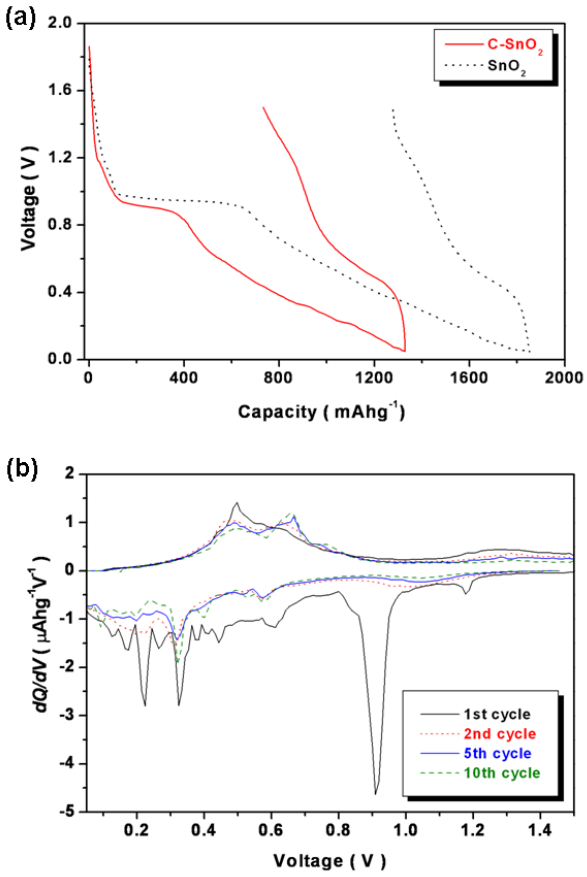

Figure 6.5: *The anodic performance of the C-encapsulated SnO_2 nanocomposite: (a) galvanostatic voltage profiles between 0.05 V and 1.50 V; and (b) differential charge–discharge versus potential plots at the first, second, fifth, and tenth cycles between 0.05 V and 1.50 V for the C-encapsulated SnO_2 nanocomposite.*

We suggest that the amorphous C phase on the surface of SnO_2 might lead to the improvement of reversible Li^+ storage and initial coulombic efficiency in the nanocomposite.[235] The other pairs of reduction peaks between 0.25 V and 0.70 V during discharging and oxidation peaks

between 0.40 V and 0.80 V during charging are related to the formation and decomposition of various Li_xSn alloys.[186] This result reveals that it is mainly SnO_2 phase that reacts with the Li^+ in the nanocomposite, while amorphous C phase also contributes to the reversible capacity of Li^+.

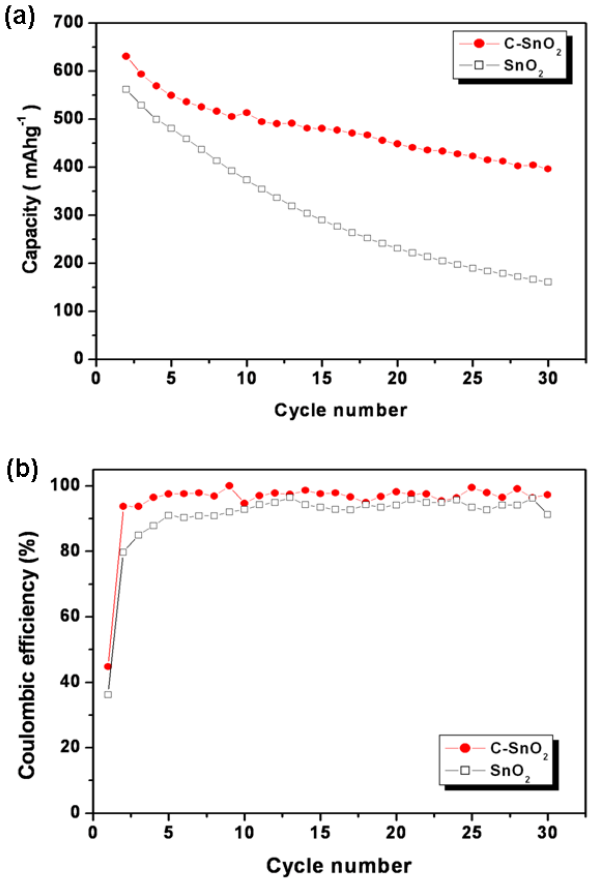

Figure 6.6: *The anodic performance of the C-encapsulated SnO_2 nanocomposite: (a) the cyclic performance of C-encapsulated SnO_2 nanocomposite and SnO_2 nanopowders up to the 50th cycle at the same current density, 100 $mA{\cdot}g^{-1}$, and (b) the coulombic efficiency of C-encapsulated SnO_2 nanocomposite and SnO_2 nanopowder electrodes up to the 50th cycle.*

The C-encapsulated SnO_2 nanocomposite electrode shows a higher reversible specific charge of over 400 $mAh{\cdot}g^{-1}$ up to the 30th cycle with relatively stable cyclic performance (Figure 6.6(a)).

Moreover, the nanocomposite shows a small capacity fading of 1.28% per cycle after the second cycle, which is much smaller than that of SnO_2 nanopowders, 2.46%. It is likely that the amorphous C layer would act as a mechanical buffer and effectively prevent the electrical disconnection between active materials that is induced by the volume expansion of Sn. As a result, the reversible capacity loss could be effectively reduced in the C-encapsulated SnO_2 nanocomposite. On the other hand, there is other evidence to show that amorphous C phase can more effectively prevent the electrical disconnection of nanosized SnO_2 particles and thus help to maintain the enhanced electrical properties in nanocomposite form (Figure 6.6(b)). Based on these results and discussion, it is believed that the reversible capacity loss or electrical disconnection induced by the volume variation of nanosized SnO_2 could be effectively reduced by amorphous C phase in this nanocomposite prepared by a simple decomposition of $C_4H_6O_5$.

6.4. Summary

In summary, we have synthesized C-encapsulated SnO_2 nanocomposite by means of thermal evaporation and decomposition of malic acid ($C_4H_6O_5$) at low temperature. The desirable crystalline structure and stoichiometry of SnO_2 were maintained, and the amorphous C layer functions as a sort of framework to maintain the electronic conduction around the active materials. As a result, the large initial irreversible capacity due to non-bonding terminations could be diminished effectively. The nanocomposite shows an enhanced reversible capacity of over 400 $mAh \cdot g^{-1}$ and stable cyclic retention. If careful attention is paid to the design and fabrication of C-encapsulation, the full potential of electrode materials will be exploited in commercial lithium-ion batteries.

7. Reduction-Free Synthesis of Carbon Encapsulated SnO_2 Nanowires and Their Superiority in Electrochemical Performance

7.1. Introduction

Various metal oxides have received considerable attention as promising candidates to substitute for the graphite that is extensively used as the main commercial anode material for lithium-ion batteries.[32,96,237-238] Even though the metal oxides show much higher capacity than graphite (theoretical gravimetric capacity of 372 $mAh \cdot g^{-1}$), their practical energy storage capability in the bulk form is highly limited, due to a myriad of charge transport and electronic conduction issues. The loss of electronic conduction due to the strain induced by volume variation in the metal phase and the poor diffusivity of Li^+ caused by complex diffusion mechanisms between the domains of the active materials during the redox process have turned out to be major disincentives to practical use.[70,239-240]

Recently, it has been generally accepted that nanostructured materials have enough potential to enhance kinetic properties thanks to their large surface area and short Li^+ diffusion length from a structural point of view.[180,222,241] In practice, SnO_2, which is one of the most promising metal oxides alloying/de-alloying with Li^+, has shown some notable electrochemical improvements in its nanowire form.[180] Despite the significant improvement in the kinetics, however, the poor electronic conduction between the active materials, delayed electron tunneling through solid-electrolyte-interphase (SEI) films, and the limited percolation of electrons to the current

collector still remain a critical drawback that has to be further investigated. These unsatisfactory findings persuaded us to pay attention to C-encapsulation on SnO_2 nanowires, on the hypothesis that ductile amorphous C phase with high conductivity could not only maintain good electronic pathways between active materials but also accommodate volume expansion of Sn phase during electrochemical reactions, resulting in stable cyclic retention and reduction of undesirable capacity loss induced by Li_2O formation.[182,242-244]

Herein, we show the effects of C-encapsulation on the electrochemical performance of SnO_2 nanowires and introduce a simple C encapsulation process based on a chemical solution route using decomposition of malic acid ($C_4H_6O_5$). The resulting C-encapsulated SnO_2 nanowires have a higher reversible capacity, in which there is no capacity contribution of the amorphous C phase. It may even be considered that the newly achieved cyclic stability and reversible capacity nearly approach the standard required for the commercial use.

7.2. Experimental

7.2.1. Preparation of C-encapsulated SnO_2 Nanowires

Abundant SnO_2 nanowires were synthesized by the thermal vapour deposition method through the evaporation of high purity SnO (99.9%, Aldrich) and Sn (99.9%, Aldrich) powders at 900 ˚C under optimized conditions, as reported in our previous work.[180] For the C encapsulation process, malic acid ($C_4H_6O_5$, 99.0%) at 50 wt% of total SnO_2 nanowires was dissolved in 100 ml of toluene (C_7H_8, 99.5%) as the C source. The solution was mixed with SnO_2 nanowires on their substrates under stirring at room temperature for 2 hours. These slurries were carefully dried at 180 ˚C for 6 hours in a vacuum oven (10^{-3} Torr) in order to prevent the formation of

undesirable impurities, as illustrated in Figure 7.1. Amongst the various carbohydrates, we selected malic acid ($C_4H_6O_5$) as a promising C source, based on our experimental strategy, because it has a low melting point at 132˚C and can be completely dissolved in toluene (C_7H_8) solvent at room temperature.

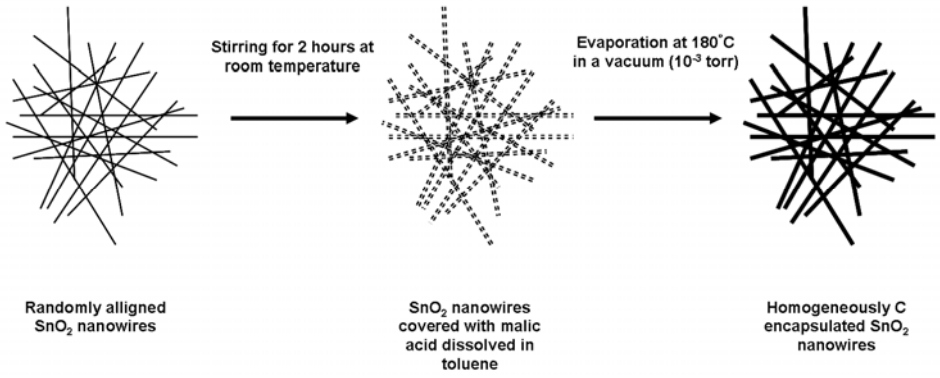

Figure 7.1: *Schematic diagram of the C-encapsulation process via a chemical solution route using malic acid ($C_4H_6O_5$) as the C source.*

7.2.2. Structural and Electrochemical Characterization

Following the procedure, the final products, the C-encapsulated SnO_2 nanowires, were peeled off from the substrates for physical and electrochemical characterisations. The morphology and microstructure of C-encapsulated SnO_2 nanowires were characterised by X-ray diffraction (XRD, Philips 1730), field emission scanning electron microscopy (FESEM, JEOL JEM-3000), and transmission electron microscopy (TEM, JEOL 2011). CR2032 coin type cells were assembled for electrochemical characterisations. The electrolyte was 1M $LiPF_6$ in a 1:1 mixture of ethylene carbonate (EC) and dimethyl carbonate (DMC). Li metal foil was used as the counter and reference electrode. The cells were galvanostatically charged and discharged at a current of 100 $mA \cdot g^{-1}$ over a voltage range of 0.05 V to 1.50 V.

7.3. Results and Discussion

7.3.1. Structural and Morphological Characterization

To address the primary challenge to the commercial use of metal oxides, the addition of C has been suggested to enhance the electronic conductivity of metal oxides and accommodate its volume expansion.[182,242-243] The previous impressive enhancements inspired us to design C-encapsulated SnO_2 nanowires in order to overcome the fundamental drawbacks of SnO_2 that exist even in its nanoscale form: (1) large initial irreversible capacity and (2) poor cyclic retention, mainly caused by poor electronic conduction.[222,241] Considering the structural perspective on SnO_2 nanowires, C-encapsulation via chemical decomposition was chosen to combine the benefits of nanostructured materials and C addition. A simple evaporation of malic acid ($C_4H_6O_5$) was sufficient to obtain a pure amorphous C layer on the SnO_2 nanowires at the low temperature of 180 °C, without any structural failure of the SnO_2 nanowires, as illustrated in Figure 7.1.

First, the formation of the amorphous C layer and other morphological changes in the SnO_2 nanowires after the decomposition of malic acid ($C_4H_6O_5$) were confirmed by XRD analysis, as shown in Figure 7.2. From the diffraction patterns, it should be noted that there is no detectable impurity phase and that only a small broad peak is observed at a low angle in the pattern for C-encapsulated SnO_2 nanowires, which is attributed to amorphous C phase. According to the Rietveld refinement, all reflections of the C-encapsulated SnO_2 nanowires are also in excellent accordance with the tetragonal rutile structure (JCPDS 41-1445), which belongs to the space group $P4_2/mnm$ (136), and its lattice parameters were calculated as $a = b = 4.736(4)$ Å and $c = 3.187(6)$ Å. Discrepancies in the lattice parameters and fundamental Raman scattering peaks of

the SnO_2 nanowires are surprisingly negligible before and after the C-encapsulation process [180], which means that the tetragonal structure of the SnO_2 nanowires was well maintained under our C-encapsulation experimental conditions. These findings are important, because they allow us to isolate the effects of C-encapsulation on the electrochemical performance of SnO_2 nanowires in this study. As confirmed by the structural analyses such as XRD and Raman spectroscopy, there was little change in the lattice parameters between SnO_2 and C-encapsulated SnO_2 nanowire due to the advantages of the low-temperature decomposition process used in this experiment.

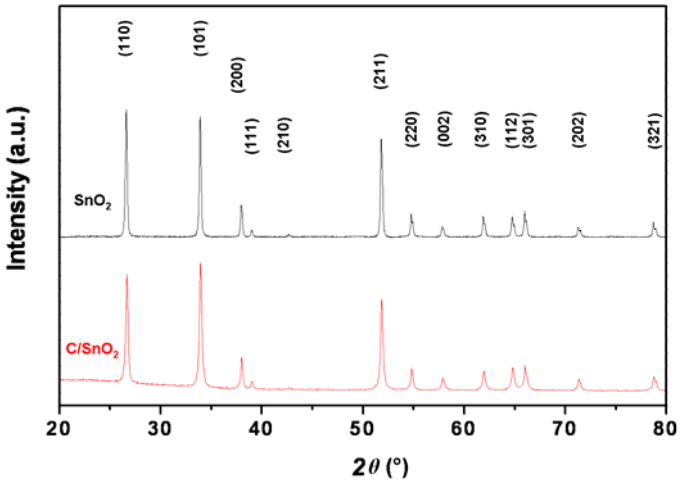

Figure 7.2: *X-ray diffraction (XRD) patterns of SnO_2 nanowires and C-encapsulated SnO_2 nanowires.*

It is well known that SnO_2 is very sensitive to reduction. Because of this attribute, SnO_2 has been utilized as a representative oxidizing catalyst or gas sensor. Supposing that the reduction of SnO_2 is chemically evolved by C, it is possible to consider it as described below:

$$SnO_2 + 2C \rightarrow Sn + 2CO \qquad (7.1)$$

Here, the formation Gibbs free energy, ΔG_f, could be easily calculated from a well-established thermodynamic database. When our experimental conditions (180 ˚C, 10^{-3} Torr) were considered, ΔG_f of this reaction was 155.384 kJ·mol^{-1}, i.e., the reaction is not spontaneous. In accordance with our previous discussion, SnO_2 does not undergo any structural change under our experimental conditions, which means that the surface of the SnO_2 definitely has a complete structure, without any dangling bonds of Sn atoms or O atoms. According to Bergenmayer et al.[236], the reaction equilibrium temperature (T_s) between oxidation and reduction of SnO_2 significantly depends on the partial pressure and its surface orientation. The lowest critical temperature for the reduction of SnO_2 should be above 447 ^{o}C, when the partial pressure is maintained at about 10^{-3} Torr. By correlating our thermodynamic calculation with this description, it could be confirmed that the structural change of SnO_2 in our experiment is thermodynamically prevented during the decomposition of malic acid.

For further inspection, field emission scanning electronic microscopy (FESEM) and transmission electron microscopy (TEM) analyses were employed to characterize the morphology and microstructure of the C-encapsulated SnO_2 nanowires. FESEM images of randomly aligned C-encapsulated SnO_2 nanowires (inset) and a close view of an individual nanowire are displayed in Figure 7.3. The typical dimensions are 200 nm for the diameter and a few microns for the length, which appears to be uniform. The diameter is also constant throughout the wire, except for a short thickening at the tip. In contrast to the reference SnO_2 nanowires[180], the C-encapsulated SnO_2 nanowires have relatively rough surface morphologies, which indicates that the nanowires are homogeneously covered with fine particulates, which are clearly visible on the surface in the FESEM image and were identified as C phase by energy dispersive X-ray spectroscopy (EDX).

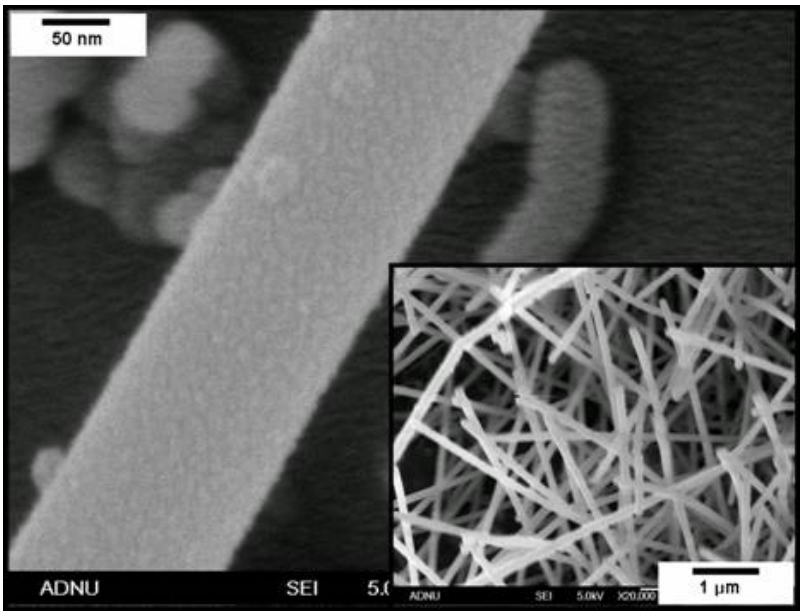

Figure 7.3: *FESEM image of C-encapsulated SnO_2 nanowires: SEM image of an individual nanowire and randomly aligned nanowires (inset).*

The fine single crystal microstructure of a C-encapsulated SnO_2 nanowire and the corresponding selected area electron diffraction pattern (SAED) characterize the crystallographic nature of the C-encapsulated SnO_2 nanowire as a rutile structure, as shown in Figure 7.4(a). The growth direction of the SnO_2 nanowire is geometrically parallel to the [101] direction. A high-resolution TEM (HRTEM) image clearly shows an amorphous C layer on the crystal lattice of the SnO_2 nanowire in Figure 7.4(b). The thickness of the C layer is approximately 7.2 nm. It can be clearly seen that the nanowire has been uniformly encapsulated by amorphous C phase to a uniform thickness.

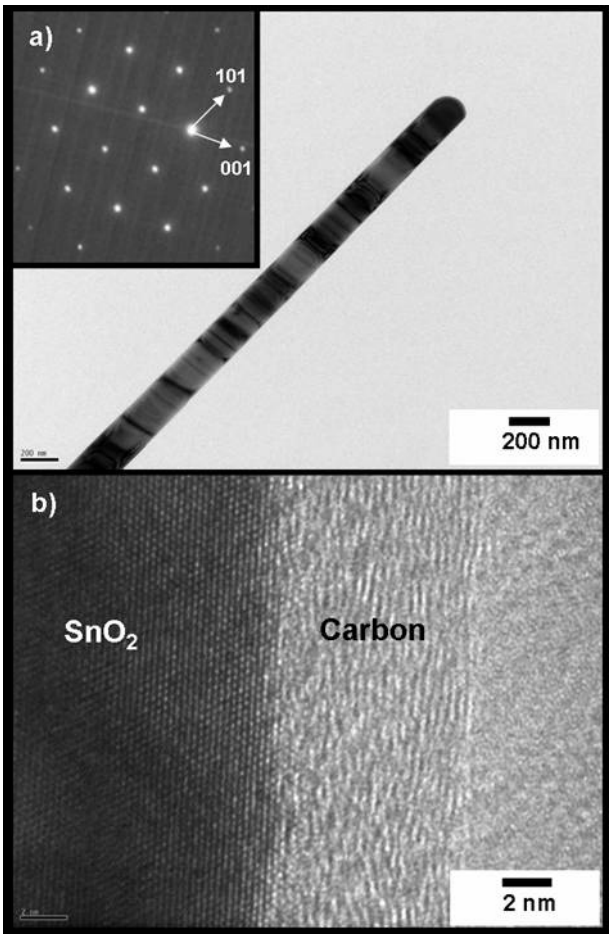

Figure 7.4: *(a) TEM image and selected area electron diffraction (SAED) pattern (inset) of a C-encapsulated SnO_2 nanowire, and (b) HRTEM image of a section of a C-encapsulated SnO_2 nanowire.*

In order to further investigate the effect of C-encapsulation on the orientation and texture of SnO_2 nanowires, X-ray texture analysis was conducted by collecting four incomplete (110), (101), (200), and (211) pole figures with an X-ray goniometer (BRUKER-AXS, D8 Discover) before and after C encapsulation. Cu-k_α radiation (wavelength of 1.5406 Å) was used for an area of 5 × 10 mm^2. We observed ω angles in the range of 0° to 60° and ϕ angles in the range of 0° to 355°, with an interval of 5° and dwell time of 1 sec. From the comparison, it is believed that both nanowires have randomly oriented fiber structures, without any notable differences in the

orientation and degree of texture, implying that there is no significant change in the SnO_2 nanowires during the C-encapsulation process. In addition, the results from the pole figures are consistent with the SEM observations displayed in Figure 7.2.

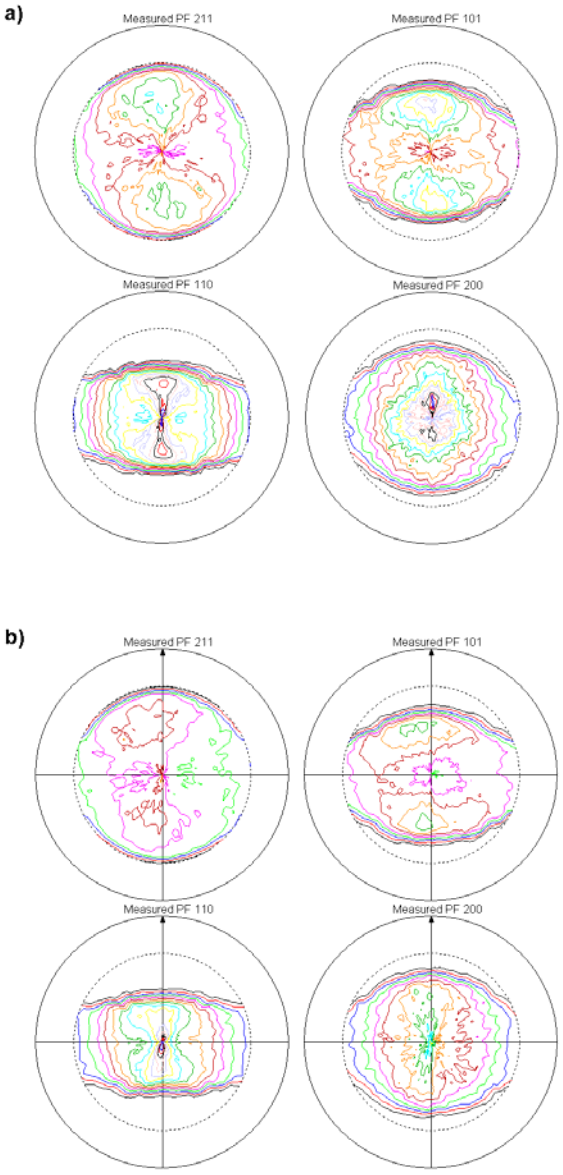

Figure 7.5: *The degree of texture and oriented distribution function profiles for the (211), (101), (110) and (200) peaks of (a) SnO_2 nanowires and (b) C-encapsulated SnO_2 nanowires.*

7.3.2. Electrochemical Properties

Figure 7.6 shows preliminary electrochemical results on the C-encapsulated SnO_2 nanowires in the potential range from 0.05 to 1.50 V (vs. Li/Li^+). For comparative purposes, all electrochemical measurements were conducted under the same conditions as in our previous work.[180] The reference SnO_2 nanowires showed a strong improvement in terms of reversible Li^+ storage and cyclic retention, due to their relatively higher surface area and shorter diffusion length. As expected, we found even more enhanced electrochemical results from the C-encapsulated SnO_2 nanowires. The initial coulombic efficiency of the C-encapsulated SnO_2 nanowires can be calculated as 50.67%, which is higher than the 46.91% of the SnO_2 nanowires at the first cycle. Moreover, it can be clearly seen that C-encapsulated SnO_2 nanowires present a higher reversible capacity and better cyclic retention up to the fiftieth cycle, as plotted in Figure 7.6(a). The increase in the C_{50}/C_2 value, which is the ratio of the discharge capacity retention at the fiftieth cycle compared to the second cycle, also can be estimated to be 53.82% for the C-encapsulated SnO_2 nanowires, compared to 25.21% for the SnO_2 nanowires. A comparison of the electrochemical results for the C-encapsulated SnO_2 nanowires and pure SnO_2 nanowires has been summarized in Table 7.1. These results reveal that the concurrent effects of the kinetically favorable structure and the conductive C phase on their electrochemical performance are greatly advantageous. The combination of these advantages could compensate for their undesirable capacity loss due to poor electronic connections. Based on the differential discharge profiles, it has been well known that a major reduction peak at around 0.90 V derived from Li_2O formation and electrolyte decomposition causes a large initial irreversible capacity in the first cycle and disappears in the second cycle as described in Figure 7.6(b).

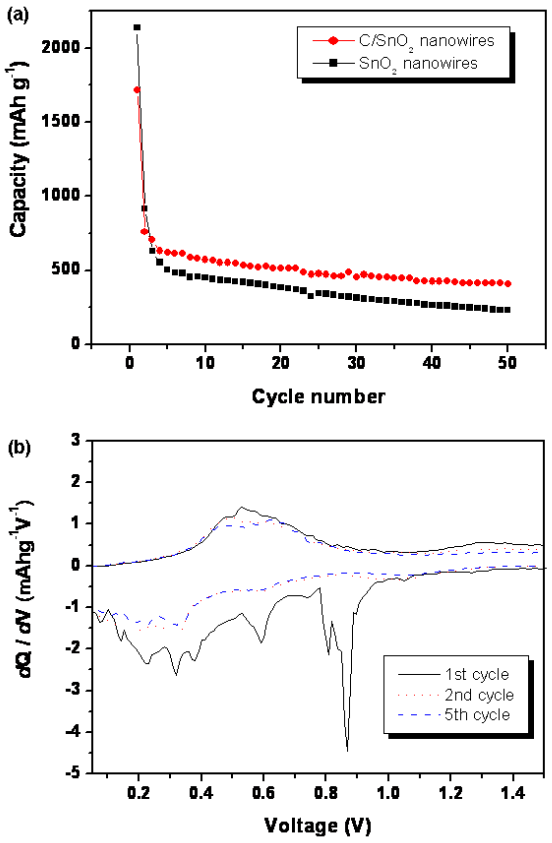

Figure 7.6: *The anodic performance of the C-encapsulated SnO_2 nanowires: (a) The cyclic performances of C-encapsulated SnO_2 nanowires and reference SnO_2 nanowires up to the fiftieth cycle at the same current density, 100 $mA{\cdot}g^{-1}$, and (b) differential charge-discharge versus potential plots of the first, second, and fifth cycles between 0.05 V and 1.50 V for the C-encapsulated SnO_2 nanowires.*

The other pairs of small reduction and oxidation peaks in the range from 0.20 V to 0.60 V are related to the formation of various Li_xSn phases, such as Li_2Sn_5, LiSn, Li_7Sn_3, Li_5Sn_2, $Li_{13}Sn_5$, Li_7Sn_2, and $Li_{22}Sn_5$, during the charge-discharge process.[245] The interesting point here is that there is no evidence to show that the amorphous C phase contributes to the capacity below approximately 0.10 V, which means that only SnO_2 phase reacts with Li^+ in the C encapsulated SnO_2 nanowires. It is apparent that the most important roles of the C phase are maintaining good electronic contact and providing more electron migration paths between active materials,

facilitating the percolation of electrons into the current collector. As a result, more Li^+ can be rapidly stored in C-encapsulated SnO_2 nanowires. Indeed, the relatively ductile nature of amorphous C phase is able to reduce the strain induced by volume variation of the Sn phase when it forms alloys with Li^+, offering better cyclic retention.

Table 7.1: *Summary of electrochemical results for C-encapsulated SnO_2 nanowires and SnO_2 nanowires.*

	Initial discharge capacity ($mAh \cdot g^{-1}$)	Initial charge capacity ($mAh \cdot g^{-1}$)	Initial irreversible capacity ($mAh \cdot g^{-1}$)	Initial coulombic efficiency (%)	C_{50}/C_2 (discharge) (%)	C_{50}/C_{10} (discharge) (%)
SnO_2 nanowires	2137.15	1003.22	1134.13	46.91	25.21	51.37
C-SnO_2 nanowires	1714.43	868.67	845.76	50.67	53.82	71.81

7.4. Summary

It is likely that Li^+ transport could be facilitated in the nanoscale form and that synergistically amorphous C phase would effectively improve electron conduction and accommodate volume expansion of active materials during alloying/de-alloying reactions, resulting in notable improvement of reversible capacity and cyclic retention. We expect that the electrochemical performance can be further enhanced by the optimization of C content and better understanding of the reaction mechanism at the interface between SnO_2 nanowires and the amorphous C layer.

8. Mesoporous Organo-Silica Nanoarray for Energy Storage Media

8.1. Introduction

Highly ordered mesoporous nanomaterials have stimulated great interest due to their potential applications in constructing functional nanoscale systems.[246-248] Recently, the excellent chemical and thermal stability of inorganic mesoporous nanomaterials such as mesoporous silica[249], mesoporous carbon[214], and template membranes[213] have drawn considerable attention because of their potential for promising new storage media. However, the structure of these traditional mesoporous materials can still not be effectively controlled yet. From the viewpoint of the periodic distribution and size control of cylindrical nanoholes, mesoporous organo-silica nanoarrays (MOSN) prepared by surfactant mediated synthesis have been considered to have strong potential in the energy storage field.[250]

Tin dioxide (SnO_2)-based nanocomposite is one of the most promising anode materials in terms of specific charge (> 600 $mAh \cdot g^{-1}$) and reaction potential with Li^+ (< 0.5 V) to substitute for commercial graphite anode in lithium-ion batteries. However, large volume changes caused by the electrochemical reactions between Sn and Li^+ lead to the loss of capacity and rechargeability during cycling.[70,101] Although some promising attempts at structure modifications to improve the cyclic performance of SnO_2 have been reported, the poor initial coulombic efficiency of the SnO_2-based nanocomposites have limited their practical utility.[251-253] The critical issues for SnO_2 based electrode materials are how to accommodate the volume expansion and how to reduce the initial irreversible capacity during electrochemical reactions.

Herein, we report on the preparation and anodic performance of SnO_2 embedded and coated mesoporous organo-silica nanoarrays (MOSN) to determine the potential use of MOSN for lithium-ion batteries. MOSN with well distributed nanoholes was successfully synthesized by a surfactant mediated process. The SnO_2–MOSN nanocomposite was prepared in such a way that the Sn based solution was inserted inside the nanoholes and oxidized in the MOSN via a sol–gel vacuum suction method. We would like to suggest the SnO_2–MOSN nanocomposite as a promising anode material and confirm the potential of the MOSN as an intriguing storage material based on its electrochemical performance.

8.2. Experimental

8.2.1. Preparation of Mesoporous Organo-Silica Nanoarray

In order to produce mesoporous organo-silica nanoarrays (MOSN), a surfactant mediated method was employed as described below. Octadecyltrimethylammonium (ODTMA) chloride surfactant (6.66 g) was dissolved in an aqueous solution of 6 M NaOH (50 ml) and distilled water (200 ml) at 50 °C, and then 8 ml of 1,4-bis(triethoxysilyl) benzene (BTEB) was added drop by drop under stirring at room temperature. The as-prepared solution was ultrasonicated for 20 min and stirred for 20 hours. The solution was dried at 95 °C for 20 hours and sieved through a filter paper (Whatman 5). The collected white product was dried in a vacuum oven. To remove the surfactant, the dried product was washed in a solution of ethanol (450 ml) and 36% HCl (18 ml) under stirring at 70 °C for 8 hours. The final product was dried at 95 °C for 20 hours again.

8.2.2. Preparation of SnO_2-MOSN Nanocomposite

SnO_2–MOSN nanocomposite was prepared via the sol–gel vacuum suction method. 10 ml of the 3 M Sn^{II} solution was prepared by dissolving $SnCl_2 \cdot 2H_2O$ in a solution of ethanol and 36% HCl. The Sn based solution was inserted inside the nanoholes and coated on the surface of the MOSN by impregnation through 10 mg of MOSN powder on a filter paper by a reduced vacuum suction process. The product was dried at 120 °C for 2 hours and sintered at 400 °C for 3 hours in a vacuum furnace under an Ar and O_2 atmosphere. Then the product was washed with distilled water to allow the Cl^- to be removed by centrifuging and finally dried in a vacuum oven.

8.2.3. Structural Characterization

The microstructure and morphology of the MOSN and SnO_2–MOSN nanocomposite were identified by X-ray diffraction (XRD, BRUKER D8), field emission scanning electron microscopy (FESEM, JEOL JEM-3000), and high resolution transmission electron microscopy (HRTEM, JEOL 2011). The pore size distributions and surface areas were estimated by the Barret–Joyner–Halenda (BJH) and the Brunauer–Emmett–Teller (BET) methods, respectively.

8.2.4. Electrochemical Characterization

To make electrodes, a mixture of 75 wt % active material and 15 wt % acetylene black was added to a solution containing 10 wt % polyvinylidene fluoride (PVdF) in n-methyl-2-pyrrolidinone (NMP). This slurry was pasted onto a copper foil current collector. After the electrode was dried at 120 °C for 2 hours in vacuum (10^{-3} Torr), it was compressed under a

pressure of about 200 kg·cm^{-2}. Test cells (CR2032 coin-type) were fabricated to evaluate the anodic performance of the SnO_2–MOSN nanocomposite. The assembly was carried out in an Ar-filled glove box (MBraun, Unilab, Germany) with less than 0.1 ppm each of oxygen and moisture. Li metal foil was used as the counter and reference electrode. 1M $LiPF_6$ was dissolved in a 1:1 (by volume, Merck KgaA, Germany) mixture of ethylene carbonate (EC) and dimethyl carbonate (DMC) to form the electrolyte, and Celgard membrane was used as the separator. The charge–discharge tests on the SnO_2–MOSN nanocomposite went on up to the 50th cycle in the range of 0.05–1.50 V (vs. Li/Li$^+$).

8.3. Results and Discussion

8.3.1. Structural and Morphological Characterization

The mesoporous organo-silica nanoarray (MOSN) was found to consist of cylindrical particles in a hexagonal array that contained periodic nanoholes. Physical and electrochemical tests revealed its potential as a superior storage material with high thermal and chemical stability in conjunction with SnO_2 as an active material for lithium-ion batteries. Figure 8.1 shows X-ray diffraction patterns of the MOSN and SnO_2–MOSN nanocomposite. All reflections of the MOSN are in good accordance with those of the mesoporous organo-silica previously reported by Inagaki et al.[250], as shown in Figure 8.1(a). According to the diffractions of the SnO_2–MOSN nanocomposite, only SnO_2 with the rutile structure (JCPDS 41-1445) and MOSN phases were detected, without any other impurity. After the oxidation of the Sn based solution, small peak shifts of MOSN to high angles were observed in the SnO_2–MOSN nanocomposite, as illustrated in Figure 8.1(b); the shifts are $\Delta(2\theta) = 0.12°$ and 0.10° for the main two peaks of MOSN, respectively. These peak shifts were induced by lattice shrinkage of the MOSN,

resulting from volume variation accompanying the phase transition inside the MOSN when the inserted Sn based solution transformed into rutile-type SnO_2 during the sintering process.

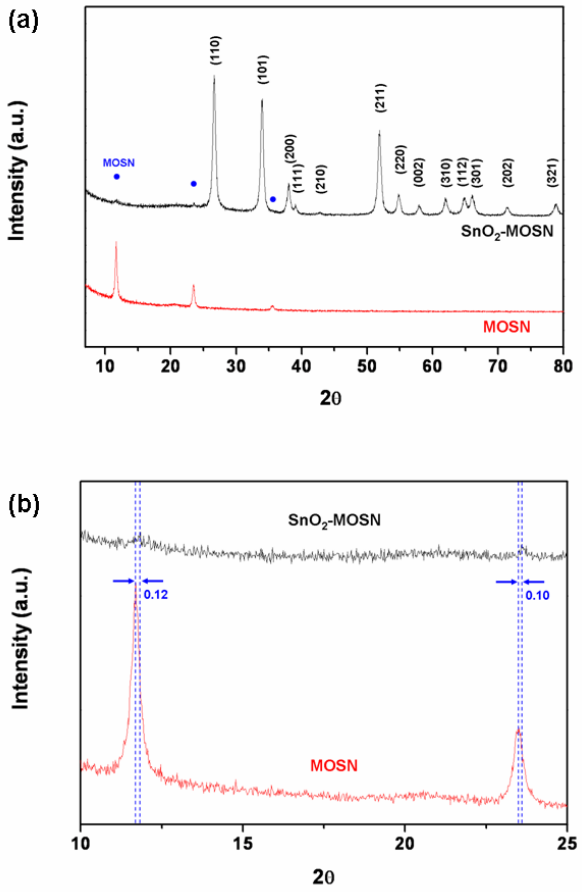

Figure 8.1: *X-ray diffraction patterns of MOSN (mesoporous organo-silica nanoarray) and SnO_2–MOSN nanocomposite in the 2θ ranges of: (a) 7°–80° and (b) 10°–25°.*

Both TEM and FESEM images (Figure 8.2) show that the MOSN consists of cylindrical structures in an array, with a high aspect ratio of length to width when aligned along the hole direction. The individual MOSN cylinders have highly ordered periodic nanoholes, which have crystal-like wall structures and a size of less than 5 nm. After the SnO_2 infiltration process, the SnO_2–MOSN nanocomposite could maintain its original structure due to the excellent mechanical stability of the aligned hexagonal nanoarray in the MOSN (Figure 8.3(a)).

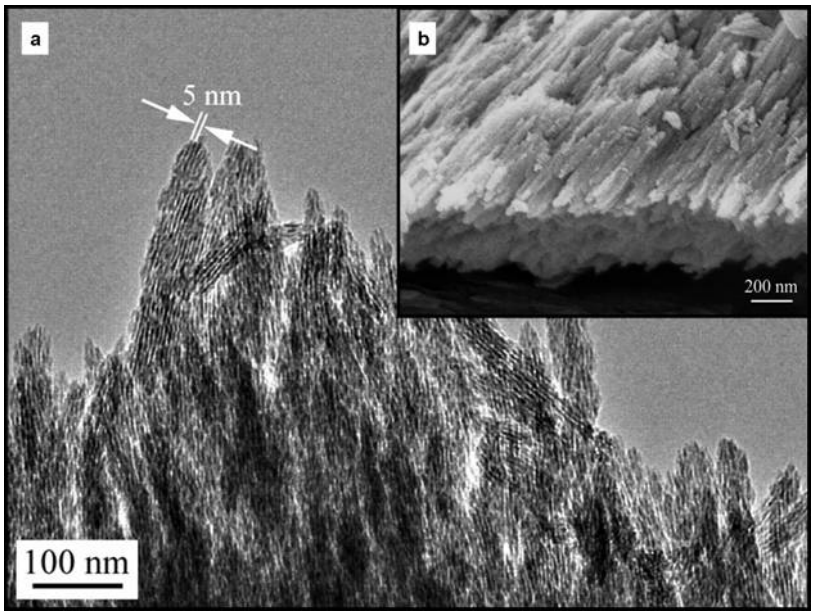

Figure 8.2: *The morphology of MOSN (mesoporous organo-silica nanoarray): (a) TEM image of MOSN and (b) FESEM image of MOSN.*

A HRTEM image (Figure 8.3(b)) shows that the periodic nanoholes, which were clearly shown in the MOSN, had disappeared, and randomly oriented SnO_2 nanocrystallites ranging from 10 to 20 nm were found on the surface of the SnO_2–MOSN nanocomposite. The ring patterns in Figure 8.3(b) indicate that the coated SnO_2 phase on the surface of the MOSN has a polycrystalline structure, which is in good agreement with the XRD results. These results clearly confirm that polycrystalline SnO_2 phase has been successfully incorporated into the nanoholes and formed a coating on the surface of the MOSN.

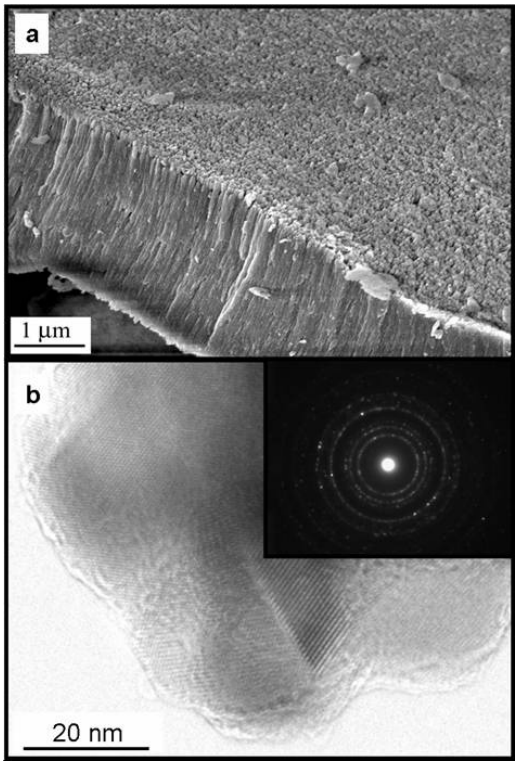

Figure 8.3: *The morphology of SnO_2–MOSN (mesoporous organo-silica nanoarray) nanocomposite: (a) FESEM image of SnO_2–MOSN nanocomposite and (b) HRTEM image and selected area electron diffraction (SAED) pattern (inset) of SnO_2–MOSN nanocomposite.*

The pore distribution and surface area have been measured to confirm the structural change after the sol–gel vacuum suction process. Obviously, pores with a size of about 4 nm are the main constituents among the various sized pores in the MOSN, whereas these pores do not appear to any significant extent in the SnO_2–MOSN nanocomposite, as presented in Figure 8.4. The disappearance of the pores with a size of about 4 nm in the SnO_2–MOSN nanocomposite demonstrates that the nanospaces in the MOSN were successfully filled with SnO_2. In addition, the surface areas of the MOSN and the SnO_2–MOSN nanocomposite came to 1065.86 $m^2 \cdot g^{-1}$ and 82.66 $m^2 \cdot g^{-1}$, respectively. The diminishment of the BET surface area of the nanocomposite indicates that the MOSN was encapsulated by SnO_2, leading to an increase in particle size.

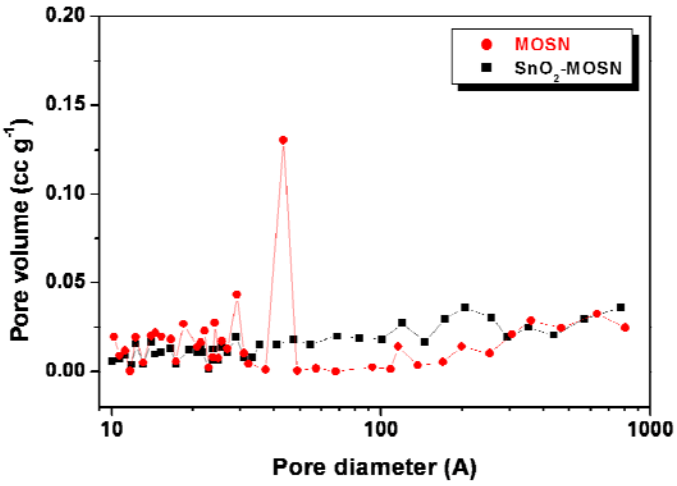

Figure 8.4: *The pore distributions of MOSN (mesoporous organo-silica nanoarray) and the SnO_2–MOSN nanocomposite, as estimated by Barret–Joyner–Halenda (BJH) method.*

8.3.2. Electrochemical Properties

The anodic performance of SnO_2–MOSN nanocomposite was tested in the potential range of 0.05–1.50 V (vs. Li/Li^+). For comparison, pure SnO_2 powder also was examined under the same conditions. The galvanostatic voltage profiles for the first cycle show a greatly improved initial coulombic efficiency for the SnO_2–MOSN nanocomposite. It should be noticed that its initial irreversible capacity is approximately 630 $mAh \cdot g^{-1}$, which is apparently much smaller than that of pure SnO_2, 1277 $mAh \cdot g^{-1}$, as plotted in Figure 8.5(a). The MOSN could reduce the electrical disconnection between active materials due to volume variations in the nanocomposite, which results in improvement of the initial coulombic efficiency. The differential charge–discharge capacity vs. voltage profile of the SnO_2–MOSN nanocomposite (Figure 8.5(b)) identifies electrochemical reactions during cycling, which are relevant to the galvanostatic voltage profiles as presented in Figure 8.5(c). The first differential discharge profile shows two apparent peaks

around 1.0 V derived from Li_2O formation when SnO_2 reacts with Li^+, and a small peak around 0.8 V corresponds to solid electrolyte interphase (SEI) film formation. These peaks disappeared, leaving a large initial irreversible capacity at the first cycle. As regards to the separate Li_2O formation peaks around 0.95 V and 1.05 V, they seem to be separated by the complex electrochemical conversion mechanisms of SnO_2 to Sn in the SnO_2–MOSN nanocomposite. We suggest that the SnO_2 coating on the surface of the MOSN would be directly reduced to Sn at 1.05 V following Equation 8.1 below, whereas incorporated SnO_2 inside the MOSN might be reduced to SnO in the initial Li^+ intercalation stage, and then the SnO reduced to Sn following Equation 8.2 below; this corresponds to a potential of 0.95 V.[213,254] The nanoarray structure with limited space might be disturbing smooth Li^+ intercalation into nanospaces inside the MOSN, which results in the formation of the separate reduction peaks. This slow lithiation process might lead to the improvement of reversible Li^+ storage and initial coulombic efficiency of the nanocomposite.

$$SnO_2 + 4Li^+ + 4e^- \rightarrow Sn + 2Li_2O \quad (8.1)$$

$$2SnO + 4Li^+ + 4e^- \rightarrow 2Sn + 2Li_2O \quad (8.2)$$

$$Sn + xLi^+ + xe^- \rightarrow Li_xSn \quad (0 \le x \le 4.4) \quad (8.3)$$

The other pairs of reduction and oxidation peaks between 0.25 V and 0.70 V during the discharge and between 0.40 V and 0.80 V during the charge cycle which remained after the second and the tenth cycles are related to the formation of Li_xSn, as described in Equation 8.3. This result reveals that only SnO_2 phase reacts with the Li^+ in the SnO_2–MOSN nanocomposite

and that the MOSN does not contribute to the capacity. The SnO_2–MOSN electrode shows a higher reversible specific charge of about 420 $mAh \cdot g^{-1}$ until the 50th cycle, with relatively stable cyclic performance as shown in Figure 8.5(d). It is likely that the cylindrical nanoarray structure of MOSN would act as a mechanical buffer and effectively prevent the electrical disconnection between active materials induced by the volume expansion during electrochemical reactions.

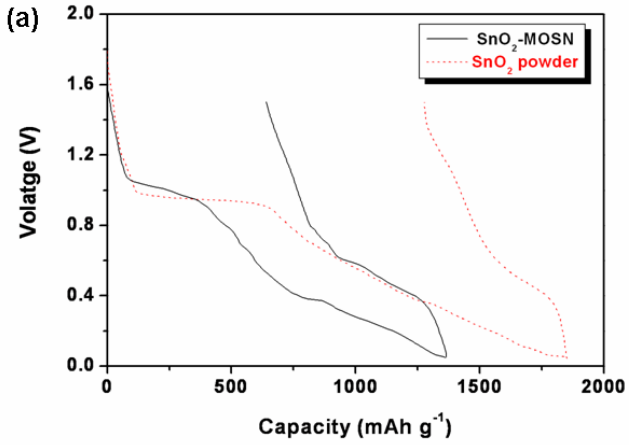

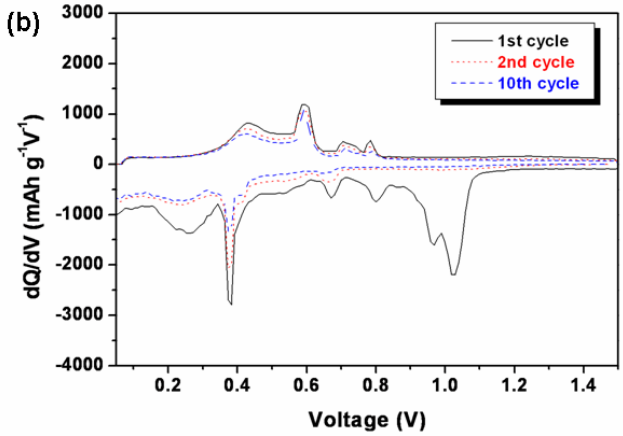

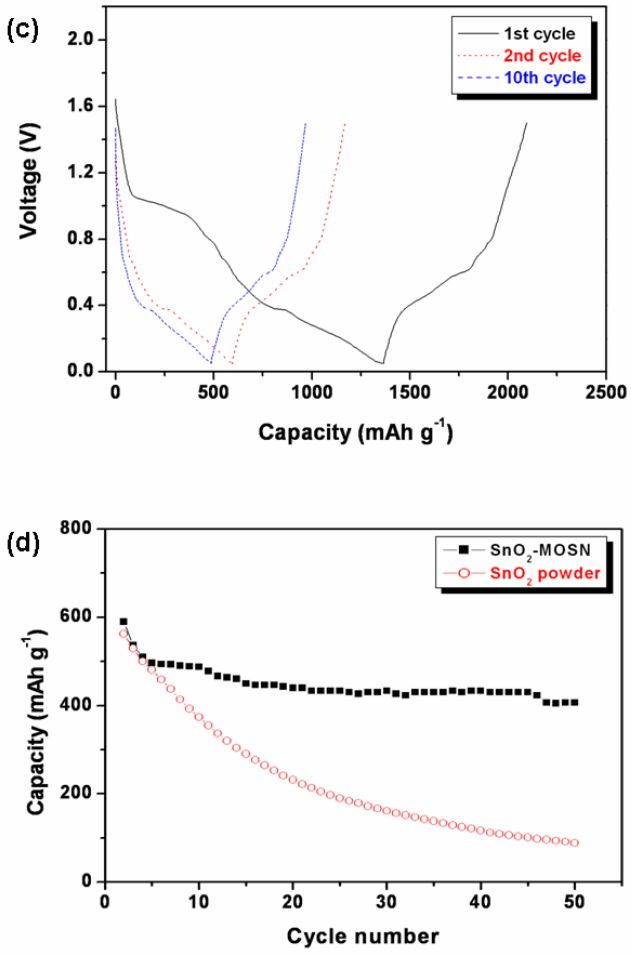

Figure 8.5: *The anodic performance of the SnO_2−MOSN (mesoporous organo-silica nanoarray) nanocomposite: (a) the galvanostatic voltage profile for the first cycle between 0.05 V and 1.50 V compared with pure SnO_2 powder; (b) the differential charge−discharge vs. potential plots; (c) the charge −discharge curves at the first, second and tenth cycles between 0.05 V and 1.50 V for the SnO_2−MOSN nanocomposite; and (d) the cyclic performance from the second cycle to the fiftieth cycle of SnO_2−MOSN nanocomposite and pure SnO_2 powder at the same current density, 100 $mA{\cdot}g^{-1}$.*

8.4. Summary

In summary, we have fabricated SnO_2–MOSN nanocomposite, consisting of a hexagonal array of cylindrical nanostructures, by a surfactant mediated method followed by a sol–gel based vacuum suction process. The SnO_2–MOSN nanocomposite shows a higher specific charge of 420 $mAh \cdot g^{-1}$ and improved cyclic performance compared with pure SnO_2 powder. Only SnO_2 phase reacted with Li^+ and the MOSN, with a high aspect ratio of the length to the width, could accommodate volume changes of SnO_2 as a mechanical buffer, resulting in improvement of the initial coulombic efficiency in the nanocomposite.

PART II

II.A. Overview

There are nanoscale Li^+ storage materials available that exhibit unique properties which are measurably distinct from those of their larger scale counterparts. The nanostructured materials can exhibit increased electronic conductivity, improved electromechanical stability, increased rate of intercalation, and an extended range of solid solution. Lithium iron phosphate ($LiFePO_4$) is currently considered as one of the most promising cathode materials, based on its low cost, non-toxicity, abaundant raw materials, excellent thermal stability, and safety characteristics.[142-144,255-256] In a pursuit of the commercialization of $LiFePO_4$ for large-scale applications, numerous research efforts have generated great debates on the Li^+ insertion/extraction mechanism and interface kinetics, as well as its phase diagram in a two-phase system of $LiFePO_4$ and $FePO_4$. The aim of this work is to highlight the advantages and drawbacks of $LiFePO_4$ at the nanoscale and then suggest further evidence to support the incomplete room-temperature phase diagram of $LiFePO_4$, which is directly related to its electrochemical behavior at room temperature. In order to identify the electrochemical reaction model and phase transition mechanism in its nanoscale form, the crystal chemistry and fundamental properties of the $LiFePO_4$ need to be systematically investigated. Herein, we introduce an optimized synthesis of $LiFePO_4$/C nanocomposites with different particle sizes to determine the relationship between particle size and electrochemical performance. For the first time, we present experimental evidence for the isolation of a single phase solid solution of Li_xFePO_4 under certain thermodynamic conditions. In addition, the electrochemical performance of $LiFePO_4$/C exposed to air as a function of exposure temperature and time has been systematically demonstrated from a structural point of view.

II.B. $LiFePO_4$ Cathode Materials

Olivine phase $LiFePO_4$ is currently attracting considerable interest as a promising cathode material for rechargeable lithium-ion batteries. It is nontoxic, non-hygroscopic, electrochemically stable, environmentally friendly, and inexpensive. The high theoretical specific energy of 170 $mAh \cdot g^{-1}$ at room temperature makes it a very attractive candidate as a cathode material in cells. In addition, the operating voltage of 3.45 V is ideal for maximizing energy while minimizing side reactions due to electrolyte decomposition.[2,8]

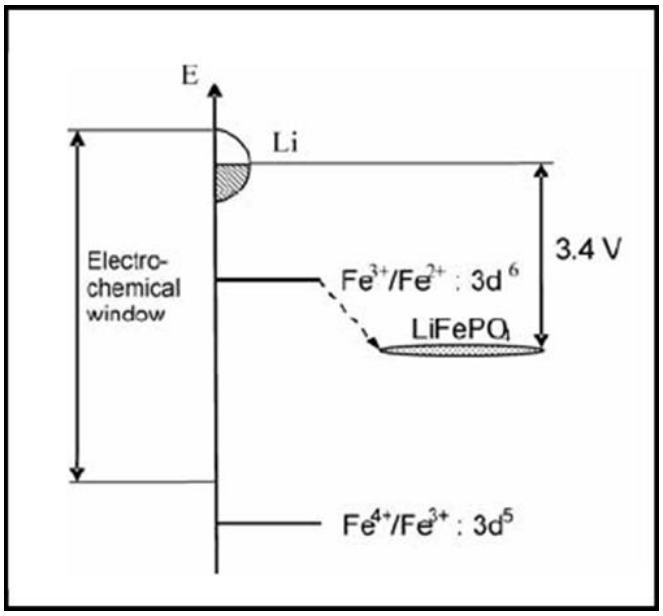

Figure II.1: *Energy diagram showing the Fe^{4+}/Fe^{3+} and Fe^{3+}/Fe^{2+} potentials in cathode materials based on iron in octahedral coordination.*

Considering the unfavorable position of the redox potentials of Fe, in general, the Fe^{3+}/Fe^{4+} potential is too distant from that of Li/Li^+ and located beyond the electrochemical window of the electrolyte, which cannot guarantee the neutrality of the electrolyte versus the cathode, as shown

in Figure II.1.[257-259] On the other hand, the Fe^{3+}/Fe^{2+} potential is close to that of Li/Li^{+}, which results in a decrease in the cell voltage. Such behavior is related to the high-spin configuration of Fe^{3+} and strong interactions between *d* electrons. However, the presence of such polyanions as $(PO_4)^{3-}$, with a strong covalent P–O bond, stabilizes the anti-bonding state, Fe^{3+}/Fe^{2+}, in the $LiFePO_4$ system. The Fe–O bond becomes less covalent due to the induction effects in the Fe–O–P system, which raises the electrode potential. The stronger the P–O bond, the weaker the Fe–O bond, and the higher is the cell voltage.

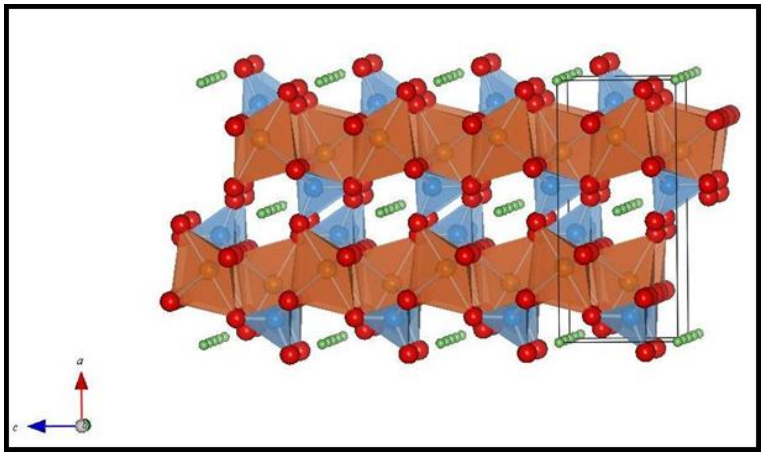

Figure II.2: *The crystal structure of olivine $LiFePO_4$, which belongs to the space group Pmna.*

The crystal structure of olivine $LiFePO_4$ is described by the space group *Pmna*. Fe is located in the middle of a slightly distorted FeO_6 octahedron, with a Fe–O average bond-length higher than expected for the Fe^{2+} valence state in octahedral coordination. Li is located in a second set of octahedral sites but distributed differently, in that LiO_6 octahedra share edges in order to form LiO_6 chains along the *b*-axis in $LiFePO_4$ as illustrated in Figure II.2.[142-144] The small volumetric expansion and structural changes during Li^{+} insertion and extraction are believed to be

beneficial for a high rate-capability. The key barrier to commercialization is its intrinsic low electronic conductivity of 10^{-9} to 10^{-10} $S \cdot cm^{-1}$, which is thought to result in considerable Ohmic drops within the electrode. In addition, it has been noted that the electrode displays limited high rate capability, with considerable loss in utilization as the current increases, suggesting transport limitations.[145-147] However, there are practical approaches to improving conductivity, including doping with supervalent cations, carbon coating, or reducing the particle size, allowing development to move forward.[147-152] In practice, these efforts to introduce dopant ions into the lattice have been shown to be very successful in improving the conductivity, and consequently the performance, of the material.[147]

II.C. Reaction Mechanism of $LiFePO_4$

Different model for the reaction mechanism of $LiFePO_4$ have been proposed and revised in various ways. The shrinking core model was proposed by Padhi et al.[142-144], with the concept of a radius-dependent process in which the $LiFePO_4/FePO_4$ interface moves inward through each particle as the outer region converts to $FePO_4$.

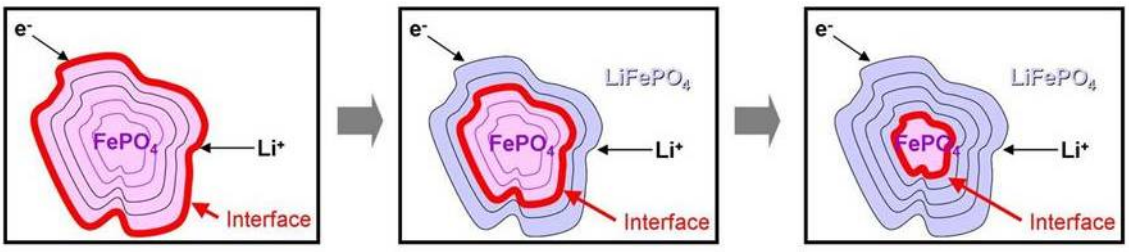

Figure II.3: *A schematic diagram of the shrinking core model in a binary system of $LiFePO_4$ and $FePO_4$.*

As Li^+ insertion proceeds over the two-phase interface of $LiFePO_4/FePO_4$, the two-phase interface moves from the surface to the bulk, and its area decreases. The total quantity of Li^+ passing through the interface can not compensate for the external current supplied to $LiFePO_4$, leading to the poor capacity and rate capabilities, as described in Figure II.3.

Following that, the mosaic model was introduced by Andersson et al.[260] with slight modifications. This model considers the feasibility of the extraction/reinsertion as it occurs at many sites within a given particle, as illustrated in Figure II.4. Srinivasan et al. mathematically consolidated the shrinking core model by taking into account both the diffusion of Li^+ through the shell and the movement of the phase boundary, and then raising the question of the partial solid solution domains that are bound to exist if a radial model is assumed.[261] On the other hand, the existence of $Li_{1-\square}FePO_4$ and $Li_{\square}FePO_4$ single-phase solid solutions were reported at elevated temperatures by Delacourt et al.[262] Yamada et al. recently suggested a miscibility gap model in which solid solutions, $Li_{\alpha}FePO_4$ and $Li_{1-\beta}FePO_4$, could exist at room temperature, as supported by Rietveld refinements of X-ray and neutron diffraction data on $LiFePO_4$ nanoparticles, as well as calorimetric measurements, which also tended to confirm the shrinking core model concept, as given in Figure II.5.[263]

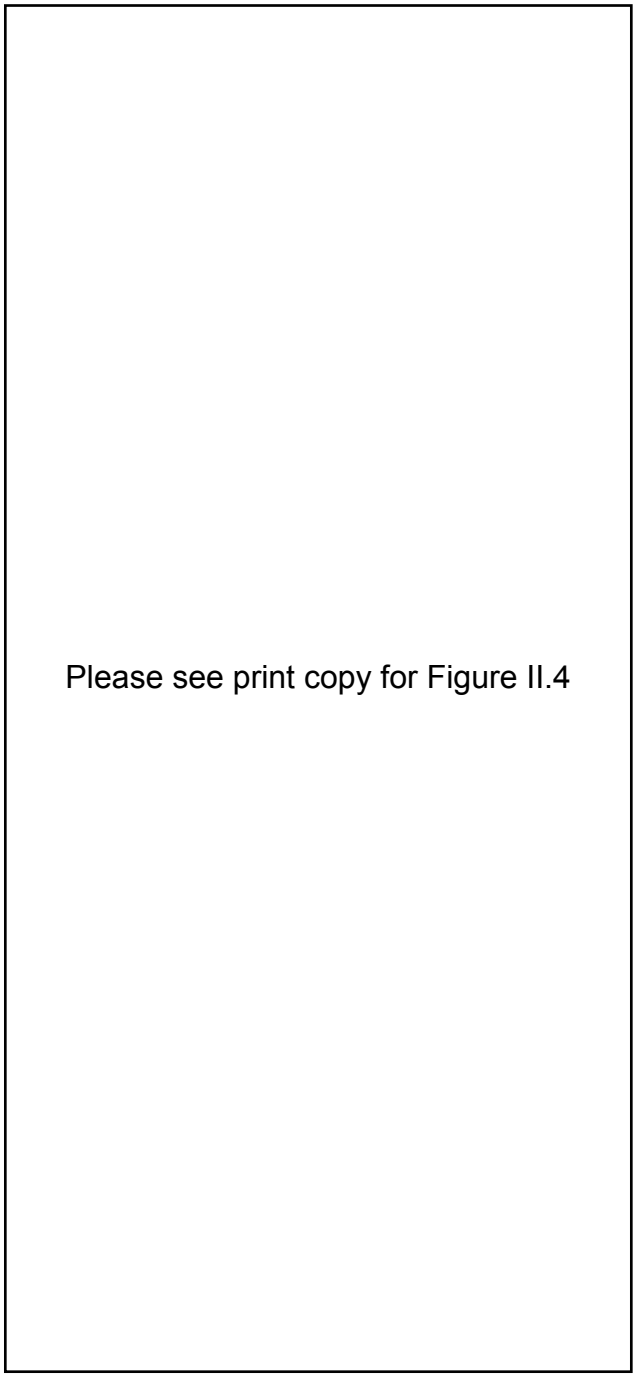

Figure II.4: *Schematic representations of two possible models for lithium extraction/reinsertion into a single particle of $LiFePO_4$: a) the radial model; and the mosaic model.*[260]

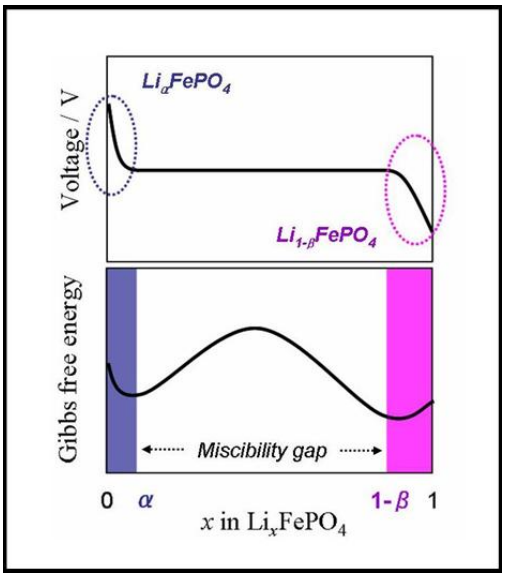

Figure II.5: *Schematic representations of miscibility gap models for lithium extraction/reinsertion into a single particle of $LiFePO_4$.*

Chen et al. studied the $LiFePO_4$-$FePO_4$ phase transition by high-resolution electron microscopy, in order to elucidate the mechanism of how such two-phase insertion proceeds.[264] They spotted the occurrence of disordered transition zones in the *bc*-plane, with the Li^+ moving in a direction parallel to the phase boundary. Although the particle size could have a critical bearing on the transport of Li^+ ions and electrons into and out of the individual particles, such a study has clearly shown that the well adopted core shell model does not apply to individual crystallites. In a recent report, Prosini even considered a model within which the delithiated phase grows from the center of the particle so as to reduce the stress originating from the volume contraction associated with the lattice mismatch between the two end-member phases.[265] Nevertheless, it should be realized that such a model is the result of simple logistic views or speculations. The accurate reaction mechanism has not been clarified yet. Therefore, there is a strong need to identify the accurate reaction mechanism in the $LiFePO_4$ system for further improvements.

II.D. Phase Diagram of $LiFePO_4$

Theoretical and experimental work has been conducted to understand the electronic structure and phase transitions in $LiFePO_4$ during Li^+ insertion and extraction. The charge compensation and phase separation in the electrochemical lithiation reaction is generally attributed to the reduction of Fe^{3+} to Fe^{2+}. It has been suggested that the PO_4^{3-} polyanion lowers the Fermi level and hence raises the cell potential, while it maintains a stable structural framework through strong P–O covalent bonds. The binary phase diagram of Li_xFePO_4 is very distinctive compared to many other Li^+ intercalated transition metal oxides, in that the material phase separates into the end members $FePO_4$ and $LiFePO_4$ at low temperature and exhibits a eutectoid transition at higher temperature. It has been reported that the ordering of electrons/holes on the Fe sub-lattice, which are localized due to electron correlation effects, coexists with the Li^+/vacancy ordering on the Li sub-lattice. The Li_xFePO_4 phase diagram is critical for understanding and improving the electrochemical performance. $LiFePO_4$ occurs in nature as the mineral triphylite (T), and its delithiated counterpart, $FePO_4$, is known as heterosite (H). Both phases are olivine-type orthorhombic structures at room temperature. Recently, the high temperature phase diagram was investigated by Delacourt et al. and by Dodd et al., as displayed in Figure II.6.[270,273] According to their work, room temperature electrochemical Li removal exhibits a miscibility gap between triphylite (T) $LiFePO_4$ and delithiated heterosite (H) $FePO_4$, and no intermediate compound Li_xFePO_4 exists between T and H. Both phases have a very limited amount of solubility in the experimental phase diagrams.

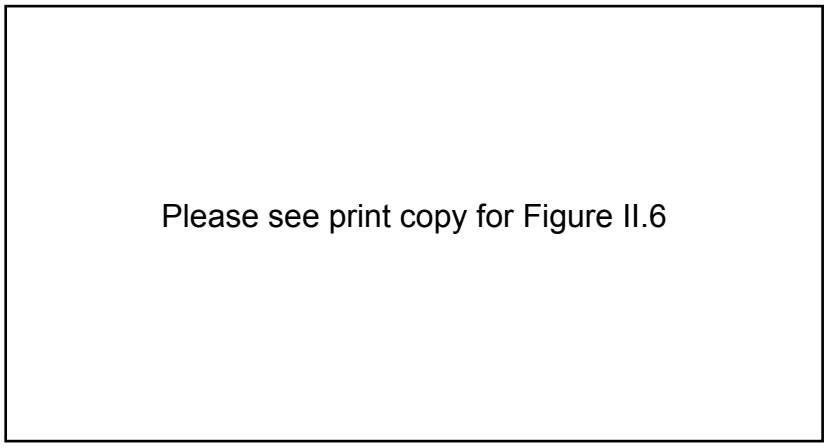

Figure II.6: *Experimental phase diagram of Li_xFePO_4. The boundary data points are taken from Delacourt et al. and from Dodd et al.*[270,273]

For comparative purposes, theoretical work by Zhou et al. is presented here in Figure II.7. The low temperature immiscibility was confirmed in this work as well, but an unusual eutectoid behavior was also reported above a transition temperature of about 150 °C or 200 °C. A disordered phase (D) emerges around x = 0.45 to 0.65 at a temperature of about 300 °C to 400 °C, where solid solution (SS) dominates all other compositions. To sum up, there is a two-phase region at low temperature, the appearance of an intermediate disordered (D) phase at the eutectoid point, and dominance of the disordered phase above two congruent points. The solubility is less than 1% at room temperature, and slightly larger in $FePO_4$ than in $LiFePO_4$.[274] Compared to the experimental reports, the eutectoid temperature is only 20 to 70 K off, and the congruent temperature is about 100 to 150 K off. These investigations are valuable to systematically build up the phase diagram of $LiFePO_4$. However, there are still many unknown factors to be clarified for a comprehensive understanding of room temperature phase transitions in the $LiFePO_4$ system.

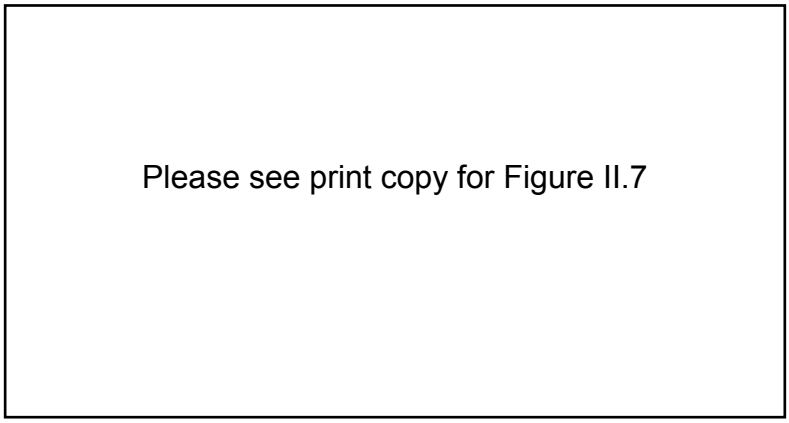

Figure II.7: *Calculated Li_xFePO_4 phase diagram in the temperature and composition space from Zhuo et al.*[274]

Following this track, Yamada et al. recently provided experimental evidence that Li_xFePO_4, at room temperature can be described as a mixture of the Fe^{3+}/Fe^{2+} mixed-valence intermediate $Li_\alpha FePO_4$ and $Li_{1-\beta}FePO_4$ phases. Using powder neutron diffraction, the site occupancy numbers for Li^+ in each phase were refined to be $\alpha = 0.05$ and $1-\beta = 0.89$. The corresponding solid solution ranges outside the miscibility gap ($0 < x < \alpha$, $1-\beta < x < 1$) were detected by an anomaly in the configurational entropy and also by the deviation of the open-circuit voltage from the constant equilibrium potential.[263] Nevertheless, these findings encourage further improvement of this important class of compounds at room temperature, even though the room-temperature phase diagram has not been fully identified yet.

9. Isolation of Solid Solution Phase in Li_xFePO_4 at Room Temperature

9.1. Introduction

The crystal chemistry of phosphor-olivine $LiFePO_4$ has received much attention, ever since it was introduced as an alternative cathode material for new generation lithium ion batteries, owing to its fast charging, as well as safer performance and extremely flat potential.[143-144,147,151,266-267] Nevertheless, its poor intrinsic electronic conductivity, on the order of 10^{-9} $S \cdot m^{-1}$, and small tap density remain problems to be solved before it can be deployed on a commercial scale.[268-269]

In order to address the primary challenges to commercial use, the pervasive trends in research into $LiFePO_4$ basically fall into understanding the fundamental crystal structure and the phase diagram of $LiFePO_4$, because its poor electronic conductivity is thought to be related to the diffusion-limited transfer of Li^+ across the interface of two phases.[264,269-276] In the pursuit of clarification of the phase diagram and kinetic mechanisms of $LiFePO_4$, C. Delacourt et al. reported the possible formation of a single-phase solid solution in Li_xFePO_4 at high temperature, and N. Meethong et al. recently suggested that the miscibility gap shrinks systematically with decreasing particle size and increasing temperature.[278-279] These intriguing findings have been regarded as a key indication for a comprehensive understanding of the poor electronic and ionic conduction of $LiFePO_4$ in nature, because the single-phase solid solution form is believed to be essential for facilitating the migration of Li^+, due to the reduction in lattice strain caused by the reduction in lattice mismatches, so as to enhance the electrochemical performance. However,

unlike the previous reports, we have found that a single-phase solid solution could be isolated outside the miscibility gap of Li_xFePO_4 at room temperature. More importantly, its room-temperature stability might be highly dependent on the particle size in narrow compositions, which gives us a new insight into the strong enhancement of the electrochemical performance of $LiFePO_4$ in nanoscale form.

Herein, we carefully demonstrate the isolation of single-phase solid solutions of Li_xFePO_4 at room temperature and their dependence on particle size by high-resolution synchrotron X-ray diffraction (XRD) analysis, in order to address further pieces of evidence, to facilitate a more comprehensive understanding of the phase transitions of Li_xFePO_4, and to support the incomplete miscibility gap model. A comprehensive understanding of the relationship between that crystal chemistry and the electrochemical behavior of Li_xFePO_4 would hasten the achievement of optimum performance for $LiFePO_4$ in lithium ion battery science.

9.2. Experimental

9.2.1. Synthesis of Li_xFePO_4

Olivine Li_xFePO_4 (x = 0, 0.60, 0.93 and 1) powders with different particle sizes were synthesized by solid state reactions of lithium carbonate (Li_2CO_3, Wako, 99.9 %), iron(II) oxalate dehydrate ($FeC_2O_4 \cdot 2H_2O$, JUNSEI, 99 %) and diammonium hydrogen phosphate ($(NH_4)_2HPO_4$, Wako, 99%), combined with chemical oxidation. A total 5g of stoichiometric quantities of precursor powders were poured into a 250 ml Cr-hardened stainless steel (Cr-SS) container, together with a mixture of Cr-SS balls (10 mm-diameter × 10 and 5 mm-diameter × 16). The precursors were thoroughly mixed and ground by a conventional planetary milling

apparatus (ITOH LA-PO4) for 6 hours. The $LiFePO_4$ phase was formed by sintering at 700 ºC for 6 hours under a purified Ar gas flow. The self-assembled $LiFePO_4$/C composites were synthesized by an initial addition of 10 wt% porous Ketjen Black (LION, ECP), and sintering was done at 600 ºC for 6 hours under Ar gas flow or 400 ºC for 6 hours under Ar/2% H_2 gas flow to minimize particle growth without sacrificing purity.

Chemical oxidation to obtain $FePO_4$ was carried out by reacting $LiFePO_4$ with nitronium tetrafluoro-borate (NO_2BF_4, Alfa Aesar, 96 %) in dehydrated acetonitrile. After about 1.7 g of NO_2BF_4 (twice the amount needed for the estimated reaction) was dissolved in 100 ml of acetonitrile, about 1g $LiFePO_4$ was added, and the mixture was stirred with bubbling purified Ar gas for 24 hours at room temperature. The products were filtered several times to remove impurities before they were dried under vacuum. Partially lithiated samples of $Li_{0.60}FePO_4$ and $Li_{0.93}FePO_4$ were prepared by reacting $FePO_4$ with LiI (Alfa Aesar, 99.9 %) in acetonitrile. The ratio of acetonitrile to $FePO_4$ was set at 150 ml to 0.3 g. The solution was stirred for 24 hours at room temperature, and the products were filtered and washed several times with acetonitrile to remove impurities before they were dried under vacuum at room temperature.

9.2.2. Structural Characterization

Synchrotron X-ray diffraction data were obtained at room temperature using a high-resolution angle-dispersive type X-ray diffractometer (BL-$4B_2$) installed at the Photon Factory (PF) in the High Energy Accelerator Laboratory (KEK, Tsukuba, Japan). The wavelength of the incident X-rays was 1.20628 Å, and a flat Ge (111) crystal was used as the analyzer crystal. Powder patterns were obtained using a parallel beam geometry (asymmetric) with $\theta = 8^{\circ}$ in the range

from 2θ = 3º to 140º at room temperature. The unit-cell parameters were carefully refined by TOPAS software ver. 3.

9.2.3. Electrochemical Characterization

Half cells (CR2032 coin-type) were fabricated to evaluate the electrochemical performance. The assembly was carried out in an Ar-filled glove box with less than 0.1 ppm of moisture. Li metal foil was used as the counter and reference electrode, and 1M $LiPF_6$ dissolved in a 3:7 (by volume, provided by Tomiyama Chemicals) mixture of ethylene carbonate (EC) and diethyl carbonate (DEC) was employed as the electrolyte. A porous polypropylene film was used as the separator. The working electrode was formulated with 90 wt % active materials (with 40 nm, 80 nm, and 200 nm particle sizes, respectively), and 10 wt % polyvinylidene fluoride (PVdF) binder, using n-methylpyrrolidone (NMP) as the solvent, and spread out on aluminum foil current collectors. The obtained cathode sheets were dried at 120 ºC under vacuum overnight. The sheet was then pressed onto aluminum mesh to form a disk 16 mm in diameter. The cells were galvanostatically charged and discharged over the potential range of 2.0 V to 4.5 V at the C/20 rate.

For open circuit voltage measurement, the cells were initially charged galvanostatically at the C/20 rate at room temperature, and then maintained at 4.5 V for 24 hours, forming $FePO_4$. Then, they were discharged under a cathodic current of about 20 μA for 24 min, which corresponds to about 2 % of the theoretical capacity. The open-circuit voltage at room temperature was measured after 24 hours. Again, the cell was discharged under a cathodic current of about 20 μA for 24 min. These procedures were repeated several times until 50 % of state of charge (SOC) was reached at room temperature.

8.3. Results and Discussion

The existence of partial solid solution phases, $Li_{\alpha}FePO_4$ and $Li_{1-\beta}FePO_4$, outside the room-temperature miscibility gap, allowing the coexistence of partial Li^+ occupancies (α) and vacancies (β), has been reported in our previous work.[263,277] Considering the fact that Li^+ diffusion over the phase boundary in the two-phase mixture has been found to be kinetically limited, these room-temperature solid solutions could be beneficial for both ionic and electronic conduction in the Li_xFePO_4 system. However, their isolation and an understanding of their phase transition mechanism at room temperature have not been achieved yet. In order to investigate the room-temperature phase transitions between $LiFePO_4$ and $FePO_4$ during electrochemical reactions, typical open circuit voltage (OCV) measurements were performed across various $LiFePO_4$ samples with different particle sizes at room temperature. It is obvious that the measured OCV values versus depth of discharge (DOD) indicate a strong dependence on the particle size, as shown in Figure 9.1. A progressive increase in the single phase region is observed for decreasing particle size. It seems that the expanded single phase effectively enhances the charge transfer and suppresses the polarization obtained from the difference between the OCV and the closed circuit voltage (CCV) in $LiFePO_4$. As a result, more homogeneous Li^+ incorporation could evolve over the electrochemical reactions. Based on the established phase diagram and typical OCV curves, we especially selected a composition near an end member, $Li_{0.93}FePO_4$, as an experimental criterion phase, since it was prepared by a careful chemical delithiation and lithiation method, and had an approximately fixed composition of $x = 0.93$, which would be around the phase transition zone between the two-phase region and the single-phase region in the binary phase diagram, whereas $Li_{0.60}FePO_4$ was selected as a reference phase, because it should be composed of a mixture of two intermediate phases.

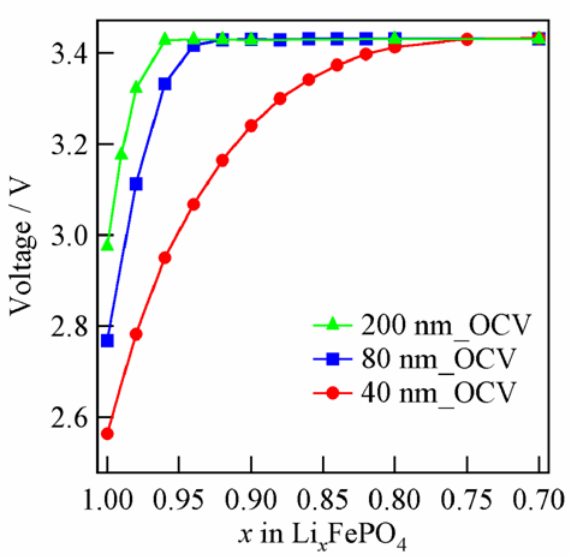

Figure 9.1: *A comparison of typical open-circuit voltage (OCV) curves versus depth of discharge (DOD) of $LiFePO_4$ as a function of particle size at room temperature.*

The room-temperature synchrotron X-ray diffraction (XRD) profiles for the $Li_{0.60}FePO_4$ and $Li_{0.93}FePO_4$ phases are displayed as a function of particle size in Figure 9.2. The supporting scanning electron microscopy (SEM) observations clearly show distinctive particle size differences, and the mean crystallite sizes could be estimated to be 39.7 nm, 76.6 nm, and 194.7 nm, respectively. For comparative purposes, the reference diffraction profiles of $LiFePO_4$ and $FePO_4$ are displayed together. From the series of diffraction patterns, it should be noted that there is no detectable impurity phase. All of the diffraction patterns were carefully refined by the use of an orthorhombic structure, which belongs to the space group *Pnma.* The carefully refined lattice parameters are summarized in Table 9.1, in which the lattice parameters and cell volumes of the intermediate phases, $Li_{0.60}FePO_4$ and $Li_{0.93}FePO_4$, were consistently reduced at each delithiation stage and are in good agreement with those of electrochemically delithiated samples.

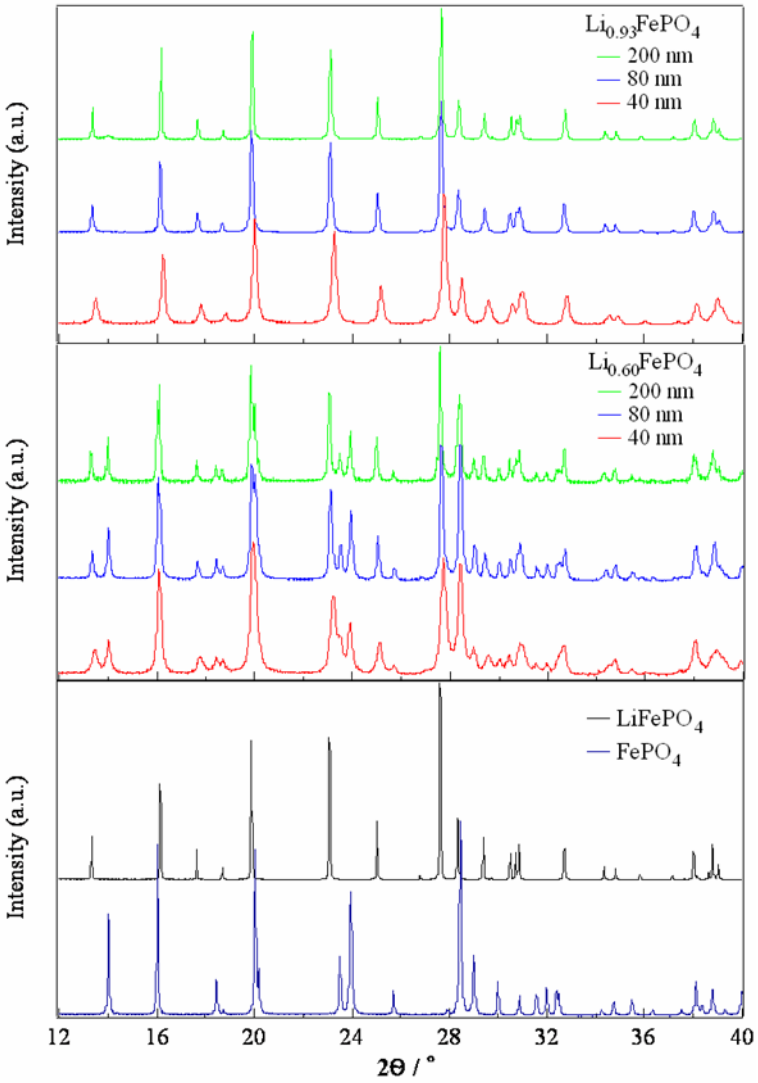

Figure 9.2: *Synchrotron X-ray diffraction profiles of a series of Li_xFePO_4 composition (x = 0, 0.60, 0.93, and 1) with different particle sizes: (a) $Li_{0.93}FePO_4$, (b) $Li_{0.60}FePO_4$, and (c) $LiFePO_4$ and $FePO_4$. The particle size varies from 40 nm to 200 nm.*

As shown in Figure 9.2, two peaks are clearly observed at 13.5° and 14.0°, corresponding to the (200) reflection of $LiFePO_4$ and the (200) reflection of $FePO_4$, respectively, in the diffraction patterns of $Li_{0.60}FePO_4$ over the whole particle size range. Only small peak broadening occurs along with particle size reduction, which is thought to be a general characteristic of

nanomaterials. In contrast, we observed a different behavior in the reflections of $Li_{0.93}FePO_4$, in that the intensity of the (200) peak of $FePO_4$ is gradually decreased when the particle size is minimized. For further inspection, we focused on low-angle peaks of $Li_{0.93}FePO_4$ indexed as $(200)_{LFP}$ and $(200)_{FP}$ at different particle sizes, together with the corresponding lattice parameter variations, as illustrated in Figure 9.3. In general, the phase transition and the ratio of solid solution phases corresponding to x in Li_xFePO_4 can be determined by the lattice parameter variations compared to those of $LiFePO_4$ and $FePO_4$. As for the 200 nm particles, two independent peaks were clearly observed and indexed as $(200)_{LFP}$ and $(200)_{FP}$, respectively, which indicates that the $Li_{0.93}FePO_4$ phase consists of two intermediate phases, $Li_\alpha FePO_4$ and $Li_{1-\beta}FePO_4$. The changes in the lattice parameters also reveal that the $Li_{0.93}FePO_4$ with a particle size of 200 nm is inside the miscibility gap at room temperature in Table 1. In addition, the limitation on solid solubility was approximately estimated to be $\beta_{200} = 0.02$ by applying Vegard's law to the refined lattice parameters. As the particle size was reduced to 80 nm, it can be clearly seen that the intensity of the $(200)_{FP}$ peak has decreased in the synchrotron XRD profile, which can be explained by the reduction of the $Li_\alpha FePO_4$ phase fraction in the two phase mixture of $Li_\alpha FePO_4$ and $Li_{1-\beta}FePO_4$, following the miscibility gap model.[263,277-279] This means that the $Li_{0.93}FePO_4$ phase with an average particle size of 80 nm contains a very small amount of $Li_\alpha FePO_4$ at room temperature, and the solid solubility, β_{80}, value has increased to 0.04, corresponding to the reduction in the $(200)_{FP}$ intensity. At the 40 nm particle size, more importantly, the $(200)_{FP}$ peak has disappeared, and the discrepancies in the lattice parameters are surprisingly negligible compared to the $Li_{1-\beta}FePO_4$ phase. This behavior reveals that the $Li_{0.93}FePO_4$ phase is in the single phase solid solution range and allows one to conclude that a solid solution of Li_xFePO_4 could be isolated as a single phase with the solid solubility of $\beta_{40} = 0.11$. This is critically important for understanding the nature of the phase transition between

$LiFePO_4$ and $FePO_4$ during electrochemical reactions and determining the stability of the intermediate phase at room temperature. Consequently, it is valuable to be able to support the incomplete room temperature phase diagram, and the miscibility gap model can be treated by extending the consideration of single-phase solid solutions in the $LiFePO_4$ system.

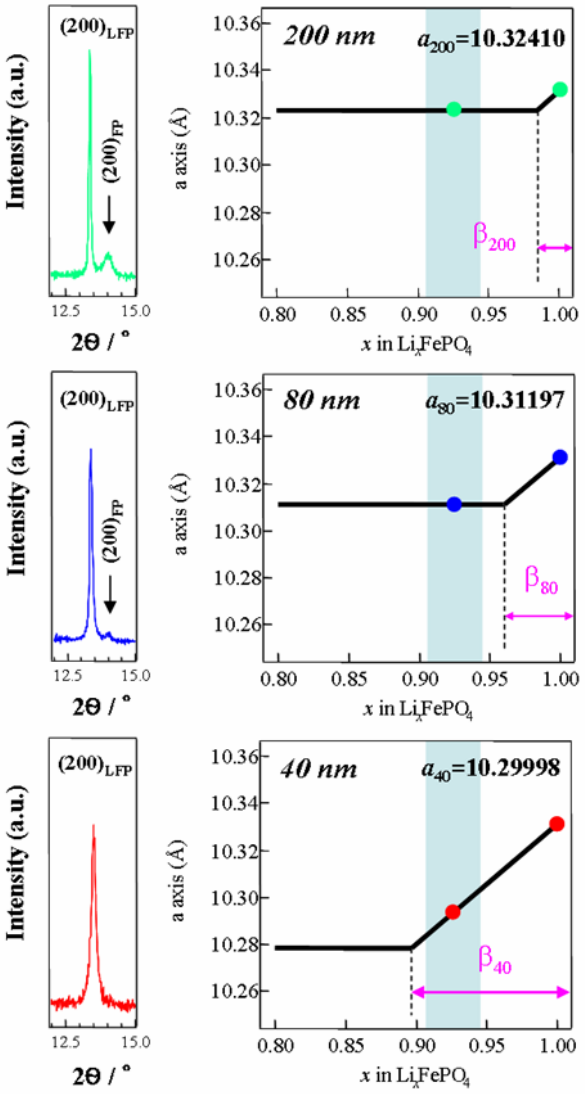

Figure 9.3: *Left: magnified view of the (200) peak correlated with different particle sizes for solid solution $Li_{0.93}FePO_4$ phase at room temperature: (a) particle size of 200 nm, (b) particle size of 80 nm, and (c) particle size of 40 nm. Right: the a-axis lattice parameter and solubility, β, as functions of the composition for different particle sizes.*

On the other hand, we also highlight the fact that the solid solubility of $Li_{1-\beta}FePO_4$ systematically increases along with the reduction in particle size. It should be noted that the particle size dependence of solid solution phases in a binary system could be explained by thermodynamic considerations and Vegard's law. The solid-solid phase transitions are thermodynamically first order and involve a change in enthalpy (ΔH), which is highly related to the particle size, as depicted by $\Delta H = \Delta H_{intinsic} + \Delta H_D$, where ΔH_D represents the particle size contribution of opposite sign.[280-281] If the particle size decreases, the Gibbs free energy (ΔG) of mixing would be decreased, resulting in extension of the single phase regions near the end members on the composition phase diagram. This relation between the solid solubility and particle size is consistent with a comparison of typical open-circuit voltage (OCV) curves versus depth of discharge (DOD) of $LiFePO_4$ as a function of particle size at room temperature, as shown in Figure 9.1. This inverse relation, moreover, give us a new insight into the strong enhancement of the electrochemical performance due to the particle size minimization. The smaller particle has a larger amount of single phase solid solution in equilibrium at room temperature, which could be directly connected to the electrochemical performance. In a two phase reaction system, expansion of the single phase region could increase the formation of a coherent interface between two separated phases, resulting in suppression of the interfacial stress at the phase boundary, because the lattice mismatch between the two separated phases becomes smaller. This has an important implication for facilitating smooth Li^+ diffusion. In practice, the lattice mismatch is gradually decreased with the growth of the single-phase solid solution form, as proved in Table 9.1.

Table 9.1: *Comparison of lattice parameters for Li_xFePO_4 (x = 0, 0.60, 0.93, 1) prepared by chemical lithiation and delithiation with different particle sizes.*

		$LiFePO_4$ phase			
Particle size (nm)	x /Li_xFePO_4	a (Å)	b (Å)	c (Å)	V (Å^3)
200	1.00	10.32845(2)	6.007381(11)	4.692470(10)	291.1534(10)
	0.93	10.32408(9)	6.00561(5)	4.69298(5)	290.976(5)
	0.60	10.32367(15)	6.00673(11)	4.69619(9)	291.218(9)
	0.00	-	-	-	-
80	1.00	10.32651(7)	6.00703(4)	4.69528(5)	291.256(4)
	0.93	10.31196(14)	6.00060(9)	4.69756(8)	290.675(8)
	0.60	10.3101(3)	6.00042(18)	4.69598(13)	290.515(15)
	0.00	-	-	-	-
40	1.00	10.32271(14)	6.00211(9)	4.69623(9)	290.969(8)
	0.93	10.2999(2)	5.99336(13)	4.70148(14)	290.231(12)
	0.60	10.2786(7)	5.9843(4)	4.7138(3)	289.94(3)
	0.00	-	-	-	-

		$FePO_4$ phase			
Particle size (nm)	x /Li_xFePO_4	a (Å)	b (Å)	c (Å)	V (Å^3)
200	1.00	-	-	-	-
	0.93	9.8599(2)	5.7677(15)	4.8487(15)	275.74(13)
	0.60	9.8272(3)	5.79682(11)	4.78243(12)	272.439(11)
	0.00	9.81622(8)	5.79096(5)	4.78400(4)	271.948(3)
80	1.00	-	-	-	-
	0.93	9.7953(11)	5.7831(10)	4.8045(3)	272.16(6)
	0.60	9.8291(4)	5.79772(15)	4.78244(16)	272.534(15)
	0.00	9.82111(12)	5.79435(7)	4.78390(6)	272.237(6)
40	1.00	-	-	-	-
	0.93	-	-	-	-
	0.60	9.8601(8)	5.8180(3)	4.7857(3)	274.53(3)
	0.00	9.82353(18)	5.799170(10)	4.785651(10)	272.631(9)

It is likely that the migration of Li^+ could be facilitated and the electronic conductivity could synergistically be improved in the single phase solid solution form, because the strain over the interface between two phases would be relaxed. Consequently, therefore, the relationship with the particle size variation is expected to be essential to understanding the room temperature kinetics of $LiFePO_4$. The isolation of a room temperature solid solution of $LiFePO_4$ gives an important indication for further improvement of Li^+ diffusivity in the $LiFePO_4$ system.

9.4. Summary

In summary, we have presented, for the first time, a direct evidence for the isolation of a single phase solid solution of Li_xFePO_4 at room temperature from high resolution synchrotron X-ray diffraction (XRD). The discovery that the single-phase solid solution region of Li_xFePO_4 is in inverse proportion to the particle size at particular compositions would be valuable for completing the currently incomplete room temperature phase diagram and miscibility gap model of $LiFePO_4$. More importantly, we suggest that the extension of the single phase region along with the particle size minimization is one of major reasons for improvement in the electrochemical performance. It is likely that the migration of Li^+ could be facilitated and the electronic conductivity would synergistically be improved in the single-phase solid solution form, because the strain over the interface between two phases would be relaxed. This study will form the basis of further investigations.

10. Air Exposure Effects on the Electrochemical Performance of $LiFePO_4$

10.1. Introduction

The lithium iron phosphate ($LiFePO_4$) is currently considered as the most promising cathode material for advanced lithium-ion batteries. The Li^+ can be reversibly extracted from the $LiFePO_4$ at a potential of 3.45 V with a very flat voltage plateau, offering a theoretical Li^+ storage capacity of 170 $mAh \cdot g^{-1}$ and high rate capability. Moreover, its non-toxicity, excellent thermal stability, safety characteristics and the high abundance of iron (Fe) are quite attractive when it is employed in the large-scale applications such as HEVs (hybrid electric vehicles) and EVs (electric vehicles).[266-267]

Much effort has been devoted to overcoming the inherently poor conductivity (10^{-9} to 10^{-10} $S \cdot cm^{-1}$) and small tap density of $LiFePO_4$, which are regarded as key barriers to its commercial use. These barriers might be induced by the fundamental olivine structure of the $LiFePO_4$, which belongs to the space group *Pmna,* because of the combination of strong ionicity and the strong bonding in the $(PO_4)^{3-}$ phosphate anions of $LiFePO_4$.[268-269] These drawbacks could be effectively diminished by doping with supervalent cations, the addition of conductive carbon, and particle size minimization, allowing development to move forward.[147-152] One of the important objectives of $LiFePO_4$ technology is to identify the precise aging mechanism, based on a comprehensive understanding of its fundamental properties, before it can be deployed in

practical applications. For this reason, numerous research efforts have been generating great debates on the Li^+ insertion and extraction mechanisms coupled with the interface kinetics in the $LiFePO_4$ system.[269-276] The stability of $LiFePO_4$ is also under extensive review as a central issue in this technology, which is directly related to the safety problems. W. Porcher et al. have discussed the influence of water contact on the electrochemical performance of $LiFePO_4$ in their recent work.[282] In parallel with their work, we have also investigated the effects of air contact. Both studies sould be able to address the aging mechanism together with the safety issues of $LiFePO_4$ in certain environments.[283] However, there is a strong need for further investigation in order to identify the factors involved in the undesirable aging problems of $LiFePO_4$.

Herein, we carefully emphasize the identification of possible side reactions induced by air exposure at elevated temperatures during materials synthesis and evaluation process. We provide direct evidence for spontaneous Li^+ extraction, accompanied by the formation of disordered phases and structural changes in $LiFePO_4$ at different temperatures, to prove its thermal stability under air atmosphere. It should be noted that air exposure at high temperature would cause significant changes in the surface and bulk properties of $LiFePO_4$, resulting in degradation of its electrochemical performance. We also would like to highlight useful information on materials treatment or storage conditions to avoid undesirable side effects.

10.2. Experimental

10.2.1. Synthesis of $LiFePO_4$

$LiFePO_4$/C nanocomposites with a particle size of 80 nm were synthesized by a solid state reaction without any air contact. A stoichiometric amount of lithium carbonate Li_2CO_3 (Wako,

99%), iron (II) oxalate dihydrate Fe(II)$C_2O_4.2H_2O$ (Aldrich, 99%) and diammonium hydrogen phosphate $(NH_4)_2HPO_4$ (Wako, 99%) were employed as starting materials. 10 wt% of Ketjen Black (Lion, ECP) was added and the mixture was thoroughly mixed and ground by a conventional planetary milling apparatus (ITOH LA-PO4) for 24 hours. The sintering was conducted using a sealed tube furnace at 600 ºC for 6 hours under Ar gas flow to form $LiFePO_4$/C nanocomposites without sacrificing purity. The sealed tube furnace permits us to avoid any contact with atmosphere during the synthesis, and the transfer into/from the glove box that was used is shown in Figure 10.1.

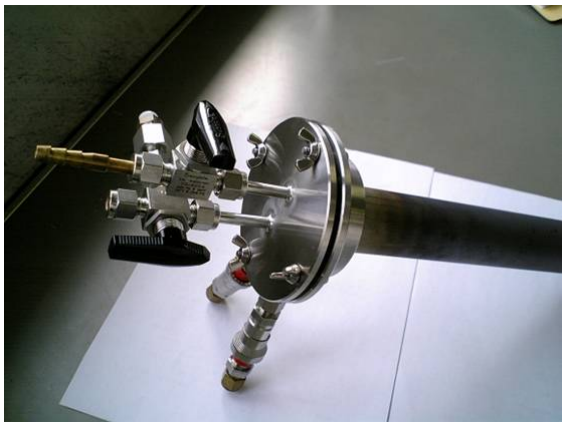

Figure 10.1: *An image of the sealed tube furnace, which allow no contact with air over the whole procedure in this work.*

The $LiFePO_4$/C nanocomposites were exposed to an air atmosphere at various exposure temperatures, which were systematically varied from 30 °C to 240 °C. For comparative purposes, the total exposure time was fixed at 36 hours, and the temperature was gradually increased step by step with a dwell time of 4 hours and a step size of 30 °C at the same heating rate to prevent thermal shock to the materials. The exposure treatments in air were conducted in a tube furnace. The $LiFePO_4$ powders were placed in an alumina boat and then loaded into the

middle of the furnace, the highest temperature region. During the treatment the stainless steel caps were kept open to allow air into the furnace.

10.2.2. Structural Characterization

X-ray diffraction analysis was performed using a Co K_α diffractometer (BRUKER AXS K. K., D8 ADVANCE) with Bragg Brentano geometry, and Rietveld refinement was carried out with TOPAS software. A sealed sample stage was used for measurements under He atmosphere. The Mössbauer spectra were measured with a Topologic System Inc. spectrometer using a ^{57}Co γ-ray source and calibrated with α-Fe as a standard. The model fitting was performed with Mosswin ver. 3.0 software. The samples were sealed between plastic sheets to avoid contact with atmosphere during the measurements. The morphology and microstructure of air-exposed $LiFePO_4$ at different temperatures were identified by field emission scanning electron microscopy (FESEM). A Nicolet 5700 spectrometer was used to collect fourier transform infrared (FTIR) transmittance spectra. The samples were palletized with KBr and the spectra were recorded at room temperature in the spectral range of 650 to 4000 cm^{-1}. X-ray photoelectron spectroscopy (physical electronics instruments, Quantum 2000 Spectrometer) using monochromatic Al $K\alpha$ (1486.6 eV) radiation was used to analyze the chemical binding energy of the samples. The C 1s (285 eV) was a reference for colleted data. The X-ray absorption measurements using the X-ray absorption near edge spectroscopy (XANES) and the extended X-ray absorption fine-structure spectroscopy (EXAFS) technique, were performed on the BL7C1 beam line of the Pohang Light Source (PLS) with a ring current of 120-170 mA at 2.5 GeV. A Si(111) double-crystal monochromator was employed to monochromatize the X-ray photon energy.

10.2.3. Electrochemical Characterization

Half cells (CR2032 coin-type) were fabricated to evaluate the electrochemical performance of air-exposed $LiFePO_4$. The assembly was carried out in an Ar-filled glove box with less than 0.1 ppm of moisture. Li metal foil was used as the counter and reference electrode, and 1M $LiPF_6$ dissolved in a 3:7 (by volume, Tomiyama Chemicals) mixture of ethylene carbonate (EC) and diethyl carbonate (DEC) was employed as the electrolyte. A porous polypropylene film was used as the separator. The working electrode was formulated with 90 wt % active materials and 10 wt % polytetrafluoroethylene (PTFE) binder without any solvent. The obtained cathode sheet was dried at 120 ºC under vacuum overnight. The sheet was then pressed onto aluminum mesh to form a disk 16 mm in diameter in a glove box. The cells were galvanostatically charged and discharged over the potential range of 2.0 V to 4.5 V at the C/20 rate.

10.3. Results and Discussion

Spontaneous Li^+ extraction from the olivine host structure when the $LiFePO_4$/C nanocomposite was exposed to air even at room temperature has been reported in our previous work, allowing the significant initial capacity loss.[283] This undesirable side reaction might be facilitated at higher temperature and longer exposure time. These findings arouse our further interest in the structural stability and surface chemistry of $LiFePO_4$ related to the air contact at different treatment temperatures. The identification of the Li^+ extraction mechanism from $LiFePO_4$ under air atmosphere is essential for understanding the aging mechanism and thermal stability of $LiFePO_4$. In addition, it also could provide further information to support an incomplete binary phase diagram of $LiFePO_4$ system.

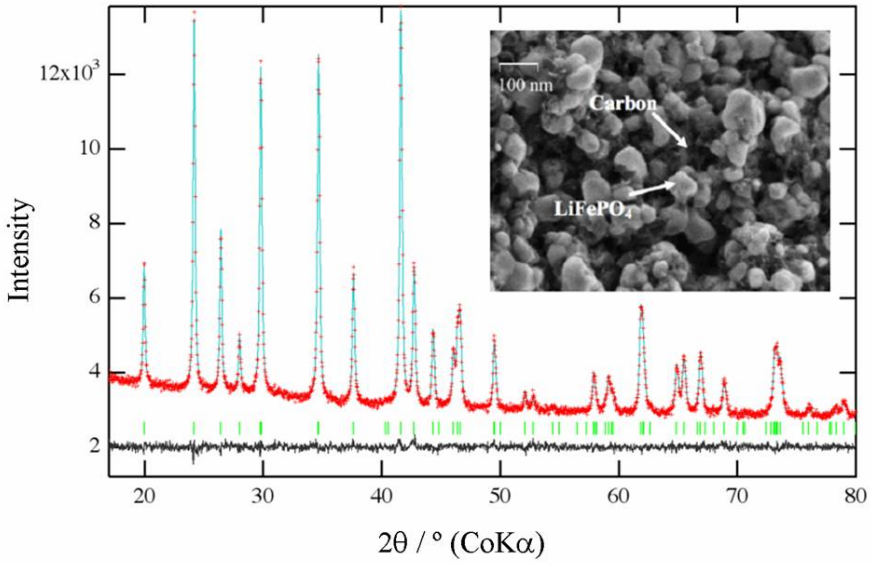

Figure 10.2: *XRD pattern and SEM image (inset) of $LiFePO_4$/C nanocomposite synthesized by solid state reaction without air contact.*

The phase purity of the $LiFePO_4$/C nanocomposite synthesized by solid state reaction without air contact was checked by powder X-ray diffraction (XRD). It confirms that all reflections correspond to the ordered olivine structure of $LiFePO_4$ indexed to the orthorhombic *Pnma* space group. There is small peak broadening at the low diffraction angle, which is a general characteristic of nanocomposites containing C phase, and no impurity phase can be detected. The morphology of the nanocomposite was observed using a field emission scanning electron microscope (FESEM). The Rietveld refinement and FESEM analysis permit us to identify the olivine crystallite size as approximately 75 nm and the particles are near-spherical in the carbon network as shown in Figure 10.2.

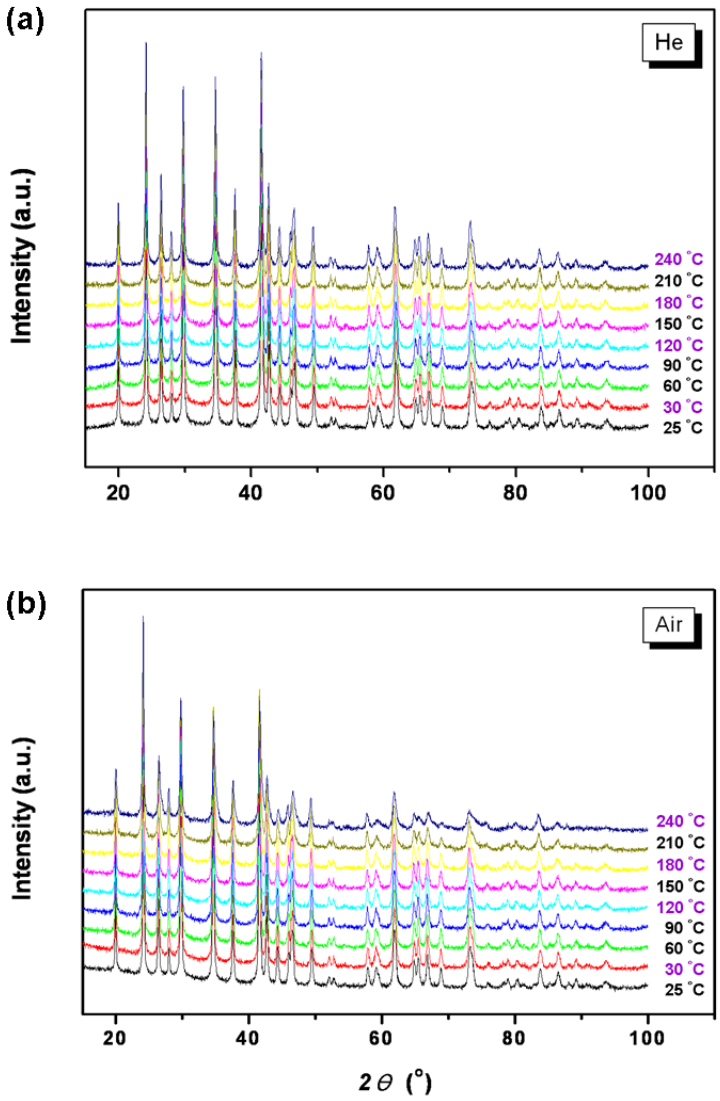

Figure 10.3: *XRD patterns for $LiFePO_4$/C nanocomposites exposed from 25 ˚C to 240 ˚C to different atmosphere: (a) Air and (b) He. The exposure time was fixed at 36 hours.*

As a prelude to an investigation of air exposure effects on the electrochemical and structural characteristics of $LiFePO_4$ at various temperatures, systematic high-temperature (HT) XRD analysis was performed across $LiFePO_4$/C nanocomposites exposed to the different atmospheres, air and helium (He), at elevated temperatures from 25 ˚C to 240 ˚C, as shown in Figure 10.3. In

order to separate out the influence of the intrinsic thermal expansion of the materials at high temperature, we employed He atmosphere as a reference. From the series of diffraction patterns, it is obvious that there was no detectable secondary phase formation or variation in peak intensity over the whole temperature range under He atmosphere. In contrast, a progressive peak-broadening together with the changes of peak intensity and asymmetry of reflections were observed along with the increase of treatment temperature under air, which might be caused by either the formation of disordered phases or structural deformation of olivine structure. Unfortunately, we can not detect any direct evidence for the formation of impurity phase from the XRD patterns during air exposure. It seems that some disordered phases might be formed by side reactions between $LiFePO_4$ and air, leading to the peak broadening under air atmosphere. These reactions, more importantly, could be systematically facilitated by an increase in treatment temperature. However, it is still unsure whether the peak broadening resulted from the formation of disordered phase or the structural changes during air exposure. There is a strong need to clarify the reason for obvious changes under air atmosphere in the XRD patterns.

For further inspection of the surface of the $LiFePO_4$ after the air exposure treatment, the morphologies of $LiFePO_4$/C nanocomposites exposed to air at different temperatures were characterized by FESEM. Figure 10.4 shows FESEM images of $LiFePO_4$/C nanocomposites exposed to air at 30 ˚C, 120 ˚C, 180 ˚C, and 240 ˚C, respectively. We found that there were no visible differences in the morphology of air exposed $LiFePO_4$/C nanocomposites subjected to different temperatures.

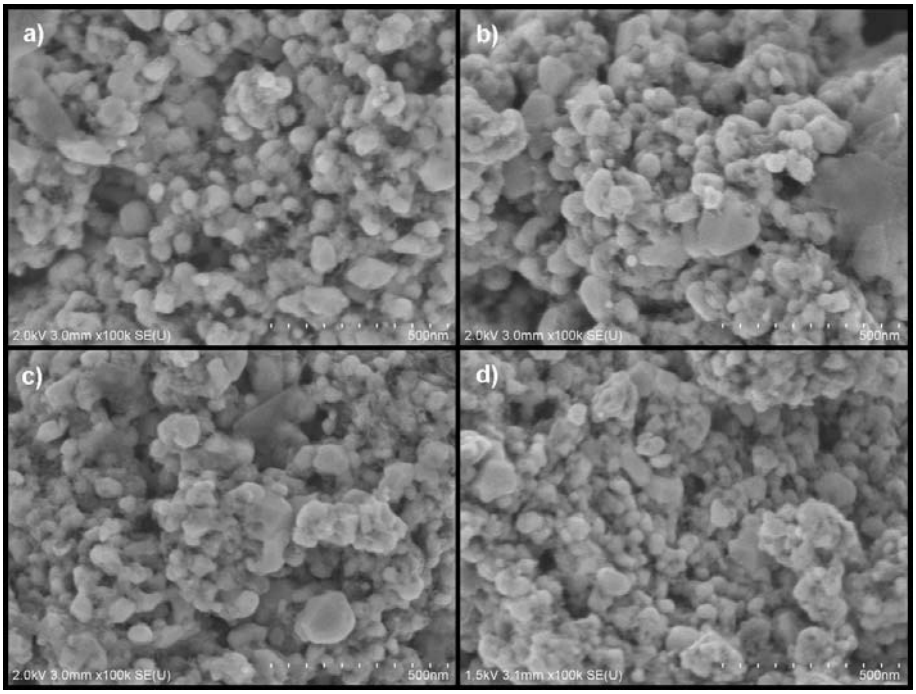

Figure 10.4: *FESEM images of the air-exposed $LiFePO_4$/C nanocomposites at different temperatures: a) 30 ˚C, b) 120 ˚C, c) 180 ˚C, and d) 240 ˚C.*

For comparative purposes, the lattice parameters and unit-cell volume of $LiFePO_4$/C nanocomposites exposed to air and He as a function of temperature were carefully refined by the use of an orthorhombic structure, which belongs to the space group *Pnma.* The refined results on the $LiFePO_4$/C nanocomposites exposed to the different atmospheres were compared in Figure 10.5 and are summarized in Table 10.1. From the comparison, we found that all lattice parameters and the unit-cell volume were gradually increased in the $LiFePO_4$/C nanocomposite treated under He atmosphere, which might be due to the thermal expansion of the unit cell in the olivine structure. In contrast, more interestingly, $LiFePO_4$/C nanocomposite exposed to air shows different behavior. The lattice parameters of *a* and *b* abruptly decreased with increasing treatment temperature under air, whereas differences in the *c* lattice parameter were very small.

The unit-cell volume also systematically decreased, corresponding to all the lattice parameter variations. These results reveal that the side reaction which occurred during air contact is likely to be related to the *a*-axis and the *b*-axis of the olivine structure. These results are in a good accordance with our previous suggestion that Li^+ could be extracted from the host materials, leading to the reduction of lattice parameters *a* and *b*. This phenomenon is somewhat consistent with the electrochemical de-lithiation process of $LiFePO_4$, in that small shrinkages of the *a*-axis and *b*-axis parameters were observed in the intermediate $Li_{1-x}FePO_4$ phase after electrochemical Li^+ extraction.[283]

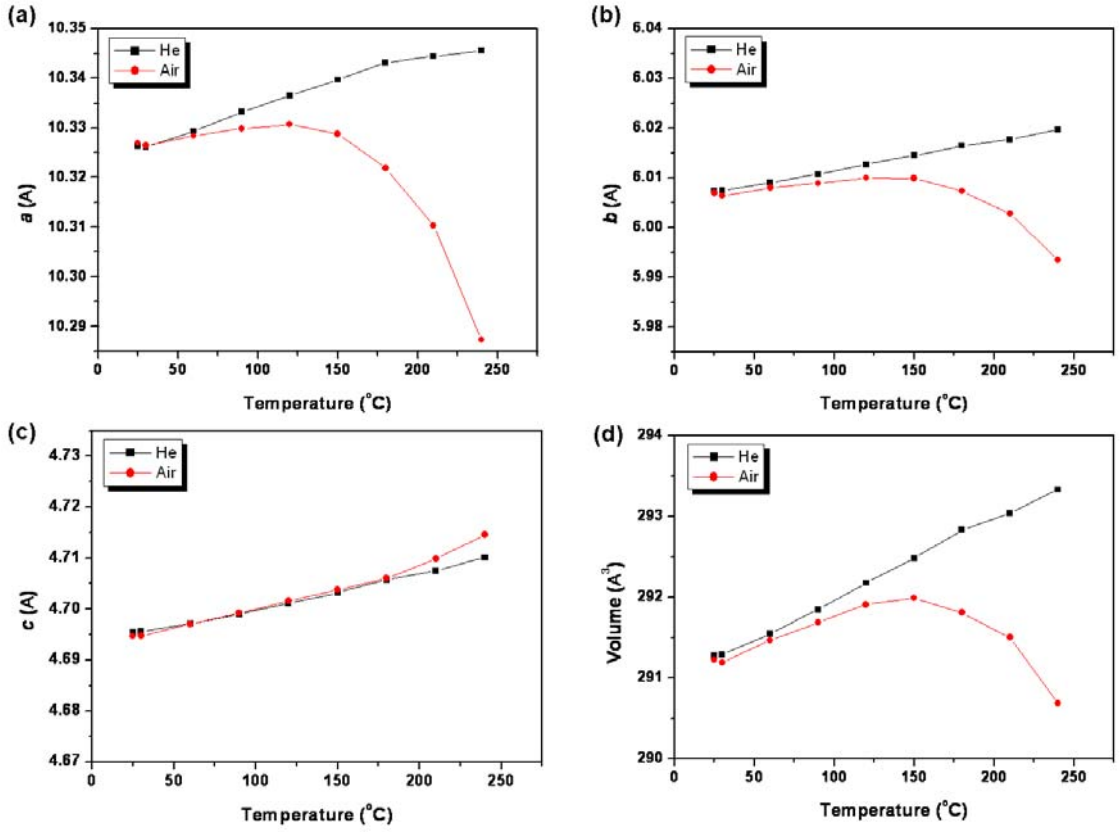

Figure 10.5: *Comparison of lattice parameters of $LiFePO_4$/C nanocomposites as a function of exposure temperatures under the air and He. The variations are shown in (a) lattice parameter a, (b) lattice parameter b, (c) lattice parameter c, and (d) the unit-cell volume in the $LiFePO_4$/C nanocomposites.*

We suggest that there is only Li^+ extraction from $LiFePO_4$ without any structural change of the host material under air atmosphere until 120 ˚C and that the Li^+ extraction can be facilitated by increasing the temperature. However, it should be noted that this hypothesis is valid for the samples treated under 120 ˚C. The discrepancy in lattice parameters *a* and *b* between the samples exposed to the different atmospheres obviously increased above 120 ˚C. Finally, it can be seen clearly that all lattice parameters were significantly reduced after treatment at 240 ˚C, which is a clear evidence of the structural change in $LiFePO_4$ system. In addition, the reduction of the *c* lattice parameter was observed after the 180 ˚C treatment under air atmosphere, which seems to indicate that other side reactions related to the structural changes of $LiFePO_4$ could take place over this temperature, because the change of *c*-axis parameter could be negligible during the electrochemical Li^+ extraction in the $LiFePO_4$ system. This point will be discussed together with the electrochemical results later.

Now, we are interested in determining the components which are involved in the side reactions causing peak broadening, as mentioned above. The components can be distinguished more precisely by a comparison of the lattice parameter changes between $LiFePO_4$ and $FePO_4$ on exposure to air. In the same way, the carefully refined lattice parameters of both phases are plotted in Figure 10.6. Unlike $LiFePO_4$, the lattice parameters and unit-cell volumes of the $FePO_4$ exposed to air were gradually increased by thermal expansion at each temperature stage. This means that there is no structural change of $FePO_4$ caused by the side reactions with air contact. According to these results, we note that the major reasons for the variations in lattice parameters would be related to the oxidation of Fe^{2+} and extraction of Li^+ in the $LiFePO_4$ system. Moreover, this observation can be thought to be consistent with increase of solid solubility along with temperature increase in a binary phase diagram between $LiFePO_4$ and $FePO_4$.

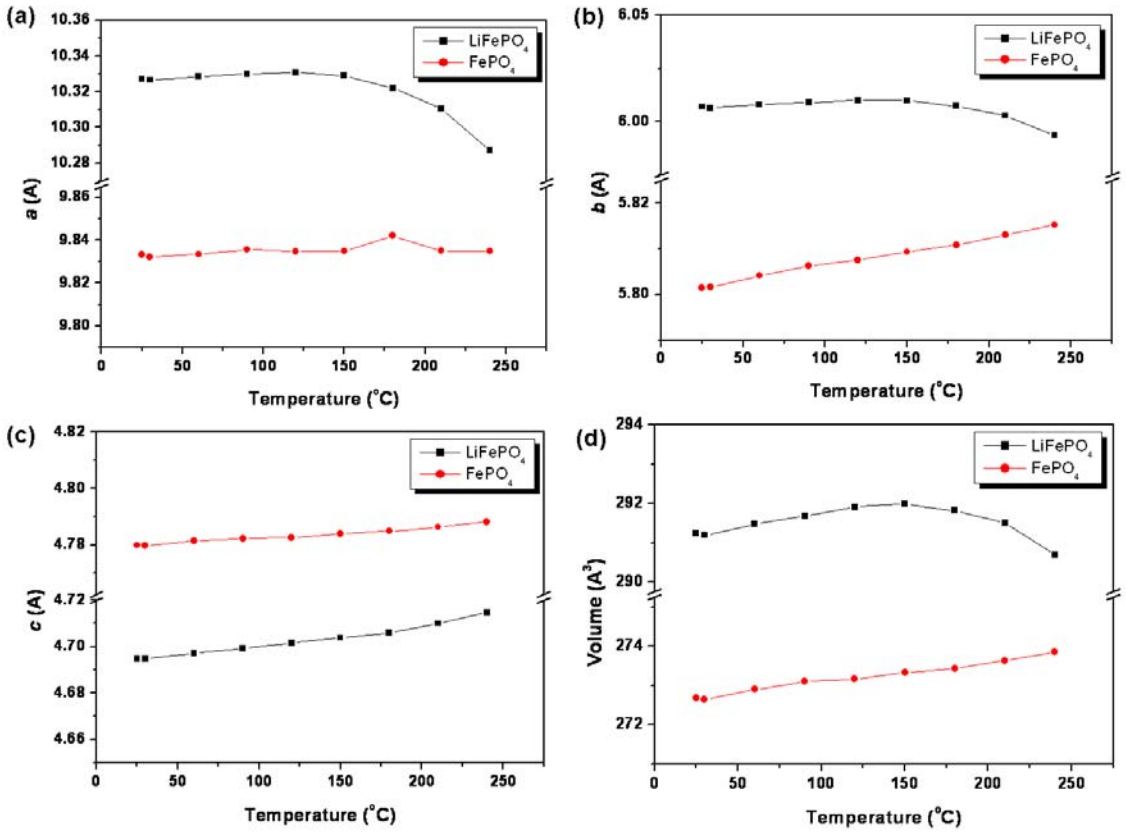

Figure 10.6: *Comparison of lattice parameters of $LiFePO_4$ and $FePO_4$ as a function of exposure temperatures under the air. The variations are shown in (a) lattice parameter a, (b) lattice parameter b, (c) lattice parameter c, and (d) the unit-cell volume in the $LiFePO_4$.*

At this point, mössbauer analysis was carried out at room temperature in order to clarify the evolution of the Fe ions to the side reactions during air exposure at different temperature. Figure 10.7 gives a comparison of the mössbauer spectra for $LiFePO_4$/C nanocomposites after air exposure treatment at different temperatures. The spectra can be fitted with two sub-spectra, indicating the magnetic order arrangement of the Fe ions. The Fe ions are mainly in the Fe^{2+} form (QS = 2.97 mm·s^{-1} and IS = 1.11 mm·s^{-1}) and 9.3% of Fe^{3+} form (QS = 0.83 mm·s^{-1} and IS = 0.35 mm·s^{-1}) could be found in the spectra in the $LiFePO_4$/C nanocomposite after air exposure at 30 ˚C. The trivalent doublet corresponding to Fe^{3+} is increased in proportion to the

temperature rise. The oxidation of Fe^{2+} to Fe^{3+} can be evaluated at 12.7% of the total Fe content for the samples exposed to air at 120 ˚C. This phenomenon is also consistent with $Li_{1-x}FePO_4$ intermediate phase with a Li^+ deficiency, which should contain a corresponding amount of Fe^{3+}. The spectrum recorded after air exposure at 180 ˚C indicates that 49.6% of Fe^{2+} could be oxidized to Fe^{3+}. More interestingly, additional magnetism with a content of 18.8% is clearly detected together with 69.0% of Fe^{3+} content in the sample after 240 ˚C treatment. This additional spectrum is very similar to that obtained from the α-Fe_2O_3 with a six-line hyperfine spectrum (IS = 0.37 mm·s^{-1}).[284,285]

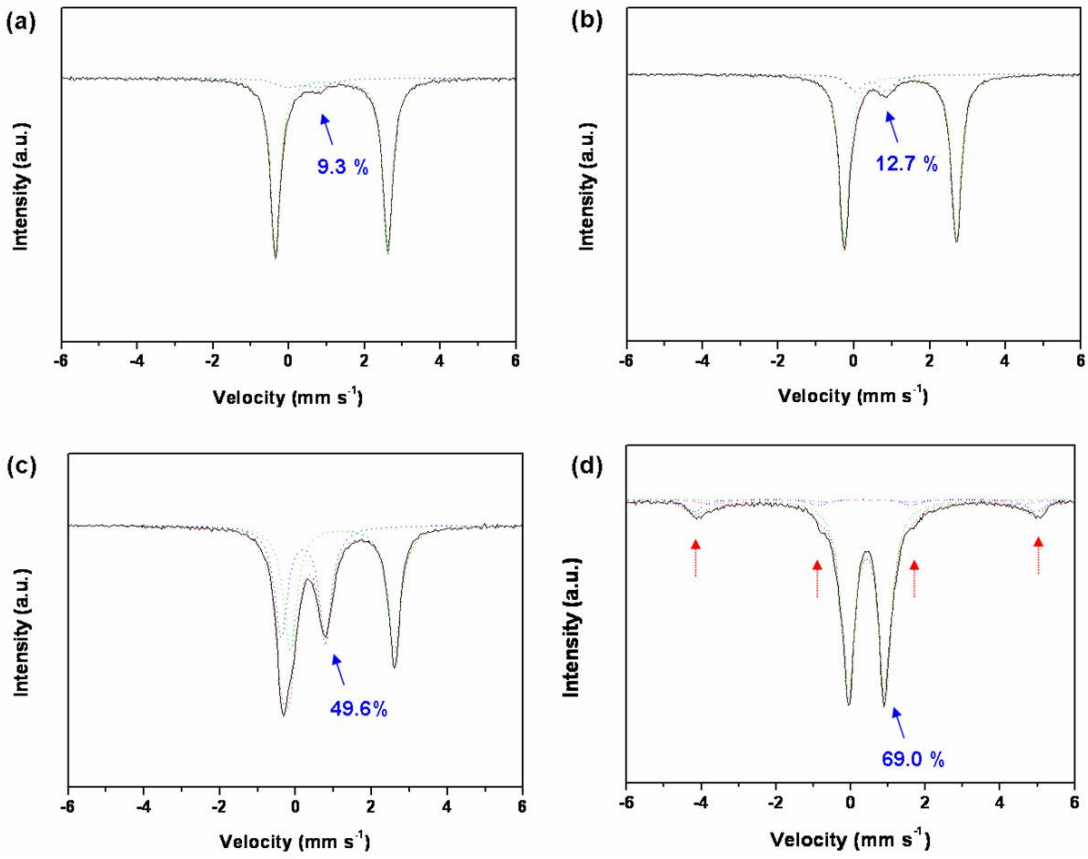

Figure 10.7: *Mössbauer spectra of the $LiFePO_4$/C nanocomposites exposed to air at different atmospheres; (a) 30 ˚C, (b) 120 ˚C, (c) 180 ˚C, and (d) 240 ˚C.*

Based on the mössbauer spectra, we can carefully come to conclusion that disordered α-Fe_2O_3 phase could be formed during air exposure at high temperature. On the other hand, significant Li^+ extraction was observed, even at 30°C, which means that Li^+ extraction might be a spontaneous reaction under air atmosphere, and temperature could facilitate this reaction. We also highlight the fact that the Fe^{3+} in $LiFePO_4$ systematically increased as the treatment temperature increased. It should be noted that the temperature dependence of Fe^{3+} in the $LiFePO_4$ system could be explained by an increase in the oxidation of Fe ions by air contact. The oxidation of Fe ions could be directly involved with side reactions generated during air exposure.

Indirectly, we performed X-ray photoelectron spectroscopy (XPS) to analyze the chemical environment variation of all components in $LiFePO_4$/C nanocompsites after air exposure as given in Figure 10.8. To allow and assess the relative surface changes of species in $LiFePO_4$/C nanocomposite due to the air exposure, Fe $2p_{1/2}$, Fe $2p_{3/2}$, P 2p, O 1s and C 1s spectra are measured for the samples treated at different temperatures. For the sample exposed to air at 30 °C, the Fe $3p_{3/2}$ XPS core level presents one component at ~710.7 eV assigned to Fe^{2+}. We note the presence of a shoulder at lower binding energies that could be attributed to reduced Fe ions or Fe^{2+} in different local environment.[286] After air exposure treatment, we found a shift toward higher binding energies due to the partial oxidation of Fe^{2+} to Fe^{3+}. But, the presence of FeO(OH) group cannot be excluded in this spectra. The P 2p peak located at 134.1 eV is the signature of the phosphate species $(PO_4)^{3-}$. After air exposure treatment, the P 2p peak shift slowly to lower binding energy. This can be attributed to a change in the PO_4 tetrahedral structure due to a change in the local electronic structure of iron ions. After air exposure, the O 1s peak shows the presence of a shoulder in the lower binding energy side due to the presence of

different oxidation state of iron and the local change in the tetrahedral PO_4 environment in the samples treated at 180 ˚C and 240 ˚C.[286] Only the contamination carbon and some carbon oxide are present on the surface of the sample. The samples treated at 30 ˚C show an asymmetry toward lower binding energies due to some charge effect on the surface of the material. Consequently, the XPS spectra reveal that the formation of disordered phases related to the iron oxides was occurred at the surface of materials due to air exposure at high temperature.

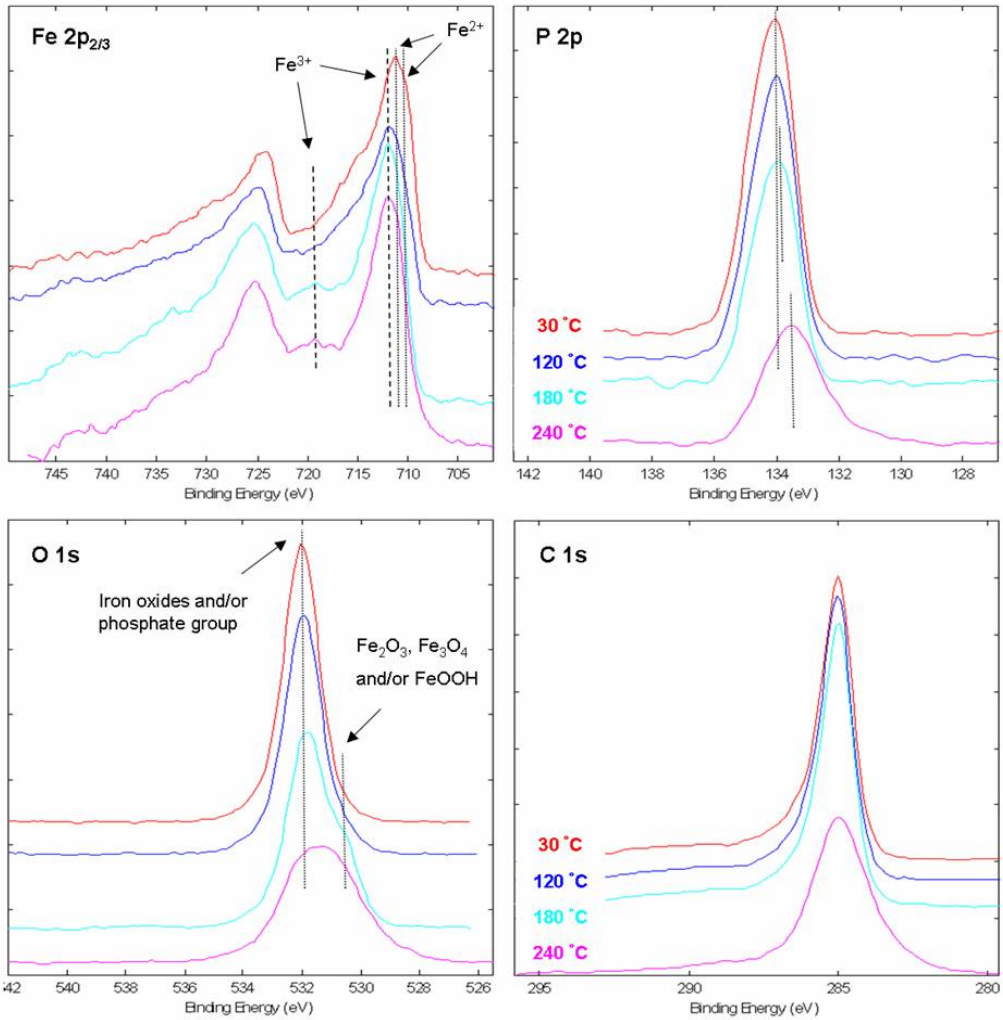

Figure 10.8: *X-ray photoelectron spectroscopy (XPS) profiles of the $LiFePO_4$/C nanocomposites after different temperatures of air exposure.*

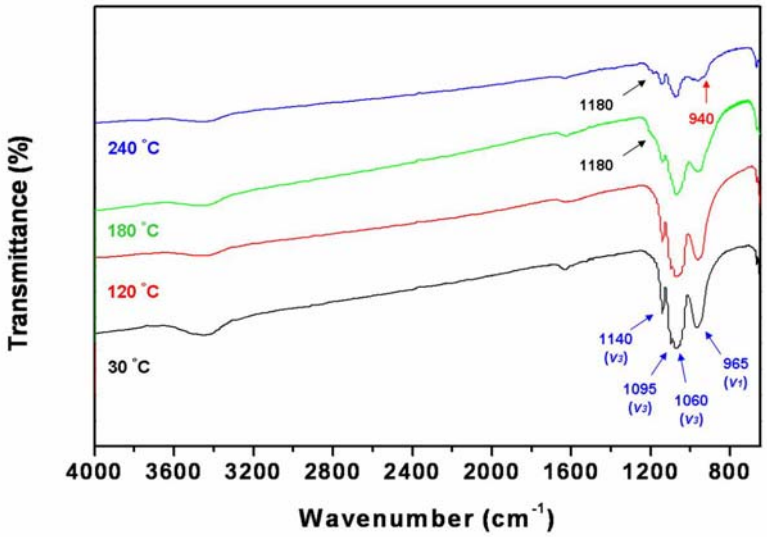

Figure 10.9: *Fourier transform infrared (FTIR) spectra of the $LiFePO_4$/C nanocomposites exposed to air at different atmospheres; (a) 30 ˚C, (b) 120 ˚C, (c) 180 ˚C, and (d) 240 ˚C.*

The fourier transform infrared (FTIR) spectra give us more precise evidence for the formation of disordered phases after air exposure at high temperature treatment. The fundamental $(PO_4)^{3-}$ stretching modes (v_1 and v_3) are observed in the FTIR spectra of air exposed $LiFePO_4$/C nanocomposites as shown in Figure 10.9. Considering a fact that v_1 and v_3 vibration modes involve the symmetry and asymmetry of the P-O bond, the decrease of IR intensity could be associated with change dipole moments derivatives due to a decreasing of Li^+ coordinated to O atoms of $(PO_4)^{3-}$. In order to investigate the change of the phosphate framework vibrations to lithium extraction, the bending mode (v_1 and v_3) at low frequencies could be excluded in this work because these modes are strongly coupled and involve some Li^+ motion in this system. Many of the bands in the FTIR spectra do not shift after air exposure treatment at different temperature. There are a few difference between the spectra present here that the intensity of the

bands decreases as the treatment temperature rise. A new band at 1180 cm^{-1}, corresponding to the formation of $Li_3Fe_2(PO_4)_3$ phase and an unknown band at 940 cm^{-1} are clearly observed after air exposure at 240 °C.[287,289]

Synchrotron X-ray absorption spectroscopy is a very effective technique to investigate the change of $(PO_4)^{3-}$ polyhedron and Fe oxidation states after the air exposure of $LiFePO_4$/C nanocomposites. X-ray absorption near edge spectroscopy (XANES) and extended X-ray absorption fine-structure spectroscopy (EXAFS) can clearly reveal the details of the local coordination, and the site symmetry, oxidation state, and bond character around the element of interest. Hence, XANES and EXAFS data were collected to investigate the neighboring structure around the Fe ion in $LiFePO_4$. Normalized XANES spectra are shown in Figure 10.10a. They show a rather strong shift of the main edge (Fe 1s → 4p transition, white line) after air exposure at 240 °C, which is mainly due to the change in the valence state of the Fe ion. Because the 1s electron of a highly oxidized element tends to be more strongly bonded to the nucleus than that of a less oxidized element, the air exposure at 240 °C seems to make the Fe ion more oxidized. A comparison between an appropriate model compound with well-defined oxidation and coordination states, α-Fe_2O_3, and $LiFePO_4$ that was air-exposed at 240 °C tells us that the oxidation state of the Fe ion changed from +2 to +3 after air exposure at 240 °C. (Position of white line peak: 7133.5 eV ($LiFePO_4$ air-exposed at 240 °C), 7133.6 eV (α-Fe_2O_3)).[290] Figure 10.10b shows the dipole forbidden pre-edge transitions attributed to the Fe 1s → 3d bands. The trend in the position of the pre-edge peak was very much in accordance with that observed for the white line peak. The pre-edge peak position (7112.4 eV) of $LiFePO_4$, which was exposed to air between 30 °C and 180 °C, are the same as that (7112.8 eV) of a representative ferrous compound, $FeCp_2$, whereas the pre-edge peak position (7114.4 eV) of

$LiFePO_4$ that was exposed to air at 240 °C is very similar to those of ferric compounds such as α-Fe_2O_3 (7114.4 eV), $Fe(acac)_3$ (7114.9 eV), and $FePO_4$ (7114.1 eV).[290] Even if the accurate edge position of an element is also defined by the coordination ligands and the local symmetry around it, the main underlying factor which determines the energy required to induce the photoelectric effect on the 1s electron is the oxidation state of the element. Hence, it is clear that the oxidation state of the Fe ion changed into +3 after air exposure at 240 °C. In order to observe the details of the Fe 3d states, the second derivative of the normalized absorption was plotted against the photon energy in Figure 10.10c. Here, we could observe a splitting induced by the coordinating oxygen atoms. This is because the ligand field from the phosphate oxygen atoms, which are octahedrally coordinated to the Fe, splits the 3d states of the Fe ion into t_{2g} and e_g states. The energy difference in the samples exposed to air between 30 °C and 180 °C was 2 eV, which is the previously observed difference between the t_{2g} and e_g states for octahedrally coordinated transition metal compounds.[291] Although the sample exposed at 240 °C maintained the octahedral oxygen symmetry, the energy difference between the t_{2g} and e_g states was increased above 3 eV. When the Fe sites are in an approximately octahedral environment, the O^{2-} ions split the 3d states into t_{2g} and e_g states, and the Fermi level lies in the Fe 3d states. So, the enhanced interaction of the O 2p and Fe 3d orbitals can easily cause further splitting between t_{2g} and e_g states. Considering that a deviation from octahedral symmetry tends to augment the degree of mixing between O 2p and Fe 3d, it could be alleged that the sample exposed to air at 240 °C underwent a serious lattice distortion. The relatively large intensity in the pre-edge peak of the sample exposed to air at 240 °C (Figure 10.10b) could be another proof of the lattice distortion resulting from the enhanced interaction between O 2p and Fe 3d. This is because the mixing of the O 2p and the Fe 3d orbitals increases the transition probability of the 1s → 3d transition. Figure 10.10d shows the corresponding radial structure function as a

function of the interatomic distance, which was obtained by Fourier transformation of the k^3-weighted [$k^3\chi(k)$] Fe EXAFS. From the previous reports [290,291], it could be known that the first, second, and third peaks from the left correspond to the Fe-O bond, the Fe-P bond and the Fe-Fe bond, respectively.

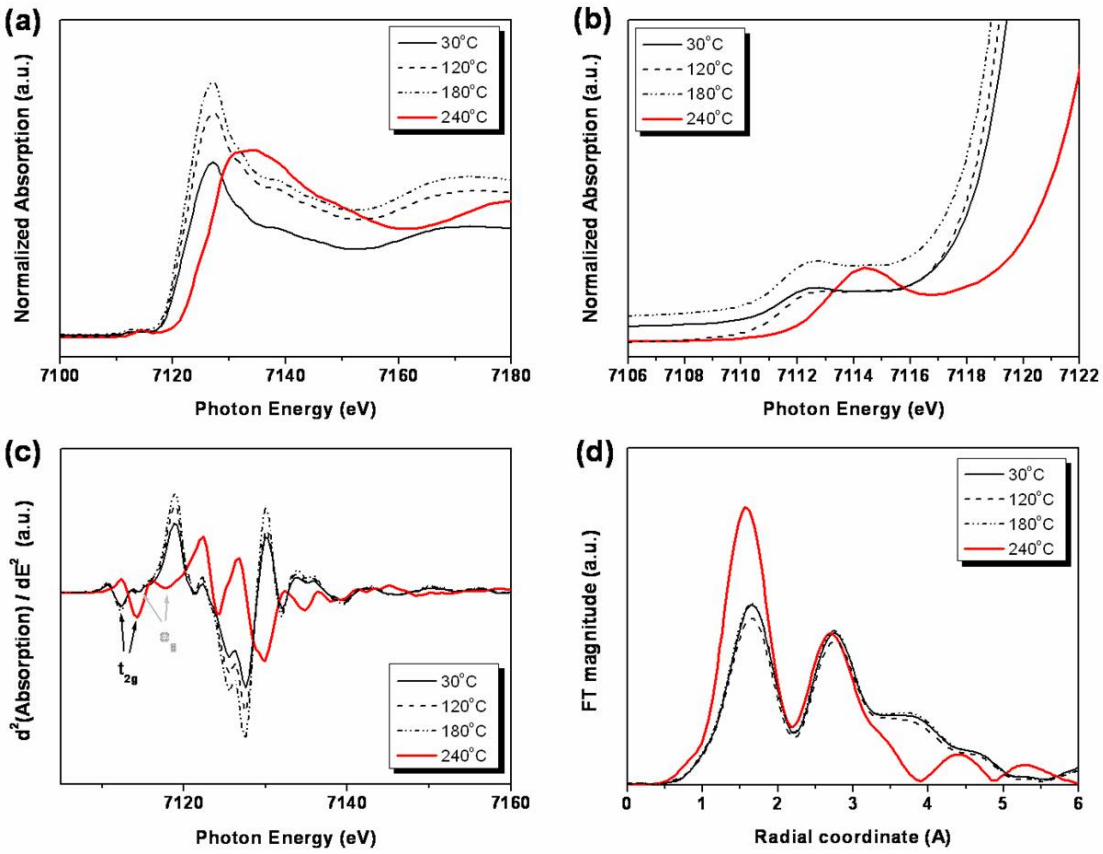

Figure 10.10: *(a) Calibrated and normalized XANES (X-ray Absorption Near Edge Spectroscopy) data at Fe K-edge of $LiFePO_4$ after air exposure at various temperatures, (b) The enlarged pre-edge region of XANES at the Fe K-edge (c) d^2(Absorption)/dE^2 vs. E (Photon Energy) plot, which shows the t_{2g} and e_g absorption bands. (d) Comparison of the radial distribution function obtained after Fourier transformation of k^3-weighted [$k^3\chi(k)$] Fe EXAFS data on $LiFePO_4$ after air exposure at various temperatures.*

Quantitative analysis was only conducted on the first peak in the radial structure function

between R = 0.5 and 2.2 Å. The Fe-O interatomic distances shown in Table 10.2a were obtained from the Free Energy Force Field (FEFF) fit analysis for each sample. The Fe-O interatomic distance obtained from X-ray Rietveld analysis (Table 10.2b) was in a good agreement with the data from EXAFS. Here, an interesting point is that the Fe-O distance continuously diminished after undergoing a slight increase when the exposure temperature was increased from 30 °C to 120 °C. This slight increase could be explained by the delithiation from $LiFePO_4$, while the shrinkage of the Fe-O distance between 180 °C and 240 °C reveals the structural changes expected from the other characterizations. Finally, together with the perfect accordance of the XANES peak position between α-Fe_2O_3 and $LiFePO_4$ that was exposed to air at 240 °C, the clear separation of the third peak may mean that a significant amount of α-Fe_2O_3 phase was evolved as a result of air exposure at 240 °C. These results agree well with the existence of additional ferromagnetism regarded to α-Fe_2O_3 phase in the mössbauer spectra and changes of binding energies in the XPS profiles as mentioned above.

The significant influence of air exposure on the electrochemical performance of $LiFePO_4$/C nanocomposites was systematically evaluated, as shown in Figure 10.11 and Figure 10.12. For electrochemical measurements, cells were carefully assembled using active materials and PTFE binders without any solvent to minimize other side effects in this work. Only a small amount of Li^+ extraction at the first charge was observed for the sample exposed to air at 30 ˚C. The initial capacity loss was recovered after the second cycle. After air exposure at 120 ˚C, a small amount of polarization occurred, and the amount of Li^+ extraction increased, but the extracted Li^+ could not be fully recovered in the subsequent cycles, leading to the reduction of reversible capacity and cyclic retention after the 10th cycle. It was further demonstrated that undesirable Li^+ loss could be occurred during air exposure at high temperature because surface or bulk properties of

the $LiFePO_4$/C nanocomposites could be changed by the formation of disordered phases or structural failure during air exposure at this temperature.

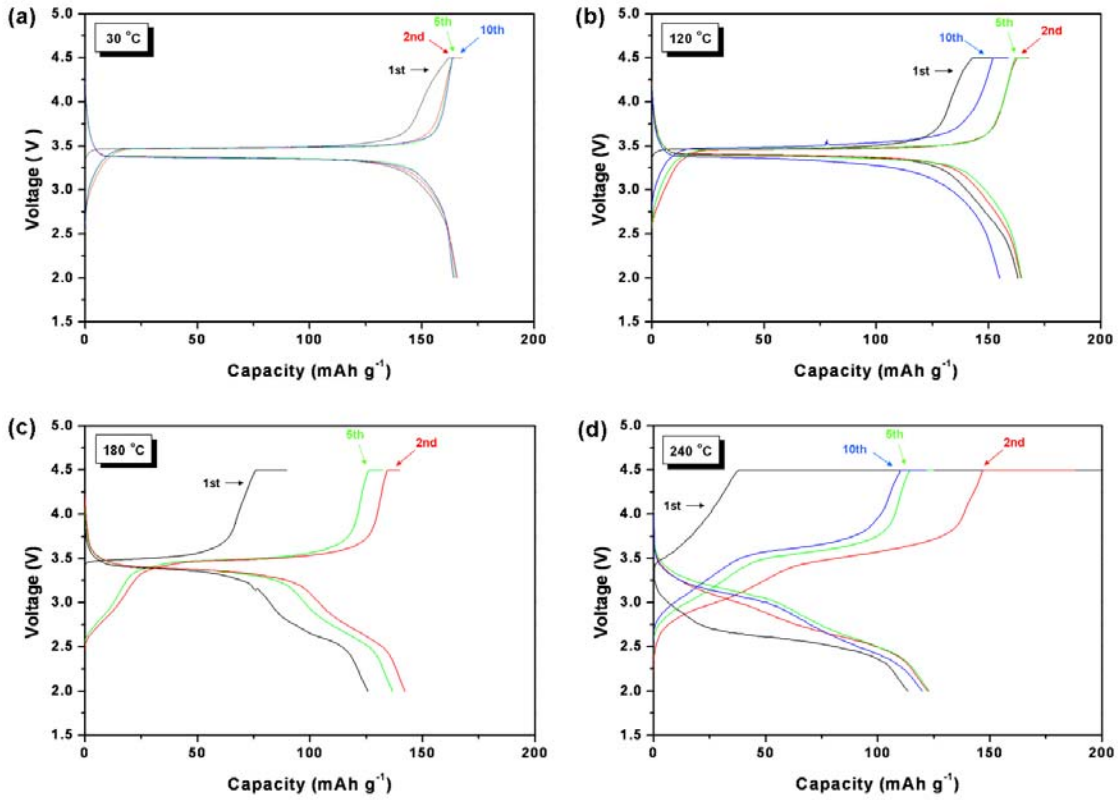

Figure 10.11: *Charge-discharge profiles of the $LiFePO_4$/C nanocomposites exposed to air at different temperature: (a) 30 ˚C, (b) 120 ˚C, (c) 180 ˚C, and (d) 240 ˚C.*

. After heat treatment at 180 ˚C under air atmosphere, the electrochemical charge-discharge profile of $LiFePO_4$/C nanocomposites changed significantly. These results are in good agreement with lattice parameter variations due to the oxidation of Fe ions, as mentioned above. The polarization during Li^+ insertion and extraction became bigger, and larger initial Li^+ extraction was exhibited at the first charge, which is consistent with the oxidation of Fe^{2+} to Fe^{3+}, as discussed in connected with mössbauer spectra (Figure 10.7). We also can see new sloppy

plateau at 2.8 V during the discharge cycle, which is electrochemical characteriatic of $Li_3Fe_2(PO_4)_3$ phase.[292] This means that the bulk and surface properties of the materials have been changed by formation of disordered $Li_3Fe_2(PO_4)_3$, as well as the α-Fe_2O_3 phase, during air exposure above 180 ˚C, resulting in reduction of the reversible capacity and cyclic retention. The charge-discharge profile of the sample exposed to air at 240 ˚C was totally different from the others. There is longer plateau corresponding to the $Li_3Fe_2(PO_4)_3$ and a distinct electrochemical performance, which means that the formation of disordered phases increases in proportion to the treatment temperature under air.

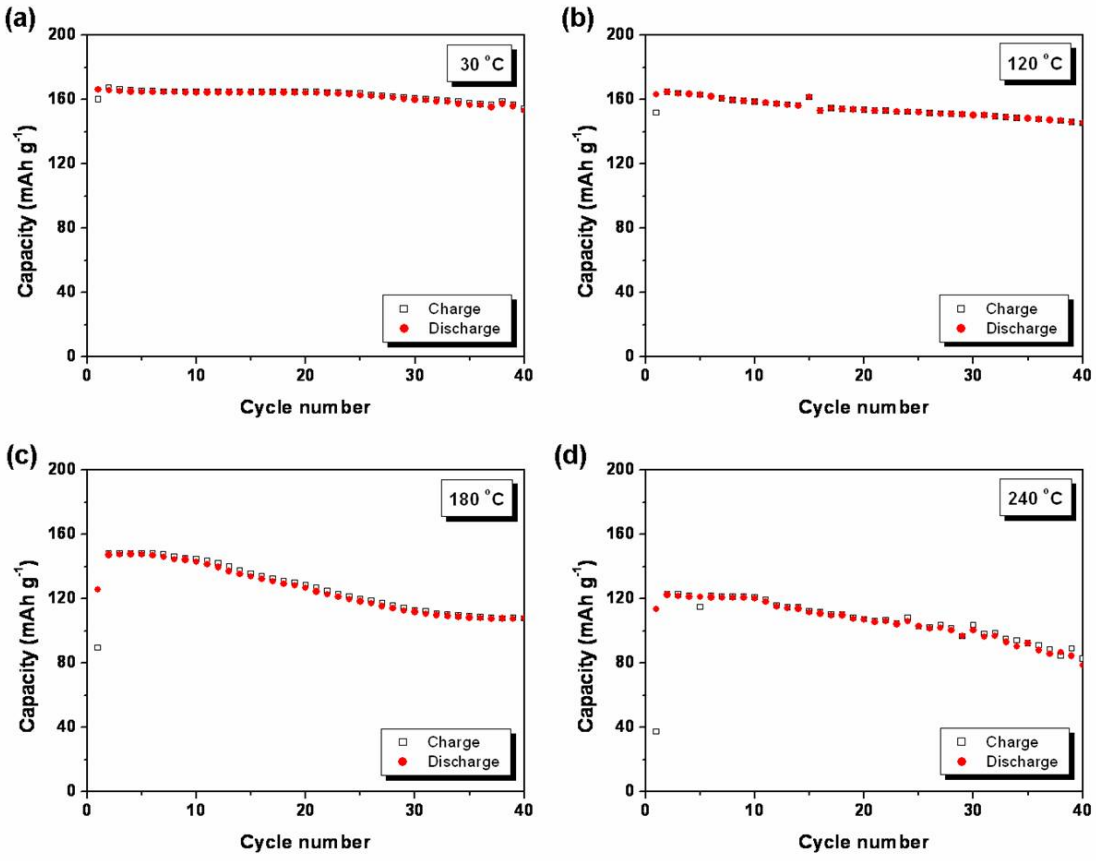

Figure 10.12: *Cyclic performance of the $LiFePO_4$/C nanocomposites exposed to air at different temperature: (a) 30 ˚C, (b) 120 ˚C, (c) 180 ˚C, and (d) 240 ˚C.*

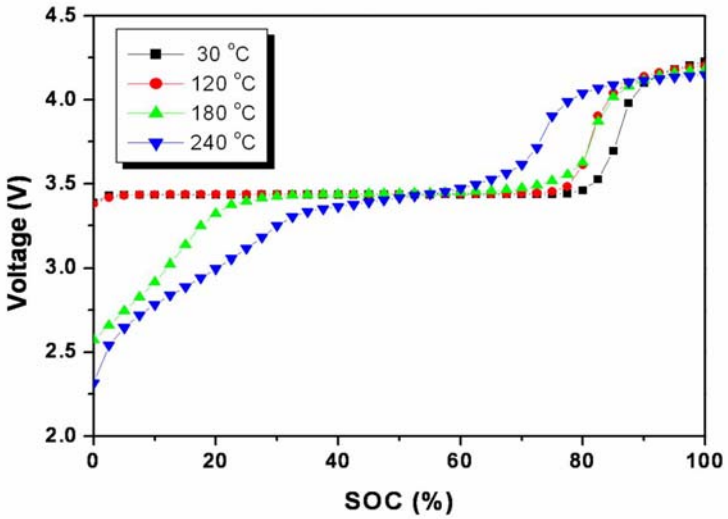

Figure 10.13: *Open circuit voltage (OCV) profiles of the $LiFePO_4$/C nanocomposites exposed to air at different temperature: (a) 30 ˚C, (b) 120 ˚C, (c) 180 ˚C, and (d) 240 ˚C.*

In order to investigate the aging mechanism of $LiFePO_4$/C nanocomposites after air exposure during electrochemical reactions, typical open circuit voltage (OCV) measurements were conducted across the $LiFePO_4$/C nanocomposites exposed to air at different temperatures. The measured OCV profiles show a strong dependence on the treatment temperature under air atmosphere, as shown in Figure 10.13. A significant reduction of Li^+ storage capacity and initial OCV are observed for increasing treatment temperature. It seems that the disordered phases suppressed the charge transfer and increase the polarization because homogeneous Li^+ incorporation could be prevented over the electrochemical reactions, resulting in the degradation of electrochemical performance. More importantly, the formation of disordered phases can be confirmed again as a new sloppy plateau clearly appeared around 2.8 V from 180 ˚C treated

sample, which indicates that additional disordered phase regarded to $Li_3Fe_2(PO_4)_3$ governing electrochemical reactions with Li^+ could be formed during air exposure at high temperature.[292]

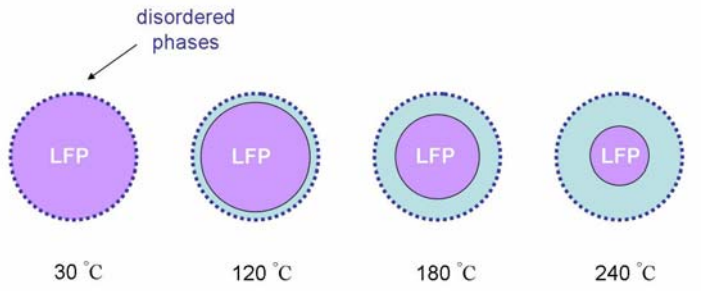

Figure 10.14: *A schematic model of air exposure effects on the $LiFePO_4$/C nanocomposites subjected to the different exposure temperatures.*

We can consider possible reaction mechanisms for the oxidation of Fe^{2+} to Fe^{3+} during air exposure and suggest a schematic model as illustrated in Figure 10.14. The structural change of $LiFePO_4$ after air exposure can be explained by the formation of core-shell structure, where crystalline $LiFePO_4$ would be able to allow the electrochemical reactions and the disordered layer surrounds the crystal $LiFePO_4$ core as a form of α-Fe_2O_3 and $Li_3Fe_2(PO_4)_3$ phase. Initially Li^+ coordinated to the surface of olivine structure could be extracted during air exposure at 30 ˚C, resulting in the formation of intermediate $Li_{1-x}FePO_4$ with an incomplete bonding structure due to Li^+ vacancies at the surface. The amount of Li^+ extraction can be gradually increased without structural deformation of the host structure after 120 ˚C air exposure. This hypothesis is good agreement with increase of solid solution phase in the binary phase diagram of $LiFePO_4$. Air exposure at 180 ˚C allows more Li^+ extraction from the host structure, resulting in the formation of disordered layer due to structural degradation of the surface of materials. The disordered layer composed of $Li_3Fe_2(PO_4)_3$ phases was formed on the

surface through the reaction between $LiFePO_4$ and air during air exposure at this temperature. As the treatment temperature rise, finally, the disordered layer could be growth from the surface to core by increase of treatment temperature and additional disordered α-Fe_2O_3 phase could be formed by variation of PO_4 structure after 240 ˚C air exposure.

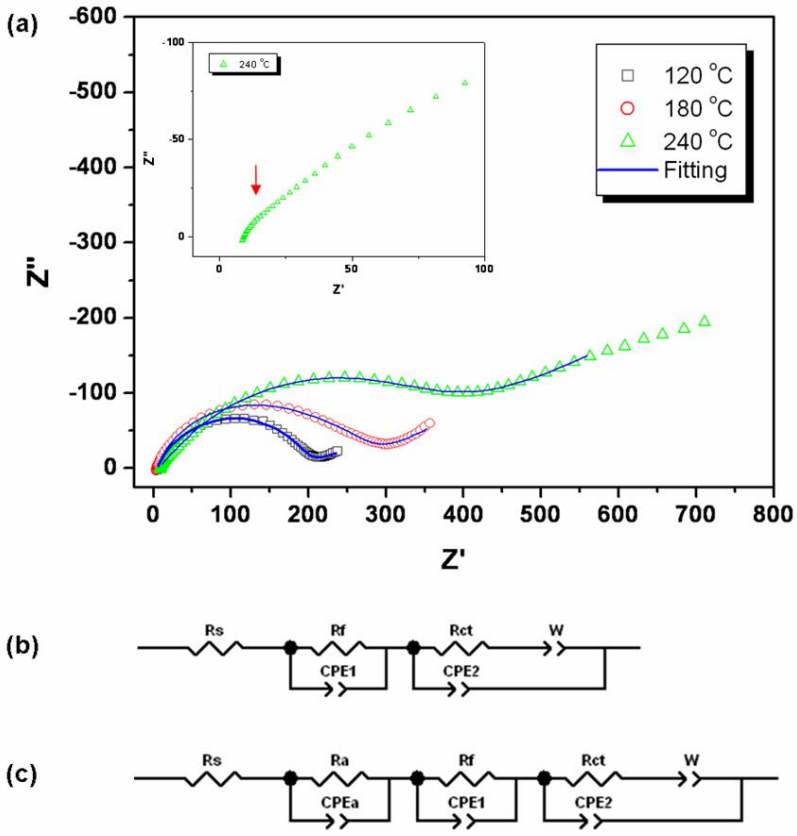

Figure 10.15: *Electrochemical impedance Spectroscopy (EIS) plots of the $LiFePO_4$/C nanocomposites exposed to air at different temperature.*

The existence of the disordered layer on the surface of $LiFePO_4$/C nanocomposites exposed air could be confirmed by electrochemical impedance spectroscopy (EIS). AC impedance measurements were performed with cells containing air exposed samples at different temperatures and lithium metal counter electrode. Electrochemical Impedance Spectroscopy

(EIS) plots and the corresponding equivalent circuit of $LiFePO_4$/C nanocomposite are given in Figure 10.15. It should be noted that the resistance R_f is monotonically increasing with air exposure treatment temperature rise while the resistance R_s is constant in all samples because it is assigned as the bulk resistance of the electrolyte. Considering the two semi-circle system, this impedance behavior could be generally explained by the formation of disordered phase at high temperature based on electron transfer theories.[283] Moreover, an additional component, resistance R_a, was clearly observed and fitted at low frequency after air exposure at 240 ˚C. The origin of R_a could be regarded as the formation of α-Fe_2O_3 phase on the surface of particles.

Table 10.1: *Comparison of lattice parameters and unit-cell volume for $LiFePO_4$/C composites and $FePO_4$ exposed to the different atmosphere.*

Atmosphere	Temperature (°C)	***$LiFePO_4$***			
		a (Å)	b (Å)	c (Å)	V (Å^3)
He	25	10.32636	6.00738	4.69537	291.27408
	30	10.32613	6.00742	4.69568	291.28855
	60	10.32939	6.00904	4.69712	291.54872
	90	10.33314	6.01068	4.69897	291.84925
	120	10.33653	6.0127	4.70113	292.17749
	150	10.33969	6.01449	4.70322	292.48365
	180	10.34302	6.01646	4.70575	292.83125
	240	10.3444	6.01769	4.70753	293.04105
Air	25	10.32695	6.00691	4.69471	291.22707
	30	10.32647	6.00641	4.69478	291.19329
	60	10.32838	6.00801	4.69707	291.46712
	90	10.32987	6.0089	4.6992	291.68515
	120	10.33071	6.00998	4.70162	291.91116
	150	10.32881	6.00988	4.70382	291.98884
	180	10.32188	6.00733	4.7061	291.81104
	240	10.31032	6.00281	4.70992	291.50134

Atmosphere	Temperature (°C)	***$FePO_4$ phase***			
		a (Å)	b (Å)	c (Å)	V (Å^3)
Air	25	9.83327	5.8014	4.77987	272.67588
	30	9.83203	5.80158	4.77977	272.64478
	60	9.83346	5.80411	4.78141	272.89667
	90	9.83559	5.80623	4.78228	273.10521
	120	9.83479	5.80753	4.78268	273.16646
	150	9.83491	5.80935	4.78405	273.33387
	180	9.84203	5.81082	4.78496	273.4357
	240	9.83499	5.81304	4.78637	273.64281

Table 10.2: *Fe-O interatomic distances in Ångstroms obtained (a) from the FEFF fit to the EXAFS spectra and (b) from Rietveld refinement of the X-ray diffraction patterns for the $LiFePO_4$/C nanocomposite exposed to air at various temperatures (30 °C, 120 °C, 180 °C, 240 °C).*

(a)

EXAFS	Fe-O(1)	Fe-O(2)	Fe-O(3)	Fe-O(4)
30 °C	2.0501	2.0859	2.1569	2.1899
120 °C	2.0524	2.0882	2.1592	2.1923
180 °C	2.0499	2.0857	2.1566	2.1896
240 °C	2.0491	2.0849	2.1557	2.1887

(b)

X-ray Rietveld	Fe-O(1)	Fe-O(2)	Fe-O(3)	Fe-O(4)
30 °C	2.06	2.105	2.205	2.254
120 °C	2.062	2.106	2.207	2.256
180 °C	2.061	2.106	2.206	2.256
240 °C	2.06	2.104	2.204	2.256

10.4. Summary

In summary, we have systematically investigated the effects of air exposure on the electrochemical performance and structure of $LiFePO_4$/C nanocomposites as a function of temperature. The discovery that Li^+ extraction from the $LiFePO_4$ would be facilitated and the structure could be changed at high temperature is valuable for extending our understanding of Li^+ insertion and extraction, as well as the aging mechanism of $LiFePO_4$. More importantly, we suggest that storage conditions, especially with regards to temperature and atmosphere, should definitely be considered to avoid undesirable electrochemical degradation of $LiFePO_4$ active materials. This study will form the basis for further identification of the aging mechanism of $LiFePO_4$.

11. Conclusion

This thesis has investigated the electrochemical properties of various SnO_2 nanostructured materials as alternative anode materials, as well as the fundamental crystal chemistry of $LiFePO_4$ as a promising cathode material for use in the next generation of rechargeable lithium-ion batteries. A systematic comparison of the different SnO_2 nanostructured materials, such as the nanopowders, nanowires, and nanotubes described herein, has clearly demonstrated that their electrochemical performance is likely to be related to their distinctive morphological features. The results highlight the advantages and drawbacks of the nanostructured materials and give an important indication for the further improvement of SnO_2 systems. On the other hand, the isolation of solid solutions of $LiFePO_4$ at room temperature as a function of particle size and the impact of air exposure on its electrochemical performance at different temperatures have been systematically demonstrated in order to achieve a comprehensive understanding of the $LiFePO_4$ system.

The specific surface areas of SnO_2 nanostructured materials are mainly responsible for increasing the Li^+ storage, and the single-crystalline SnO_2 nanowire form is better for maintaining electronic conductivity and allowing enhancement of Li^+ diffusion into the SnO_2 structure. Despite the fact that porous SnO_2 nanotube structures are generally more suitable for accommodating volume variations of the Sn phase during cycling, they may also trap more Li^+ during electrochemical cycling, resulting in large irreversible capacities. In addition, the benefit of some structural modifications has been proved in this work. We introduced a novel carbon encapsulation process at low temperature, using carbohydrates as C sources to form C

encapsulated SnO_2 nanopowders and nanowires. This technique is very advantageous to form a homogeneous C layer on the nanostructured materials, without any structural failure. In practice, the desirable crystalline structure and stoichiometry of SnO_2 nanostructured materials were maintained, and the amorphous C layer functions as a sort of framework to maintain the electronic conduction around the active materials. As a result, the large initial irreversible capacity due to non-bonding terminations could be diminished effectively. We expect that the electrochemical performance can be further enhanced by the optimization of C content and better understanding of the reaction mechanism at the interface between SnO_2 nanostructured materials and the amorphous C layer. Another promising structural modification is the formation of nanocomposites with inactive buffer materials which could suppress large volume variation of SnO_2. A mesoporous organosilica nanoarray (MOSN), consisting of a hexagonal array of cylindrical mesoporous organosilica, was employed as a promising buffer phase in SnO_2–MOSN nanocomposite, in which only SnO_2 phase reacted with Li^+. The MOSN, with a high aspect ratio of the length to the width, could effectively accommodate volume changes of SnO_2 as a mechanical buffer, resulting in improvement of the initial coulombic efficiency in the composite.

With regards to $LiFePO_4$, we have presented, for the first time, direct evidence for the isolation of a single phase solid solution of Li_xFePO_4 at room temperature from high resolution synchrotron X-ray diffraction (XRD). The discovery that the single-phase solid solution region of Li_xFePO_4 is in inverse proportion to the particle size at particular compositions would be valuable for completing the currently incomplete room temperature phase diagram and miscibility gap model of $LiFePO_4$. This study will form the basis of further investigations on the room temperature phase diagram of $LiFePO_4$. The first experimental evidence of the effects of

atmosphere exposure has been demonstrated for $LiFePO_4$. We have proven that $LiFePO_4$/C nanocomposites react with ambient air and that some Li^+ is extracted from the particle surface, which leads to a loss of capacity for the first charge and significant changes in bulk and surface properties of the material at high temperatures. This undesirable side reaction has a clear effect on the initial impedance of the cathode. As the reaction is initiated at the particle surface, we should give more attention to this parameter when reducing the size of the olivine particles.

"The unleashed power of the atom has changed everything save our modes of thinking, and we thus drift toward unparalleled catastrophes."

-Albert Einstein (American Physicist, 1879-1955)-

12. References

[1]. S. Coe, *World Rechargeable Battery Markets for Mobile IT and Communication Devices*, in *Environment & Energy series*, **2003**, New York: Frost and Sullivan Research Service, p. 254.

[2]. J.M. Tarascon, M. Armand, *Nature*, **2001**, 414: p. 359.

[3]. R.M. Dell, D.A.J. Rand, *Understanding Batteries*, 1st ed. RSC Paperbacks, **2001**, Cambridge: Royal Society of Chemistry, P. 264.

[4]. C.D.S. Tuck, A. Gilmour, in *Modern Battery Technology* (Ed: C.D.S. Tuck), **1991,** Ellis Horwood, Hemel Hempsted, UK, p. 31.

[5]. I. Buchmann, *Batteries in a Portable World: A Handbook on Rechargeable Batteries for Non-Engineers*, 2nd ed., **2001**, New York: Cadex Electronics Inc., p. 292.

[6]. J.L. Tirado, *Mater. Sci. Eng. R*, **2003**, 40: p. 103.

[7]. D. Linden, T. Reddy, *Handbook of Batteries*, 2nd ed., **1995**, McGraw-Hill Professional.

[8]. J.B. Goodenough, A. Manthiram, B. wnetrzewski, *J. Power Sources*, **1993**, 43: p. 269.

[9]. M. Winter, J.O. Besenhard, M.E. Spahr, P. Novak, *Adv. Mater.*, **1998**, 10: p. 725.

[10]. R.M. Dell, *Solid State Ionics*, **2000**, 134: p. 139.

[11]. A. Robinson, *Science*, **1974**, 184: p. 554.

[12]. K.M. Abraham, D.M. Pasquariello, F.J. Martin, *J. Electrochem. Soc.*, **1986**, 133: p. 661.

[13]. J.N. Carides, D.W. Murphy, *J. Electrochem. Soc.*, **1977**, 124: p. 1309.

[14]. J.J. Auborn, Y.L. Barberio, K.J. Hanson, D.M. Schleich, M.J. Martin, *J. Electrochem. Soc.*, **1987**, 134: p. 580.

[15]. M. Wakihara, *Mater. Sci. Eng. R*, **2001**, 33: p. 109.

[16]. J.R. Dahn, A.K. Sleigh, H. Shi, B.M. Way, W.J. Weydanz, J.N. Reimers, Q. Zhong, U. von Sacken, *Lithium Batteries - New materials, developments and perspectives*, ed. G. Pistoia, **1994**, Amsterdam: Elsevier, p. 707.

[17]. M.S. Whittingham, *Prog. Solid State Chem.***, 1978,** 12: p. 1.

[18]. P. Palvadeau, L. Coic, J. Rouxel, J. Portier, *Mater. Res. Bull.*, **1978**, 13: p. 221.

[19]. D.W. Murphy, P.A. Christian, F.J. DiSalvo, J.N. Carides, *J. Electrochem. Soc.*, **1979**, 126: p. 497.

[20]. G.L. Holleck, J.R. Driscoll, *Electrochim. Acta*, **1977**, 22: p. 647.

[21]. D.W. Murphy, F.J. DiSalvo, J.N. Carides, J.V. Waszczak, *Mater. Res. Bull.*, **1978**, 13: p. 1395.

[22]. M. Lazzari, B. Scrosati, *J. Electrochem. Soc.*, **1980**, 127: p. 773.

[23]. B.D. Pietro, M. Patriaca, B. Scrosati, *J. Power Sources*, **1982**, 8: p. 298.

[24]. S. Basu, *Ambient temperature rechargeable battery*, Patent number US 4,423,125: filing date, 13 Sept. 1982; publication date, 27 Dec. **1983**.

[25]. M. Mohri, N. Yanagisawa, Y. Tajima, H. Tanaka, T. Mitate, S. Nakajima, M. Yoshida, Y. Yoshimoto, T. Suzuki, H. Wada, *J. Power Sources*, **1989**, 26: p. 545.

[26]. T. Nagaura, K. Tozawa, *Prog. Batteries Solar Cells*, **1990**, 9: p. 209.

[27]. K. Sekai, H. Azuma, A. Omaru, S. Fujita, H. Imoto, T. Endo, I. Yamaura, I. Nishi, H. Mashiko, M. Yokogewa, *J. Power Sources*, **1993**, 43-44: p. 241.

[28]. Y. Kida, K. Yanagida, A. Funahashi, T. Nohma, I. Yoneza, *J. Power Sources*, **2001**, 94: p. 74.

[29]. H. Abe, T. Murai, K. Zaghib, *J. Power Sources*, **1999**, 77: p. 110.

[30]. H. Higuchi, K. Uenae, A. Kawakarni, *J. Power Sources*, **1997**, 68: p. 212.

[31]. T. Iwahori, Y. Ozaki, A. Funahashi, H. Momose, I. Mitsuishi, S. Shiraga, S. Yoshitake, H. Awata, *J. Power Sources*, **1999**, 81-82: p. 872.

[32]. Y. Idota, T. Kubota, A. Matsufuji, Y. Maekawa, T. Miyasaka, *Science*, **1997**, 276: p. 1395.

[33]. M.M. Thackeray, W.I.F. David, P.G. Bruce, J.B. Goodenough, *Mater. Res. Bull.*, **1983**, 18: p. 461.

[34]. A.K. Padhi, K.S. Nanjundaswamy, J.B. Goodenough, *J. Electrochem. Soc.*, **1997**, 144: p. 1188.

[35]. A.J. Bard, L.R. Faulkner, *Electrochemical Methods*, 2nd ed., **2001**, New York: John Wiley and Sons Inc., p. 45.

[36]. J.J. Lingane, *Electroanalytical Chemistry*, 2nd ed., **2001**, New York: Wiley Interscience, **1958**, Chap. 3.

[37]. W.C. Gardiner, Jr., *Rates and Mechanisms of Chemical Reactions*, **1969,** New York: Benjamin,.

[38]. K.B. Oldham, *J. Am. Chem. Soc.*, **1955**, 77: p. 4697.

[39]. R.A. Marcus, *J. Chem. Phys.*, **1965**, 43: p. 679.

[40]. B.E. Conway, *Theory and Principles of Electrode Process*, New York: Ronald, **1965**, Chap. 6.

[41]. R.A. Huggins, *Binary Electrodes under Equilibrium or Near-equilibrium Conditions*, in *Materials for Lithium-Ion Batteries*, C. Julien, Z. Stoynov (Eds), **2000**, New York: Kluwer Academic Publishers, p. 74.

[42]. R.A. Huggins, *Lecture note in KAIST*, **2007**, Daejeon, Republic of Korea.

[43]. K. Brandt, *Solid State Ionics*, **1994**, 69: p. 173.

[44]. R. Nesper, *Prog. Solid State Chem.*, **1990**, 20: p. 1.

[45]. *Handbook of Chemistry and Physics*, 68th ed. (Ed: R.C. Weast), **1987,** CRC Press, Boca Raton, FL.

[46]. D. Billaud, E. McRae, A. HØrold, *Mater. Res. Bull.*, **1979**, 14: p. 857.

[47]. S. Dresselhasu, G. Dresselhasu, K. Sugihare, I.L. Spain, H.A. Goldberg, *Graphite Fibres and Filaments*, in *Cardona Manual*, **1988**, New York: Springer, p. 726.

[48]. K. Konishita, *Carbon - Electrochemical and Physicochemical Properties*, **1988**, New York: Wiley-Interscience, p. 560.

[49]. J.R. Dahn, T. Zheng, Y. Liu, J.S. Xue, *Science*, **1995**, 270: p. 590.

[50]. J.O. Besenhard, H. P. Fritz, *Angew. Chem. Int. Ed.*, **1983**, 95: p. 950.

[51]. J.O. Besenhard, M. Winter, in *Proc. of the 2. Ulmer Elektrochemische Tage*, Ladungsspeicherung in der Doppelschicht (Ed: W. Schmickler), Universitätsverlag Ulm, Germany, **1995**, p. 47.

[52]. J.R. Dahn, *Phys. Rev. B*, **1991**, 44: p. 9170.

[53]. K. Kinoshita, *Carbon: Electrochemical and Physicochemical Properties*, **1987**, New York: Wiley.

[54]. R. Yazami, *Lithium Batteries - New Materials, Developments and Perspectives*, ed. G. Pistoia, **1994**, Amsterdam: Elsevier, p. 49.

[55]. T.D. Tran, K. Kinoshita, *J. Electroanal. Chem.*, **1995**, 386: p. 221.

[56]. X.Y. Song, K. Kinoshita, T.D. Tran, *J. Electrochem. Soc.*, **1996**, 143: p. L120.

[57]. R. Moret, in *Intercalation in Layered Materials* (Ed: M.S. Dresselhaus), *NATO ASI Series B*, **1986**, Vol. 148, p. 185.

[58]. J. Rossat-Mignod, D. Fruchart, M.J. Moran, J.W. Milliken, J.E. Fisher, *Synth. Met.*, **1980**, 2: p. 143.

[59]. M. Inaba, Z. Siroma, A. Funabiki, Z. Ogumi, *Langmuir*, **1996**, 12: p. 1535.

[60]. M. Inaba, Z. Siroma, Y. Kawadate, A. Funabiki, Z. Ogumi, *J. Power Sources*, **1997**, 68: p. 221.

[61]. K.A. Hirasawa, T. Sato, H. Asahina, S. Yamaguchi, S. Mori, *J. Electrochem. Soc.*, **1997**, 144: p. L81.

[62]. R. Fong, U. von Sacken, J.R. Dahn, *J. Electrochem. Soc.*, **1990**, 137: p. 2009.

[63]. M. Winter, J.O. Besenhard, P. Novak, *GDCh-Monogr.*, **1996**, 3: p. 438.

[64]. R. Kanno, Y. Kawamoto, Y. Takeda, S. Ohashi, N. Imanishi, O. Yamamoto, *J. Electrochem. Soc.*, **1992**, 139: p. 3397.

[65]. J.Y. Eom, J.W. Park, H.S. Kwon, S. Rajendran, *J. Electrochem. Soc.*, **2006**, 153: p. A1678.

[66]. J. Yin, M. Wada, Y. Kitano, S. Tanase, O. Kajita, T. Sakai, *J. Electrochem. Soc.*, **2005**, 152: p. A1341.

[67]. Z.P. Guo, Z.W. Zhao, H.K. Liu, S.X. Dou, *Carbon*, **2005**, 43: p. 1392.

[68]. M.S. Park, S.A. Needham, G.X. Wang, Y.M. Kang, J.S. Park, S.X. Dou, H.K. Liu, *Chem. Mater.*, **2007**, 19: p. 2406.

[69]. J.O. Besenhard, M. Hess, P. Komenda, *Solid State Ionics*, **1990**, 40-41: p. 525.

[70]. J.O. Besenhard, J. Yang, M. Winter, *J. Power Sources*, **1997**, 68: p. 87.

[71]. A.N. Dey, *J. Electrochem. Soc.*, **1971**, 118: p. 1547.

[72]. R.A. Huggins, in *Fast Ion Transport in Solids* (Eds: B. Scrosati, A. Magistris, C.M. Mari, G. Mariotto), **1993,** Kluwer, Dordrecht, The Netherlands, p. 143.

[73]. R.A. Huggins, *J. Power Sources*, **1989**, 26: p. 109.

[74]. J. Wang, I.D. Raistrick, R.A. Huggins, *J. Electrochem. Soc.*, **1986**, 133: p. 457.

[75]. J.O. Besenhard, H.P. Fritz, *Electrochim. Acta*, **1975**, 20: p. 513.

[76]. A. Anani, S. Crouch-Baker, R.A. Huggins, *J. Electrochem. Soc.*, **1987**, 134: p. 3098.

[77]. I. Hauke, S. Machill, D. Rahner, K. Wiesener, *J. Power Sources*, **1993**, 43-44: p. 421.

[78]. S.V. Sazhin, A.V. Gorodskii, M.Y. Khimchenko, *J. Power Sources*, **1994**, 47: p. 57.

[79]. M. Morita, Y. Matsuda, *J. Power Sources*, **1989**, 26: p. 573.

[80]. R.A. Huggins, *J. Power Sources*, **1988**, 22: p. 341.

[81]. I. Hauke, S. Machill, D. Rahner, K. Wiesener, *J. Power Sources*, **1993**, 43-44: p. 421.

[82]. B.A. Boukamp, G.C. Lesh, R.A. Huggins, *J. Electrochem. Soc.*, **1981**, 128: p. 725.

[83]. A.A. Anani, S. Crough-Baker, R.A. Huggins, *J. Electrochem. Soc.*, **1988**, 135: p. 2103.

[84]. C.K. Huang, S. Subbarao, D.H. Shen, F. Deligiannis, A. Attia, G. Halpert, *Proc. Electrochem. Soc.*, **1991**, 91-93:p 395.

[85]. J.O. Besenhard, H.P. Fritz, E. Wudy, K. Dietz, H. Meyer, *J. Power Sources*, **1985**, 14: p. 193.

[86]. J. Yang, M. Winter, J.O. Besenhard, *Solid State Ionics*, **1996**, 90: p. 281.

[87]. J.O. Besenhard, P. Komenda, A. Paxinos, E. Wudy, M. Josowicz, *Solid State Ionics*, **1986**, 18-19: p. 823.

[88]. T. Nohma, S. Yoshimura, K. Nishio, Y. Yamamoto, S. Fukuoka, M. Hara, *J. Power Sources*, **1996**, 58: p. 205.

[89]. A.M. Wilson, J.R. Dahn, *J. Electrochem Soc.*, **1995**, 142: p. 326.

[90]. N. Koshiba, T. Ikehata, K. Takada, *Natl. Tech. Rep.*, **1991**, 37: p. 64.

[91]. M. Maxfield, T.R. Jow, S. Gould, M.G. Sewchock, L.W. Shacklette, *J. Electrochem. Soc.*, **1988**, 135: p. 299.

[92]. J.O. Besenhard, M. Heû, J. Huslage, K. Jurewicz, U. Krebber, *J. Power Sources*, **1993**, 43-44: p. 493.

[93]. M.M. Thackery, W.I.F. David, J.B. Goodenough , *J. Solid State Chem.*, **1984**, 55: p. 280.

[94]. M.M. Thackery, S.D. Backer, K.T. Andendorff, *Solid State Ionics*, **1985**, 19: p. 175.

[95]. J.J. Auborn, Y.L. Baberio, *J. Electrochem. Soc.*, **1987**, 134: p. 638.

[96]. P. Poizot, S. Laruelle, S. Grugeon, L. Dupont, J.M. Tarascon, *Nature*, **2000**, 407: p. 496.

[97]. M. Dolle, P. Poizot, L. Dupont, J.M. Tarascon, *Electrochem. Solid State lett.*, **2002**, 5: p. A18.

[98]. S. Grugeon, S. Laruelle, R. Herrera-Urbina, L. Dupont, P. Poizot, J.M. Tarascon, *J. Electrochem. Soc.*, **2001**, 148: p. A285.

[99]. G.X. Wang, Y. Chen, K. Konstantinov, J. Yao, J, Ahn, H.K. Liu, S.X. Dou, *J. Alloy Compd.*, **2002**, 340: p. L5.

[100]. D. Larcher, G. Sudant, J.B. Leriche, Y. Chabre, J.M. Tarascon, *J. Electrochem. Soc.*, **2002**, 149: p. A234.

[101]. I.A Courtney, J.R. Dahn, *J. Electrochem. Soc.*, **1997**, 144: p. 2045.

[102]. I.A Courtney, J.R. Dahn, *J. Electrochem. Soc.*, **1997**, 144: p. 2943.

[103]. W. Liu, X. Huang, Z. Wang, H. Li, L. Chen , *J. Electrochem. Soc.*, **1997**, 145: p. 59.

[104]. S.H. Elder, L.H. Doerrer, F.J. DiSalvo, J.B. Parise, D. Guyomard, J.M. Tarascon, *Chem. Mater.*, **1992**, 4: p. 928.

[105]. M. Nishijima, N. Tadokoro, Y. Takeda, N. Imanishi, O. Yamamoto, *J. Electrochem. Soc.*, **1994**, 141: p. 2966.

[106]. S. Suzuki, T. Shodai, *Solid State Ionics*, **1999**, 116: p. 1.

[107]. T. Shodai, Y. Sakurai, T. Suzuki, *Solid State Ionics*, **1999**, 122: p. 85.

[108]. N. Pereira, L.C. Klein, G.G. Amatucci, *J. Electrochem. Soc.*, **2002**, 14: p. A262.

[109]. T. Ohzuku, A. Ueda, N. Yamamoto, *J. Electrochem. Soc.*, **1995**, 142: p. 1431.

[110]. T. Ohziku, K. Tatsumi, N. Matoba, K. Sawai, *J. Electrochem. Soc.*, **2000**, 147: p. 3592.

[111]. L. Kavan, M. Grätzel, *Electrochem. Solid-State Lett.*, **2002**, 5: p. A39.

[112]. K. Kobayashi, K. Kosuge, S. Kachi, *Mater. Res. Bull.*, **1969**, 4: p. 95.

[113]. J.C. Anderson, M. Schieber, *J. Phys. Chem. Solids*, **1964**, 25: p. 961.

[114]. W.D. Johnston, R.R. Heikes, D. Sestrich, *J. Phys. Chem. Solids*, **1958**, 7: p. 1.

[115]. J.B. Goodenough, D.G. Wickham, W.J. Croft, *J. Appl. Phys.*, **1958**, 29: p. 382.

[116]. J.B. Goodenough, D.G. Wickham, W.J. Croft, *J. Phys. Chem. Solids*, **1958**, 5: p. 107.

[117]. K. Kang, Y.S. Meng, J. Bréger, C.P. Grey, G. Ceder, *Science*, **2006**, 311: p. 977.

[118]. A. Andersson, *Surface Phenomena in Li-ion Batteries*. Comprehensive Summaries of Uppsala Dissertations from the Faculty of Science and Technology, Vol. 656, **2001**: Acta Universitatis Upsaliensis, p. 54.

[119]. R. Alcantara, P. Lavela, J.L. Tirado, R. Stoyanova, E. Zhecheva, *J. Solid State Chem.*, **1997**, 134: p. 265.

[120]. G. Ceder, Y.M. Chiang, D.R. Sadoway, M.K. Aydinol, Y.I. Jang, B. Huang, *Nature*, **1998**, 392: p. 694.

[121]. A. Ueda, T. Ohzuku, *J. Electrochem. Soc.*, **1994**, 141: p. 2010.

[122]. W. Li, J.C. Currie, *J. Electrochem. Soc.*, **1997**, 144: p. 2773.

[123]. S. Venkatraman, V. Subramanian, S. Gopukumar, N.G. Renganathan, N. Muniyandi, *Electrochem. Commun.*, **2000**, 2: p. 18.

[124]. T. Ohzuku, A. Ueda, M. Nagayama, Y. Iwakoshi, H. Komori, *Electrochim. Acta*, **1993**, 38: p. 1159.

[125]. M. Broussely, F. Perton, P. Biensan, J.M. Bodet, J. Labat, A. Lecerf, C. Delmas, A. Rougier, J.P. Peres, *J. Power Sources*, **1995**, 54: p. 109.

[126]. S.A. Campbell, C. Bows, R.S. McMillan, *J. Electroanal. Chem.*, **1990**, 284: p. 195.

[127]. R. Kanno, H. Kubo, Y. Kawamoto, T. Kamiyama, F. Izumi, Y. Takeda, M. Takano, *J. Solid State Chem.*, **1994**, 110: p. 216.

[128]. T. Ohzuku, A. Ueda, T. Hirai, *Chem. Express*, **1992**, 7: p. 193.

[129]. R.J. Gummow, D.C. Liles, M.M. Thackeray, *Mater. Res. Bull.*, **1993**, 28: p. 1249.

[130]. J.N. Reimers, E.W. Fuller, E. Rossen, J.R. Dahn, *J. Electrochem. Soc.*, **1993**, 140: p. 3396.

[131]. I. Koetschau, M.N. Richard, J.R. Dahn, J.B. Soupart, J.C. Rouche, *J. Electrochem. Soc.*, **1995**, 142: p. 2906.

[132]. T. Ohzuku, A. Ueda, *Solid State Ionics*, **1994**, 69: p. 201.

[133]. J.M. Tarascon, D. Guyomard, *Solid State Ionics*, **1994**, 69: p. 222.

[134]. M.M. Thackeray, *Mater. Res. Soc. Symp. Proc.*, **1995**, 369: p. 17.

[135]. J.M. Tarascon, D. Guyomard, G.L. Baker, *J. Power Sources*, **1993**, 43-44: p. 689.

[136]. G.T.-K. Fey, W. Li, J.R. Dahn, *J. Electrochem. Soc.*, **1994**, 141: p. 2279.

[137]. N. Kumagai, T. Fujiwara, K. Tanno, T. Horiba, *J. Electrochem. Soc.*, **1993**, 140: p. 3194.

[138]. R.J. Gummow, A. de Kock, M.M. Thackeray, *Solid State Ionics*, **1994**, 69: p. 59.

[139]. J.M. Tarascon, E. Wang, F.K. Shokoohi, W.R. McKinnon, S. Colson, *J. Electrochem. Soc.*, **1991**, 138: p. 2859

[140]. L. Guohua, H. Ikuta, T. Uchida, M. Wakihara, *J. Electrochem. Soc.*, **1996**, 143: p. 178.

[141]. K. Amine, H. Tukamoto, H. Yasuda, Y. Fujita, *J. Electrochem. Soc.*, **1996**, 143: p. 1607.

[142]. A.K. Padhi, V. Manivannan, J.B. Goodenough, *J. Electrochem. Soc.*, **1998**, 145: p. 1518.

[143]. A.K. Padhi, K.S. Nanjundaswamy, C. Masquelier, J.B. Goodenough, *J. Electrochem. Soc.*, **1997**, 144: p. 2581.

[144]. A.K. Padhi, K.S. Nanjundaswamy, C. Masquelier, S. Okada, J.B. Goodenough, *J. Electrochem. Soc.*, **1997**, 144: p. 1609.

[145]. O. Garcia-Martin, M. Alvarez-Vega, F. Garcia-Alvarado, J. Garcia-Jaca, J.M. Gallardo-Amores, M.L. Sanjuán, U. Amador, *Chem. Mater.*, **2001**, 13: p. 1570.

[146]. S. Yang, Y. Song, P.Y. Zavalij, M.S. Whittingham, *Electrochem. Commun.*, **2002**, 4: p. 239.

[147]. S.Y. Chung, J.T. Bloking, Y.M. Chiang, *Nat. Mater.*, **2002**, 1: p. 123.

[148]. N. Ravet, J.B. Goodenough, S. Besner, M. Simoneau, P. Hovington, M. Armand, *Proceedings of the 196th ECS Meeting*, **1999**, Abstract 127.

[149]. H. Huang, S.C. Yin, L.F. Nazar, *Electrochem. Solid-State Lett.*, **2001**, 4: p. A170.

[150]. F. Croce, A. D'Epifanio, J. Hassoun, A. Deptula, T. Olczac, B. Scrosati, *Electrochem. Solid-State Lett.*, **2002**, 5: p. A47.

[151]. P.S. Herle, B. Ellis, N. Coombs, L.F. Nazar, *Nat. Mater.*, **2004**, 3: p. 147.

[152]. C. Delacourt, P. Poizot, S. Levasseur, C. Masquelier, *Electrochem. Solid-State Lett.*, **2006**, 9(7): p. A352.

[153]. J.S. Kim, C.S. Johnson, M.M. Thackeray, *Electrochem. Commun.*, **2002**, 4: p. 205.

[154]. G.J. Moore, C.S. Johnson, M.M. Thackeray, *J. Power Sources*, **2003**, 119-121: p. 216.

[155]. T. Numata, C. Amemiya, T. Kumeuchi, N. Shirakata, M. Yonezawa, *J. Power Sources*, **2001**, 97-98: p. 358.

[156]. J.R. Owen, *Chem. Soc. Rev.*, **1997**, 26: p. 259.

[157]. D. Aurbach, *Nonaqueous Electrochemistry*, **1999**, New York: Marcel Dekker, p. 608.

[158]. B. Marcus, P. Touzain, *J. Solid State Chem.*, **1988,** 77: p. 223.

[159]. A.N. Dey, B.P. Sullivan, *J. Electrochem. Soc.*, **1970**, 117: p. 222.

[160]. D. Guyomard, J. M. Tarascon, *Solid State Ionics*, **1994**, 69: p. 222.

[161]. B. Scrosati, C.A. Vincent, *in Mordern Batteries*, 2nd ed., **1997**, New York: John Wiley & Sons, p. 213.

[162]. J.M. Tarascon, D. Guyomard, G.L. Baker, *J. Power Sources*, **1993**, 43-44: p. 689.

[163]. D. Guyomard, J.M. Tarascon, *J. Electrochem. Soc.*, **1993**, 140: p. 3071.

[164]. J.M. Tarascon, D. Guyomard, *Solid State Ionics*, **1994**, 69: p. 293.

[165]. J.O. Besenhard, M.W. Wagner, M. Winter, A.D. Jannakoudakis, P.D. Jannakoudakis, E. Theodoridou, *J. Power Sources*, **1993**, 43-44: p. 413.

[166]. Y. Ein-Eli, S.R. Thomas, V.R. Koch, *J. Electrochem. Soc.*, **1997**, 144: p. L195.

[167]. B.B. Lakshmi, C.J. Patrissi, C.R. Martin, *Chem. Mater.*, **1997**, 9: p. 2544.

[168]. Y. Wang, J.Y. Lee, H.C. Zeng, *Chem. Mater.*, **2005**, 17: p. 3899.

[169]. W.Y. Li, L.N. Xu, J. Chen, *Adv. Funct. Mater.*, **2005**, 15: p. 851.

[170]. J. Chen, L. Xu, W. Li, X. Gou, *Adv. Mater.*, **2005**, 17: p. 582.

[171]. X. Li, F. Cheng, B. Guo, J. Chen, *J. Phys. Chem. B*, **2005**, 109: p. 14017.

[172]. Y. Wang, K. Takahashi, K. Lee, G. Cao, *Adv. Funct. Mater.*, **2006**, 16: p. 1133.

[173]. S. Nordlinder, L. Nyholm, T. Gustafsson, K. Edström, *Chem. Mater.*, **2006**, 18: p. 495.

[174]. A.R. Armstrong, G. Armstrong, J. Canales, P.G. Bruce, *J. Power Sources*, **2005**, 146: p. 501.

[175]. A.R. Armstrong, G. Armstrong, J. Canales, P.G. Bruce, *Angew. Chem.*, **2004**, 43: p. 2286.

[176]. A.R. Armstrong, G. Armstrong, J. Canales, R. García, P.G. Bruce, *Adv. Mater.*, **2005**, 17: p. 862.

[177]. G. Armstrong, A.R. Armstrong, J. Canales, P.G. Bruce, *Electrochem. Solid-State Lett.*, **2006**, 9: p. A139.

[178]. G. Armstrong, A.R. Armstrong, J. Canales, P.G. Bruce, *Chem. Comm.*, **2005**, 19: p. 2454.

[179]. G.X. Wang, M.S. Park, D. Wexler, J. Chen, H.K. Liu, *Appl. Phys. Lett.*, **2006**, 88: p. 193115.

[180]. M.S. Park, G.X. Wang, Y.M. Kang, D. Wexler, S.X. Dou, H.K. Liu, *Angew. Chem. Int. Ed.*, **2007**, 46: p.750.

[181]. G.X. Wang, J.S. Park, D. Wexler, M.S. Park, J.H. Ahn, *Inorg.Chem.*, **2007**, 46: p.4778.

[182]. C. J. Brinker, G. W. Sherer, *Sol-Gel Science*, **1990**, Academic Press, San Diego.

[183]. M.S. Park, Y.M. Kang, J.H. Kim, G.X. Wang, S.X. Dou, H.K. Liu, *Carbon*, **2008**, 46: p.35.

[184]. M.S. Park, Y.M. Kang, G.X. Wang, S.X. Dou, H.K. Liu, *Adv. Funct. Mater.*, **2008**, 18: p.455.

[185]. G.X. Wang, J.S. Park, M.S. Park, X.L. Gou, *Sensors and Actuators B : Chemical.*, **2008**, in press.

[186]. M.S. Park, G.X. Wang, S.Y. Kim, Y. M. Kang, H.K. Liu, S.X. Dou, *Electrochem.Commun.*, **2007**, 9: p. 71.

[187]. P. Atkins, *Physical Chemistry*, 7th ed., **2002**, New York: Oxford University Press Inc..

[188]. S.J. Kwon, C.W. Kim, W.T. Jeong, K.S. Lee, *J. Power Sources*, **2004**, 137: p. 93.

[189]. P. Scherrer, *Nachr. Ges. Wiss. Goettingen*, **1918**, 2: p. 98.

[190]. B.D. Cullity, *Elements of X-ray diffraction*, 2nd ed., **1977**, Notre Dam, Indiana.

[191]. D.A. Skoog, F.J. Holler, T.A. Nieman, *Principles of Instrumental Analysis*, 5th ed., **1998**, Harcourt Brace & Company.

[192]. S. Brunauer, P.H. Emmett, E. Teller, *J. Am. Chem. Soc.*, **1938**, 60: p. 309.

[193]. P. Gütlich, B.W. Fitzsimmons, R. Rüffer, H. Spiering, *Mössbauer Spectroscopy*, 1st ed., **2003**, Springer.

[194]. D.H. Evans, *Review of voltammetric methods for the study of electrode reactions in microelectrodes: Theory and Applications* in *Nato ASI Series E*, M.I. Montenegro, M.A. Queirós, and J.L. Daschbach (Eds), **1991**, Dordrecht: Kluwer, p. 17.

[195]. J. Kawakita, K. Kobayashi, *J. Power Sources*, **2001**, 101: p. 47.

[196]. J.W. Braithwaite, A. Gonzales, G. Nagasubramanian, S.J. Lucero, D.E. Peebles, J.A. Ohlhausen, W.R. Cieslak, *J. Electrochem. Soc.*, **1999**, 146: p. 448.

[197]. J. Kim, J. Cho, *Electrochem. Solid-State Lett.*, **2006**, 9: p. A373.

[198]. T. Brousse, R. Retoux, U. Herterich, D. Schleich, *J. Electrochem. Soc.*, **1998**, 145: p. 1.

[199]. Y. Yu, C.H. Chen, Y. Shi, *Adv. Mater.*, **2007**, 19: p. 993.

[200]. W. Xiong, Y Wang, C. Yuan, J.Y. Lee, L.A. Archer, *Adv. Mater.*, **2006**, 18: p. 2325.

[201]. L. Yuan, Z.P. Guo, K. Konstantinov, H.K. Liu, S.X. Dou, *J. Power Sources*, **2006**, 159: p. 345.

[202]. R.A. Huggins, *Ionics*, **1998**, 4: p. 129.

[203]. A. Anani, R.A. Huggins, *Proceedings - Electrochemical Society*, **1988**, 88-6 (Proc. Symp. Primary Second. Ambient Temp. Lithium Batteries), **1987**: p.635.

[204]. J. Wang, I.D. Raistrick, R.A. Huggins, *J. Electrochem. Soc.*, **1986**, 133: p. 457.

[205]. R.A. Huggins, *NATO Science Series, 3: High Technology*, **2000**, 85 (Materials for Lithium-Ion Batteries): p. 47.

[206]. R.A. Huggins, *Ionics*, **1998**, 4: p. 129.

[207]. R.A. Huggins, *Ionics*, **1997**, 3: p. 245.

[208]. A. Anani, R.A. Huggins, *J. Power Sources*, **1992**, 38: p. 351.

[209]. A.M. Morales, C.M. Lieber, *Science*, **1998**, 279 : p. 208.

[210]. Z.W. Pan, Z.R. Dai, Z.L. Wang, *Science*, **2001**, 291: p. 1947.

[211]. Kim, M. Noh, M. Choi, J. Cho, B. Park, *Chem. Mater.*, **2005**, 17: p. 3297.

[212]. C.R. Sides, C.R. Martin, *Adv. Mater.*, **2005**, 17: p. 125.

[213]. N. Li, C.R. Martin, *J. Electrochem. Soc.*, **2001**, 148: p. A164.

[214]. J. Fan, T. Wang, C. Yu, B. Tu, Z. Jiang, D. Zhao, *Adv. Mater.*, **2004**, 16: p. 1432.

[215]. S. Han, B. Jang, T. Kim, S.M. Oh, T, Hyeon, *Adv. Funct. Mater.*, **2005**, 15: p. 1845.

[216]. Z. Ying, Q. Wan, H. Cao, Z.T. Song, S.L. Feng, *Appl. Phys. Lett.*, **2005**, 87: p. 113108.

[217]. I.H. Campbell, P.M. Fauchet, *Solid State Commun.*, **1986**, 58: p. 739.

[218]. Y. Cui, Q.Q. Wei, H.K. Park, C.M. Lieber, *Science*, **2001**, 293: p. 1289.

[219]. Y. Huang, X. Duan, Y. Cui, L.J. Lauhon, K.H. Kim, C.M. Lieber, *Science*, **2001**, 294: p. 1313.

[220]. P.G. Collins, M.S. Arnold, P. Avouris, *Science*, **2001**, 292: p. 706.

[221]. A. Bachtold, P. Hadley, T. Nakanishi, C. Dekker, *Science*, **2001**, 294: p. 1317.

[222]. Y. Wang, H.C. Zeng, J.Y. Lee, *Adv. Mater.*, **2006**, 18: p. 645.

[223]. X.W. Lou, Y. Wang, C. Yuan, J.Y. Lee, L.A. Archer, *Adv. Mater.*, **2006**, 18: p. 2325.

[224]. S.A. Needham, G.X. Wang, H.K. Liu, *J. Powder Sources*, **2006**, 159: p. 254.

[225]. M.N. Obrovac, R.A. Dunlap, R.J. Snaderson, J.R. Dahn, *J. Electrochem. Soc.*, **2001**, 148: p. A576.

[226]. H. Li, X. Huang, L. Chen, Z. Wu, Y. Liang, *Electrochem. Solid-State Lett.*, **1999**, 2: p. 547.

[227]. Y.M. Kang, S.M. Lee, S.J. Kim, G.J. Jeong, M.S. Sung, W.U. Choi, S.S. Kim, *Electrochem. Commun.*, **2007**, 9: p. 959.

[228]. S. Yang, H. Song, X. Chen, *Electrochem. Commun.*, **2006**, 8: p. 137.

[229]. Y.M. Kang, J.Y. Go, S.M. Lee, W.U. Choi, *Electrochem. Commun.*, **2007**, 9: p. 1276.

[230]. Y.M. Kang, M.S. Park, M.S. Song, J.Y. Lee, *J. Powder Sources*, **2006**, 162: p. 1336.

[231]. N. Dimov, S. Kugino, M. Yoshio, *Electrochim. Acta*, **2003**, 48: p. 1579.

[232]. W.X. Chen, J.Y. Lee, Z. Liu, *Electrochem. Commun.*, **2002**, 4: p. 260.

[233]. M.S. Park, Y.J. Lee, S. Rajendran, M.S. Song, H.S. Kim, J.Y. Lee, *Electrochim. Acta*, **2005**, 50: p. 5561.

[234]. M. Yoshio, H. Wang, K. Fukuda, T. Umeno, N. Dimov, Z. Ogumi, *J. Electrochem. Soc.*, **2002**, 149: p. A1598.

[235]. S.H. Ng, J. Wang, D. Wexler, K. Konstantinov, Z.P. Guo, H.K. Liu, *Angew. Chem. Int. Ed.*, **2006**, 45: p. 6896.

[236]. W. Bergermayer, I. Tanaka, *Appl. Phys. Lett.*, **2004**, 84: p. 909.

[237]. S. Grugeon, S. Laruelle, L. Dupont, J.M. Tarascon, *Solid State Sci.*, **2003**, 5: p. 895.

[238]. D. Larcher, D. Bonnin, R. Cortes, I. Rivals, L. Personnaz, J.M. Tarascon, *J. Electrochem. Soc.*, 2003, 150: p. A1643.

[239]. M.M. Thackeray, J.T. Vaughey, A.J. Kahaian, K.D. Kepler, R. Benedek, *Electrochem. Commun.*, **1999**, 1: p. 111.

[240]. M. Winter, J.O. Besenhard, *Electrochim. Acta*, **1999**, 45: p. 31.

[241]. N. Li, C.R. Martin, B. Scrosati, *Electrochem. Solid-State Lett.*, **2000**, 3: p. 316.

[242]. A. Concheso, R. Santamarıa, C. Blanco, R. Menendez, J.M. Jimenez-Mateos, R. Alcantara, P. Lavela, J.L. Tirado, *Carbon*, **2005**, 43: p. 923.

[243]. H. Huang, E.M. Kelder, J. Schoonman, *J. Power Sources*, **2001**, 97-98: p. 114.

[244]. R. Zhang, J.Y. Lee, Z.L. Liu, *J. Power Sources*, **2002**, 112: p. 596.

[245]. J.S. Gnanaraj, R.W. Thompson, S.N. Iaconatti, J.F. DiCarlo, K.M. Abraham, *Electrochem. Solid-State Lett.*, **2005**, 8: p. A128.

[246]. S. Guan, S. Inagaki, T. Ohsuna, O. Terasaki, *J. Am. Chem. Soc.*, **2000**, 122: p. 5660.

[247]. C.T. Kresge, M.E. Leonowicz, W.J. Roth, J.C. Vartuli, J.S. Beck, *Nature*, **1990**, 359: p. 710.

[248]. L. Zhao, M. Yosef, M. Steinhart, P. Göring, H. Hofmeister, U. Gösele, S. Schlecht, *Angew Chem. Int. Ed.*, **2006**, 45: p. 311.

[249]. J.Y. Ying, C.P. Mehnert, M.S. Wong, *Angew Chem. Int. Ed.*, **1999**, 38: p. 56.

[250]. S. Inagaki, S. Guan, T. Ohsuna, O. Terasaki, *Nature*, **2002**, 416: p. 304.

[251]. N. Pereira, L.C. Kleina, G.G. Amatuccia, *Solid State Ioics*, **2004**, 167: p. 29.

[252]. Y. Wang, J.Y. Lee, *Electrochem. Commun.*, 2003, 5: p. 292.

[253]. J. Read, D. Foster, J. Wolfenstine, W. Behl, *J. Power Sources*, **2001**, 96: p. 277.

[254]. J. Isidorsson, C.G. Granqvist, L. Haggstrom, E. Nordstrom, *J. Appl. Phys.*, **1996**, 80: p. 2367.

[255]. A. Manthiram, J.B. Goodenough, *J. Power Sources*, **1989**, 26: p. 403.

[256]. M.S. Whittingham, *Chem. Rev.*, **2004**, 104: p. 4271.

[257]. Y. Takeda, K. Nakahara, M. Nishijima, N. Imanishi, O. Yamamoto, M. Takano, R. Kanno, *Mater. Res. Bull.*, **1994**, 29: p. 659.

[258]. A. Le Mehaute, G. Ouvrard, R. Brec, J. Rouxel, *Mater. Res. Bull.*, **1977**, 12: p. 1191.

[259]. R. Brec, A. Dugast, A. Le Mehaute, *Mater. Res. Bull.*, **1980**, 15: p. 619.

[260]. A.S. Andersson, J.O. Thomas, B. Kalska, L. Häggström, *Electrochem. Solid-State Lett.*, **2000**, 3: p. 66.

[261]. V. Srinivasan, J. Newman, *J. Electrochem. Soc.*, **2004**, 151: p. 1517.

[262]. C. Delacourt, P. Poizot, J.M. Tarascon, C. Masquelier, *Nat. Mater.*, **2005**, 4: p. 254.

[263]. A. Yamada, H. Koizumi, S.I. Nishimura, N. Sonoyama, R. Kanno, M. Yonemura, T. Nakamura, Y. Kobayashi, *Nat. Mater.*, **2006**, 5: p. 357.

[264]. G. Chen, X. Song, T.J. Richardson, *Electrochem. Solid-State Lett.*, **2006**, 9: p. A295.

[265]. P.P. Prosini, *J. Electrochem. Soc.*, **2005**, 152: p. A1925.

[266]. A. Yamada, S.C. Chung, K. Hinokuma, *J. Electrochem. Soc.*, **2001**, 148: p. A224.

[267]. K. Amine, H. Yasuda, M. Yamachi, *Electrochem. Solid-State Lett.*, **2000**, 3: p. 178.

[268]. P.P. Prosini, M. Carewska, S. Scaccia, P. Wisniewski, M.Pasquali, *Electrochim. Acta*, **2003**, 48: p. 4205.

[269]. S.Y. Chung, Y.M. Chang, *Electrochem. Solid-State Lett.*, **2003**, 6: p. 278.

[270]. J.L. Dodd, R. Yazami, B.Fultz, *Electrochem. Solid-State Lett.*, **2006**, 9: p. A151.

[271]. C. Delacourt, J. Rodriguez Carvajal, B. Schmitt, J.M. Tarascon, C. Masquelier, *Solid State Sci.*, **2005**, 7: p. 1506.

[272]. J.L. Allen, T. R. Jow, J. Wolfenstine, *Chem. Mater.*, **2007**, 19 : p. 2108.

[273]. C. Delacourt, P. Poizot, J.M. Tarascon, C. Masquelier, *Nat. Mater.*, **2005**, 4: p. 254.

[274]. F. Zhou, T. Maxisch, G. Ceder, *Phys. Rev. Lett.*, **2006**, 97: p. 155704.

[275]. V. Srinivasan, J. Newman, *Electrochem.Solid-State Lett.*, **2006**, 9: p. A110.

[276]. L. Laffont, D. Delacourt, P. Gibot, M.Y. Wu, P. Kooyman, C. Masquelier, J.M. Tarascon, *Chem. Mater.*, **2006**, 18: p. 5520.

[277]. A. Yamada, H. Koizumi, N. Sonoyama, R. Kanno, *Electrochem. Solid-State Lett.*, **2005**, 8: p. A409.

[278]. N. Meethong, H.Y.S. Huang, S.A. Speakman, W.C. Carter, Y.M. Chiang, *Adv. Funct. Mater.*, **2007**, 17: p. 1115.

[279]. N. Meethong, H.Y.S. Huang, W.C. Carter, Y.M. Chiang, *Electrochem. Solid-State Lett.*, **2007**, 10: p. A134.

[280]. M. Wagemarker, W.J.H. Borghols, F.M. Mulder, *J. Am. Chem. Soc.*, **2007**, 129: p. 4323.

[281]. M. Wagemarker, D.R. Simon, E.M. Kelder, J. Schoonman, C. Ringpfeil, U. Haake, D. Lützenkirchen-Hecht, R. Frahm, F.M. Mulder, *Adv. Mater.*, **2006**, 18: p. 3169.

[282]. W. Porcher, P. Moreau, B. Lestriez, S. Jouanneau, D. Guyomard, *Electrochem. Solid-State Lett.*, **2008**, 11: p. A4.

[283]. J.F. Martin, A. Yamada, G. Kobayashi, S. Nishimura, R. Kanno, D. Guyomard, N. Dupréb, *Electrochem. Solid-State Lett.*, **2008**, 11: p. A12.

[284]. W. Kündig, H. Bömmel, *Phys. Rev.*, **1966**, 142: p. 327.

[285]. Q.A. Pankhurst, C.E. Johnson, M.F. Thomas, *J. Phys. C*, **1986**, 19: p. 7081.

[286]. Y.H. Rho, L.F. Nazar, L. Perry, D. Ryan, *J. Electrochem. Soc.*, **2007**, 154: p. A283.

[287]. C.M. Burba, R. Frech, *J. Electrochem. Soc.*, **2004**, 151: p. A1032.

[288]. A.A. Salah, P. Jozwiak, K. Zaghib, J. Garbarczyk, F. Gendron, A. Mauger, C.M. Julien, *Spectrochim. Acta Part A*, **2006**, 65: p. 1007.

[289]. A. Deb, U. Bergmann, S.P. Crammer, E.J. Cairns, *Electrochim. Acta.*, **2005**, 50: p. 5200.

[290] S. Scaccia, M. Berrettoni, *Inorgarnic chem*, **2006**, 45: p. 2750.

[291] M. Morcrette, C. Wurm, C. Masquelier, *Solid State Sciences*, **2002**, 4: p. 239.

List of Figures

Figure 9.3: *Left: magnified view of the (200) peak correlated with different particle sizes for solid solution $Li_{0.93}FePO_4$ phase at room temperature: (a) particle size of 200 nm, (b) particle size of 80 nm, and (c) particle size of 40 nm. Right: the a-axis lattice parameter and solubility, β, as functions of the composition for different particle sizes.*

Figure 10.1: *An image of the sealed tube furnace, which allow no contact with air over the whole procedure in this work.*

Figure 10.2: *XRD pattern and SEM image (inset) of $LiFePO_4$/C nanocomposite synthesized by solid state reaction without air contact.*

Figure 10.3: *XRD patterns for $LiFePO_4$/C nanocomposites exposed from 25 ˚C to 240 ˚C to different atmosphere: (a) Air and (b) He. The exposure time was fixed at 36 hours.*

Figure 10.4: *FESEM images of the air-exposed $LiFePO_4$/C nanocomposites at different temperatures: a) 30 ˚C, b) 120 ˚C, c) 180 ˚C, and d) 240 ˚C.*

Figure 10.5: *Comparison of lattice parameters of $LiFePO_4$/C nanocomposites as a function of exposure temperatures under the air and He. The variations are shown in (a) lattice parameter a, (b) lattice parameter b, (c) lattice parameter c, and (d) the unit-cell volume in the $LiFePO_4$/C nanocomposites.*

Figure 10.6: *Comparison of lattice parameters of $LiFePO_4$ and $FePO_4$ as a function of exposure temperatures under the air. The variations are shown in (a) lattice parameter a, (b) lattice parameter b, (c) lattice parameter c, and (d) the unit-cell volume in the $LiFePO_4$.*

Figure 10.7: *Mössbauer spectra of the $LiFePO_4$/C nanocomposites exposed to air at different atmospheres; (a) 30 ˚C, (b) 120 ˚C, (c) 180 ˚C, and (d) 240 ˚C.*

Figure 10.8: *X-ray photoelectron spectroscopy (XPS) profiles of the $LiFePO_4$/C nanocomposites after different temperatures of air exposure.*

Figure 10.9: *Fourier transform infrared (FTIR) spectra of the $LiFePO_4$/C nanocomposites exposed to air at different atmospheres; (a) 30 ˚C, (b) 120 ˚C, (c) 180 ˚C, and (d) 240 ˚C.*

Figure 10.10: *(a) Calibrated and normalized XANES (X-ray Absorption Near Edge Spectroscopy) data at Fe K-edge of $LiFePO_4$ after air exposure at various temperatures, (b) The enlarged pre-edge region of XANES at the Fe K-edge (c) $d^2(Absorption)/dE^2$ vs. E (Photon Energy) plot, which shows the t_{2g} and e_g absorption bands. (d) Comparison of the radial distribution function obtained after Fourier transformation of k^3-weighted $[k^3\chi(k)]$ Fe EXAFS data on $LiFePO_4$ after air exposure at various temperatures.*

Figure 10.11: *Charge-discharge profiles of the $LiFePO_4$/C nanocomposites exposed to air at different temperature: (a) 30 ˚C, (b) 120 ˚C, (c) 180 ˚C, and (d) 240 ˚C.*

Figure 10.12: *Cyclic performance of the $LiFePO_4$/C nanocomposites exposed to air at different temperature: (a) 30 ˚C, (b) 120 ˚C, (c) 180 ˚C, and (d) 240 ˚C.*

Figure 10.13: *Open circuit voltage (OCV) profiles of the $LiFePO_4$/C nanocomposites exposed to air at different temperature: (a) 30 ˚C, (b) 120 ˚C, (c) 180 ˚C, and (d) 240 ˚C.*

Figure 10.14: *A schematic model of air exposure effects on the $LiFePO_4$/C nanocomposites subjected to the different exposure temperatures.*

Figure 10.15: *Electrochemical impedance Spectroscopy (EIS) plots of the $LiFePO_4$/C nanocomposites exposed to air at different temperature.*

List of Tables

List of Symbols and Abbreviations

Symbol/Abbreviation	Name
A	Area
Å	Anstrom
AAO	Anodic Aluminum Oxide
AB	Acetylene black
a	Molar weight of adsorbed species
atm	Atmospheric pressure
BET	Brunauer-Emmett-Teller specific surface area
BJH	Barret−Joyner−Halenda algorithm
BTEB	1,4-bis(triethoxysilyl) benzene
b_a	Anodic Tafel slope
b_c	Cathodic Tafel slope
C	C-rate
C_{50} / C_2	Ratio of capacity retention 50^{th} cycle to 2^{nd} cycle
C_{50} / C_{10}	Ratio of capacity retention 50^{th} cycle to 10^{th} cycle
C	Number of components
C_{dl}	Double layer capacitance
C_f	Passive film capacitance
ccp	Cubic close packed
cm	Centimetre
CCV	Closed circuit voltage
CNT	Carbon nanotube

Cr-SS	Cr-hardened stainless steel
CV	Cyclic voltammetry
D	Diffusion coefficient
d	Interfacial spacing
DC	Direct current
DEC	Diethyl carbonate
DMC	Dimethyl carbonate
DOD	Depth of discharge
DTA	Differential Thermal Analysis
e	Electron charge
EC	Ethylene carbonate
EDX	Energy dispersive x-ray spectroscopy
E_b	Electron binding energy
E_k	Kinetic energy
E_w	Work function
e.g.	Exempli gratia, in Latin meaning “for example”
E_g	Energy gap at room temperature
EIS	Electrochemical impedance spectroscopy
et al.	Latin, meaning “and others”
eV	Electron volt
E	Cell potential
E^0	Standard cell potential
E_A	Anodic potential
E_A^0	Standard anodic potential

E_C	Cathodic potential
E_C^0	Standard cathodic potential
E_g	Electrolyte stability window
exp	Exponential
F	Faraday constant, 95484.56 $Cmol^{-1}$
F	Degrees of freedom
FESEM	Field Emission Scanning Electron Microscopy
FP	Iron phosphate ($FePO_4$)
FWHM	Full width at half maximum
fcc	Face centered cubic
g	Gram
ΔG	Gibbs free energy change
ΔG_f	Gibbs free energy of formation
ΔG^0	Standard gibbs free energy change
ΔH	Enthalpy change
$\Delta H_{\text{int}\,rinsic}$	Intrinsic Enthalpy change
ΔH_D	Dimensional Entalphy change
h	Hour
HEV	Hybrid electric vehicle
Hz	Hertz
I	Intensity
I	Current
i_0	Exchange current density

i_a	Anodic current
i_c	Cathodic current
ICDD	International Centre for Diffraction Data
i.e	Latin meaning “that is”
ISEM	Institute for Superconducting & Electronic Materials
J	Flux of diffusing species
JCPDS	Joint Committee on Powder Diffraction Standards
K	Kelvin
K	Rate constant
K_{eq}	Equilibrium constant
κ, κ_B	Boltzmann constant, J/K
Li^+	Lithium ion
LFP	Lithium iron phosphate ($LiFePO_4$)
log	Logarithm
m	Mass
M	Molar concentration
$mAhg^{-1}$	Milli ampere hour per gram
min	Minute
mm	Millimetre
MOSN	Mesoporous organo silica nanoarray
M_r	Molecular mass
NP	Nanopowders
NT	Nanotubes

NW	Nanowires
n	Number of moles
nm	Nanometer
N	Avogadro's number
NMP	N-methyl pyrrolidinone
OCV	Open circuit voltage
ODF	Orientation distribution function
ODTMA	Octadecyltrimethyl ammonium
P	Pressure
P	Number of phases
PC	Propylene carbonate
PVdF	polyvinylidene fluoride
Q	Capacity
R	Electrical resistance
r	Resistance of the cell
R	Gas constant, 8.314472 $J.K^{-1}mol^{-1}$
R_{ct}	Charge transfer resistance
R_f	Resistance of passive film
R_p	Profile refinement factor, %(Rietveld)
R_s	Sheet resistance
R_s	Resistance of solution
R_{wp}	Weighted pattern refinement factor, %(Rietveld)
ppm	Parts per million
pvdF	Polyvinylidenfluoride

S	Siemens
SS	Solid Solution
s	Adsorption cross section
S_{BET}	Specific surface area
$S_{BET,total}$	Total surface area
ΔS	Entropy change
SAED	Selected area electron diffraction
sccm	Standard cubic centimeters per minute
sec	Second
SEI	Solid electrolyte interphase
SEM	Scanning electron microscopy
SOC	State of charge
t	Time, sec, min, h
T	Temperature, K
T_s	Equilibrium temperature
TEM	Transmission electron microscopy
TGA	Thermo-gravimetric analysis
Torr	Unit of pressure
V	Volt
V	Volume
V_{cell}	Cell potential
V_{oc}	Open circuit voltage
v	Scan rate

Ver.	Version
VLS	Vapor-Liquid-Solid
vs.	Versus
W	Electrical work
W	Warburg diffusion in bulk solid (EIS)
w	Weight, mg, g, kg
wt%	Weight percent
XPS	X-ray photoemission spectroscopy
XRD	X-ray diffraction
ZDF	Zero degree of freedom
1D	One dimensional
χ	Magnetic susceptibility
μ	Absorption co-efficient or micro
h	Planck constant, Js
μ_{Li}	Chemical potential of Lithium
μ_i	Chemical potential of reactant *i*
ν	Frequency of light
ν	Kinetic velocity
ν_0	Initial frequency
ν_{vib}	Vibrational frequency
ν_i	Stoichiometric reaction coefficient of reactant *i*
2θ	Diffraction angle (XRD)
Ω	Ohm
°	Degree

$^{\circ}$ C	Degree Celsius
ϕ	Phi angle
ψ	Azimuthal angle
ξ	Extent of reaction in one mole
ρ	Density
η	Overvoltage or polarization
α	Symmetry factor of the electrical double layer
β	Full width at half maximum (Scherrer Eqn)
λ	Wavelength
θ_p	Pauli-Weiss temperature
χ^2	Chi squared test (Statistical method)
ε	Permittivity of SEI layer

List of Materials and Chemicals

Chemical Name/Material	Reagent	Grade,%	Supplier
Acetone	C_3H_6O	99	Aldrich
Acetonitrile	C_2H_3N	99	Aldrich
Acetylene black	C	99.99	Lexel
Ammonium dihydrogenphosphate	$NH_4H_2PO_4$	99	Wako
1,4-bis(triethoxysilyl) benzene	$C_6H_4(Si(OC_2H_5)_3)_2$	99	Aldrich
Diethylcarbonate	$(C_2H_5O)_2CO$	99	Aldrich
Ethanol	C_2H_5OH	100	Aldrich
Ethylene carbonate	$C_3H_4O_3$	99	Aldrich
Hydrochloric acid	HCl	2M	Aldrich
Iron oxalate dehydrate	$FeC_2O_4.2H_2O$	99	JUNSEI
Ketjen Black	C	99	LION
Lithium carbonate	Li_2CO_3	99.9	Wako
Lithium hexafluorphosphate	$LiPF_6$	1M	Aldrich
Lithium hydroxide	$LiOH.H_2O$	99.95	Aldrich
Lithium iodide	LiI	99.8	Aldrich
Malic acid	$C_4H_6O_5$	99	Aldrich
N-methylpyrrolidinone, NMP	C_5H_9NO	99.5	Aldrich
Nitronium tetrafluoro-borate	NO_2BF_4	96	Alfa Aesar
Octadecyltrimethylammonium	$C_{21}H_{46}CIN$	99.5	Aldrich
Polypropylene separator	$(C_3H_6)_n$	100	Celgard
Polyvinylidene fluoride, PVdF	$(C_2H_2F_2)_n$	99	Aldrich

Sodium citrate dehydrate	$Na_3C_6H_5O_7.2H_2O$	99	BCH
Sodium hydroxide	NaOH	>98	Aldrich
Tin	Sn	99.9	Aldrich
Tin (II) chloride dehydrate	$SnCl_2.\ 2H_2O$	98	Aldrich
Tin (II) oxide	SnO	99.9	Aldrich
Tin (IV) oxide	SnO_2	99.9	BCH
Toluene	C_7H_8	99.5	Aldrich

List of Publications

International publications

(1) Yong-Mook Kang, Min-Sang Song, Jin-Ho Kim, Hyun-Seok Kim, **Min-Sik Park**, Jai-Young Lee, H.K. Liu, S.X. Dou, A study on the charge-discharge mechanism of Co_3O_4 as an anode for the Li ion secondary battery, *Electrochimica Acta*, Vol.50, Iss.18, pp.3667-3673 (2005).

(2) S.Rajendran, Min-Sang Song, **Min-Sik Park**, Jin-Ho Kim, and Jai-Young Lee, Lithium ion conduction in PVC-$LiN(CF_3SO_2)_2$ electrolytes gelled with PVdF, *Materials Letters*, Vol.59, Iss.18, pp.2347-2351 (2005).

(3) Hyun-Seok Kim, Ho Lee, Kyu-Sung Han, Jin-Ho Kim, **Min-Sik Park,** Jai-Young Lee and Jung-Ku Kang, Hydrogen Storage in Ni Nanoparticles-Dispersed Multi-Walled Carbon Nanotubes, *The Journal of Physical Chemistry B*, Vol.109, Iss.18, pp.8983-8986 (2005).

(4) Kyu-Sung Han, Hyun-Seok Kim, Min-Sang Song, **Min-Sik Park**, Sang-Soo Han, Jai-Young Lee and Jung-Ku Kang, Atmospheric-pressure plasma treatment to modify hydrogen storage properties of multiwalled carbon nanotubes, *Applied Physics Letters*, Vol.86, 263205 (2005).

(5) **Min-Sik Park**, Yong-Ju Lee, S.Rajendran, Min-Sang Song, Hyun-Seok Kim, and Jai-Young Lee, Electrochemical properties of Si/Ni alloy-graphite composite as an anode material for Li-ion batteries, *Electrochimica Acta*, Vol.50, Iss.28, pp.5561-5567 (2005).

(6) **Min-Sik Park**, S. Rajendran, Yong-Mook Kang, Kyu-Sung Han, Young-Soo Han and Jai-Young Lee, Si/Ni alloy-graphite composite synthesized using arc-melting and high energy ball-milling for use as anode in lithium ion batteries, *Journal of Power Sources*, Vol.158, Iss.1, pp.650-653 (2006).

(7) **Min-Sik Park**, Yong-Mook Kang, S. Rajendran, Hyuk-Sang Kwon and Jai-Young Lee, Si-Ni-C composite synthesized using high energy mechanical milling for use as an anode in lithium ion batteries, *Materials Chemistry and Physics*, Vol. 100, Iss.2-3, pp. 496-502 (2006).

(8) **Min-Sik Park**, Yong-Ju Lee, Young-Soo Han and Jai-Young Lee, Effects of mechanical milling and arc melting processes on the electrochemical performance of Si-based composite materials, *Materials Letters*, Vol.60, Iss.25, pp.3079-3093 (2006).

(9) **M. S. Park**, G.X. Wang, H.K. Liu and S.X. Dou, Electrochemical properties of Si thin film prepared by Pulsed Laser Deposition for lithium ion micro-batteries, *Electrochimica Acta*, Vol.51, Iss.25, pp.5246-5249 (2006).

(10) G.X. Wang, **M.S. Park**, D. Wexler, J. Chen and H.K. Liu, Synthesis and characterisation of one dimensional CdSe nanostructures, *Applied Physics Letters*, Vol.88, 193115 (2006).

(11) Yong-Mook Kang, **Min-Sik Park**, Min-Sang Song and Jai-Young Lee, A relation between the enhanced Li ion transfer and the improvement of electrochemical performance in Si-Cu-Carbon composite, *Journal of Power Sources*, Vol.162, Iss.2, pp.1336-1340 (2006).

(12) **M.S. Park**, G.X. Wang, S.Y. Kim, Y. M. Kang, H.K. Liu and S.X. Dou, Mesoporous organo-silica nanoarray for energy storage media, *Electrochemistry Communications*, Vol. 9, pp. 71-75 (2007).

(13) **Min-Sik Park**, Guo-Xiu Wang, Yong-Mook Kang, David Wexler, Shi-Xue Dou and Hua-Kun Liu, Preparation and electrochemical properties of abundant SnO_2 nanowires for application in lithium ion batteries, *Angewandte Chemie - International Edition*, Vol.46, Iss.5, pp.750-753 (2007).

(14) Yong-Mook Kang, **Min-Sik Park**, Min-Sang Song, Young-Soo Han, Jai-Young Lee, A relation between the electrochemical behaviors and morphology of Ni-Co_3O_4 composites prepared by the chemical reduction method or the mechanical milling, *Materials Chemistry and Physics,* Vol.105, Iss.2-3, pp.245-249 (2007).

(15) **Min-Sik Park**, Scott Andrew Needham, Guo-Xiu Wang, Yong-Mook Kang, Jin-Soo Park, Shi-Xue Dou and Hua-Kun Liu, Nanostructured SnSb/carbon nanotube composites synthesized by reductive precipitation for lithium ion batteries, *Chemistry of Materials,* Vol.19, Iss.10, pp.2406-2410 (2007).

(16) Yong-Mook Kang, **Min-Sik Park**, Jai-Young Lee and Hua-Kun Liu, Phase-controlled Si/Cu-Carbon composite as an anode material for Li ion secondary battery, *Carbon*, Vol.45, Iss.10, pp.1928-1933 (2007).

(17) Gou-Xiu Wang, Jin-Soo Park, David Wexler, **Min Sik Park**, and Jung-Ho Ahn, Synthesis, characterization and optical properties of In_2O_3 semiconductor nanowires, *Inorganic Chemistry,* Vol.46, Iss.12, pp.4778-4780 (2007).

(18) **Min-Sik Park**, Yong-Mook Kang, Jung-Ho Kim, Guo-Xiu Wang, Shi-Xue Dou and Hua-Kun Liu, Effects of low-temperature carbon encapsulation on the electrochemical performance of SnO_2 nanopowders*, Carbon,* Vol.46, Iss.1, pp.35-40 (2008).

(19) **Min-Sik Park**, Yong-Mook Kang, Gou-Xiu Wang, Shi-Xue Dou and Hua-Kun Liu, The effect of morphological modification on the electrochemical properties of SnO_2 nanomaterials for lithium ion battery, *Advanced Functional Materials,* Vol.18, Iss.3, pp.455-461 (2008).

(20) **Min-Sik Park**, Yong-Mook Kang, Shi-Xue Dou and Hua-Kun Liu, Reduction-free synthesis of carbon encapsulated SnO_2 nanowires and their superiority in electrochemical properties, *The Journal of Physical Chemistry C* (2008) accepted.

(21) G.X. Wang, J.S. Park, **M.S. Park**, X.L. Gou, Synthesis and high gas sensitivity of tin oxide nanotubes, *Sensors and Actuators B : Chemical.* Vol.131, Iss.1, pp.313-317 (2008).

(22) G. Kobayashi, S.I. Nishimura, **Min-Sik Park**, A. Yamada, R. Kanno and T. Ida, Isolation of solid solution phase in Li_xFePO_4 at room temperature, *Advanced Materials* (2008) submitted.

(23) **Min-Sik Park**, G. Kobayashi, S.I. Nishimura , A. Yamada, R. Kanno, S.X. Dou, H.K. Liu and Y.M. Kang, The effect of air exposure on the electrochemical properties of $LiFePO_4$ and its temperature dependence, *Advanced Materials* (2008) submitted.

National publications

(1) Yong-Mook Kang, Yong-Ju Lee, Min-Sang Song, **Min-Sik Park**, and Jai-Young Lee, A Relation between the Electrochemical Behaviors and Morphology of Co_3O_4 and Ni-Co_3O_4 Composites as Anode Materials for Li Ion Secondary Batteries, Trans. of the Korean Hydrogen and New Energy Society, Vol. 14, No. 3, pp. 217-228 (2004).

Conference

International conferences

(1) **Min-Sik Park**, Yong-Mook Kang, Min-Sang Song, Hyuk-Sang Kwon and Jai-Young Lee, Electrochemical properties of the Si-Cu-C composite as an anode material of Li-ion batteries, The 207th Meeting of The Electrochemical Society, Quebec city, Canada, May 15-20 (2005).

(2) Min-Sang Song, Yong-Mook Kang, Hyun-Seok Kim, **Min-Sik Park**, Kyu-Sung Han, Hyuk-Sang Kwon, Jai-Young Lee, Synthesis and Improvement of Electrochemical Properties of $LiFePO_4$ by Microwave Heating, The 208th ECS meeting, Los Angeles, USA, October 16-21 (2005).

(3) **M.S. Park**, G.X. Wang, H.K. Liu and S.X. Dou, Electrochemical properties of Si thin film prepared by Pulsed Laser Deposition for lithium ion micro-batteries, International Symposium on Electromaterials Science, Wollongong, Australia, Feb. 15-17 (2006).

(4) G.X. Wang, **M.S. Park**, D. Wexler, J. Chen and H.K. Liu, Synthesis and characterisation of one dimensional CdSe nanostructures, International Symposium on Electromaterials Science, Wollongong, Australia, Feb. 15-17 (2006).

(5) G.X. Wang, **M.S. Park**, S.A. Needham, J. Yao and H.K. Liu, Nanostructured anode materials for lithium-ion batteries, The 13th International Meeting on Lithium Batteries, Biarritz, France, June 18-23 (2006).

(6) **M.S. Park**, Y.M. Kang, G.X. Wang, J. Park, S.X. Dou and H.K. Liu, Low-Temperature Carbon Coating on SnO_2 Nanopowders for Lithium Ion Batteries, The 211th Meeting of The Electrochemical Society, Chicago, USA, May 6-10 (2007).

(7) **M.S. Park**, G.X. Wang, Y.M. Kang, D. Wexler, S.X. Dou and H.K. Liu, Controlled Growth of SnO_2 Nanowires for Application in Lithium Ion Batteries, The 211th Meeting of The Electrochemical Society, Chicago, USA, May 6-10 (2007).

(8) J.S. Park, **M.S. Park**, G.X. Wang, Tin (IV) oxide nanotubes for gas sensor applications, Nanoelectronic Devices for Defense & Security Conference 2007, Crystal city, Virginia, USA, June 18-21 (2007).

(9) **M.S. Park**, G.X. Wang, Y.M. Kang, S.X. Dou and H.K. Liu, The effect of morphological modification on the electrochemical properties of SnO_2 nanomaterials, International Conference

on Nanoscience and Nanotechnology 2008, Melbourn, Victoria, Australia, Feb. 25-29 (2008) submitted.

Domestic conferences

(1) **Min-Sik Park**, Yong-Mook Kang, Min-Sang Song, and Jai-Young Lee, A Study on the electrochemical properties of the Si-Ni-C composite as an anode material of Li-ion batteries, Korean Institute of Metals and Materials, Fall Meeting, Busan Oct.(2004).

(2) Kyu-Sung Han, Hyun-Seok Kim, Jin-Ho Kim, **Min-Sik Park** and Jai-Young Lee, A Study on the Characteristics of Hydrogen Storage and Structure of CNTs prepared by Thermal CVD, Korean Institute of Metals and Materials, Fall Meeting, Busan Oct. (2004).

(3) **M.S. Park**, G.X. Wang, H.K. Liu and S.X. Dou, Electrochemical properties of Si thin film electrodes, 30th annual condensed matter and materials meeting, Wagga Wagga, Australia, Feb. 7~10 (2006).

(4) G.X. Wang, **M.S. Park**, D. Wexler, J. Chen and H.K. Liu, Preparation of cadmium selenide nanowires and nanotubes, 30th annual condensed matter and materials meeting, Wagga Wagga, Australia, Feb. 7~10 (2006).

(5) **M.S. Park**, S.A. Needham, G.X. Wang, Y.M. Kang, J.S. Park, S.X. Dou and H.K. Liu, Nanostructured SnSb/carbon nanotubes composites synthesized by reductive precipitation for lithium ion batteries, ARC centre meeting on Electromaterials Science, Wollongong, Australia, Feb. 5~7 (2007).

Patent

(1) The method to modify the structure of a carbon nanotube for hydrogen storage by atmospheric pressure plasma, 10-2005-0035061 (Korea).

(2) The method for improvement of cycle life and capacity of Si-based anode materials for lithium ion secondary batteries by adding Ni, (2005) patent applied for Korea, Japan and USA.

Additional Responsibility

- 2006 autumn semester: Laboratory Demonstrator of undergraduate course – Current Perspective in Nanotechnology at University of Wollongong.

- 2006 spring semester: Teaching Assistant (TA) of undergraduate course – Current Perspective in Nanotechnology at University of Wollongong.